Vilnius University

Diversiform black silicon for bio-sensing

Lena Golubewa

DOCTORAL DISSERTATION
2023

Natural Sciences
Physics **N 002**

https://doi.org/10.15388/vu.thesis.493
https://orcid.org/0000-0003-2125-6366

VILNIUS UNIVERSITY
CENTER FOR PHYSICAL SCIENCES AND TECHNOLOGY

Lena Golubewa

Diversiform black silicon for bio-sensing

DOCTORAL DISSERTATION

Natural Sciences,
Physics (N 002)

VILNIUS 2023

This dissertation was prepared between 2019 and 2023 (State research institute Center for Physical Sciences and Technology). The research was supported by the Research Council of Lithuania with scholarships that were granted for academic accomplishments twice: for the years 2020 and 2021, and financial support for research visit to the University of Eastern Finland (Joensuu, Finland) for four weeks during the first semester in 2022.

Academic supervisor – Dr. Renata Karpicz (Center for Physical Sciences and Technology, Natural Sciences, Physics – N 002).
Academic consultant – Prof. Dr. Polina Kuzhir (Center for Photonics Sciences, University of Eastern Finland, Natural Sciences, Physics – N 002)

This doctoral dissertation will be defended in a public meeting of the Dissertation Defense Panel:

Chairman – Prof. Habil. Dr. Gediminas Niaura (Center for Physical Sciences and Technology, Natural Sciences, Physics – N 002),
Members:
Prof. Dr. Justinas Čeponkus (Vilnius University, Natural Sciences, Physics – N 002),
Assoc. Prof. Dr. Silvana Morello (University of Salerno, Natural Sciences, Biology – N 010),
Prof. Dr. Valdas Šablinskas (Vilnius University, Natural Sciences, Physics – N 002),
Dr. Martynas Talaikis (Center for Physical Sciences and Technology, Natural Sciences, Chemistry – N 003).

The dissertation shall be defended at a public meeting of the Dissertation Defense Panel at 11:00 on the 15th of September, 2023 in Room A101 of the State research institute Center for Physical Sciences and Technology. Address: Sauletekio av. 3, Room No. A101, Vilnius, Lithuania
Tel. +370 5 264 8884; e-mail: office@ftmc.lt

The text of this dissertation can be accessed at the libraries of the State research institute Center for Physical Sciences and Technology, Vilnius University, as well as on the website of Vilnius University:
www.vu.lt/naujienos.ivykiu-kalendorius

https://doi.org/10.15388/vu.thesis.493
https://orcid.org/0000-0003-2125-6366

VILNIAUS UNIVERSITETAS
FIZINIŲ IR TECHNOLOGIJOS MOKSLŲ CENTRAS

Lena Golubewa

Skirtingų formų juodasis silicis biojutikliams

DAKTARO DISERTACIJA

Gamtos mokslai,
Fizika (N 002)

VILNIUS 2023

Disertacija rengta 2019–2023 metais Fizinių ir technologijos mokslų centre.

Mokslinius tyrimus rėmė Lietuvos mokslo taryba skirdama stipendijas 2020 ir 2021 metais už akademinius pasiekimus, bei 2022 paskirdamas finansavimą stažuotei Rytų Suomijos universitete (Suomijoje).

Mokslinė vadovė – dr. Renata Karpicz (Fizinių ir technologijos mokslų centras, gamtos mokslai, fizika – N 002).
Mokslinė konsultantė – prof. dr. Polina Kuzhir (Rytų Suomijos universitetas, gamtos mokslai, fizika – N 002).

Gynimo taryba:
Pirmininkas – prof. habil. dr. Gediminas Niaura (Fizinių ir technologijos mokslų centras, gamtos mokslai, fizika – N 002).
Nariai:
prof. dr. Justinas Čeponkus (Vilniaus universitetas, gamtos mokslai, fizika – N 002),
doc. dr. Silvana Morello (Salerno universitetas, gamtos mokslai, biologija – N 010),
prof. dr. Valdas Šablinskas (Vilniaus universitetas, gamtos mokslai, fizika – N 002),
dr. Martynas Talaikis (Fizinių ir technologijos mokslų centras, gamtos mokslai, chemija – N 003).

Disertacija ginama viešame Gynimo tarybos posėdyje 2023 m. rugsėjo mėn. 15 d. 11:00 val. Nacionalinio fizinių ir technologijos mokslų centro A101 konferencijų salėje. Adresas: Saulėtekio al. 3, Vilnius, Lietuva), tel. +370 5 264 8884; el. paštas office@ftmc.lt

Disertaciją galima peržiūrėti Fizinių ir technologijos mokslų centro bibliotekose ir VU interneto svetainėje adresu:
https://www.vu.lt/naujienos/ivykiu-kalendorius

ABBREVIATIONS

AFM – Atomic force microscopy
CAM – Cell adhesion molecule
CARS – Coherent anti-Stokes Raman scattering
CM – Chemical mechanism
CNT – Carbon nanotubes
DDA – Discrete dipole approximation
DNA – Deoxyribonucleic acid
ECM – Extracellular matrix
EF – Enhancement factor
EM – Electro-magnetic mechanism
FDTD – Finite-difference time-domain (method)
FEM – Finite element method
GQD – Graphene quantum dots
GO – Graphene oxide
LSPR – Localized surface plasmon resonance
MACE – Metal-assisted chemical etching
MPO – Myeloperoxidase
NP – Nanoparticle
PI – Propidium iodide
PML – Perfectly matched layer
PTE – Photoinduced thermal effect
PyC – Pyrolytic carbon
RRS – Resonant Raman scattering
RSD – Relative standard deviation
SAM – Self-assembled monolayer
SD – Standard deviation
SERS – Surface-enhanced Raman scattering
SEM – Scanning electron microscopy
SHINERS – Shell-isolated nanoparticle-enhanced Raman spectroscopy
SP – Surface plasmon
SPR – Surface plasmon resonance
SWCNT – Single-walled carbon nanotube
TT – Tissue culture treated (plastic)

CONTENTS

INTRODUCTION

Material and photonic sciences are actively introduced into modern biomedicine, contributing to the improvement of human well-being, and making a significant investment to the sustainable development of mankind. Within the framework of interdisciplinary research and industry, they offer new classes of materials with unique properties aimed at performing various tasks, including the creation of biosensor systems for monitoring of the functional state of individual cells, determination of the concentrations of drugs, viruses, and bacteria, development of scaffolds, artificial tissues, and even whole organs.

Generally, the concept of "biosensor" combines (i) a sensing element for specific capturing of the analyte or determining physical value of interest; (ii) an interface for providing an appropriate working environment for sensing elements; (iii) a transducer for converting one type of information into another one (for example, converting chemical bonding of analyte molecule with the receptor into electric current); and (iv) system for signal readout, amplification, processing, and analysis. The physical principles underlying the mechanism of signal conversion serve as the basis for dividing biosensors into the following types: electrochemical, piezoelectric, calorimetric, thermal, and optical ones [1]. The latter type has several advantages over the rest. The optical approach allows for remote, predominantly non-invasive, and non-destructive data acquisition, leaving it possible to use, for example, the electrical capabilities of the sensor to determine additional characteristics of the analyzed system or to control measurement parameters such as temperature.

Surface-enhanced Raman scattering spectroscopy ensures this capability and is, by now, a reliable sensing technique suitable for detecting low concentrations of molecules [2], e.g., pesticides [3] and poisons [4], studying the interaction between molecules [5] and/or between molecules and interfaces [6]. Recently, the application of SERS has been extended from fundamental research to everyday use, penetrating deeper into such applied areas as biomedicine [7], forensics [8], environment [9], and food safety [10]. SERS provides specific information about the analyte, including its structure, changes associated with the environment, purity, etc. Fundamental physical principles underlying the SERS phenomena predict its significant efficiency and sensitivity down to single-molecule level, but in practice, theoretical predictions fail because of specific obstacles, which are related to the fabrication of the platforms aimed at boosting the Raman intensity. Colloids of noble metal nanoparticles, specifically silver (Ag), indeed, provide

exceptional Raman signal enhancement when forming aggregates of metal nanoparticle and molecules of analyte caged in between, surpassing many other analogues, and allowing research at a single-molecule level. However, stability, reproducibility, and ease of routine use [11] are sacrificed to an exceptional signal enhancement: colloidal solutions are unstable [12], and very sensitive to storage conditions [13] (temperature, inorganic salt impurities, shaking, direct light, etc.).

The other general approach of SERS substrates fabrication bases on the use of nanostructured surfaces covered with plasmonic nanoparticles (either immobilized from colloid solutions [14] or created on top by noble metal sputtering, evaporation or chemical deposition). This allows achieving high uniformity, large useful areas, controlling the density of hot spots, but losing in cost and highest limit of Raman signal enhancement. Thus, the design and fabrication of SERS substrates, required to boost the Raman intensity, is often a trade-off between stability, cost, reliability, homogeneity, and scalability from one side and efficiency and Raman signal enhancement from the other side.

Materials for biosensors meet a range of performance and safety requirements [1]. No matter what the final goal is (either biosensing system or scaffold implanted in the human body), bio-implied materials are claimed to possess controllable (i) interface morphology, (ii) physical properties (viscoelasticity, stiffness, porosity, etc.) [15], and (iii) biochemical characteristics (chemical stability, biocompatibility, affinity, etc.) [16] to address high sensing performance and the possibility of integrating this material into more complex devices. Due to the dominance of silicon microelectronics, compatibility with silicon photonics is highly welcomed from a technological point of view [17].

Silicon is the most obvious candidate to serve as an interface of a biosensor. It has already been employed as a supporting substrate for plasmonic noble metal nanoparticles [18]. The micro-structuring of a silicon surface can endow the material with new optical properties, such as increased absorbance and suppressed reflectance, which, in their turn, can benefit nano-plasmonic applications, including SERS. Silicon with developed surface comprising pyramids, needles, cones, holes, pillars, columns, etc., is collectively referred to as "black silicon". Besides increased absorbance, specific surface morphology of black silicon can contribute to a directional growth of cells *in vitro* by analogy with patterned surfaces [19], a significant increase in effective surface area suitable for hot spots formation in case of SERS, and, thus, can support the appearance of many sites available for the binding of analyte molecules. Over the past decades, several attempts have

been made to adapt black silicon as a biosensor for SERS, but its use has faced some obstacles. Firstly, black silicon was demonstrated to be non-biocompatible and showed antibacterial properties [20]. Secondly, the layers of noble metals, the thickness of which ranged from 100 [21] to more than 1000 nm [22], hardly allow considering the obtained substrates as cheap and affordable biosensors for widespread use. Despite this, black silicon is still of great interest for biosensing, since the full potential of this material has not yet been fully exploited.

Biosensing is inspired by the demands of human health and wellbeing. According to the World Health Organization, cancer is one of the leading causes of human death worldwide, counting one in six deaths over the last years [23]. Theranostics is one of the most promising approaches for cancer treatment. It combines both diagnostic and therapeutic modalities in one specific nano-agent [24] capable both of visualizing the tumor and its destruction. The latter occurs when the agent is activated by some specific internal chemical (e.g., pH of the cancer cell cytoplasm [25]) or external physical (ultrasound, irradiation, etc. [26]) stimuli. These nanoagents must be efficient and safe and solve the everlasting problem of their biodegradation and further elimination from the body. The development of effective theranostic methods based on the use of such safe nanoagents supported by the established mechanisms of their biodegradation, will ensure the generalization of theranostic approach.

At this stage, affordable, diversiform, and reliable biosensing components, based on black silicon and relied on SERS, can be successfully introduced to practical biomedicine, and span their application from accurate and probe-specific detection of low concentrations of analytes to the analysis of living cell functions and generalization of therapeutic approaches.

Goals of the research work

The goal of the Thesis is to develop a biocompatible, low-cost, stable, reliable, uniform, and scalable black silicon-based substrate suitable for SERS of nanomaterials, biomolecules and living cells by varying surface geometry of substrate, thickness, and integrity of gold plasmonic layer.

Tasks of the research work

To achieve the goals set above, the following tasks were formulated and solved within the framework of the Thesis:

1. To demonstrate how the micro- and nano-structuring of a silicon substrate modified by changing the etching conditions and combined with a cover of various graphene-based 2D structures affect the cell growth and adhesion, preserve cell viability.

2. To utilize the biocompatible black silicon covered with a thin gold pseudo-layer, as a substrate for SERS analysis of small organic molecules and living cell; estimate specific characteristics of black silicon-based SERS substrate, such as enhancement factor, uniformity, and sensitivity, provide specific information about the biochemical composition of glioma cells.

3. To perform numerical simulations and suggest most possible mechanism of electric filed enhancement provided by the fabricated black silicon sputtered with 50 nm-thick gold pseudo-layers aiming to explain the measured enhancement factor (EF) and predict the influence of the morphology of the black silicon surface and the gold layer thickness on SERS efficiency; to fabricate and analyze black silicon-based substrates with surface geometry and gold pseudo-layer of thicknesses estimated in numerical simulations.

4. To investigate the mechanisms of interaction of carbon-based nanomaterials with cancer and immune cells, and establish the mechanism of biodegradation of these nanomaterials after their release from damaged cells by applying black silicon-based SERS substrate.

Statements of the Thesis

1. Surface micro-structuring, nano- and micro-roughness of black silicon is tuned by the fabrication procedure and results in: (i) hydrophilic biocompatible interfaces with cone-like silicon structures for living cell analysis when produced by cryogenic ICP-RIE technique, (ii) robust hydrophobic surfaces with dense lace-like silicon structures, suitable for analytical applications, when produced by RT ICP-RIE.

2. Cone-like black silicon fabricated by cryogenic reactive ion etching and sputtered with 50 nm gold pseudo-layer, exhibits an enhancement factor of 10^8, is uniform at a macroscale and is suitable for a living cell investigation.

3. Silicon core of the black silicon/gold structures and 3D spatial organization of gold nanostructures endows the black silicon-based SERS substrate with a pronounced optical resonance in the spectral range 700-800

nm, which can be further red shifted by the thinning of gold pseudo-layer down to about ten nanometers.

4. Cancer cells can be destroyed by a photoacoustic mechanism guided by the interaction of picosecond laser pulses and agglomerates of carbon nanomaterials, which subsequently, upon neutrophil activation, are biodegraded by a hypochlorite-mediated mechanism disclosed using a SERS-active black silicon/gold substrate.

Novelty and relevance

During the Thesis implementation, the biocompatible black silicon substrate was fabricated and applied for SERS analysis of living (not fixed) cells for the first time, expanding the application of black silicon to bio-sensing applications. Such an expansion of the black silicon usage in the field of bio-sensing was supported by results of numerical simulations, which predicted that black silicon covered with ultrathin gold layer should perform well in SERS. The black silicon substrates covered by 10 nm thick gold layer drastically reduce fabrication cost, while the presence of silicon/gold core-shell nanostructures shifts the plasmon resonance to NIR and provides signal enhancement sufficient to outperform conventional SERS substrates (EF 10^6-10^8). We performed a proof-of-the-concept experimental study of cold photo-thermo-acoustic destruction of cancer cells through photo-activation of acoustic waves generated by agglomerates of SWCNTs, supporting the theoretical predictions made in [27] by another research group. These findings push forward the creation of the additional branch in theranostics associated with the development of nanoagents whose properties are regulated and largely determined by the microenvironment of the cancer cell, which are activated by accessible NIR light and are capable of effectively destroying a tumor without causing unwanted hyperthermia of neighboring normal tissues. By applying the developed black silicon-based SERS substrate, we disclosed the structural changes occurring in carbon-based nanomaterials during their interaction with immune system cells and suggested the mechanism of hypochlorous acid-guided biodegradation of carbon nanomaterials, demonstrating their suitability for cancer theranostics. The obtained results pave the way for the transition from complex and expensive laboratory research to a wide and affordable application of the SERS method in practice due to the development of a cheap, but stable, reliable, and effective black silicon-based SERS substrate suitable for various applications extending from detecting low analyte concentrations to the analysis of the structure of carbon nanomaterials and living cell functioning.

1. LITERATURE OVERVIEW

1.1. Materials for biomedical applications: requirements and restrictions

The progress of modern medicine is inextricably linked to the development of the material and nanomaterial sciences [28]. At the micro- and macro-scales new classes of materials are constantly being introduced in the form of artificial tissues, implants, supporting basis for creating new organs, microelectrode systems for restoring signal transmission in the brain or innervation of various types of muscles (for example, electrical heart muscle stimulators), etc. At the nanoscale, nanomaterials have already formed a whole class of compounds used to image, diagnose [29], and treat several diseases [30], including cancer, and are also applied for wound healing [31], [32], tissue repair [33], [34], antibacterial treatment [35], tackling the problem of antibiotic resistivity [36].

The development of materials for the medical domain encounters several strict requirements, which must be met, otherwise failure to comply with these requirements can provoke serious inflammation, tissue necrosis and rejection of the employed material. Any material for biosensor or any other material which faces living cells or tissues, must provide good attachment of cells, their viability, preserve sterility, and be preferably integrated in silicon photonics to support generally accepted silicon-based microelectronics. The properties of the material-cell interface define the range of potential effects. For instance, contact between granulocytes (cells of immune system, including neutrophils, eosinophils and basophils) and the surface affects the production of reactive oxygen species, the key process in the inflammatory response [37], [38]. Platelet activation, aggregation and blood clot formation during blood vessel injury is also triggered by the interaction of specific GPIb receptors with immobilized surface receptors vWF after cell adhesion [39]. The cell adhesion to the extracellular matrix and other cells also plays a crucial role in defining stem/progenitor cell proliferation, differentiation, and migration, which are involved in tissue self-renewal or repair processes [40].

The cell-surface contact and, as a result, cellular structure and function is mostly guided by three features of the microenvironment: its stiffness (mechanical properties), morphology (or topology) and surface chemistry [41] (Figure 1).

Each organ is characterized by a distinct value of stiffness defined by specific content of ECM and cross-linking proteins and interrelation between cells and the matrix of specific stiffness regulates, e.g., the early stage of stem cell differentiation [42]. The increase in the substrate stiffness and adhesion

energy density results in traction force and cortical tension increase leading to mechanosensitive channels (MS) opening, water and ions expelling and up to 50% cell volume decrease and spread area enlargement, which, in turn, results in higher contractility of actomyosin cortical layer [43]. Changes in substrate stiffness also cohere with integrin expression and regulate the process of hUC-MSCs differentiation into myocardium [44].

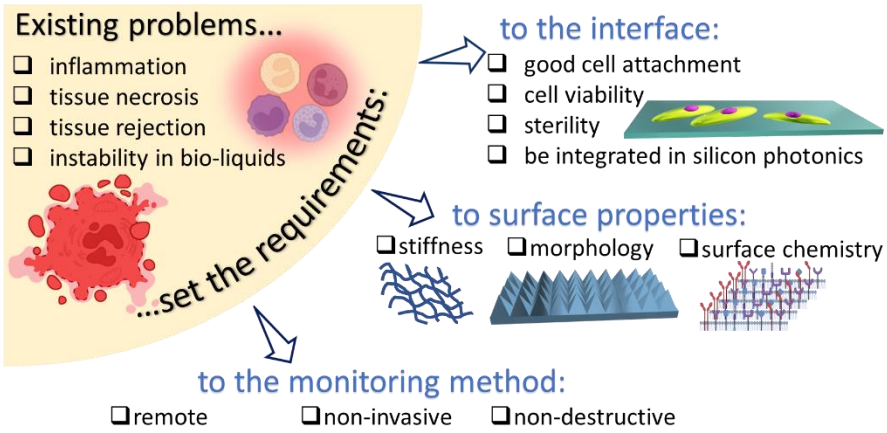

Figure 1. Requirements that apply to materials for the medical and biological fields. Created with BioRender.com.

Surface topology regulated by micro-/nano-patterning with linear groves, nano-posts, pillars, etc., changes the area available for cell spreading, forcing the cell to adapt its shape and remodel its actin cytoskeleton this way. Nanotopography of the substrate is employed to enhance the detachment force of low-spread osteoblast-like cells, while micropatterning induces cell elongation and its reorientation [45]. Patterning of a single crystal diamond surface with large-scale nanopillar arrays of various dimensions is shown to support the growth of a network of primary mouse hippocampal neurons with their preferential spreading along the nanopillar grid axes and excellent physical adhesion of a cell membrane to the nanopillar apex [46]. These results suggest a nanophotonic quantum sensing platform for label-free neuronal activity recording with sub-cellular resolution due to quantum sensing capabilities of nitrogen-vacancy centers in diamond, allowing real-time detection of action potentials of neurons.

The cell-surface interaction is governed by cell adhesion molecules (CAM), which include integrins, selectins, cadherins, nectins, mucins, several enzymes (such as vascular adhesion protein 1) and some others [47]. Initial cell adhesion is driven by the electrostatic interaction with the surface,

initiated by single molecules, and is continued by binding of integrins to the substrate, cell spreading and maturation of the focal adhesions contacts [48]. Chemical modification of surface with functional groups is one of the effective routes to regulate cell-surface contact and adhesion-associated signaling, stimulating proliferation, or causing cell death. Covering the surface with graphene-like layers (e.g., pyrolytic carbon, PyC, or ensembles of graphene quantum dots, GQDs, or graphene oxide sheets, GO) may serve as an effective way to modify the surface chemistry and to manage the interaction between proteins and the surface. Such materials often display many hydroxyl, carbonyl, carboxyl, and carboxylate groups on their surface, which accelerates the adhesion of the cell to the surface through electrostatic, covalent, and hydrogen bonds [49].

In the case of materials for light-coupled biosensing devices, one more significant issue must be considered. Lasers are widely used as an excitation source in biomedicine. The irradiation of living cells and tissues with coherent light beams results in a variety of effects, spanning from photobiomodulation, photochemical interactions, to thermal interactions (e.g., coagulation and vaporization), photoablation, and photodisruption [50]. The degree of the light-tissue interaction and possible negative side-effects depend on both the properties of a biological object (absorption, reflection, and scattering coefficients) and irradiation parameters (wavelength, pulsed or continuous mode, laser pulse duration, repetition rate, intensity, exposure time, etc.). In addition, near infrared (NIR) irradiation is preferred to provide deeper tissue penetration [51] and overcome light-induced damage that often occurs when a sample is excited with light in the visible spectral range due to strong light absorption and rapid overheating of the sample. For instance, living cell irradiation with a laser source with wavelengths of 488 and 514.5 nm and 5 mW power induces cell overheating and death, while 785 nm irradiation for more than 1 h with 115 mW power does not affect cell viability [52].

It is worth noting that the materials, even those which are widely used in clinics now, still possess unfavorable drawbacks, such as tissue scar formation or inflammation, forcing the research of suitable alternative materials among both newly developed and traditional ones. In this regard, biocompatibility, and the possibility to use these materials as scaffolds with tunable properties ensuring the control of cell and tissue growth, as well as application of NIR radiation in light-coupled biosensors, are the key requirements for biomaterials.

To sum up, the development of new materials and nanomaterials is crucial for advancing modern medicine, ensuring imaging, diagnosing, and treating diseases, including cancer, wound healing, and tissue repair. Although

much effort has been put into this area, inflammation, tissue rejection, material instability and chemical reactivity still accompany the integration of functional materials into the biological environment. Thoughtful design of surface properties as well as surface patterning and creation of specific structures, able to govern cell-surface interactions, may correct and regulate cell behavior and function and, thus, in future, will enable the transition to safer, more durable, and efficient biomedical materials.

1.2. Surface-enhanced Raman scattering spectroscopy

Light-tissue interaction is a complex process, which includes reflection at a material interface, refraction inside a tissue with a refractive index different to that of the external medium, absorption of photon energy, and scattering of photons in the material. The probability of inelastic scattering, during which an exchange of energy between the photon and the scattering object occurs, is lower than that for elastic scattering by a factor of about 10^6 [53]. The major inelastic scattering process is Raman scattering, underlying methods such as Raman vibrational spectroscopy and surface-enhanced Raman scattering (SERS) spectroscopy.

Raman spectroscopy is an accurate technique which allows specific detection and analysis of chemical compounds through analysis of vibrational spectra of molecules serving as compound „fingerprints“. It is commonly used in biosensing [54], in part, due to its ability to utilize NIR radiation. Raman spectroscopy also eliminates the need for specific sample preparation and keeps the object intact [55]. The sensitivity and accuracy of Raman measurements can be greatly enhanced through the use of specific substrates, composed of noble metal nanostructures, that support Raman signal enhancement and form the basis for SERS implementation.

1.2.1. Physical principles underlying SERS

The technique of SERS involves leveraging the amplified local field enhancements, which occur on metallic plasmonic surfaces under specific conditions to intensify the Raman scattering signal of molecules located at or near the surface [56]. Therefore, SERS combines two main pillars: Raman scattering and local filed enhancements provided by the implication of substrates with special properties.

Pillar I: Principles of Raman spectroscopy

In elastic Rayleigh scattering (size of scattering objects << incidence wavelength λ_{inc}) the incident and scattered photons have the same energy, and the molecule after the scattering event remains in the same energy state as before scattering, and therefore the scattered photons do not carry significant information about the internal structure of the molecule. In contrast, Raman scattering is an inelastic one [57]. In inelastic scattering, the energy of a scattered photon is different from that of the incident one, which is due to the molecule transition between vibrational/rotational levels. The process can occur without electronic transitions and direct absorption of the photon by molecules, allowing to apply as an incident irradiation the light from the spectral region, where the sample is transparent (e.g., NIR in case of biological objects) (Figure 2).

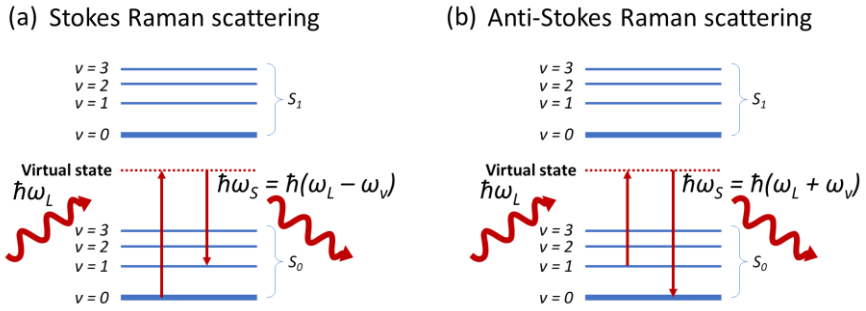

Figure 2. Schematic illustration of inelastic Stokes (a) and anti-Stokes (b) Raman scattering process on a simplified Jablonski diagram. The incident photon energy is $\hbar\omega_L$, the scattered photon energy is $\hbar\omega_S$, the energy of the transition between vibration levels is $\hbar\omega_v$; ν_0 indicates the ground vibrational state, $\nu_{1,\ldots,i}$ corresponds to 1^{st}, …, i^{th} excited vibrational state, S_0 is the ground electronic state, S_1 is the first excited electronic state (singlet states).

The phenomenon of Raman scattering has both phenomenological and quantum descriptions. In terms of the phenomenological (classical) approach, the electromagnetic field originates from oscillating electric dipoles. The scattering process occurs when the primary incident electromagnetic field disturbs the electronic charge distribution in molecules inducing the dipole moments both in polar and non-polar molecular systems, and the sum of these dipole moments is considered as a source of a secondary electric field irradiated by the molecules, or the scattered light [57], [58].

The induced dipole moment can be written as

$$\boldsymbol{\mu}_{ind} = \alpha \boldsymbol{E} = \alpha \boldsymbol{E_0} \cos(\omega_0 t), \quad (1)$$

where $\boldsymbol{\mu}_{ind}$ is the induce dipole moment, $\boldsymbol{E} = \boldsymbol{E_0} \cos(\omega t)$ is the incident electromagnetic field oscillating with the frequency ω and amplitude E_0, α is a polarizability tensor (a second rank tensor) of the molecular system which describes to what extent the incident field can disturb the electrons of the molecular system with respect to their equilibrium states (states before electromagnetic perturbation). Polarizability, in turn, is non-static and can be expanded into a Taylor series around the equilibrium nuclear geometry Q_0, as follows:

$$\alpha_{ij} = (\alpha_{ij})_0 + \sum_k \left(\frac{\partial \alpha_{ij}}{\partial q_k}\right)_0 q_k + \frac{1}{2} \sum_{k,l} \left(\frac{\partial^2 \alpha_{ij}}{\partial q_k \partial q_l}\right)_0 q_k q_l + \cdots, \quad (2)$$

where $\{q_i\}, i = \overline{1, \mathrm{N}}$ are individual normal modes and each normal coordinate oscillates with amplitude q_i^0 and individual frequency ω_q, i.e., $q_i = q_i^0 \cos(\omega_q t)$; $(\alpha_{ij})_0$ is a polarizability tensor at the equilibrium state; the subscript 0 indicates that the derivative is taken at the equilibrium position [59]. Reducing the number of normal coordinates to one normal mode q_i and leaving only the linear component of a Taylor series, without loss of generality, induced dipole moment along the normal coordinate q_i can be expressed as follows:

$$\mu_i(t) = \left[\alpha_0 + \left(\frac{\partial \alpha}{\partial q_i}\right)_0 \cdot q_i^0 \cdot \cos(\omega_{q_i} t)\right] \cdot E_0 \cdot \cos(\omega_0 t) =$$

$$= \underbrace{\alpha_0 \cdot E_0 \cdot \cos(\omega_0 t)}_{Rayleigh\ scattering} +$$

$$+ \frac{1}{2} \cdot \underbrace{\left(\frac{\partial \alpha_i}{\partial q_i}\right)_0 q_i^0 \cdot E_0 \cdot \cos[(\omega_0 - \omega_{q_i})t]}_{Stokes\ Raman\ scattering} +$$

$$+ \frac{1}{2} \cdot \underbrace{\left(\frac{\partial \alpha_i}{\partial q_i}\right)_0 q_i^0 \cdot E_0 \cdot \cos\left[(\omega_0 + \omega_{q_i})t\right]}_{anti-Stokes\ Raman\ scattering}. \quad (3)$$

Therefore, inelastic Raman scattering occurs in case when the derivative of the polarizability taken along the normal coordinate q_i is non-

zero $\left(\frac{\partial \alpha}{\partial q}\right)_{q_i} \neq 0$, providing the Raman scattering selection rule for molecules. Phenomenological description is useful from an experimental point of view as it explains the phenomenon of Raman scattering in terms of polarizability and covers such important issues as symmetry of molecules and selection rules, later becoming very important in SERS implementation.

The electronic structure of molecules is accurately described by quantum theory and explains some issues which are not disclosed by the classical approach. In terms of a schematical representation of a quantum perturbation theory, designed to describe the phenomenon of Raman scattering, the latter is often a two-step process: (i) absorption of an incident photon accompanied by a molecule transition to a virtual higher-energy level, which in general does not exist and is a form of a mathematical construction, and (ii) spontaneous emission of the incident photon. If the virtual state coincides with the existing electronic level, the process of scattering can be enhanced significantly, and it refers to so-called resonant Raman scattering (RRS). The scattered photon may have energies both lower and higher magnitudes than that of the incident photon, although the latter is much weaker. Lower energy (Stokes process) corresponds to the case of excitation from the vibrational ground state (ν=0) with relaxation through the virtual state to the first excited vibrational state (ν=1), while higher energy of a scattered photon (anti-Stokes process) corresponds to the excitation of the molecule from the first excited vibrational state with relaxation through the virtual state to the ground vibrational state (ν=0) [57].

Pillar II: Role of local field enhancement

SERS is a surface spectroscopy technique, which means that useful signal containing the information about the molecules structure is accumulated only from the molecules attached to the surface or those being in the surface proximity. Enhancement of the signal of Raman scattering by molecules at (or near) the surface is achieved by a significant increase of the local electromagnetic field that can exist on metal surfaces during their interaction with the incident electromagnetic field. It originates predominantly from two EM effects. The first one is associated with the induced dipole moment $\boldsymbol{\mu}_{ind} = \alpha \boldsymbol{E}_{Loc}(\omega_{SPR})$ due to a significant increase of the local field $|\boldsymbol{E}_{Loc}|$ near the metal surface originated from surface plasmon resonances when the system is excited with the wavelength close to the SPR resonance one $\lambda_{SPR,}$ (SPR is discussed in section 1.2.2). This dipole would radiate in free-space (non-proximal to metal surface) energy proportional to $|\boldsymbol{\mu}_{ind}|^2$,

resulting in the field enhancement by factor $M_{Loc}(\omega_{SPR}) = |\boldsymbol{E}_{Loc}(\omega_{SPR})|^2/|\boldsymbol{E}_0|^2$, also known as the **local field intensity enhancement factor**. The second EM effect consists in a strong influence of the environment (metal surface) on the process of the irradiation by a dipole and considers it in proximity to the surface. It manifests in the **radiative enhancement factor**, which is the ratio of the total power radiated by a dipole P_{Rad}, to the power radiated by the same dipole in free-space P_0 and is dependent on substrate parameters (geometry, optical properties, dipole orientation and its emission frequency ω_R: $M_{Rad}(\omega_R) = P_{Rad}(\omega_R)/P_0(\omega_R)$). Total enhancement factor for a single molecule (SMEF) is often considered as:

$$SMEF \approx M_{Loc}(\omega_{SPR}) \cdot M_{Rad}(\omega_R) =$$

$$= \{\text{let us assume that } M_{Rad}(\omega) \to M_{Loc}(\omega)\} \approx$$

$$\approx \frac{|\boldsymbol{E}_{Loc}(\omega_{SPR})|^2}{|\boldsymbol{E}_0|^2} \cdot \frac{|\boldsymbol{E}_{Loc}(\omega_R)|^2}{|\boldsymbol{E}_0|^2} \approx \{\text{approx. } \omega_R \approx \omega_{SPR}\} \approx$$

$$\approx \frac{|\boldsymbol{E}_{Loc}(\omega_{SPR})|^4}{|\boldsymbol{E}_0|^4} \quad . \tag{5}$$

The last formula is known as a $|E|^4$-approximation and is, despite its very approximate value, useful quantitative estimation, which forms a bridge between computational electromagnetics of SERS and experimentally obtained results [60].

The enhancement of the electromagnetic field on the surface of the metal may have two possible mechanisms: the electromagnetic (EM) and the chemical (CM) ones [61]. The EM mechanism is applicable to all analytes and **relies on the phenomenon of surface plasmon resonance** (Section 1.2.2). CM is probe-specific, applicable not for all analytes. It also requires the formation of the chemical bonds between the investigated molecule and the substrate material. This bonding affects the analyzed molecule's polarizability under laser irradiation excitation and, subsequently, the intensity of Raman scattering.

SERS enhancement factor (EF) is a key quantitative characteristic of different systems designed and fabricated to boost the Raman signal. It is used to evaluate the efficiency of SERS substrate. The experimentally measured EF gives the enhancement of the Raman signal with respect to one obtained for the same molecule under non-SERS conditions.

Basing on the origin of SERS enhancement, the EF is considered as a multiplicative contribution of (i) electromagnetic (EM) enhancement factor (F_{EM}), which is considered as the main one, and (ii) chemical enhancement (CE) factor, EF_{Chem}, which contribution is supposed to be much smaller than that of EF_{EM}. Experimentally determined EF is a combination of EFs of all possible origins [60]. However, as it was already mentioned, the contribution of EF_{Chem} to the total EF does not exceed 10^0-10^2, while EF_{EM} provides up to 10^{11} times enhancement and can be regulated by the design of plasmonic nanostructures.

The SERS EFs often vary significantly over the substrate as it depends on the proximity of the analyte molecule to the region of very large local field enhancements, called 'hot spots', which, in turn, is determined by the geometry of the plasmonic nanostructure and the type of the substrate and can be spatially limited at nanometer scale. High non-uniformity of 'hot spots' and, as a result, strong variability of EFs is beneficial for some approaches like single-molecule analysis, while for most analytical applications it is an obstacle. Measurement of averaged EFs, which reflect the average properties of the substrate, turns to be an acceptable solution to the existing problem.

The SERS EF experimental estimation often relies on the following formula:

$$EF = \frac{I_{SERS}/N_{Surf}}{I_{RS}/N_{Vol}}, \quad (6)$$

where I_{SERS} is intensity of SERS signal of the analyte molecules, N_{Surf} is the number of analyte molecules adsorbed on the surface, N_{Vol} is the average number of analyte molecules in the scattering volume for the non-SERS measurements, I_{RS} is Raman signal intensity for non-SERS measurements. It is also must be considered that the SERS EF for substrates depends on many factors, including excitation wavelength λ_L, wavenumber $\bar{\nu}_k$ for which the EF was calculated, Raman polarizability tensor $\tilde{\alpha}_k$, molecular orientation, substrate orientation with respect to the incident light polarization, and scattering configuration [60].

Although this estimation (6) is considered as one of the best for measuring average EF of the substrate, it is not strictly rigorous and there are some circumstances that make the assessment complicated and reduce its accuracy. Firstly, the coverage of the substrate should be a monolayer of molecules or beyond, as the Raman signal enhancement decreases significantly with the distance and is sufficient only for molecules in the

proximity of the surface. Secondly, in some cases, estimation of the N_{Vol} value may also face some problems.

Nevertheless, $|E|^4$-approximation and SERS EF calculations according to formula (6) are simple methods of theoretical and experimental evaluation of SERS efficiency, respectively, and allow one to accurately describe real systems, which makes these approaches extremely important from a practical point of view. The availability of robust and reliable methods for the qualitative and quantitative evaluation of the amplification properties of various SERS materials is essential to enable the rapid adoption of this sensitive and analyte-specific method into routine laboratory testing, replacing costly, less selective, and difficult-to-use techniques.

1.2.2. Conditions of surface plasmon resonance

Noble metals, such as gold, silver, copper, and aluminum, posses specific optical properties, which make these metals suitable for SERS applications [62]. These particular properties originate from the presence of free conduction electrons, or free-electron plasma, which governs the optical response of noble metals [57]. Collective dipolar oscillations of conducting electrons excited by the incident light are called surface plasmons (SPs). If the frequency of the incident electromagnetic wave coincides with the eigenfrequency of these collective oscillations, the phenomenon of surface plasmon resonance (SPR) occurs (Figure 3). In case of the particle smaller than the wavelength of the excitation wave, SPR is denoted as a localized one (localized surface plasmon resonance, LSPR). A full analytical solution of the problem of a metallic sphere which interacts with an incident plane wave is provided by Mie theory [63] and such LSPR resonances are often described in terms of extinction, scattering, and absorption cross sections (σ_{ext}, σ_{sca}, and σ_{abs}, respectively) and local electromagnetic field enhancement [62].

In electrostatic approximation, the electric field $\boldsymbol{E}_{in}$ around the spherical metal nanoparticle, induced by the incident field (constant field $\boldsymbol{E}_{Inc}$), can be expressed as:

$$\boldsymbol{E}_{in} = \left(1 - \frac{\epsilon(\omega) - \epsilon_m}{\epsilon(\omega) + 2\epsilon_m}\right)\boldsymbol{E}_{inc}\,, \tag{7}$$

where $\epsilon(\omega)$ is a metal dielectric function dependent of the frequency, ϵ_m is a dielectric permittivity of the surrounding medium. And the LSPR in the electrostatic approximation is determined from the condition that the denominator tends to zero. The same resonance condition, determined by the

predominant contribution from the electric dipole term, follows from the accurate solution of the electromagnetic problem according to Mie theory.

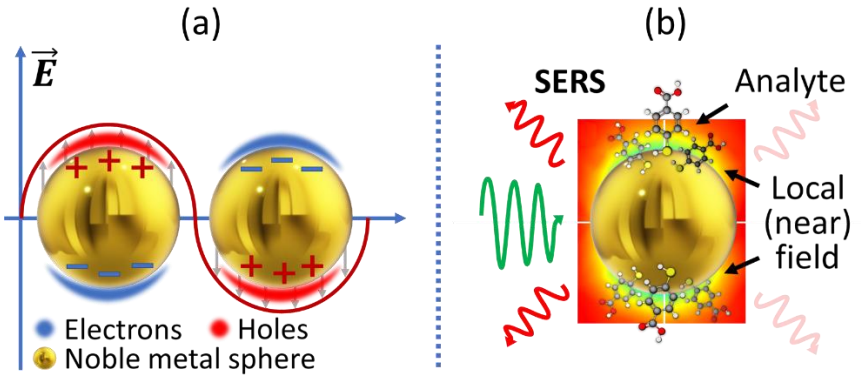

Figure 3. Schematic diagram of a local surface plasmon resonance effect (a) and enhancement of the Raman signal from probe molecule located in the near-field of the plasmonic nanoparticle (b). Adapted from [64].

Thus, optical response of metals and resonance phenomena are described in terms of the frequency dependence of the metal dielectric function, which itself is a complex value $\tilde{\epsilon}(\omega)$. Accurate description of the optical response can be very complicated and may require different levels of refinement, because many phenomena can affect the free-electron plasma behavior, e.g., electron-electron correlations, electron-impurities and/or electron-phonon interactions, etc. Several models of $\tilde{\epsilon}(\omega)$ exsist. But the most sufficient in many cases is the Drude model, which is based on the free electron approximation (electrons are not bound and uniformly and randomly distributed in metal). The complex dielectric function $\tilde{\epsilon}(\omega)$ in this case is represented as follows:

$$\tilde{\epsilon}(\omega) = \epsilon_\infty \left(1 - \frac{\omega_p^2}{\omega^2 + i\gamma_0\omega}\right) = \underbrace{\epsilon_\infty \left(1 - \frac{\omega_p^2}{\omega^2 + \gamma_0^2}\right)}_{\mathbf{Re}(\tilde{\epsilon}(\omega))} + i\underbrace{\frac{\epsilon_\infty \omega_p^2 \gamma_0^2}{(\omega^2 + \gamma_0^2)}}_{\mathbf{Im}(\tilde{\epsilon}(\omega))}, \quad (8)$$

where $\omega_p = \sqrt{\frac{ne^2}{m\epsilon_0\epsilon_\infty}}$ [rad s^{-1}] is an oscillation frequency of the free-electron-plasma charge density (or plasma frequency); ϵ_∞ is a constant background real dielectric function, which takes into account the contribution of the fixed ions of the lattice ($\epsilon_\infty \geq 1$); γ_0 [rad s^{-1}] is a damping constant, which arises from the collision of electrons with the crystal lattice and (or) impurities ($< \omega$); ω [rad

s^{-1}] is a frequency of the incident electromagnetic wave; n [m^{-3}] is the number of free electrons per volume unit; m [kg] is the effective mass of electrons.

The resonance conditions which occur in metals under the interaction with the incident electromagnetic field of frequency ω, are, thus, determined by both the real and imaginary parts of the complex dielectric function $\tilde{\epsilon}(\omega)$. As it follows from Formula (8), they are: (i) $\mathbf{Re}\left(\tilde{\epsilon}(\omega)\right) < 0$, which is possible if the frequency of the incident electromagnetic wave is $\omega < \omega_p$ ($\lambda > \lambda_p$), and, simultaneously, (ii) ω is not very small (but $\gamma_0 < \omega$), then $\mathbf{Im}\left(\tilde{\epsilon}(\omega)\right)$ is also small. These two conditions make many optical effects, including plasmonic resonance, be possible for noble metals in visible and NIR spectral range and are not observed for dielectric materials because of $\mathbf{Re}\left(\tilde{\epsilon}(\omega)\right) \in (1{,}10)$.

The metal dielectric function depends on the size of nanoparticles, and it is close to the dielectric function of bulk metal for big enough nanoparticles. If the size of a nanoparticle decreases down to few nanometers, the dielectric function of a bulk metal cannot describe the optical properties of the NP properly [65]. Metal dielectric function is governed by interband (described in terms of a Lorentz oscillator model) and intraband transitions, which are described by the free-electron model. This limits the application of free-electron models (such as Drude model) for the description of real metals. For the noble metals, the influence of the interband transitions becomes noticeable in the visible spectral range (1.9 – 3.1 eV). Thus, the complex dielectric function described by the Drude model should be complimented with additional interband transition components [66], [67].

The complex dielectric function, being the major parameter, which describes the optical response of metals under interaction with the electromagnetic field, allows theoretical explanation and/or prediction of the experimentally observed surface plasmon-related effects. This allows the possibility to design the plasmonic materials with a desired, pre-modeled set of optical features. The relation between the complex dielectric function (for non-magnetic materials) and complex refractive index ($\tilde{\epsilon}(\omega) = \tilde{n}(\omega)^2$) makes it widely applicable in practice. Complex refractive indexes of many materials are available, for instance, in a regularly updated opensource RefractiveIndex.info database [68], which was created in 2008 and since then has been constantly updated with data available in scientific publications and from material datasheets provided by manufacturers.

Correct choice of the refractive index $\tilde{n}(\omega)$ and the correct formulation of the problem of interaction of electromagnetic radiation with the structures under study (or designed ones) will allow minimizing production errors, increasing the efficiency of functional materials and predicting hitherto

unknown solutions to existing practical problems, including the development of SERS-active substrates.

1.2.3. Computational electromagnetics

Finding the actual solution of the problem of the interaction of electromagnetic field with nanostructures or their systems of a particular geometry may disclose the upper limit of boosting the Raman signal from investigated molecules and structures and provide assumptions on how and to what extent the SERS-substrate design can be improved. The solution often comes down to determination of the electric field in near field region, thus representing the local field enhancement in comparison with the incident electromagnetic field and allowing for estimation of EF using $|E|^4$-approximation. This bases on the solution of Maxwell's equations for dielectric media comprising metallic nanostructures of different shapes and requires the use of appropriate dielectric functions of both media, interacting with the incident electromagnetic field (often a plane wave with linear polarization), and corresponding boundary conditions. The optical response of the noble metal nanoparticle is defined by absorption and scattering cross-sections, calculated through the energy absorbed by the nanoparticle due to ohmic losses and energy scattered per unit area, respectively.

As the analytically problem of light scattering is solved only for simple geometries such as spherical particle [69] or infinitely long cylinder [70], such a problem for other particles and, moreover, surfaces of more complex geometry can be solved only by numerical methods and provide approximate solutions. For this reason, several numerical approaches have been developed and are now actively used. The most popular and widely used ones include: (i) discrete dipole approximation (DDA), (ii) finite-difference time-domain method (FDTD), and (iii) finite element method (FEM) (Figure 4).

DDA method is a semi-analytical method, which exists as Maxwell's equations' solvers only. This numerical method considers the object as a set of cells, each of those is considered as a polarizable dipole. When interacting with the external electromagnetic field, the induced dipole affects other neighboring dipoles in the set. Therefore, the solution of a coupled system of 3N linear equations with 3N complex unknowns is needed and, thus, DDA implementation is often complex. Another complexity arises from choosing appropriate polarizabilities of the cells, which is related to the dielectric function $\tilde{\epsilon}(\omega)$ of the material. DDA method gives good predictions of far-field properties of the system but fails to describe the local field in the nanostructure

proximity as the solution close to the surface is strongly affected by the neighboring dipoles, thus, giving artifacts in the solution.

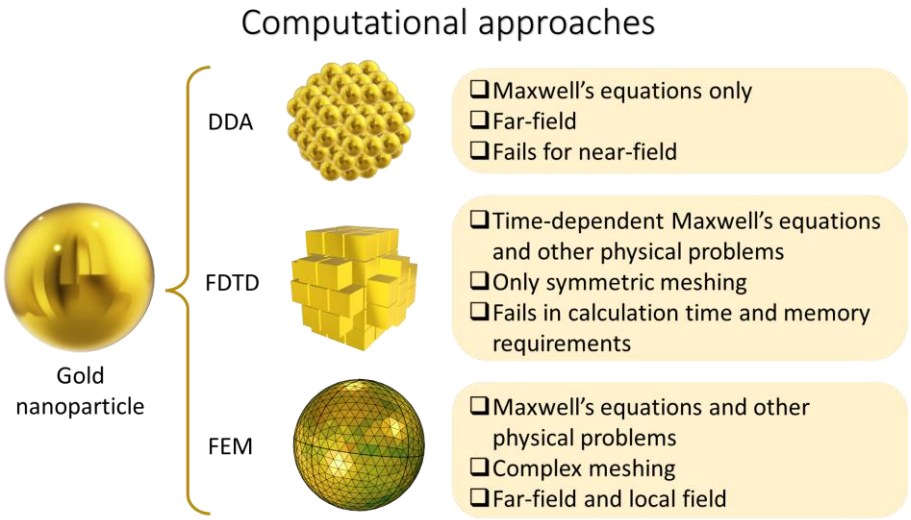

Figure 4. Existing computational approaches, schematic representation of nanoparticle meshing, and limits of applicability.

FDTD is based on solving the time-dependent Maxwell's equations using a finite-difference approach. The method is applicable both for cases of external electromagnetic field oscillating at a given frequency ω and under a short pulse excitation. It is worth mentioning that time-dependent calculations, like in the case of pulsed excitations, are in favor, as FDTD is a time-domain solver. Nevertheless, frequency analysis is also possible using the Fast Fourier Transform (FFT). One of the major disadvantages of FDTD is the requirement to use symmetric meshing of the object, predominantly cubic, although some approaches to employ, e.g., tetrahedral and hexahedral elements [71], exist. In the case of complex nanostructures of arbitrary geometry accurate particle description requires extremely small sizes of mesh, significantly increasing the calculation time (for 3D simulations it is proportional to $\sim V(\lambda/dx)^4$) and memory requirements ($\sim V(\lambda/dx)^3$) [72]. The latter often occurs in the case of nanostructures simulated for SERS.

FEM is a numerical approach for solving boundary-value problems. It is based on the dividing the continuous solution domain into a finite number of subdomains, the replacement of the unknown function over the entire solution domain with a set of simple interpolation functions with unknown coefficients defined over small subdomains of the entire domain. Thus, the original boundary-value problem is converted into a problem with a finite

number of degrees of freedom and comes down to the solution of the system of algebraic equations [73]. The difference from FDTD is that FEM is applicable for harmonic electromagnetic fields oscillating with a constant frequency ω. To obtain the solution for a range of frequencies, the FEM solver should be applied independently for each given frequency. Nevertheless, one-frequency solution is less time-consuming than solving the full time-dependent problem as in the FDTD method. Moreover, FEM is appropriate for EM problems when objects are meshed complexly with varying dimensions, which allows for fine covering the proximity of the surface of the nanostructure and calculating the local field on the metal-dielectric surface with high accuracy. Thus, FEM is appropriate for solving EM problems for inhomogeneous and anisotropic objects of various arbitrary shapes and geometries.

Together with FDTD, FEM can be applied for solving numerous physical problems, not only EM. Although FEM and FDTD are not specifically optimized for EM, as DDA method, some software packages and additional modules targeted to solving EM problems in terms of wave optics are now being actively developed (wave optics domain in Comsol Multiphysics [74] based on FEM or Ansys Lumerical FDTD [75] for simulations of photonic components). These packages are widely used in research, since they make it possible to explain and even predict the optical response of nanostructured systems, which is important for solving many applied problems for SERS.

Summing up, application of numerical methods for solving problems of the interaction of an electromagnetic field with metal, semiconductor, dielectric, layered, etc. nanostructures of arbitrary shapes, when an analytical solution is impossible, makes it possible to predict the optical response of such structures, select their optimal design and composition, and predict the efficiency of using these structures for the needs of SERS. Among the available methods, FEM is the most optimal method that allows describing arbitrary structures quite simply and qualitatively and providing an estimate of both the near and far fields. These advantages ensure active use of FEM to solve applied problems, such as the efficiency of SERS substrates, making it an indispensable assistant in the development and production of new materials.

1.3. Types of SERS-substrates

Efficiency of measuring SERS is affected by many factors, such as excitation source characteristics (wavelength, power, polarization, etc.), configuration

and type of detection setup, intrinsic parameters of molecules under investigation (polarizability tensor, Raman scattering cross-section), molecule interaction with the interface (its adsorption, covalent/non-covalent bonding, etc.), properties of the environment or media (i.e., refractive index) and properties and design of a SERS substrate [60]. The factors related to the measurement equipment and analyzed molecules can hardly be changed over a wide range of values. But the parameters characterizing the properties of the SERS-substrate itself can be adjusted to the desired ones.

The SERS approach obviously extends its applications from fundamental science to practice, including biomedicine, forensics, environment, security, etc. This has led to the emergence of numerous SERS-active substrates for analysis and research (Figure 5).

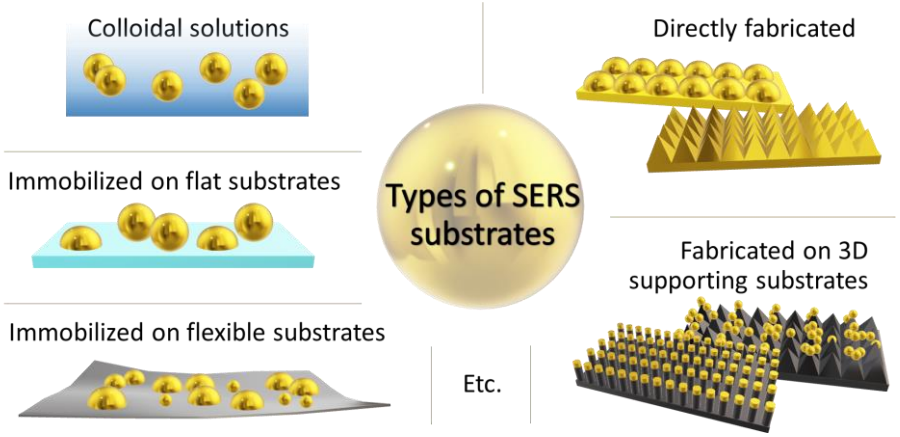

Figure 5. Types of SERS substrates.

By now, all the employed substrates can be sub-divided into groups according to their fabrication:

(i) **Colloidal** solutions of noble metal nanoparticles [76], magnetic nanoparticles [77], dielectric-metal core-shell nanoparticles [78], metal-metal core-shell nanoparticles [79], metal-dielectric/oxide/polymer nanoparticles (which form SERS sub-approach known as Shell-isolated nanoparticle-enhanced Raman spectroscopy, or SHINERS [80]), etc.;

(ii) Nanoparticles from **colloidal** solutions (all types) **immobilized** on a solid **flat** substrate (Si, SiO_2, glasses, etc.) [81], [82] or **flexible** substrates (cellulose paper [83], cotton fabric [84], PDMS [85], etc.);

(iii) Noble metal nanoparticles **directly fabricated** (e.g., lithographically produced nanoparticles [86], sputtered with magnetron [87],

evaporated [88], etc.) on a solid **flat** substrate (Si, SiO_2, glasses, etc.) or ***in situ*** **grown** on a **flexible** substrate (cellulose paper, cotton fabric, etc.) [89];

(iv) One-pot **self-assembled** plasmonic nanostructures [90];

(v) Noble metal nanoparticles **directly fabricated** on 3D supporting substrates (pillar arrays [91], grooves [92], wires [93], holes [94], etc. in Si, SiO_2, glasses, etc.).

Although there is a variety of employed in laboratory research SERS substrates as well as some substrates are already commercially available, there are still several drawbacks and limitations which significantly hinder the introduction of technology into widespread use and keep it quite aside from realistic implementation.

Commonly used colloidal solutions of noble metal nanoparticles (or other types of particles as mentioned above) provide significant enhancement of Raman intensity, but often suffer from poor stability [12], strong dependance on the storage conditions [13], poor reproducibility and uniformity [11], [14], and are fairly inconvenient in routine use [11]. Immobilization of nanoparticles complicates the measurement procedure, the nanoparticle spatial distribution is inhomogenious which reflects in a strong variation of the Raman signal over the surface, impossibility to apply for quantitative analysis, short exploitation times of SERS substrates and disposability in use. Immobilization of nanoparticles on 3D structures as well as their direct fabrication or *in situ* growth (e.g., metal-capped structured arrays [95] and nano- wires [96], Au-coated flexible polymer “fingers” [97], etc.) greatly benefits in repeatability, while high enhancement is sacrificed. However, fabrication of 3D structures is often a multistep, complex, and not cost-efficient procedure and is carried out by electron-beam lithography [98], [99], [100], [101], focused ion-beam lithography [102], and MACE [103].

Therefore, fabrication of a reliable and sensitive substrate is still an unresolved issue and is always a trade-off between efficiency and enhancement factor from one side and stability, reliability, uniformity from the other side. And both sides face the problem of simplification and cost-reduction, leaving a lot of space for creating new types of SERS-substrates.

1.4. Silicon-based sensors and SERS substrates: recent achievements and limitations

Biosensors form a big class of devices aimed at the detection, amplification, and conversion of information about biological processes into a detectable signal, most often electrical or optical [104]. Silicon is one of the most widely

used semiconducting materials in electronics and photonics. A polished silicon is reflective in the UV [105], visible and NIR ranges [106]. The micro-structuring of silicon remarkably modifies its optical properties and makes it highly absorptive in the spectral range from UV to NIR [107], [108], endowing the material with a deep black color. For this reason, this material has received its own name "black silicon". The surface of black silicon can be represented by structures of various shapes, such as pyramids, cones, needles, pillars, holes, etc., which enhance absorption [109] owing to efficient light trapping [110]. This effect is complemented by the absorbance caused by the structural defects in the Si lattice or impurities (specifically sulfur) during surface micro-structuring [109], which create IR absorbing states in the band gap and are also responsible for the trapping of photo-excited carriers [111]. Thus, the overall mechanism of wide-range black silicon absorbance originates from the absorbance by these defects, enhanced by multiple reflections between the microstructures of black silicon, suppressing specular reflection (Figure 6).

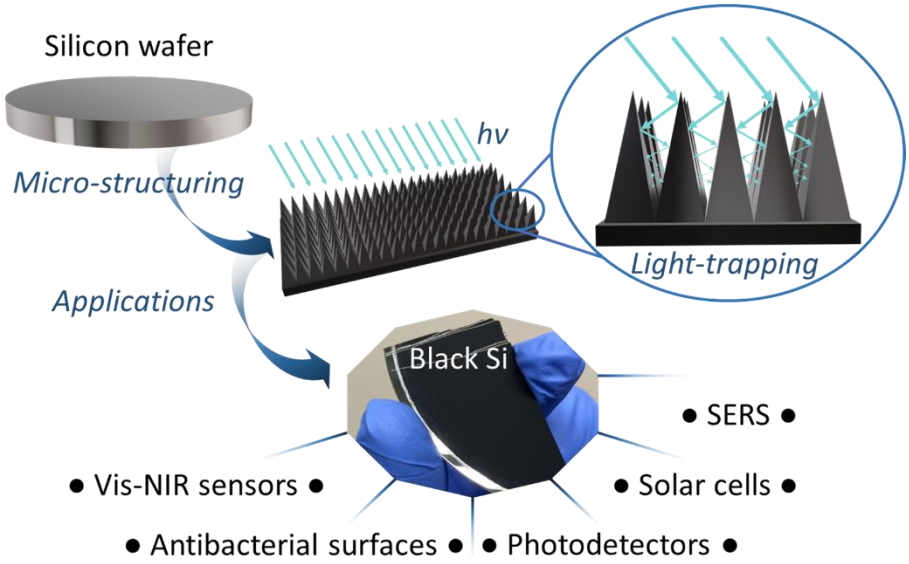

Figure 6. Micro-structuring of silicon, acquired light-trapping properties and related to micro-structuring applications.

There are several methods to achieve nano- and micro-structuring of silicon surface, including metal-assisted chemical etching (MACE), femtosecond laser assisted fabrication [110], [112], laser chemical etching [109], wet chemical etching and reactive ion etching (RIE) [113], which enables to obtain uniform coverage of the surface with identical structures on the large scale. The principal mechanism underlying the creation of a highly

developed surface is the bombardment of the sample surface with highly reactive ions from the plasma and a chemical reaction with silicon, which causes selective erosion of the silicon wafer surface [114].

Application of silicon for creation of 3D micro- and nano-structures, which serve as a supporting or precursor substrate to form plasmonic nanoparticles responsible for Raman signal enhancement, is attracting more and more attention for several reasons. Firstly, silicon is the most suitable material to be integrated in electronic devices, lab-on-chip systems, microfluidics, etc. Secondly, silicon is a more malleable material for structuring than, for instance, cheaper glass materials. The rate of silicon etching with fluorine radicals is 40 times higher than that of glass [115], making the micro-structuring of glasses by ICP-RIE techniques more complex and time-consuming. Silicon also surpasses glass materials due to chemical and structural homogeneity. Moreover, the charging effects which occur during etching of dielectrics like glass drastically affect the progress and the direction of the reaction, significantly complicating 3D and even 2D patterning of glass materials [116]. Finally, due to the long history of silicon microelectronics, many approaches to structure the silicon surface exist, and the technological processes are well established.

Micro-structuring of silicon for SERS is gradually being introduced into research. In [117] micro-/nano-nested structures in silicon obtained by MACE with deposited gold nanoparticles allowed reaching a satisfactory EF of around 10^6 and providing acceptable performance as part of a microfluidic cell for almost 120 days of storage. Arrays of silicon nanopillars capped with noble metals produced by plasma-etching ensured significant Raman signal enhancement (the authors stated the value of EF around 10^{11}) and sensitivity [118], but disposable and fragile because of the nanopillar breakage caused by surface tension upon contact with the analyte. Silicon nanowires fabricated by a complex combination of nano sphere lithography and metal assisted chemical etching, coated with gold also outperformed good enhancement with 10% Raman signal variability and picomolar detection limit, although suffered from the same problem as silicon nanopillars [103].

Black silicon, belonging to the same class of micro-structured materials, is a simple to implement, cheap and mechanically stable alternative to the types of silicon described above. Black silicon was discovered accidentally and has long been regarded as an unwanted side-product [119], but now its remarkable absorbance has made black silicon a versatile material for various applications. Among them are solar cells [111], THz emission sources [120], microfluidic devices [121], antibacterial surfaces [20], [122], visible light and NIR sensors [111], [123]. Black silicon is cost-effective and

enables integration into a silicon platform, thus, it has started replacing indium gallium arsenide and germanium in commercial NIR photodetectors [124]. Hyper-doped black silicon fabricated by femtosecond-laser irradiation is demonstrated to be a superior ammonia-sensing material [125]. Specifically functionalized ICP-RIE black silicon provides nitroaromatic compound detection with 10^{-12} ppt limit by fluorimetric approach with excitation in UV spectral range [125].

The apexes of the microstructures of black silicon have high curvature and being capped with noble metals, can serve as active sites for electromagnetic field enhancement. Microstructures themselves are rigid, do not deform under the action of surface tension caused by the contact with analyte. Due to wide-range light absorption, trapping, and localization effects, specified by surface nano- and micro-structuring, black silicon becomes a perspective material for designing nanobiophotonic devices. Basic principle of nanophotonic devices is based on the ability of nanophotonic structures to tightly confine light near their surface in sub-wavelength volumes (down to distances of less than ten nanometers), create regions of strong electromagnetic fields, called 'hot spots', resulting in enhanced light-matter interactions [126]. Surface-enhanced Raman scattering spectroscopy uses this phenomenon to boost the signal from the molecules of analyte. Plasmonic excitation can provide Raman signal enhancement by up to 10 orders of magnitude making this approach immensely useful in numerous vital areas, where reaching very low detection limits is urgent, such as healthcare [4], pharmaceutics [127], food safety [10], etc. Black silicon nano- and micro-structures successfully cope with the function of light trapping, thus, their combination with plasmonic nanostructures which have the resonance properties complying with the aims of the research and spatially are co-located with the molecules of analyte, make them a promising basis for creating SERS-based type of nanobiophotonic sensors.

The high wide-range absorbance of black silicon is also beneficial for nanoplasmonic applications. Black silicon performance as a SERS-substrate was demonstrated for detecting individual algal cells (Chlorella vulgaris) [128] and rhodamine 6G molecules [21], however, gold layers of 200-400 nm thickness make these substrates economically less viable and also, possibly, inferior in properties to other existing materials.

Appropriate choice of the fabrication approach of black silicon can significantly simplify the production and reduce the cost. MACE, which allows large-scale production of black silicon, requires using gold (Au), silver (Ag), aluminum (Al), copper (Cu) and nickel (Ni) as catalysts [129]. Chemical etching of silicon surface occurs in one step, when metal on the silicon surface

emerges from the etching aqueous solutions, containing, e.g., metal nitrates, or in two steps, when, firstly, metals are physically deposited on the silicon surface (by sputtering, evaporation, etc.) and only then the surface is chemically etched [130]. In MACE, metal catalyst moves deep in the created silicon pores and is often located at the bottom of the chemical structures, making it difficult for analyte molecules to access the hotspot. ICP-RIE technique constitutes another group of methods of large-scale fabrication of black silicon and it outperforms other techniques, including MACE. In ICP-RIE, plasma consisting of highly reactive ion species reacts with the surface of the sample and causes its selective erosion [114]. ICP-RIE performed at cryogenic temperatures allows precise control of the surface geometry of black silicon, sidewall orientation of micropillars, and the level of roughness, which is achieved through the combination of etching and passivation processes [131], [132]. Black silicon obtained by ICP-RIE at room tempterature is characterized by higher porosity and micro-roughness which is reflected in increased effective surface area, although the micro-structures themselves are less controllable than those obtained by more complex and expensive cryogenic ICP-RIE [133]. High effective surface area and 3D arrangement of noble metal nanoparticles which serve as hotspots may increase the probability of the analyte molecule trapping in hotspot proximity and thus improve the sensitivity. All the mentioned above enables an efficient, simple, large-scale and low-cost approach for the fabrication of black silicon-based surfaces for SERS.

Considering all the features and specific properties described above, it can be concluded that black silicon produced by ICP-RIE represents an excellent alternative material as a support for plasmonic nanostructures for creating stable, efficient, and scalable substrates. However, existing examples of the use of black silicon for SERS with relatively thick noble metal layers and issues of black silicon non-biocompatibility still leave room for the development of new designs of these nano-micro-structured materials for cheap, scalable, and applicable for living cell analysis SERS-active substrates.

1.5. Carbon nanomaterials for cancer treatment: efficiency and safety concerns

In the past decades, a conceptual shift in cancer treatment has occurred. Several independent processes, such as tumor imaging, tracking of drug delivery and cancer treatment, can be realized by using one nano-agent. Such a combination of diagnostics and therapy is called theranostics. Theranostic nano-agent must meet the following requirements: (i) be a source of imaging signal (magnetic, fluorescent, radioactive, acoustic, etc.), (ii) serve as a therapeutic drug or (iii) be a carrier of a therapeutic drug, and (iv) be selectively accumulated in the tumor [134] (Figure 7).

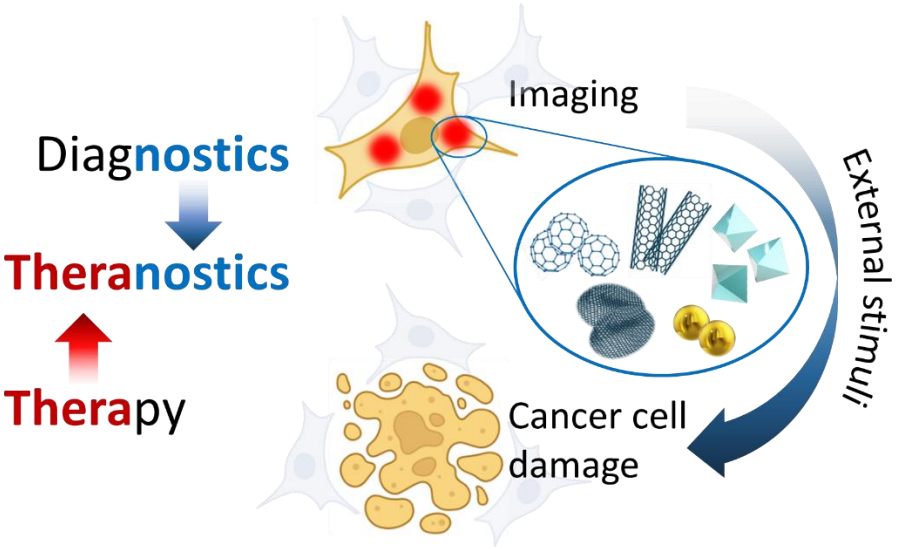

Figure 7. Theranostics conceptual scheme. Created with BioRender.com.

Carbon nanomaterials and graphene derivatives (graphene oxide, GO; graphene nanosheets; graphene quantum dots, GQDs; single-walled and multi-walled carbon nanotubes, SWCNTs and MWCNTs) depending on the process of production or post-processing have enormous surface functional groups which determine the efficiency of nanomaterial complexation with biomolecules and, thus, their redistribution between cells in tissue and accumulation inside the cells [135], [136] as well as their interaction with the cells of immune system.

Specific properties of both SWCNTs and MWCNTs [137], [138], [139] make them suitable for theranostic applications. High aspect ratio and nano-needle shape determines drug delivery capacity [140], functionalization of CNTs through edge groups makes them selective and capable of targeting

distinct tumors [141], intense characteristic Raman spectrum allows imaging CNTs distribution inside the cell [142]. Significant absorbance of SWCNTs in NIR [143] enables their application in photothermal therapy [144], which surpasses less specific and more aggressive conventional chemo- and radiotherapies.

Despite the obvious theranostic potential of SWCNTs, their implementation as theranostic nanoagents runs into serious obstacles. The strong Van der Waals interaction between individual CNTs in water solutions results in their significant agglomeration [145], which induces immune cell activation (inflammation) [146], [147] and platelet activation and aggregation (thrombosis) in the living systems [148]. Uniform stable water suspensions of SWCNTs are among the key requirements for efficient and safe theranostics. Moreover, SWCNTs demonstrate length-dependent cytotoxicity [149], [150] which is exacerbated by metal catalyst contamination [151], thus, as-produced SWCNTs of several microns in length are unsuitable for bio-applications. However, recent advances in mass-production of high-quality extra-purified SWCNTs [152] of single chirality [153] and the emergence of approaches that allow gentle cutting of SWCNTs down to 100 nm length [154] together with their proper and effective functionalization [135] have reawakened interest to this type of nanomaterials.

Embedding the biological materials (cells, tissues, organs) with carbon-based nanoparticles (NPs) may change their physical and chemical properties significantly [155], thus affecting the response of the biological material to the external stimuli. The increase in thermal conductivity of water suspensions after the addition of just 1wt.% of CNTs is one of such possible changes [156]. Variation of SWCNTs functionalization or the time of their interaction with the biological object also determines the localization of SWCNTs either inside the cell [157], on the cell membrane [158], or in the external media. This, in turn, together with nanoparticle organization in a form of individual NPs, ensembles, bundles, agglomerates, will govern the efficiency of theranostics and define the presence and severity of side effects.

All the applied nanomaterials for theranostics face very similar problems of their elimination from the body, and inflammation concerns. In this context, possible pathways of biodegradation and knowing the exact mechanism of this process could simplify the process of the creation of the theranostic nano-agents and provide an objective criterion of nano-agents selection, excluding the materials which are unsuitable and incapable of biodegradation according to the established mechanisms. At present, very little is known about the exact mechanisms of possible degradation of nanomaterial-based theranostic agents in living organisms, although some

efforts have been made recently to estimate the possibility of destruction of MWCNTs and SWCNTs when interacting with immune cells [159]. Empirical data demonstrate the involvement of heme-containing enzyme myeloperoxidase (MPO) [160], secreted predominantly by immune cells neutrophils and macrophages, responsible for the generation of various reactive oxygen species and being the only enzyme, which can produce hypochlorous acid [161]. However, the exact mechanism of the interaction between the immune cell and graphene-based nanomaterials is currently undisclosed and requires additional research.

2. METHODS EMPLOYED IN THIS RESEARCH WORK

2.1. Materials and reagents

2.1.1. Black silicon fabrication and gold sputtering

For all experiments 2-inch <100> p-doped (bulk resistivity 1–30 Ohm·cm) silicon wafers of 275 ± 25 μm and 0.5 mm thickness were used. Gold pseudo-layers of different thickness were magnetron sputtered. Quartz slides (SiO_2) or polished silicon wafers were used as a flat reference throughout all experiments. The silicon wafers or quartz slides were cleaned by oxygen plasma for 2 min before etching or any other further use.

Cone-like black silicon was fabricated using a cryogenic, inductively coupled plasma reactive ion etching procedure as reported in [131], [162].

Lace-like black silicon was obtained by room temperature (RT) one-step mask-free inductively coupled plasma reactive ion etching and carried out in a PlasmaLab80 system (Oxford Instruments). Etching process was conducted using the two-gas mixture of SF_6 and O_2 with a flow of 10 and 9 sccm, respectively. The dry anisotropic silicon etching was performed for 10 min at 30 mTorr chamber pressure, 15 W of RF power and 200 W of ICP power. The temperature of the cooling system was 20 °C.

Pillar-like black silicon with different surface profiles was obtained by cyclic Bosch etching process with the variation of the etching time in the range of 18–30 min [163], [164]. It is a self-masked process, which consists of a step of the formation of plasma-polymerized fluorocarbon islands from C_4F_8 gas [165] acting as a mask, followed by etching with SF_6/O_2 gas combination. The temperature of the wafer was controlled throughout the etching.

Gold deposition on top of cone-like and lace-lice black silicon substrates was carried out by magnetron sputtering for 80 s and 120 s using the gold target (Target gold, 99.99%, 57 mm, 91017-AU, Electron Microscopy Sciences, USA). Gold pseudo-layer was sputtered using a Quorum Q150T ES Plus-Turbomolecular pumped coater (sputter current 50 mA, argon pressure 2 mBar). Gold deposition on pillar-like black silicon was done under the same conditions when a 25 nm gold layer is formed on a flat quartz slide.

Formation of a self-assembled monolayer (SAM) of 4-mercaptobenzoic acid (4-MBA, $HSC_6H_4CO_2H$; Sigma, USA) molecules on the analyzed surfaces was done their incubation in a 5×10^{-3} mol/L 4-MBA solution for 4 h followed by washing with ethanol flow for 10 drying with N_2, further kept in hermetically closed containers until experiments. For living cell analysis, the prepared substrates were additionally sterilized at 110 °C for 2 h and then

placed in plastic Petri dishes in the cell culture medium DMEM/F12. The principal scheme of the experiment is presented in Figure 8.

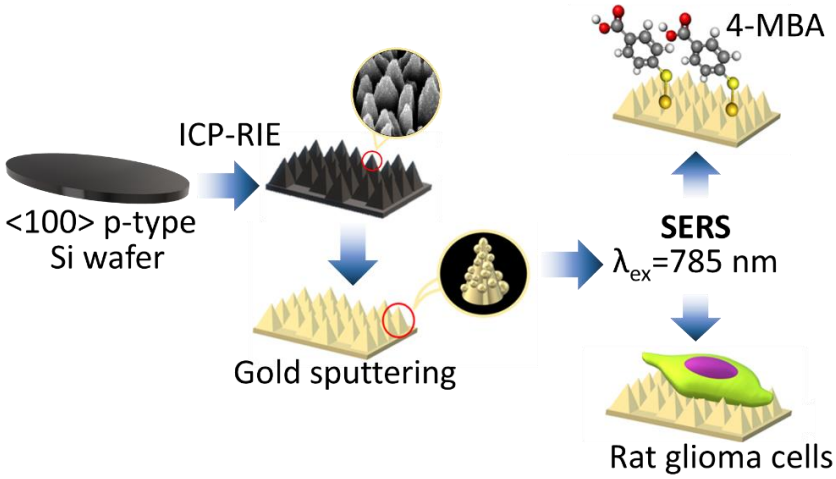

Figure 8. Fabrication and SERS applications of black silicon.

2.1.2. Green fluorescent graphene quantum dots

Water-dispersed green fluorescent GQDs (CAS 7440-44-0, Sigma-Aldrich, USA) of topographic height of about 1.0–2.0 nm and diameter less than 5 nm were used as a model of graphene-based nanomaterial in biodegradation studies. To exclude osmotic shock to living cells, GQDs were dissolved in phosphate-buffer saline (PBS) at a final concentration of 2.5–50.0 μg/mL. PBS was adjusted to pH = 7.2 and prepared as follows: 136.9 mM NaCl, 2.7 mM KCl, 2.0 mM $MgSO_4$, 2.0 mM $CaCl_2$, 8.9 mM $Na_2HPO_4 \times 7H_2O$, 1.5 mM KH_2PO_4. The solutions of hydrogen peroxide (H_2O_2, Sigma-Aldrich, USA) or sodium salt of hypochlorous acid (NaClO, Sigma-Aldrich, USA) (final concentrations of 0.01–10.0 mM) were used to create model conditions of neutrophil response caused by carbon-based nanomaterials.

2.1.3. Single-walled carbon nanotubes

HiPCO SWCNTs (Nanointegris Technology Inc., Batch PO568) of a diameter from 0.8 nm to 1.4 nm (mean value is 1.0 nm) in bundles, purified from metal impurities (> 98%), with metallic to semiconducting nanotubes ratio of 1:2, were used for the development of a theranostic carbon-based nano-agent. The shortening of SWCNTs down to 100–500 nm in length was performed as described in [154] and functionalized by salmon DNA (Sigma-Aldrich, USA) (Figure 9). Stable suspension of SWCNTs non-covalently functionalized with

DNA was prepared through several steps of sonication and centrifugation, in more details described in Paper (E). SWCNT concentration in suspension was determined spectrophotometrically as described in [142]. The obtained SWCNT-DNA suspensions were stable for at least 4 months and were further applied for cancer cell imaging and destruction.

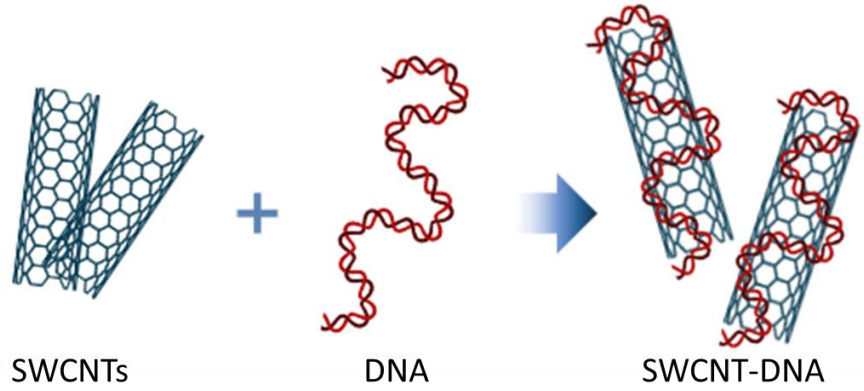

Figure 9. SWCNT-DNA complexes which were used in the study. Created with BioRender.com.

2.1.4. Cancer cell line

Rat glioma cells C6 (ATCC, CCL-107), obtained from ATCC, LGC Standards (Ogrodowa 27/29, Kielpin, Poland), were grown in DMEM/F12 (Gibco, USA) medium supplemented with 10% newborn calf serum (Capricorn, Germany) and 80 μg/mL gentamycin sulfate (BelMedPreparaty, Belarus) at 37 °C, 100% humidity, and 5% CO_2.

To analyze SWCNT distribution inside the cell, 10^5 cells per Petri dish were seeded on pieces of flat polished silicon (1 cm × 1 cm) to avoid strong background during measurements. When cells were attached to the silicon surface, suspensions of SWCNTs (in-dish concentration was adjusted to 5 μg/mL of SWCNTs) were added to Petri's with growing cells 18 or 24 h before analysis – the time acquired for SWCNT accumulation inside the cells. Afterwards, the monolayer of cells grown on Si slide was washed twice with PBS.

2.2. Surface morphology characterization of substrates

Analysis of surface geometry of black silicon, pyrolytic carbon on black silicon or SiO_2, graphene nano-walls, and black silicon sputtered with pseudo-layer of gold was performed by scanning electron microscopy (SEM) using a

Helios NanoLab 650 model microscope, manufactured by FEI. The nominal beam voltage was 3 kV. Geometrical parameters were extracted from micrographs of investigated samples using open-source software ImageJ [166].

2.3. Raman and surface-enhanced Raman spectroscopies

Raman and surface-enhanced Raman spectroscopies and Raman laser-scanning microscopy were performed for the following types of objects: living glioma C6 cells on flat silicon substrates and on cone-like black silicon substrate, SAM of 4-MBA deposited on all types of black silicon sputtered with gold and SiO_2 slides sputtered with gold, living glioma C6 cells with accumulated SWCNT inside the cytoplasm grown on flat silicon substrates, GQDs and DOX deposited on lace-like black silicon, sputtered with gold. For each type of the analyzed object, conditions were selected in such a way as not to cause damage to the object.

Raman spectral measurements were conducted using three different setups to accomplish the requirements and specificity of the experiment. Evaluation of SWCNT-DNA accumulation inside the living glioma cells was performed with 3D Laser Raman Microspectroscopy System Nanofinder HE (Tokyo Instruments TII, Japan) in up-right configuration. Microspectrometry system was equipped with: (i) thermoelectrically cooled CCD UV-VIS-NIR camera (1024×127, Andor Technology, UK) operated at – 80 ºC for Raman signal detection; (ii) piezo-stage Nanocontrol NS4312 for scanning (mapping range 100×100×20 μm); (iii) built-in excitation laser 785 nm, 75 mW; (iv) built-in Czerny-Turner spectrometer with a focal length of 550 mm, maximum spectral resolution 0.7 cm^{-1}/pixel (measured for laser 532 nm, grating 1800 lines/mm, CCD 1024 pixels); (v) built-in calibration light source (hollow cathode spectral lamp) to provide accurate spectrometer calibration before each set of experiments; (vi) grating 1800 lines/mm. Confocal measurements were performed with a square pinhole set to 25×25 μm. To ensure cell integrity and viability all measurements were performed with water-immersion objective UMPLFLN Olympus (Japan), 40×, NA 0.8, working distance 3.3 mm, directly in liquid Hepes-buffer solution with cells grown on silicon slides placed inside the Petri dish (diameter 3.5 cm). The scanning step was 1.5-2.0 μm and exposure time was 0.5–2 s, depending on the experimental series.

SERS measurements of 4-MBA SAMs and living cells on black silicon sputtered with gold pseudo-layer were performed using an inVia confocal microscopic Raman system (Renishaw, UK) equipped with a thermoelectrically cooled (−70 °C) CCD camera with the 785 nm diode laser

used for excitation with grating 1200 lines/mm. For 4-MBA observations the laser power at the samples was 10 μW (50× air objective). Living cell detection was performed at 10 mW laser power with 20× air objective. High power values are associated with energy dissipation and signal loss caused by 0.5 cm of liquid Hepes-buffer solution above the cells in Petri dishes. The exposure time was 10 s, and the spectra were collected three times to obtain a better signal-to-noise ratio.

Remaining Raman and SERS measurements were performed with Raman spectrometer RamanFlex 400 (PerkinElmer, Inc.) equipped with a CCD camera thermo-electrically cooled to −50 °C. The excitation wavelength was λ_{ex} = 785 nm for all experiments. The diameter of the laser spot was ∼200 μm. The working power was 50 mW, otherwise used for laser power and time exposure screening when the parameters varied from 3.8 to 90.9 mW and from 1 to 60 s, respectively. Spectra were accumulated 30 times per 10 s to exclude possible irradiation-induced damage of the sample, collected from 5 different points and then averaged.

2.4. Numerical simulations

The finite element method (FEM) was applied to obtain optical properties of nanostructures localized on the surface of black silicon. Simulations were performed with a software Comsol Multiphysics 5.5.

The 3D organization of gold nanostructures on the surface of nano- and micro-structured black silicon allows achieving all possible variations of the direction of particle-wave interactions because of multiple reflections from the sides of silicon microstructures and light-trapping effect of black silicon. Thus, without a loss of generality, excitation was approximated as a plane wave with linear polarization propagating from a fixed direction towards the nanostructure surrounded by air. Size and shape of simulated nanostructures were taken from SEM micrographs of black silicon sputtered with gold and was varied to disclose the tendencies in optical parameters change and make predictions for the future black silicon structure fabrication and for choice of the conditions for gold sputtering. The dielectric functions of gold and silicon are static parameters, involved in calculations and taken from the Comsol Multiphysics library.

The simulations by FEM were performed for the full field formulation. The initial electromagnetic field was defined analytically as $\mathbf{E_{in}} = \mathbf{E_0}\, e^{-ikz}$ (k is a wavenumber, $\mathbf{E_0}$ is the amplitude of the incident plane wave). Meshing sizes were less than $\lambda_{in}/8$ for free space and less than $r_0/6$ for nanostructures, where λ_{in} is the wavelength of the incident light and r_0 is the radius of a spherical part

of a nanostructure, respectively. Simulations were performed for λ_{in} varying from 400 nm to 1200 nm. Nanostructures and media were surrounded by a perfectly matched layer (PML). Then local field $\mathbf{E}_{Loc}(\mathbf{r})$ was calculated and $|\mathbf{E}_{Loc}|/|\mathbf{E}_0|$ was obtained and used for estimation of EF using $|E|^4$-approximation. Absorption cross-section σ_{Abs} of the particle was calculated to reveal the resonance conditions (λ_{SPR}) for the analyzed structures.

2.5. UV-vis, steady-state, and time-resolved fluorescence spectroscopies

Measurements of absorbance of GQD water suspensions were performed using UV–vis spectrophotometer JASCO V-670 (Jasco, Japan).

Fluorescence spectra and time-decay measurements were conducted using time-correlated single-photon-counting fluorescence spectrometer F900 (Edinburgh Instruments Ltd, UK). The temporal evolution of the fluorescence of GQD solutions at λ_{em} = 530 nm was fitted using a built-in software (Edinburgh advanced lifetime analysis software) with the following function:

$$Fit = A + B_2 \cdot e^{t/\tau_1} + B_2 \cdot e^{t/\tau_2}, \quad (9)$$

where τ_1 and τ_2 are characteristic lifetimes and $B_{1,2}$ are relevant pre-exponential factors of the fast and slow components of the fluorescence, respectively; A describes an additional background intensity. Sample parameters $b_{1,2}$, presented in the Results and Discussion section, are relative fluorescence intensities of the i^{th} component and are defined as:

$$b_{1,2} = \frac{B_{1,2}\tau_{1,2}}{B_1\tau_1 + B_2\tau_2}, \quad (10)$$

2.6. Fluorescence microscopy and cell viability determination

Fluorescent microscopy and light exposure studies of living cells were performed using rat glioma C6 cells which were seeded at low density (10^4 cells per channel) in a 6-channel slide (sticky-Slide VI 0.4, Ibidi, Martinsried, Germany) with a glass coverslip as a substrate. Measurements were conducted in Hepes buffer solution of the following composition (in mM): NaCl – 126, KCl – 3, $MgSO_4$ – 2, $CaCl_2$ – 2, Hepes – 10, and glucose – 6.

Fluorescent microscopy of neutrophils was performed on fixed cells prepared as follows. Neutrophils isolated from whole blood were exposed to 50 μg/mL water suspension of GQDs (in PBS), allowed to adhere to the glass or silicon wafer surface for 30 and 90 min at 37 °C. The slides with adherent

cells were washed twice with PBS, fixed with 4% paraformaldehyde (Sigma-Aldrich, USA) for 10 min at RT. The fixed cells were washed with PBS and deionized water. Adherent and fixed neutrophils were treated with 0.2% Triton X-100 for permeabilization. The CytoPainter Phalloidin-iFluor 532 (Abcam, UK) was used to stain the cytoskeleton of neutrophils, the MPO distribution in neutrophils was assessed using the MPO-FITC antibodies (Beckman Coulter, France). The stained cells were washed with PBS and deionized water.

Rat glioma C6 cell viability was determined using fluorescent dye propidium iodide (PI). Living cells were exposed to the external buffer containing PI at the final concentration of 10^{-6}. If the cell membrane damage occurred, PI penetrates the cell and intercalates into DNA or RNA and becomes highly fluorescent, indicating cell death.

Fluorescence imaging of cells was performed with an inverted Nikon Eclipse Ti-U microscope with 60× NA 1.2 WI Plan Apo VC objective (Nikon, Japan) in the wide-field epi-illumination mode. The choice of the excitation source and detection configuration was determined by spectral characteristics of antibodies, dyes or GQDs. Fluorescence images were detected with DU-897E-CS0-UVB EMCCD (Andor, UK).

Interaction of pulsed NIR laser radiation with living cells which accumulated SWCNTs was performed by using a home-made CARS system with a picosecond 1 MHz laser source (EKSPLA Ltd., Lithuania) with dual-wavelength, combined with Microscope Olympus IX71 and a piezo scanning system (P-517.3CL, Physik Instrumente GmbH & Co, Germany). An oil-immersion objective (Olympus, Plan Apochrom., 60X, NA 1.42, Japan) was used to focus a laser beam on the sample. CARS signal was detected with the avalanche photodiode (SPCM-AQRH-14, Perkin Elmer, UK), connected to a multifunctional PCI board (7833R, National Instruments, Lithuania).

3. RESULTS AND DISCUSSION

3.1 Impact of nano- and micro-roughness of silicon- and graphene-based substrates in biocompatibility

The development of biosensors, scaffolds, implants, drug-eluting coatings, and wearable devices involves the integration of living systems into inorganic platforms. Fragility and sensitivity of living systems impose restrictions on the physical and chemical properties of the interface between artificial material and a living cell or tissue. The substrate materials used for living cell applications need to meet several requirements, including sterility and the ability to maintain cell viability, while also allowing for real-time analysis and control of cellular activity.

Within the framework of the present research, astrocyte-like glioma cell line was utilized to examine the potential of micro-structured silicon-based materials and their combination with nanocarbon-based cover for directing cell growth without the use of poly-L-lysine or other biopolymers to control cell adhesion. Specific focus was on analyzing the cell viability and preservation of specific cell morphological features and functions when influenced by the nano-micro-structuring of the bio-interface.

Five candidate substrates with various micro- and nano-roughness included: (i) cone-like black silicon, fabricated by cryogenic ICP-RIE technique (production is provided in Section 2.1.1), (ii) cone-like black silicon covered with 20 nm thick PyC layer – model of 3D micro-structuring with different nano-roughness because of PyC cover; (iii) flat SiO_2 covered with (19 ± 7) nm thick PyC layer (further referred to as "PyC (20 nm)"), (iv) flat SiO_2 covered with (42 ± 11) nm thick PyC layer (further referred to as "PyC (40 nm)"), and (v) flat silicon wafer densely covered with graphene nano-wall (GNW) film composed of micron-sized vertically oriented graphene flakes.

Tissue culture-treated plastic Petri dishes were used as a control substrate for living cell growth. To reveal the specific surface morphology features of the fabricated substrates, AFM, SEM analysis were performed (SEM micrographs of surfaces are shown as insets in Figure 10). Control of the PyC and GNW layer quality was made by Raman spectroscopy analysis. PyC films on the flat SiO_2 of both thicknesses exhibit grainy structure, however, PyC (20 nm) is smoother than PyC (40 nm) as it follows from their AFM-measured parameters (R_q^{20nm} = 0.9 ± 0.2 nm vs. R_q^{40nm} = 2.9 ± 1.3 nm, respectively). The analyzed black silicon consists of cone-like silicon structures, which geometrical dimensions are summarized in Table 2. The PyC film deposition leads to the smoothing of the cone surface which is

quantitatively supported by the decrease in the roughness from 81 ± 12 nm to 75 ± 9 nm (AFM data) and increase of the apex curvature of the cones.

Biocompatibility and affinity of the substrates to living cells was evaluated basing on the cell confluence (average area occupied by cells in culture), average cell number, cell spreading (the average area per one cell), and morphological features of cells (shape, processes, etc.). The characteristic fluorescence images of glioma cells fixed on the substrates are summed in Figure 10, and main cell characteristics are summarized in Table 1. According to these data, in terms of biocompatibility, cone-like black silicon is very similar to specific tissue culture treated (TT) plastic, which ensures good cell adhesion and growth. Black silicon provides a higher division rate of cells and promotes preservation of normal cell morphology. But, in contrast to flat specifically modified plastic, black silicon possesses nano-roughed 3D micro-structures.

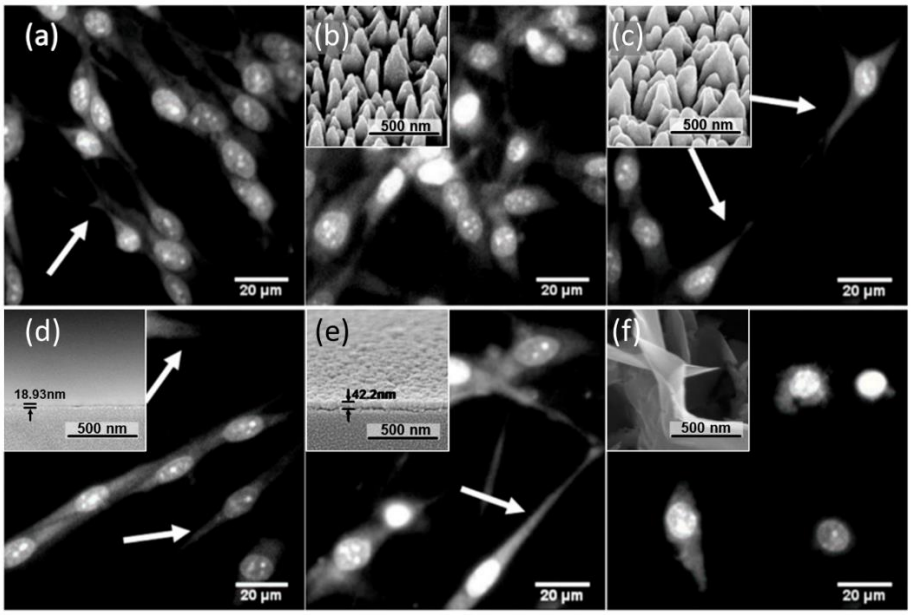

Figure 10. Typical fluorescent images of glioma cells grown on substrates with different roughness: (a) TT plastic (control); (b) cone-like black silicon; (c) PyC (20 nm) on cone-like black silicon; (d) PyC (20 nm) on SiO_2; (e) PyC (40 nm) on SiO_2; (f) graphene nanowalls on flat silicon. Insets represent SEM images of the analyzed substrates. Long cell processes are marked with arrows. Cells were stained with PI. Fluorescence image size is 115 × 115 µm. Adapted from **Paper (A)**.

Table 1. Influence of substrate type on the morphological features of glioma cells.

Parameter	TT Plastic	PyC (20 nm) on SiO_2	PyC (40 nm) on SiO_2	Cone-like bSi	Cone-like bSi with PyC	GNWs on flat Si
Confluence, %	63.3±10.3	33.7±7.1*	55.1±10.3	68.9±28.2	$^{\#}$20.7±4.6*	11.6±5.1*
Av. cell number per 200×200 μm²	36.0±3.7	15.6±1.1*	25.2±2.6*	53.8±15.2***	$^{\#\#}$13.0±0.7*	7.3±0.4*
Area per cell, μm²	703±115	864±183**	875±164**	513±209	636±143	637±280
Cell morphology characteris-tics	Elongated, spindle-shaped, 2-3 long processes, numerous intercellular contacts	Elongated, spindle-shaped, 2-3 long thin processes, few intercellular contacts	Elongated, spindle-shaped, 2-3 long thin processes, few intercellular contacts	Spindle-shaped, rounded, many middle-sized processes, many intercellular contacts	Elongated, spindle-shaped, 2-3 long thin processes, few intercellular contacts	Rounded, no processes or short wide processes, no intercellular contacts

Footnotes: Data are presented as the means ± SDs. The statistical significance of the results was analyzed by an unpaired t-test (*$p < 0.001$, **$p < 0.01$, ***$p < 0.05$ vs. sample on plastic, $^{\#}p < 0.05$, $^{\#\#}p < 0.001$ vs. sample on black silicon, bSi). Adapted from **Paper (A)**.

Deposition of PyC layer at high temperature, 1100 ^{o}C smooths the sides of the cones of black silicon, and, as a result, reduces its adhesive properties which is reflected in weakening of cell-surface contact and decreasing of the division rate of cells (poor confluence). The same trend is observed for PyC layers on flat SiO_2 with some restoration of cell proliferation efficiency for a thicker PyC layer. PyC layer cover preserves biocompatibility of all substrates, as cells have their usual morphology characteristics, indicating the possibility to apply conductive PyC layers for endowing the substrate-cell interface with photo-electrical properties for future sensing applications.

Further decrease in the roughness of the substrate to nanoscale (as in case of GNWs) leads to a significant loss in cell adhesion and biocompatibility. Cells lose long processes, do not form intercellular contacts, stay round shaped, and thus, lose the ability of effective cell division.

Cell adhesion to the substrate is governed by specific protein complexes located in the plasma membrane. All the structures, responsible for cell sensing environment, cytoskeleton dynamics, cell movement [167], have specific dimensions, which are critical for the formation of the contact between cell and the interface as they strongly correlate with the interspike

distance. These structures, or focal adhesions, include sub-micron-sized (200-500 nm) “dot”-like, or point contacts, in the active edge of the cell, and elongated “dash” contacts (2–10 μm in length, 0.5 μm in width), which are partially located under the nucleus [168]. Thus, textures of low- and intermediate-roughness support cell attachment promotion, while the increase in the interspike distance to 4.5 μm inhibits cell adhesion [169]. These assumptions are in a good agreement with the experimental results: the distance between the prominences on biocompatible surfaces varies from approx. 70 nm for PyC on SiO_2 to approximately 260 nm for cone-like black silicon and PyC film on cone-like black silicon, which allows the cells to spread successfully over the substrate, establish the neighbour focal adhesion contacts with surface prominences in any direction. On the contrary, sharp edges of the graphene sheets in GNWs, which do not reach the minimal size required for the focal adhesion contact, in combination with their hydrophobicity, forbid the formation of the focal adhesion contact.

Therefore, the cell adhesion and selective biocompatibility can be regulated by changing the macro-, micro-, and nano roughness. Cone-like black silicon is suitable for cell culturing. Surface modification with PyC reduces cell adhesion by mimicking nanoscale roughness and shielding electric charges. Lowering the dimension of surface roughness to the nanoscale using vertical GNW-covered Si wafers results in poor biocompatibility, but it can be used for the formation of superhydrophobic tracks for directed neuron network formation. The regulation of cell adhesion by changing roughness allows for the development of sensor platforms with unique optical and electrical properties.

Depending on the etching method, different types of black silicon geometries are obtained. RT ICP-RIE gives less controlled structures than cryogenic ICP-RIE, however, nano- and micro-structuring of the surface is more pronounced. This switches the type of black silicon from hydrophilic to hydrophobic substrate (see Figure 11b and Figure 11c for cone-like and lace-lice black silicon, respectively), making it unsuitable for living cell analysis because of the abovementioned reasons (see Figure 11d and Figure 11e), but does not exclude analytical applications as it allows forced concentration of a few molecules per surface area unit when the droplet of analyte solution is dried (Figure 11f and Figure 11g) [170].

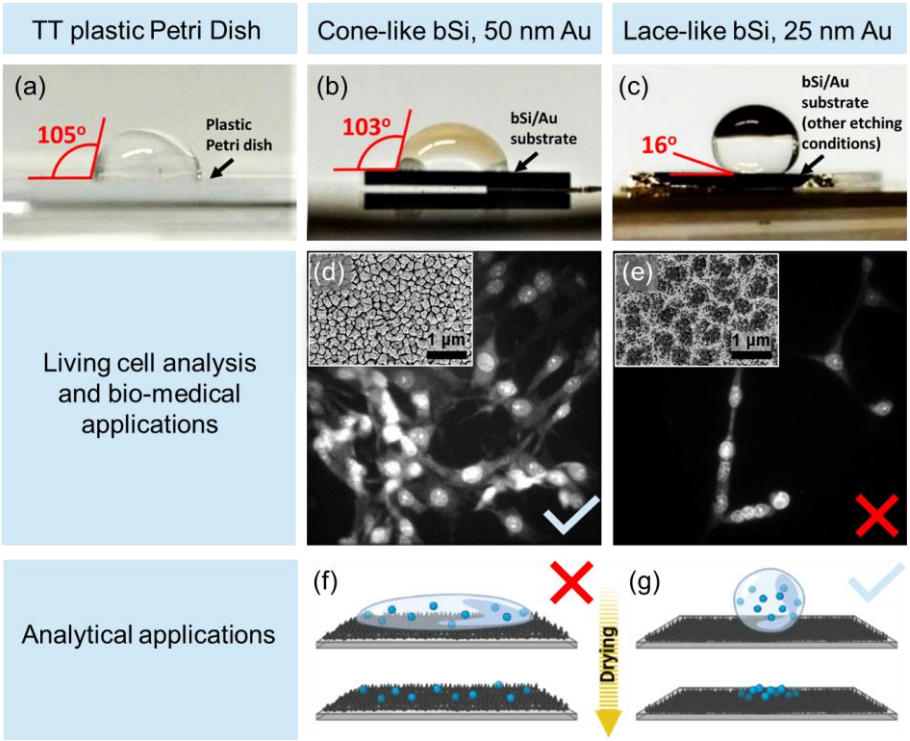

Figure 11. Hydrophilicity drop-cast test of black silicon, fabricated by cryogenic ICP-RIE (cone-like, central panel) and RT ICP-RIE (lace-like, right panel) and possible applications resulting from the property of hydrophobicity/hydrophilicity: (a) drop-cast on a specific plastic for cell culture, (b) on a cone-like black silicon and (c) lace-like black silicon sputtered with gold; (d) dense monolayer of glioma cells grown on a cone-like black silicon and rarely damaged singular cells on lace-like black silicon (all the conditions were similar for both experiments); (f) and (g) – schematic illustration of advantages of hydrophobic (g) over hydrophilic (f) surfaces for low concentration determination consisting of the spatial self-concentration of analyte molecules on the substrate after drying. Created with BioRender.com. Adapted from **Paper (B)**.

This was summarized in the **first statement** of the thesis: Surface micro-structuring, nano- and micro-roughness of black silicon is tuned by the fabrication procedure and results in: (i) hydrophilic biocompatible interfaces with cone-like silicon structures for living cell analysis when produced by cryogenic ICP-RIE technique, (ii) robust hydrophobic surfaces with dense lace-like silicon structures, suitable for analytical applications, when produced by RT ICP-RIE.

3.2 Application of biocompatible black silicon with ~50-60 nm gold layer for SERS of 4-MBA and living cells

Combination of black silicon with gold plasmonic nanoparticles defines such analytical application as SERS. Covering the cone-like black silicon with approx. 50 nm gold layer allows applying this type of black silicon for 4-MBA SAM. It is necessary to mention that before all the experiments, empty freshly prepared cone-like black silicon/gold substrate was always analyzed in terms of the presence of the impurities (see Figure A1, Appendix) and, unfortunately, complete exclusion of them could not be reached. However, appropriate storage and implementation eliminates possible effects of contamination on spectra of measured analytes. Moreover, the fabricated substrates (both cone-like and lace-like) demonstrate long term stability when storing hermetically in air atmosphere and ambient conditions (see Figure A2 and A3, Appendix).

Cone-like black silicon covered with gold pseudo-layer provides significant Raman signal enhancement of 4-MBA molecules when excited with NIR irradiation (λ_{ex} = 785 nm) as compared to the Raman signal intensities of 4-MBA SAM on flat SiO_2 sputtered with a gold layer of the same thickness (see Figure 12a, spectra 1 and 3 from bottom to top) and measured at the same conditions. All observed bands in SERS spectra are in good correspondence with the Raman spectrum of 4-MBA (see Figure 12a, spectrum 3 from bottom to top) and allow the assumption of the 4-MBA molecule orientation with respect to the surface in accordance with the surface selection rules. Firstly, there is a significant increase in ν_{12} (a_1) aromatic ring breathing mode (1077 cm^{-1}) and ν_{8a} (a_1) totally symmetric ν C–C (a_1) (1587 cm^{-1}) intensities. The band at 713 cm^{-1} responsible for out-of-plane vibration of the aromatic ring γ (CCC) as well as the band 848 cm^{-1}, which corresponds to β (COO^-), are practically vanished in 4-MBA SAM SERS spectra, which means that the orientation of the 4-MBA molecules is unlikely the flat one, since it is the high intensity of these lines that indicates such an orientation. Moreover, the band 1706 cm^{-1} which originates from C=O stretching vibrations of non-dissociated COOH groups is present in the spectra, which supports vertical orientation of molecules with respect to the interface.

The EF of the cone-like black silicon sputtered with approx. 50 nm gold layer is estimated to be around 10^8 (for 4-MBA SAM) according to formula (9), which gives significant cost reduction and improvement of already existing approaches, which are based on application of black silicon of other geometries and require 100-400 nm gold covering. However, because of the extremely low thickness of gold, there are obvious regions between the cones and sometimes on their side walls, which are not sputtered with gold. For this

reason, in what follows, the gold layer will be referred to as a pseudo-layer of gold.

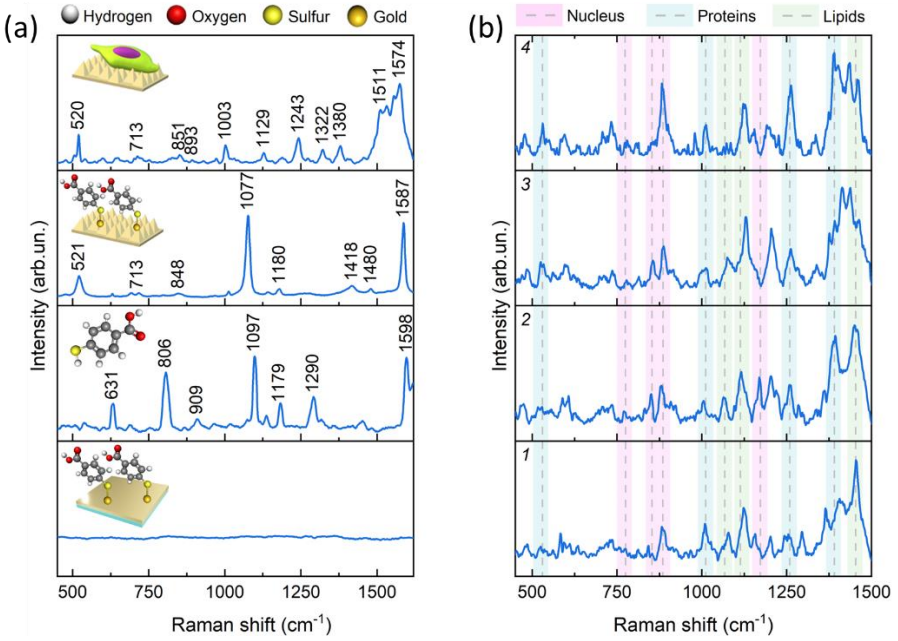

Figure 12. Application of cone-like black silicon sputtered with gold for 4-MBA SAM and C6 rat glioma cells detection: (a) from bottom to top, comparison of the Raman spectra (fingerprint region) of the 4-MBA SAM on the SiO_2/Au smooth substrate, of 4-MBA powder, SERS spectra of 4-MBA, and a living rat glioma cell on the cone-like black silicon surface with gold pseudo-layer; (b) SERS spectra of a living rat glioma cell on the cone-like black silicon surface with gold pseudo-layer, measured from one point in 1 min intervals (the numbers correspond to the sequence of measurements). Specific bands assigned to nucleic acids, proteins and lipids are marked with pink, blue and green zones, respectively. The excitation wavelength is 785 nm. Adapted from **Paper (B)**.

The nanoscale roughness of submicron regular silicon cone structures evenly distributed over the entire surface ensures high sensitivity for living cell detection. Biocompatibility of cone-like black silicon opens the possibility of obtaining spectra of living cells and visualize the characteristic bands of nucleic acids, proteins, and lipids in the “fingerprint” region of the SERS spectrum with low excitation intensities and short times of signal accumulation (see Figure 12a, upper spectrum). The latter also creates the potential of applying the cone-like black silicon for real-time monitoring of

cells, however, strong dependence of the SERS signal on the distance between the molecule of interest and plasmonic nanostructures, which is constantly changing over time because of cell mobility, imposes certain restrictions on the interpretation of the results.

Significant uniformity of the substrate which is reflected high hot spot density and low RSD of SERS signal (evaluated for 1076 cm^{-1} band in 4-MBA spectrum, see Figure 13), less than 13%, allows significant stability, reliability, and reproducibility of spectra of objects of interest (low concentrations of molecules, living cells, etc.). This was summarized in the **second statement** of the thesis: Cone-like black silicon fabricated by cryogenic reactive ion etching and sputtered with 50 nm gold pseudo-layer, exhibits an enhancement factor of 10^8, is uniform at a macroscale and is suitable for a living cell investigation.

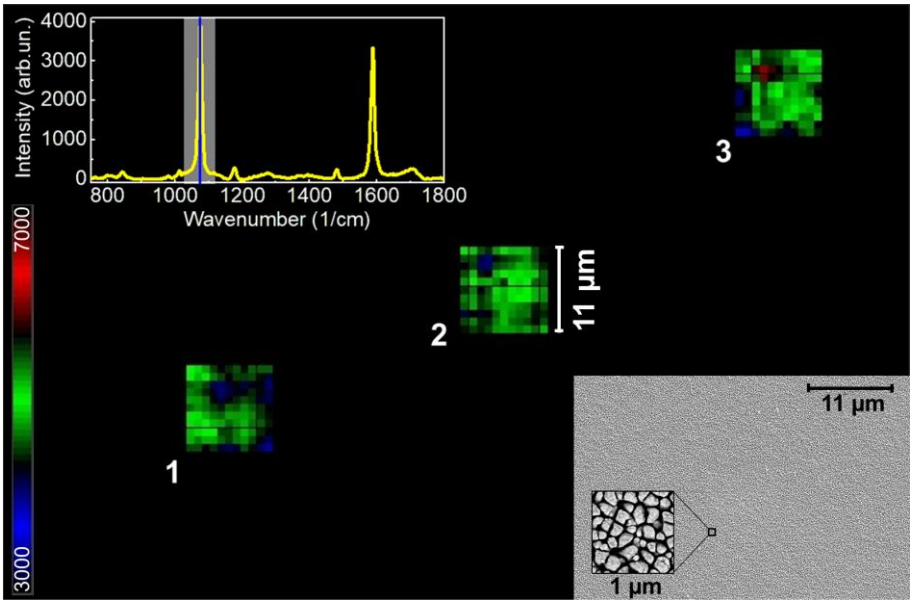

Figure 13. Uniformity of the cone-like black silicon with gold pseudo-layer represented as a 2D map of the background-corrected Raman intensity of the band 1077 cm^{-1}. The map resolution is 1 µm, the numbers 1, 2, 3 correspond to the separate 10×10 µm maps taken randomly from a 75×115 µm area. Insets: (top left) a SERS spectrum of 4-MBA monolayer from 1×1 µm pixel; (bottom right) top-down SEM image of the cone-like black silicon with a gold pseudo-layer with zoomed 1×1 µm area. Adapted from **Paper (B)**.

3.3 Computational electromagnetics: theoretical substantiation of the modification of black silicon-based substrates

3D FEM Simulation of the interaction of the plane wave with the gold nanostructures (see Figure 14), which imitate the gold plasmonic nanostructures combined in gold pseudo-layer on the micro-structured cone-like black silicon, allowed explanation and generalization of the obtained experimental results. Considering four types of nanostructures (the core–shell Si@Au for imitation of black silicon cone apex covered with gold layer, and various overlapped, non-overlapped and dumbbell-like spheres for side nanostructures) allowed the identification of the influence of nanoparticle orientation (distribution along the cone), silicon core, gold layer thickness, interparticle gold bridges or free space on the optical response, which defines the EF of the fabricated substrates. All the geometrical parameters were extracted from SEM micrographs and varied in a certain range: (i) the radius of the Si core was 36-44 nm, thickness of the gold shell 13-21 nm, (ii) bi-spheres of r = 25 nm and distances between the centers from 35 nm (overlapped) to 60 nm (non-overlapped), (iii) dumbbell structures with r = 25 nm spheres and distances between the centers of 50-60 nm.

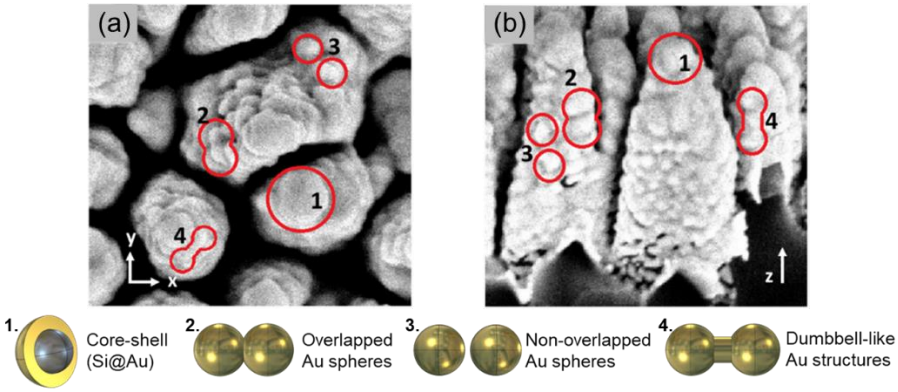

Figure 14. Structure selection for FEM simulations of optical response: (a) Top-view SEM image and (b) side-view SEM image of cone-like black silicon sputtered with gold (50 nm) with marked horizontally and vertically oriented bi-spheres and dumbbell-like particles formed in gold pseudo-layer. Schematical illustration of the selected types of particles is summarized below the SEM micrographs. SEM image size is 500×500 μm. Adapted from **Paper (B)**.

It was demonstrated that isolated gold spherical nanoparticles with the distance between the centers > 50 nm exhibit one observable maximum in the absorption cross section, which floats around 510-515 nm, and its position does not depend on the mutual orientation of particles and the direction of the incident wave propagation. I.e., at these interparticle distances, gold nanoparticles behave as individual ones and are characterized by one plasmon resonance in the visible range (Figure 15c, yellow, black, and gray spectra, and Figure 15f).

For thin gold layers (13-21 nm) the presence of silicon core significantly changes the optical response of the spherical nanoparticle. There are two absorption maxima, one of which is around 500-510 nm repeating the case of individual nanoparticle, and the second one is in NIR range and around one order of magnitude more intense than the first one. The growth of the silicon core leads to the increase of the σ_{abs} in NIR. The thinning of the gold layer provokes the red shifting of this maximum, although it leads to a slight decrease in the intensity (see Figure 15a and 15b).

For overlapped bi-spheres, as well as for 'bridged' bi-spheres (dumbbell-like particles), the mutual orientation of particles and the direction of the incident wave propagation and its polarization governs the optical response. In case of the co-incidence of the wave polarization and the major axis of the complex nanoparticle, two distinct plasmon resonances are observed: transverse (visible range) and longitudinal (NIR) peaks, the latter being the highest one (see Figure 15c and 15d). Changes in the interparticle distances or the length of the 'bridge' between the spheres allow tuning the intensity and the position of the NIR, which is important for biomedical applications, because NIR prevents light-induced tissue or cell damage, which often occurs in case of visible light application. If the major axis of the elongated nanoparticle is normal to the polarization of the incident wave, only transverse resonance (visible range) maximum in the absorption cross-section is observed.

Numerical calculation of the $|E_{loc}/E_0|$ ratios on the interface of the core-shell Si@Au nanoparticle (44 nm@21 nm), gold bi-sphere (r = 25 nm, distance 47.5 nm) and gold dumbbell-like structure (r_0 = 13.5 nm) at the excitation of λ_{ex} = 785 nm gives 21.6, 72.0 and 18.7, respectively, meaning that the EF ($\sim |E_{loc}/E_0|^4$) is estimated to reach the value of EF $\approx 2.4 \times 10^7$ (see insets in Figure 15a, 15c and 15d). The performed numerical simulations confirm the strong enhancement of the local field surface of the black silicon covered with gold pseudo-layer and demonstrate that E-filed enhancement occurs mostly due to the EM mechanism.

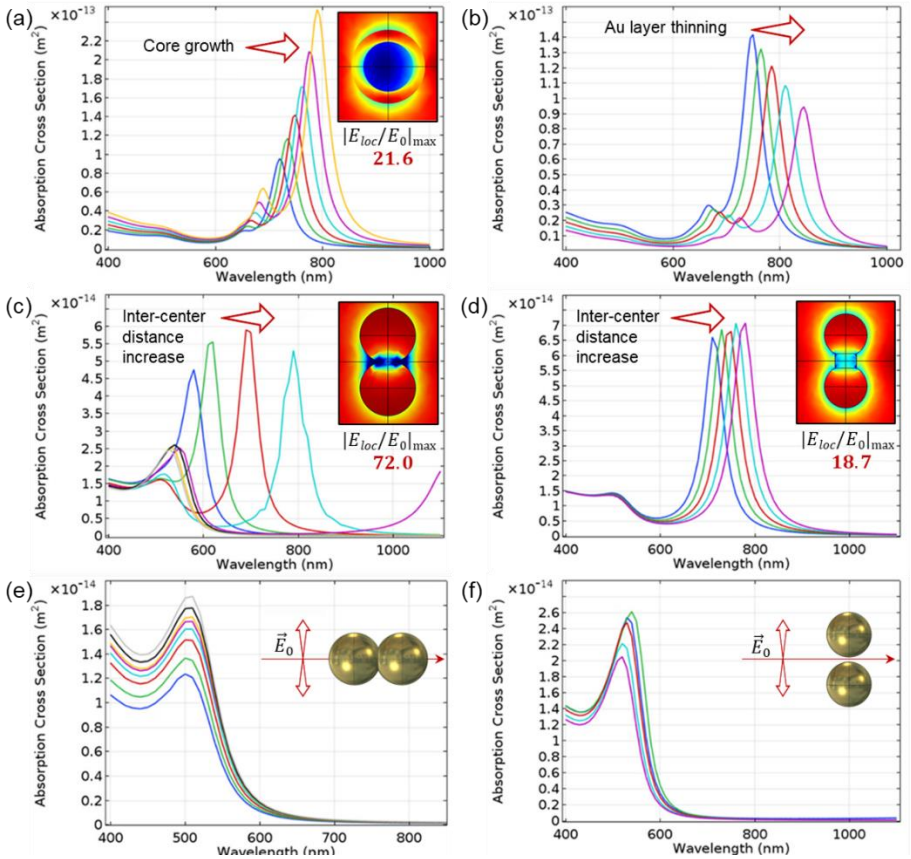

Figure 15. Absorption cross sections as a function of wavelength simulated for (a) a Si@Au spherical nanoparticle with Si-core radius changing from 34 to 44 nm and Au-shell thickness of 21 nm, (b) a Si@Au spherical nanoparticle with a constant Si-core radius of 38 nm and changing Au-shell thickness from 13 to 21 nm, (c) the Au bi-spheres (r = 25 nm) having distances between the sphere centers from 35 (overlapped spheres) to 55 nm (nonoverlapped spheres) with E_0 in the same plane with a large axis of nanoparticles, (d) Au dumbbell-like nanoparticle (r = 25 nm) with different distances between the sphere centers (from 50 nm to 60 nm, non-overlapped spheres) with E_0 in the same plane with large axis of nanoparticles, (e) the Au bi-spheres (r = 25 nm) having distances between the sphere centers from 35 (overlapped spheres) to 55 nm (nonoverlapped spheres) with large axis normal to E_0, (f) Au bi-spheres with different distances between the sphere centers (from 50 nm to 60 nm, non-overlapped spheres) with large axis normal to E_0. False color map insets: E_{loc}/E_0 spatial distribution over Si@Au, overlapped bi-spheres and dumbbell nanostructures, when NIR maxima assigned to SPPR longitudinal peaks appear. Adapted from **Paper (B)**.

Thus, the presence of a silicon core, spatial distribution of gold plasmonic nanoparticles, and their distinct orientation with respect to the polarization of the incident wave play the defining role in the tuning of the intensity and NIR position of plasmon resonance. These results predicted the possibility to modify the route of black silicon fabrication through its simplification (shifting from cryogenic to RT ICP-RIE) and cheapening (significantly reducing the gold consumption down to tens of nanometers). As a result, two more generations of black silicon-based substrates were fabricated: lace-like black silicon with 30%-reduced gold pseudo-layer (Figure 16b and 16g) as compared to initial cone-like black silicon (Figure 16a and 16f) and pillar-like black silicon with gold pseudo-layer of 13-25 nm (Figure 16c-e and 16h-j). Morphological features of all types of black silicon, focal points of fabrication and gold pseudo-layer characteristics are summarized in Table 2.

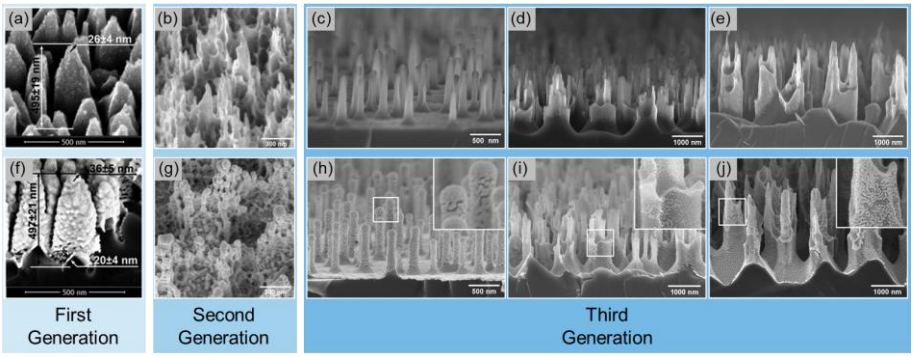

Figure 16. Three generations of black silicon substrates without gold (a-e) and sputtered with gold pseudo-layer (f-j): (a) and (b) – cone-like black silicon, (b) and (g) – lace-like black silicon, (c-e) and (h-j) – pillar-like black silicon substrates. Adapted from **Papers (B), (C), and (D)**.

The comparison of the SERS efficiency of all the generations of black-silicon-based substrates is performed using 4-MBA SAM. Corresponding SERS spectra of 4-MBA SAM on cone-like black silicon, lace-like black silicon, and pillar-like black silicon substrates with gold pseudo-layers of various thickness are presented in Figure 17. All the substrates provide good Raman signal enhancement, the obtained spectra of 4-MBA SAM on black silicon substrates covered with gold pseudo-layers are coherent with the Raman spectrum of 4-MBA powder (see Figure 17a, spectrum 1 from bottom).

Table 2. Summary of black silicon geometrical and gold pseudo-layer parameters for all types of fabricated structures

Black silicon type	**Method of fabrication, time, Au layer thickness** (as estimated for flat surface)	**Height (nm)**	**Apex thickness (nm)**	**Base thickness (nm)**	**Vertical structure density (pcs/μm²)**	**Thickness of Au layer (nm)**
Cone-like	Cryo ICP-RIE, 50 nm, **hydrophilic**	**497** ± 21	**36** ± 5*	**221** ± 24	**45** ± 7	**30-50**
Lace-like	RT ICP-RIE, 10 min, 50-60 nm, hydrophobic	**1000** ± 413	n/a[&]	**150** ± 52	n/a[&&]	(i) **10.8** (ii) **34.6** (iii) **109.7**[#]
Pillar-like	RT ICP-RIE, 18 min, 25 nm, hydrophobic	**639** ± 126	**112** ± 21	**110** ± 32	**4.33**[$]	**25**±5
	RT ICP-RIE, 25 min, 25 nm, hydrophobic	**1625** ± 298	**125** ± 36	**638** ± 155	**1.12**[$]	**14**±5
	RT ICP-RIE, 30 min, 25 nm, hydrophobic	**2217** ± 433	**144** ± 63	**832** ± 377	**0.56**[$]	**13**±4

Footnotes: * – apex curvature radius; [&] – difficult to estimate due to significant structure sharpness; [&&] – difficult to estimate due to huge effective surface area; [#] – average diameters of gold hemispheres formed on lace-like surface; [$] – SD is not mentioned because of low value of density. Data are presented as mean ± SD. Adapted from **Papers (B), (C), and (D)**.

The effect of gold consumption reduction by 30% applied to the cone-like black silicon structures led to the drop of the intensity of the 1076 cm^{-1} band by 4.6 times (see Figure 17, spectra 2 and 3 from bottom to top). According to the simulation results, a decrease in the thickness of the gold layer leads to a decrease in the EF, but the presence of a silicon core can compensate for this. Lace-like black silicon, fabricated by RT ICP-RIE, has more developed surface area than that of cone-like black silicon (see Figure 16b), although less controlled, with many vertically oriented silicon blade-like

structures, which enable a larger number of hot spots even in case of 30%-reduced gold sputtered on black silicon (Figure 16g). As a result, the effective surface area of lace-like black silicon, calculated from SEM micrographs, is 20 times higher than that of cone-like black silicon, and provides 3 times more intensive signal than cone-like black silicon with the reduced gold pseudo-layer of the same thickness (see Figure 17a, spectra 3 and 4 from bottom to top). The EF estimated according to the formula (6) for the band 1076 cm^{-1} gives the magnitude of 1.1×10^6.

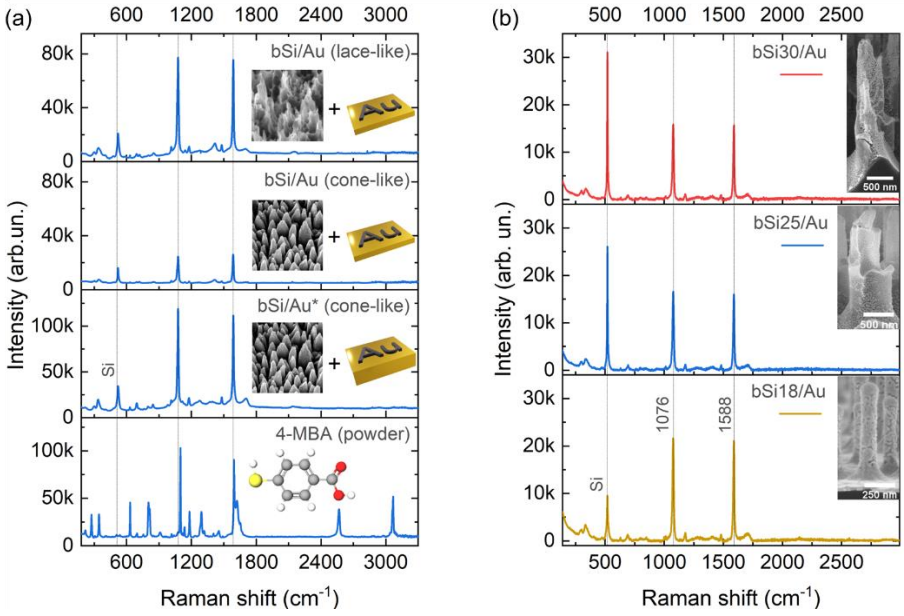

Figure 17. Comparison of Raman spectrum of 4-MBA powder and SERS spectra of 4-MBA SAM obtained by using all generations of black silicon substrates with gold pseudo-layer thickness varied from 30-50 nm to 13-20 nm: (a) cone-like and lace-like types of black silicon (Raman spectrum of 4-MBA powder, bSi/Au* (cone-like), bSi/Au (cone-like), and bSi/Au (lace-like) from bottom to top, respectively; (b) pillar-like black silicon (etching times 18 min, 25 min and 30 min from bottom to top, respectively). '*' mark indicates 30% thicker gold layer sputtered on the surface of bSi than in other cases (bSi/Au (cone-like) and bSi/Au (lace-like)). Adapted from **Paper (C)** and **Paper (D)**.

In contrast to cone-like black silicon with gold pseudo-layer, the molecules of 4-MBA more likely have a flat orientation on the surface of lace-like black silicon sputtered with gold. There are the bands 849 and 1417 cm^{-1},

which correspond to bending β(COO^-) and stretching ν(COO^-) vibrations and indicate the presence of deprotonated carboxylic groups [171]. In dried samples, both β(COO^-) and ν(COO^-) testify to the presence of direct interaction of COO^- groups with the metal surface, forcing the flat orientation of the aromatic ring of 4-MBA molecules [172]. The appearance of γ(CCC) out-of-plane ring vibrations at 718 cm^{-1} [171] and a weak aromatic ν(CH) stretching band at 3074 cm^{-1} in SERS spectra of 4-MBA also supports the presence of flat-oriented aromatic rings due to surface selection rules.

The pillar-like black silicon substrates are obtained through increasing the etching time during RT ICP-RIE fabrication. Stepwise increase of the etching time leads to the enlargement of the vertically oriented structures but reduces the number of smaller structures in the space between the main large structures (pillars). As a result, the density of pillars decreases, reducing the number of sites for hot spot formation (see Figure 17b and Table 2). Gold pseudo-layer of 13-25 nm thickness with numerous cracks in the defected gold layer on the sides of huge pillars restricts the estimation of EF as the area occupied by 4-MBA molecules becomes imprecise: not all the free surface is covered with gold and, as a result, only part of the effective surface is covered with molecules and serves for SERS. Nevertheless, all three types of substrates are uniform with RSD, determined for 1588 cm^{-1} band intensity, of 6.1%, 5.2% and 4.3% for pillar-like black silicon fabricated by 18 min, 25 min and 30 min etching during ICP-RIE, respectively.

Focusing on achieving key performance indicators, which were formulated in the goals of the thesis and included fast simple and low-cost fabrication of black silicon-based substrate, high EF (measurable), high density of hot spots, low gold consumption, uniformity, repeatability, the most suitable type of the fabricated black silicon substrates is lace-like black silicon. Although it is not biocompatible, it is the most promising for mass large-scale production and use for analytical applications. Nevertheless, the tasks which require biocompatibility, can be covered by using more expensive and complicated in fabrication cone-like black silicon.

Lace-like black silicon covered with gold pseudo-layer is highly uniform. RSD determined for 1076 and 1588 cm^{-1} bands is around 6 % over 100×100 μm area with 1 μm resolution and the medians of these bands intensities almost completely coincide in magnitude with the mean values. Therefore, in uniformity and hot spot density, lace-like black silicon-based SERS substrate surpasses the cone-like black silicon-based substrate (see Figure 18). It is worth noting that the spectra of impurities are also detected (grey spectra in Figure 18). Impurities on large areas of the substrate are, unfortunately, unavoidable, and originate from preparatory manipulations

and/or precipitate from the environment during the measurement itself. However, the percentage of impurity spectra is 4% (434 out of 10201 spectra) and can be easily excluded from the dataset, significantly increasing the accuracy of analysis by leaving only the spectra of probe molecules.

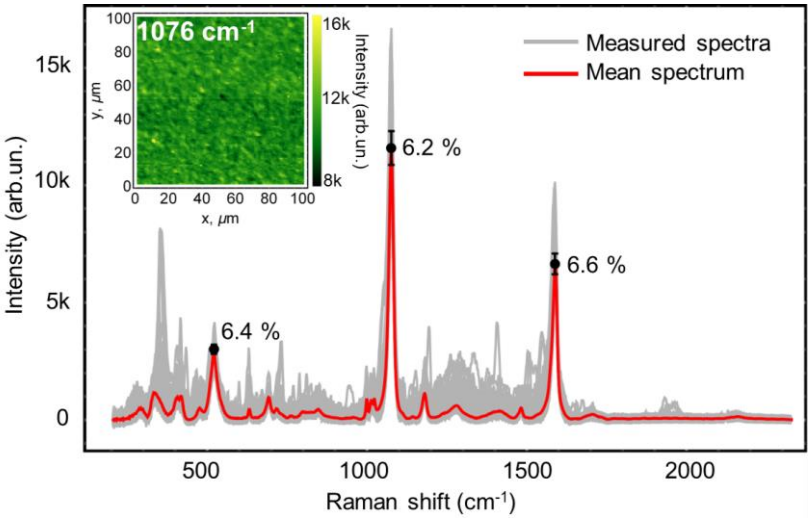

Figure 18. Uniformity of lace-like black silicon with gold pseudo-layer, demonstrated using SERS spectra of 4-MBA molecules. Inset: two-dimensional (2D) distribution of the peak intensity at 1076 cm^{-1} of SERS spectra of the 4-MBA monolayer deposited on top of the bSi/Au substrate. Measurement parameters: λ_{ex} = 785 nm, exposure time is 1s, laser power is 0.05 mW, scanning step is 1 μm, 50× objective. Adapted from **Paper (D)**.

One of the concerns around SPR-based systems, obviously including all types of materials for SERS, is the photoinduced thermal effect (PTE). Overheating of plasmonic nanostructures reduces EF and may lead to the damage of the molecules of analyte and their degradation [173], [174], [175]. Evaluation of PTE for lace-like black silicon-based substrate was performed in a wide range of laser powers (from 3.8 to 90.9 mW) and excitation times (from 1 to 60 s) for 4-MBA SAM in the range of 990−1030 cm^{-1} (Figure 19). The PTE in the case of 4-MBA molecules manifests itself in the appearance of monosubstituted benzene derivatives, which indicate that the 4-MBA molecules are decarboxylated. This, in turn, is reflected in the presence of the bands at 996 and 1021 cm^{-1}, which out-of-plane and in-plane ring deformations of monosubstituted benzene derivatives, respectively (see Figure 19b and 19c) [176]. Based on the results, the upper limit for the total

energy delivered to the analyte, avoiding the PTE, was estimated to be close to 1.0 J.

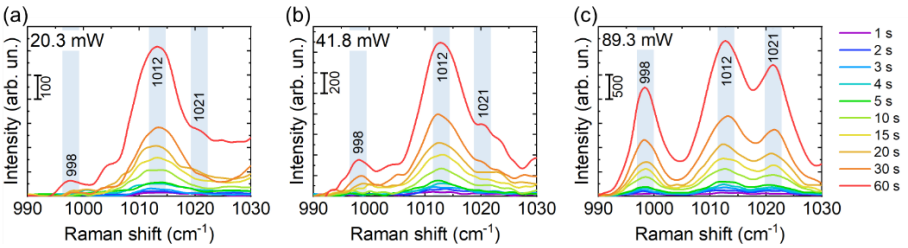

Figure 19. Photothermal effect of lace-like black silicon sputtered with gold on 4-MBA molecules, reflected in SERS spectra of 4-MBA in the range 990-1030 cm^{-1}, caused by laser excitation at the power of: (a) 20.3 mW; (b) 41.8 mW; (c) 89.3 mW. The time of sample exposure to laser irradiation varies from 1 to 60 s. Adapted from **Paper (D)**.

Moreover, the fact that the role of silicon as the core for gold plasmonic nanostructures is among the majors for supporting the NIR plasmonic resonance and SERS efficiency, thus, EF is not strictly limited by the gold layer deposition. The efficiency of Raman signal enhancement by lace-like black silicon with gold pseudo-layer, which was determined for the intensities of two characteristic bands 1076 and 1588 cm^{-1} of 4-MBA molecules, over 20 months of storage. These intensities decreased by less than 5% after 120 days and by 40% after the whole storage period.

Raman signal enhancement occurs from molecules in the proximity of the surface of the substrate. Thus, most SERS substrates are disposable ones without any options of being reused, because the elimination of covalently bonded or electrostatically absorbed molecules is complicated. The cleaning of the effective surface can lead to the modification of the metal surface and/or destruction of hot spots. Mild oxygen plasma cleaning at room temperature (widely accessible in laboratories) was applied to refresh the surface of lace-like black silicon with a gold pseudo-layer. Elimination of residues from the effective surface of the substrate occurred after 35 min of oxygen plasma treatment. Thereafter, the substrate, rinsed in deionized water and dried, can be further reused up to 10 times (see Figure 20a).

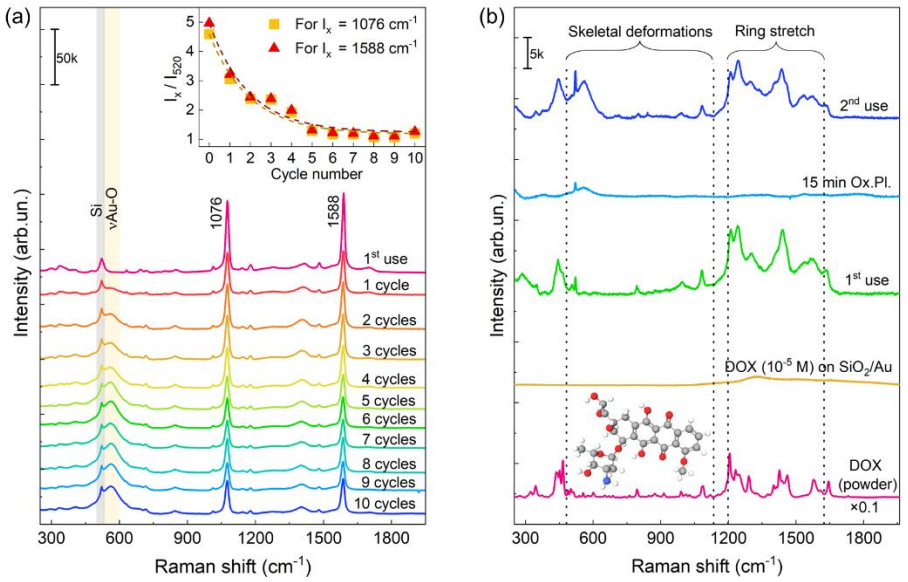

Figure 20. Re-using of lace-like black silicon with gold pseudo-layer: (a) SERS spectra of covalently bonded molecules of 4-MBA on the bSi/Au substrate over 10 reusability cycles; (b) from bottom to top: Raman spectrum of DOX (powder), spectrum of 10^{-5} M of DOX deposited on SiO_2/Au, SERS spectrum of 10^{-5} M of DOX on bSi/Au substrate before oxygen plasma cleaning, spectra of bSi/Au substrate after 15 min of oxygen plasma treatment, and SERS spectrum of 10^{-5} M DOX on the reused bSi/Au substrate. Inset in (a): dependence of the 1076 and 1588 to 521 cm^{-1} intensity ratios on the number of cycles of reuse. Adapted from **Paper (D)**.

The recycling induces gold layer oxidation (manifested in the growth of 560 cm^{-1} band, which is assigned to ν(Au-O) [177]). In [178] it was demonstrated that treatment of gold nanoparticles with O_2 flow under conditions of 160 W output power and 600 mTorr in-chamber pressure resulted in the formation of 0.8 nm layer of AuO_x after 30 minutes of exposure with the saturation of the layer thickness up to 1.2 nm after 50 minutes of exposure. In our plasma-cleaning experiments the experimental parameters were set as follows: output power 12.5 W (output current 48 mA, output voltage 260 V), in-chamber pressure 0.1 mbar (or 75 mTorr) for air flow, meaning that the partial pressure of O_2 was around 15.8 mTorr. As the output power was 12.8 times lower and in-chamber pressure was 38 times lower than in [178], one can expect that the formation of AuO_x layer of ultimate thickness of 1.2 nm will be reached after several cycles of plasma cleaning, as one cycle takes 35 minutes, although additional structural studies of the AuO_x layer were

not performed in terms of the Thesis and assumptions are made on the basis of the available scientific data from other research groups. Even though the oxidation reduces the number of sites for molecule binding it will not modify the plasmonic properties of gold nanostructures drastically. Moreover, such 'mild' plasma does not reduce the gold layer itself, thus this will not significantly affect the Raman signal from the supporting silicon layer. For this reason, silicon band was chosen further for normalizing the intensities of SERS signal arising from adsorbed molecules of 4-MBA. It is not affected by oxygen plasma cleaning and its usage as a reference allows excluding possible laser intensity fluctuations in different experiments.

The relative SERS intensity of the characteristic bands 1076 and 1588 cm^{-1} with respect to the intensity of the silicon characteristic band 520 cm^{-1} decreases less than by 5 times in the fifth cycle of use and does not change over subsequent uses, which could be probably associated with the saturation in the AuO_x layer thickness. Besides the intensity decrease, the EF is acceptable for analyte molecule detection. Sensitivity of the reused substrates can also be improved by collecting spectra over large areas with further integration of the signal, which becomes possible due to high density and uniformity of hot spots [179].

The concept of reusability of lace-like black silicon with gold pseudo-layer has been confirmed for molecules which are not covalently bonded to gold surface, such as molecules of doxorubicin (DOX). Firstly, lace-like black silicon is suitable for SERS-based detection of low concentration of DOX solutions. The SERS spectrum of 10 nM of DOX is presented in Figure 20b (spectrum 3 from bottom) and it is in good agreement with Raman spectrum of DOX powder (Figure 20b, spectrum 1 from bottom). Oxygen plasma treatment of the substrate with adsorbed DOX molecules for 15 min completely regenerates the substrate. Reuse of the substrate for the same 10 nM DOX detection gives SERS spectrum of DOX with almost the same line intensity. However, some gold oxidation occurs and should be considered when reusing the substrate.

Summing up all the above, the **third statement** of the thesis was claimed: Silicon core of the black silicon/gold structures and 3D spatial organization of gold nanostructures endows the black silicon-based SERS substrate with a pronounced optical resonance in the spectral range 700-800 nm, which can be further red shifted by the thinning of gold pseudo-layer down to about ten nanometers. These results ensure a simple and low-cost fabrication of effective and reusable diversiform black silicon/gold structures for SERS.

3.4 Carbon-based theranostics and related nanoparticle biodegradation problem

Specific and sensitive analytical methods, such as SERS-based ones, become a powerful and irreplaceable tool in solving many existing problems, e.g., in nanobiotechnological research. One of the constantly emerging and still unsolved problems in the use of nanomaterials for therapy and diagnostics is the analysis of structural changes of nanomaterials when they are accumulated inside the target (usually cells or tissues) and mechanisms of their elimination from the human body. Within this scope of the thesis development of theranostics of cancer with carbo-based nanomaterials (specifically SWCNTs) was developed and lace-like black silicon with gold pseudo-layer was applied to reveal the mechanism of biodegradation of carbon-based nanomaterials by neutrophils by means of SERS.

Rat glioma cells are among the most common cellular models in neuro-oncology and are often used to simulate glioblastomas in vitro. Interaction of these cells with SWCNTs non-covalently functionalized by DNA molecules induces rapid accumulation of SWCNTs inside the cell cytoplasm, which is accompanied by F-actin reorganization (sign of endocytosis), quick mitochondria hyperpolarization and ROS production due to energy consumption during the first stages of endocytosis. However, the mitochondrial function restores when the concentration of SWCNTs reaches saturation and SWCNTs form micron-sized agglomerates inside the glioma cell [180]. When accumulated inside the cell, SWCNTs are chemically inert and do not affect the cell functioning, which makes these carbon nanomaterials perfect candidates for visualization of the tumor using Raman spectroscopy. Based on the theoretical predictions of the light-induced generation of acoustic wave by highly absorbing micro-particles, which is enough to damage the plasma membrane of the living cell [27], experimental investigation of the interaction of laser radiation (continuous and pulsed modes) with SWCNTs inside and outside the cells was performed. The experimental part was further verified though loading the theoretical model with the experimental parameters.

The distribution of the SWCNTs inside the cancer cells, which were exposed to SWCNTs for 24 h, and their agglomeration rate is visualized by means of laser-scanning Raman microscopy with excitation in NIR (λ_{ex} = 785 nm, continuous mode) employing the integral intensity of G-band (1590 cm^{-1}) of the SWCNT Raman spectrum for 2D mapping (see Figure 21a and 21c, spectrum 2 for a typical spectrum of SWCNTs). SWCNTs form micron-sized agglomerates in the cell cytoplasm and do not penetrate the

nucleus (Figure 21a). The exposure of the cell with SWCNT agglomerates to laser irradiation in continuous mode (λ_{ex} = 785 nm, 2.4 × 10^6 W/cm^2, laser spot diameter 2 μm) for 30 min did not lead to any significant change neither in a living cell (preserved cell morphology, intact cell membrane) nor in the SWCNT spectrum (Figure 21b and 21c, spectrum 2), meaning that no significant local heating of SWCNTs caused by the conversion of absorbed laser radiation into heat occurred.

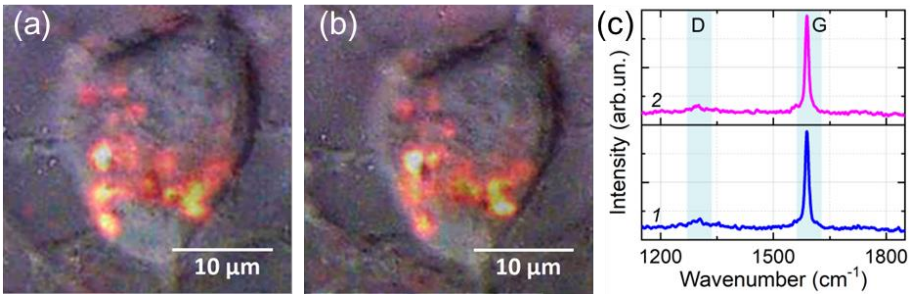

Figure 21. Intracellular accumulation of SWCNT-DNA complexes inside living cells and structural integrity of C6 rat glioma cells exposed to continuous laser irradiation with λ_{ex} = 785 nm (demonstrated by laser-scanning Raman microscopy): (a) image of C6 cells in reflected light superimposed on the map of the Raman G-mode of SWCNTs before irradiation; (b) image of C6 cells in reflected light superimposed on the map of the Raman G-mode of SWCNTs after laser irradiation for 30 min at the intensity of 2.4 × 10^6 W/cm^2; (c) Raman spectra of SWCNT-DNA complexes before (*1*) and after (*2*) laser irradiation for 30 min at the intensity of 2.4 × 10^6 W/cm^2, respectively. Adapted from **Paper (E)**.

The switching of the laser radiation to the pulsed mode significantly changed the result. Interaction of pulsed NIR laser radiation with living cells was tested for three experimental designs: (i) bare glioma cells as a control, as ultra-short laser pulses of high intensity can cause cell damage (protein coagulation, vaporization, photoablation) [181], [182] (Figure 22a); (ii) glioma cells after 24h exposure to SWCNTs, accumulated micron-sized agglomerates inside the cytoplasm (Figure 22b); (iii) bare glioma cells growing in the culture medium with suspended individual SWCNTs (Figure 22c).

To evaluate the biological effect of the ultra-fast NIR laser pulses or light induced effect of SWCNTs on glioma cells, all three cellular systems were exposed to picosecond laser irradiation (λ_{ex} = 910.5/1064 nm, 10 ps),

which was simultaneously used for fast cancer cell visualization by coherent anti-Stokes Raman spectroscopic (CARS) imaging technique (Figure 22, column 'Irradiation') performed at 1585 cm^{-1} wavenumber (C=C bending mode in proteins [183]) and as a source of stimulating picosecond NIR laser pulses of intensity 10^6 W/cm^2, influencing the cellular system for 7 min. Cell viability was determined before (Figure 22, column 'Before irradiation') and after picosecond pulsed irradiation using fluorescent probe propidium iodide (PI) (Figure 22, column 'After irradiation'). Irradiation of bare cells as well as bare cells in the medium containing suspended individual SWCNTs were not affected by the NIR picosecond laser pulsed irradiation as no plasma permeabilization occurred and no PI fluorescence was detected (Figure 22a and 13c). In contrast, interaction of ultra-fast picosecond pulses with micron-sized agglomerates inside the cytoplasm of glioma cell caused photo-induced destruction of cancer cells, which follows from the pronounced damage to the plasma membrane and fluorescence of PI inside the affected cells (Figure 22b).

Loading the theoretical model with experimental parameters (calculations were carried out by our colleagues from another research group and are presented in the Thesis to support the obtained experimental results) allowed distinguishing photothermal, photothermoacoustic, and photoacoustic regimes of the interaction of light pulses with SWCNT agglomerates embedded in cytoplasm depending on the input parameters (laser pulse power and duration). The experimental design implemented in this research ensures the 'cold' photoacoustic destruction of glioma cells, which means that interaction of 10 ps laser pulses with micron-sized agglomerates induces the generation of a photoacoustic wave ($|\Delta P| > 0.7$ MPa), or tensile stress in SWCNT agglomerate, which is enough for cell membrane breakage, without generation of excessive heat ($\Delta T << 20$ K). Thus, employing SWCNTs for light-guided cancer therapy, firstly, surpasses, side effects associated with the tissue overheating and, secondly, prevents non-specific cell damage, because SWCNT-based therapy is determined mainly by the agglomerates which are formed inside the target cell, while individual SWCNTs being present in the extracellular adjacent fluids and tissues are photoacoustically inactive.

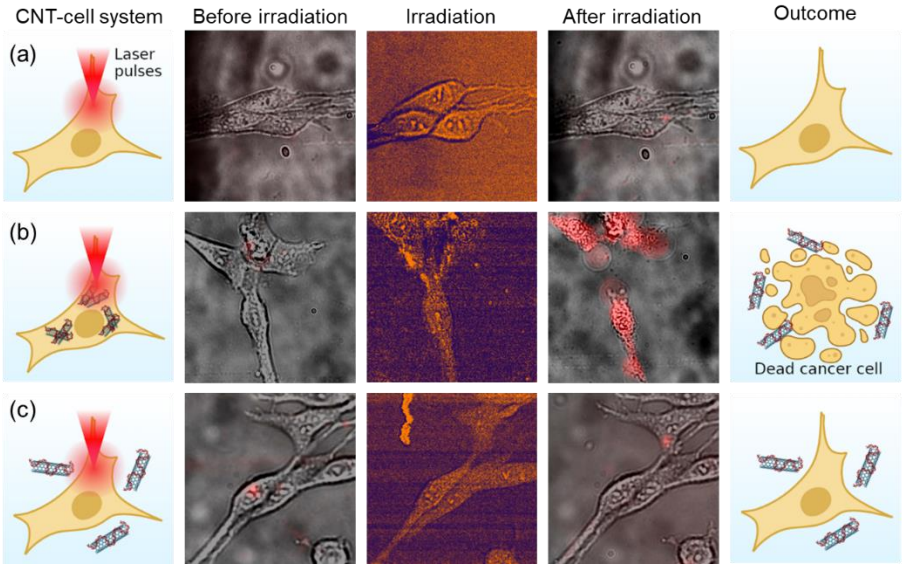

Figure 22. Photo-induced SWCNT-mediated destruction of glioma cells by NIR pico-second pulsed irradiation: (a) Bare C6 glioma cells; (b) C6 glioma cells with accumulated micron-sized SWCNT agglomerates, (c) C6 glioma cells in the presence of the SWCNTs suspension in the extracellular medium. Each line of images, moving from left to right, represents (moving from left to right) scheme of SWCNT-cell interaction; bright-field images superimposed with PI fluorescence images before irradiation; CARS images obtained during irradiation; bright-field images superimposed with PI fluorescence images after irradiation with 10 ps laser pulses (910.5/1064 nm, 10^6 W/cm^2) for 7 min; schematic illustration of outcome (cells are viable or dead). Adapted from **Paper (E)**. Schematic illustrations are created with BioRender.com.

Despite all the advantages of the developed approach, it has the same drawback as other nanoparticle-based ones, namely the problem of biodegradation of the used nanomaterials. According to the principal scheme of the photoacoustic destruction of cancer cells (Figure 23), photoacoustically induced cancer cell destruction results in cancer cell residues and carbo-based nanomaterials which initiate the immune system response. To evaluate the mechanism of the immune system cells interaction with carbon-based nanomaterials released from the damaged cells, human neutrophils, isolated from the whole blood, were used as a cellular model, and green fluorescent graphene quantum dots (GQDs) were chosen as a carbon-based nanoparticle model, because GQDs exhibit fluorescence coupled with their structure and it allows imaging of the accumulation of NPs inside the cell. Structural changes

which occurred during the interaction of GQDs with neutrophils were analyzed using lace-like black silicon with gold pseudo-layer by means of SERS.

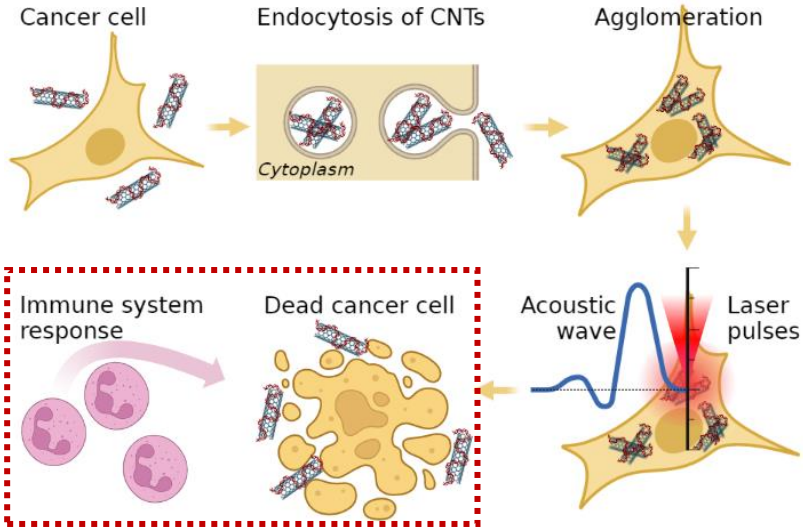

Figure 23. Photoacoustic destruction of cancer cells with carbon-based nanomaterials. Created with BioRender.com.

Interaction of GQDs with neutrophils induces their activation, which is accompanied by myeloperoxidase redistribution inside the cell with its subsequent release to the external environment (see Figure 24a). This process is accompanied by the reorganization of the F-actin cytoskeleton (Figure 24b), which is reflected, firstly, in the vigorous spreading of cells on the surface and the appearance of wide lamellipodia, secondly, in the disruption of cellular membrane integrity and the disturbance of the shape-supporting frame in the area proximal to the membrane. Both these processes considered together may indicate the NETosis (neutrophil extracellular traps), induced by GQDs.

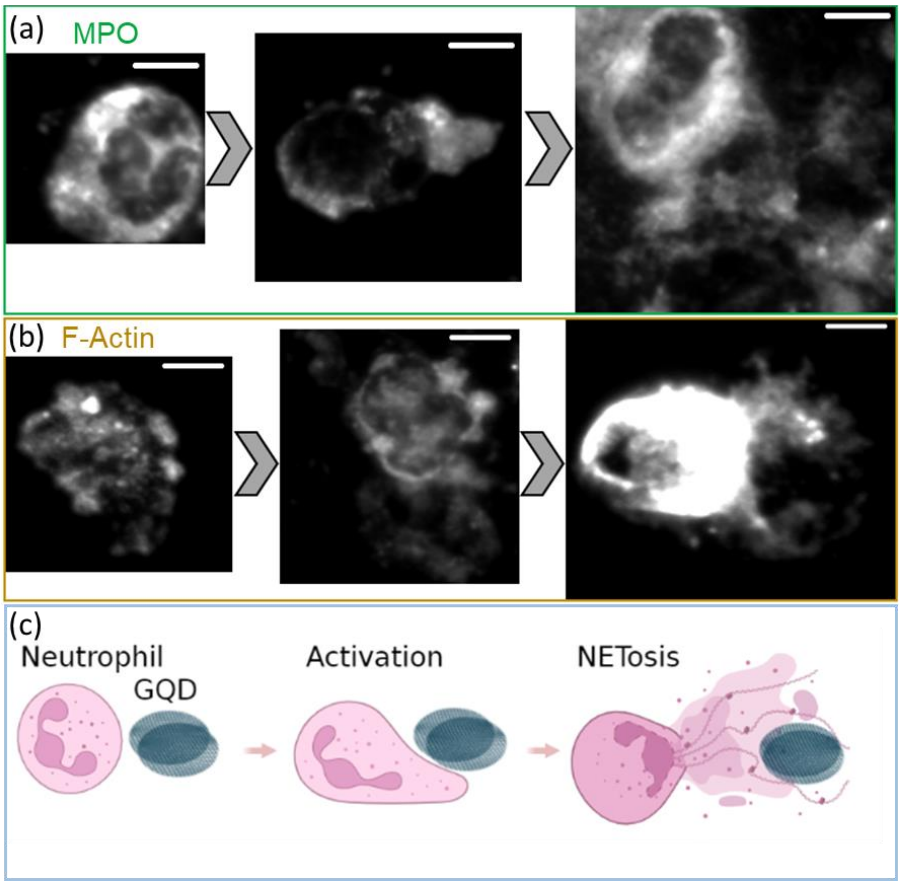

Figure 24. Activation of neutrophils exposed to 50 μg/mL of GQDs via adhesion over 30 min: (a) MPO redistribution in neutrophils over time; (b) F-Actin redistribution in neutrophils over time; (c) schematic description of GQD interaction with neutrophils (created with BioRender.com). MPO antibodies stained with FITC (ex/em: 470 nm/530 nm). F-Actin stained with CytoPainter Phalloidin-iFluor 532 (ex/em: 532 nm/620 nm). Scale bar 15 μm. Adapted from **Paper (F)**.

Fluorescence spectra detected from neutrophils, which were interacting with 50 μg/mL water solutions for 30 min and 90 min, indicate that GQDs are accumulated inside the cells, however, after 90 min of GQD-neutrophil interaction, significant decrease in the GQD fluorescence intensity and maximum position redshift are observed (Figure 25a). GQDs accumulation of GQDs from solution is also depicted by fluorescence microscopy. To exclude the impact of the autofluorescence of neutrophils, fluorescence images were collected both for bare neutrophils and neutrophils exposed to GQDs at the same experimental conditions (Figure 25b). As follows from Figure 25b, 30

min exposure of cells to GQDs leads to the formation of wide lamellipodia by some cells. The integrity of the membrane is disrupted for several neutrophils, and the content of the cell is released into outer space (Figure 24(b), right upper panel, marked with arrows). Longer exposure of cells to the same concentration of GQDs leads to the total violation of the cell membrane integrity and the release of the intracellular content into the external environment (Figure 25b, right lower panel). The way GQDs are distributed on the surface around the activated cells points to the morphological similarity of the activated neutrophils to cells that form neutrophil extracellular traps (NETs) (Figure 25b, right lower panel, marked with arrows).

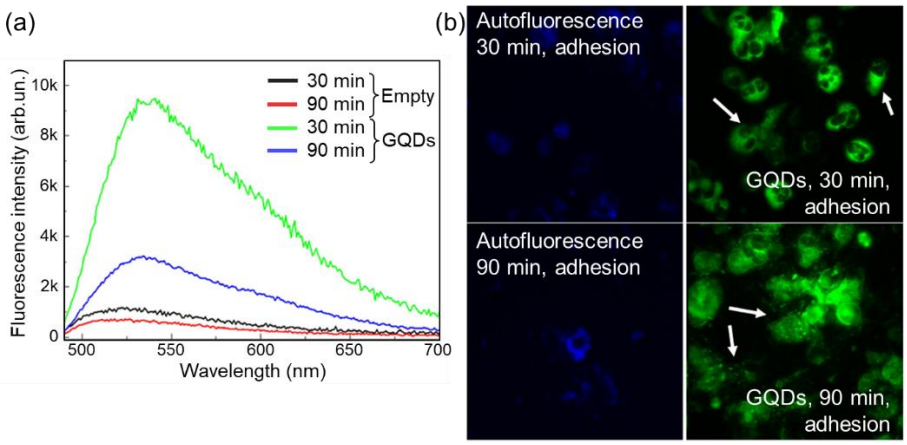

Figure 25. Effect of interaction of GQDs with neutrophils on fluorescence of GQDs: (a) (auto)fluorescence spectra of neutrophils in control samples (black and red lines, "Empty") and pretreated with GQDs (green and blue lines, "GQDs") for 30 and 90 min, respectively; (b) fluorescence images of neutrophils without (left column) and in presence of GQDs (right column) after 30 (the first row) and 90 min (the second row) of cell adhesion. Spectra are averages of spectra from 5 different points in the sample. Excitation was at 470 nm. Arrows indicate the disruption of the integrity of the cell membrane. Adapted from **Paper (F)**.

The MPO release can be associated with high local concentrations of strong oxidants: hydrogen peroxide (H_2O_2), which serves as a substrate for MPO, and hypochlorous acid (HClO), which is the main product of neutrophil activation.

To evaluate the origin of the GQD fluorescence changes, which occur during neutrophil activation, modification of the spectroscopic parameters of GQDs under the influence of key oxidants were analyzed in the model system.

Interaction of GQDs with 0.01–10.0 mM water solutions of NaClO (source of OCl^-) causes significant spectroscopic changes which are reflected in the modification of absorbance, excitation, and fluorescence properties (see Figure 26a and 26c, Table 3). Absorbance maxima redshift and practically vanish at 10 mM NaClO concentration (Figure 26a). Concentration-dependent fluorescence intensity decreases and redshifts (Figure 26c), repeating the fluorescence intensity behavior observed during GQD interaction with neutrophils (Figure 25a). Regarding hydrogen peroxide, spectroscopic properties of GQDs (absorbance, fluorescence spectra, characteristic lifetimes) are not affected by the H_2O_2 in a wide range of concentrations (0.01–10.0 mM) (see Figure 26b and 26d, Table 3).

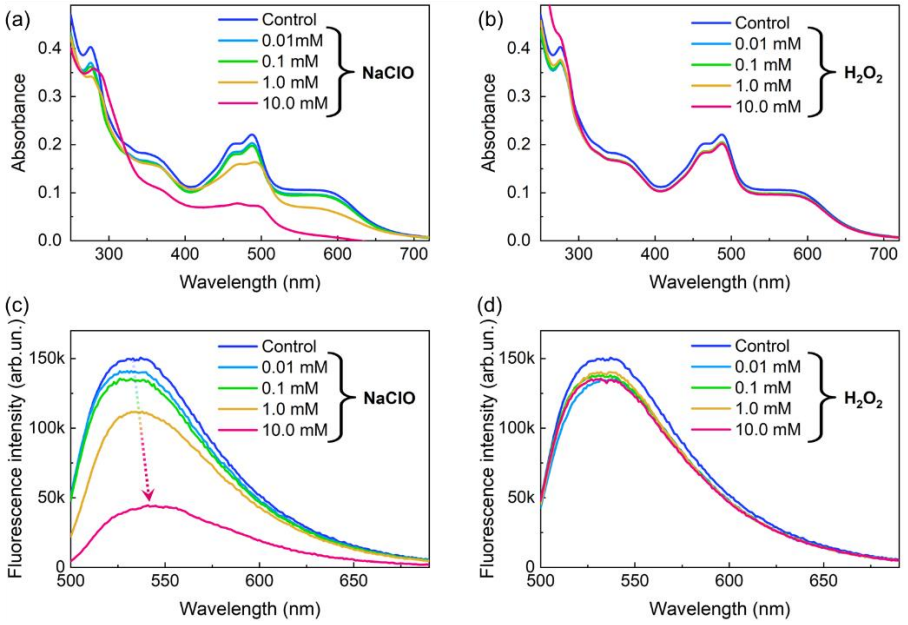

Figure 26. Effect of NaClO and H_2O_2 on the GQD absorbance and fluorescence spectra: (a) and (b) GQD absorbance spectra, (c) and (d) GQD fluorescence spectra when treated with NaClO and H_2O_2 respectively. GQD concentration in water was 50 μg/mL. Excitation wavelength was λ_{ex} = 470 nm. Adapted from **Paper (F)**.

Table 3. Fluorescence lifetime data for GQD under 0.01–10 mM NaClO and H_2O_2 treatment for 30 min. Adapted from **Paper (F)**.

		Control		**0.01 mM**		**0.1 mM**		**1.0 mM**		**10.0 mM**	
		τ, ns	B_i, %	τ, ns	B_i, %	τ, ns	B_i, %	τ, ns	B_i, %	τ, ns	B_i, %
NaClO	Fast	**2.7**	62.3	**2.7**	61.4	**2.7**	63.2	**2.4**	39.5	**1.7**	17.0
	Slow	**5.0**	37.7	**5.0**	38.6	**5.1**	36.8	**4.3**	60.5	**3.8**	83.0
H_2O_2	Fast	**2.7**	62.3	**3.7**	65.8	**3.7**	72.0	**3.7**	72.4	**3.7**	74.5
	Slow	**5.0**	37.7	**5.7**	34.2	**5.9**	28.0	**6.0**	27.6	**6.1**	25.5

Fluorescent GQDs employed in this study have a complex structure. Absorbance spectra of intact GQDs have absorption peaks at 276, 356, 460 and 488 nm. The first one corresponds to the π–π* transition of sp2 carbon atoms and originates from the quantum confinement effect [29]. The maximum at 356 nm originates from the n–π* transition and is mainly associated with the oxygen-containing functional groups (C=O/COOH) at the GQD edges [184], [185], [186]. The last two maxima at 460 and 488 nm are rarely observed in as-prepared GQDs. They are most often associated with various surface functional groups, which form surface states with energies between π and π* states of C=C [187], or they may originate from C–O groups [186].

The complexity of the structure was confirmed by using lace-like black silicon with gold pseudo-layer by means of SERS (Figure 27). Raman spectroscopy analysis of GQDs allowed getting low intensive and very broaden bands centered at 1358 cm^{-1} and 1589 cm^{-1} (Figure 27a, red spectrum and inset). SERS spectra, on the contrary, revealed multiple very intense bands, which correspond to the vibrations which were enhanced according to surface selection rules (Figure 27a, blue spectrum). It could be argued that these multiple bands in the 'fingerprint' region originate from some organic compounds and surfactants, which can be added to stabilize hydrophobic graphene sheets in water and, which is even more difficult, in salt solutions and buffers which are often used for biomedical research. However, the addition of surfactants, like sodium dodecyl sulfate which is widely used for the dispersion of the graphene sheets, may significantly affect the living cell itself. Another way to stabilize graphene sheets in the suspension is their postprocessing, which results in the formation of many defective cites, densely decorated with in-plane epoxy (C–O–C) functional groups, COOH/C–OH and C=O/C–O edge functional groups, etc. [188]. The way of fabrication and post-

processing of GQDs, which were investigated within the Thesis (green luminescent, water-dispersed, CAS 7440-44-0, Sigma-Aldrich, USA), was not disclosed by the supplier. No mentions of any surfactants added as stabilizers were present in the material description (product description and safety data sheet can be found in [189]), and the implementation form is dispersion. For this reason, GQDs are considered as GQDs only without additional organics present in the suspension.

The multiple bands, which are observed in Figure 27a (blue line) can be disclosed as follows. The range 580-1280 cm^{-1} corresponds to the vibrations originating from C–O–C [185], C–O [190], edge defects, COOH or ring type C–OH functional groups [184] and CH_2 deformation modes [191]. Appearance of the band around 1560 cm^{-1} may indicate the G band split due to symmetry break [190], [192].

Oxygen plasma treatment for 5 min of the black silicon surface with adsorbed GQDs reduced the most defective external layer of GQDs, which, as we suppose, could not be described as intact layer of graphene, and is likely composed of several heterocycles terminated with oxygen-containing functional groups. Therefore, oxygen plasma treatment allowed eliminating most oxygen-based defects, which is expressed in vanishing of bands in 580-1280 cm^{-1} range and exhibiting narrow D and G bands of GQDs at 1376 cm^{-1} and 1583 cm^{-1}, respectively. Nevertheless, some of the oxygen-containing defects in the GQD structure remained.

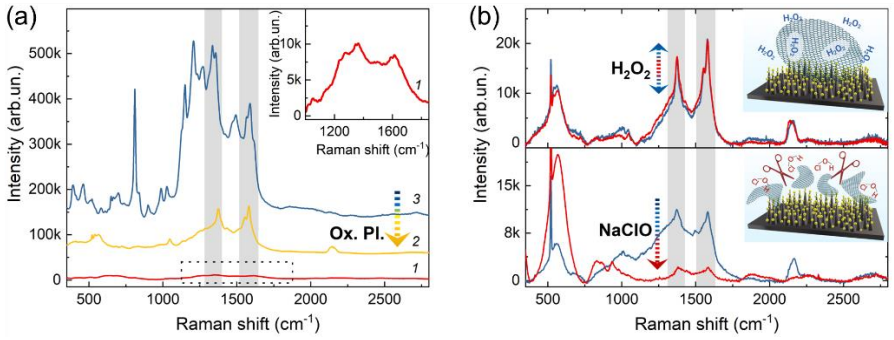

Figure 27. Interaction of GQDs with NaClO and H_2O_2: (a) (from bottom to top) Raman spectrum of 1 mg/mL water solution of GQDs, SERS spectrum of GQDs deposited on lace-like black silicon with gold pseudo-layer and then treated oxygen plasma, SERS spectrum of GQDs deposited on lace-like black silicon with gold pseudo-layer; (b) SERS spectrum of GQDs deposited on lace-like black silicon with gold pseudo-layer after interaction with 10 mM solutions of H_2O_2 and NaClO for 30 min. Adapted from **Paper (F)**. Schematic illustration is created with BioRender.com.

Further exposure of oxygen plasma treated and untreated GQDs to H_2O_2 led to no changes in their SERS spectrum (Figure 27b, shown for treated GQDs). Interaction of GQDs with NaClO led to significant SERS spectrum change, indicating the modification of C–O–C/C–O/C–O–H groups and the damage of the carbonic core of GQDs, reflected in almost total elimination of D and G bands (Figure 27b). more likely the mechanism of the hypochlorous acid-induced structure damage of GQDs is based under basic conditions on the epoxy-ring opening (C–O–C) through the nucleophilic hydroxide ion attack on one of the adjacent carbons. This is followed by the formation of hydroxyl groups which, in their turn, can be oxidized to carbonyl groups (C=O) in the presence of hypochlorous acid as an oxidizing agent, while the bond between the adjacent carbinol carbons breaks. This leads to the formation of excessive C=O groups on the sites of epoxy-groups localization. This mechanism explains the disappearance of absorption bands in GQD spectra in a dose-dependent manner. The increase of C=O groups content per GQD and disruption of the carbonic core of the nanoparticle may also be the reason of the fluorescence redshift, caused by the increase of the contribution of radiating transitions in C=O bonds under NaClO treatment [185].

This was summarized in the fourth statement of the thesis: Cancer cells can be destroyed by a photoacoustic mechanism guided by the interaction of picosecond laser pulses and agglomerates of carbon nanomaterials, which subsequently, upon neutrophil activation, are biodegraded by a hypochlorite-mediated mechanism disclosed using a SERS-active black silicon/gold substrate.

CONCLUSIONS

1. Nano- and/or micro-structuring of the silicon surface (black silicon) and combination of micro-structured silicon with PyC films or graphene nano-wall films composed of graphene flakes oriented perpendicular to the silicon substrate governs cellular viability by tuning cell adhesion, spreading and morphology. **Cone-like black silicon**, produced by cryogenic ICP-RIE, demonstrates good biocompatibility, preserving proliferation rate of cells, spindle-shape morphology, and formation of intercellular contacts, thus being promising for further biosensing applications. PyC films over cone-like black silicon weaken cell attachment and, consequently, proliferation rate, but still are cell-friendly coatings and can be used without poly-l-lysine or other biopolymers for controlling cell adhesion. **Lace-like black silicon**, fabricated by RT ICP-RIE, stays in line with as-grown graphene nano-walls and is highly hydrophobic and non-biocompatible due to specific nano-roughness and sharp edges. Nevertheless, lace-like black silicon exhibits the potential for analytical applications.

2. **Cone-like black silicon** sputtered with 80 nm gold layer is applicable for SERS of organic molecules and living cells, allowing visualization of the characteristic bands of nucleic acids, proteins, and lipids in the "fingerprint" region applying low excitation intensities and short accumulation time. Cone-like black silicon possesses high sensitivity and significant EF of 10^8 and less than 13% of RSD of the Raman signal, which is achieved through dense distribution of gold nanostructures of different shapes over submicron regular silicon cones evenly distributed over the entire surface.

3. The numerical FEM simulations of plane wave interaction with various gold and silicon-gold core-shell nanostructures, which shapes and dimensions were extracted from SEM micrographs of cone-like black silicon sputtered with gold, supported the experimentally obtained EF of this type of black silicon. Simulations revealed the presence of a LSP resonance in the NIR spectral region for some of the analyzed structures. Based on the $|E|^4$-approximation, the numerically estimated electromagnetic EF of simulated structures with NIR excitation was 10^7, with dominating impact of the enhancement in the gap between the overlapping bi-spheres and Si@Au core-shell structures. Simulations of the decrease of the gold layer thickness for Si@Au structures and the increase to some extent of the interparticle distance for gold structures demonstrated the possibility to further reduce the gold layer thickness and enlarge the silicon structures with practically no loss to the enhancement efficiency with NIR excitation. This theoretical prediction was used to fabricate new generations of optimized lace-like and pillar-like black

silicon by simplified ICP-RIE technology with significantly reduced gold pseudo-layer showing a good SERS performance.

4. Lace-like black silicon with a thin gold pseudo-layer fabricated by RT ICP-RIE (100 min etching) possesses SERS EF of 10^6. The fabricated substrates have prominent uniformity (with less than 6% SERS signal variations over 100 × 100 μm^2 area) and are durable, as the storage of these substrates in an ambient environment reduces the SERS signal by less than 3% in 1 month and not more than 40% in 20 months. Lace-like black silicon with nano-meter thick gold pseudo-layer can be reused after oxygen plasma cleaning for at least 10 cycles, although the decrease in Raman signal intensity occurs. Black silicon reusability was proved both for covalently bonding molecules (4-MBA) and adsorbed molecules of chemotherapeutic drug doxorubicin, which do not form covalent bonding. Reusability, stability, reliability, durability, and low cost of black silicon-based SERS substrates make this type of nano-/micro-structured material a promising tool for routine research in different areas of science and healthcare.

5. SWCNTs are suitable nanomaterials for effective cancer theranostics. Efficient accumulation of SWCNTs inside cancer cells in the form of relatively large agglomerates, enables both cancer cell imaging by means of Raman microscopy applying NIR laser excitation in continuous mode and photo-induced destruction of cancer cells using picosecond laser irradiation. Individual SWCNTs dispersed in the extracellular environment are not photo-acoustically active under the same irradiation conditions. This defines the selectivity of the method: only SWCNTs agglomerated inside the cytoplasm by cellular endocytic activity are destroyed, while individual nanotubes present around in the extracellular environment cause no damaging effect on adjacent fluids and tissues.

6. Combination of SERS analysis of GQDs (a model of carbon nanomaterial) performed with lace-like black silicon covered with gold pseudo-layer and other spectroscopic techniques allowed revealing the mechanism of carbon nanomaterial biodegradation. GQDs induce the activation of neutrophils, the cells of the first line immune system defense, accompanied by myeloperoxidase release, which leads to the disruption of GQD structure by the produced hypochlorous acid predominantly through opening epoxide ring C–O–C, forming excessive C=O bonds and damaging the carbonic core of GQDs. The obtained results reveal the evolution of graphene-based nanomaterials used in cancer therapy after the treatment procedure, disclosing the mechanism of their elimination, thus supporting their safety. These data demonstrate the effectiveness of black silicon-based SERS substrates in solving practical issues in the field of biomedicine.

BIBLIOGRAPHY

1. Song, M.; Lin, X.; Peng, Z.; Xu, S.; Jin, L.; Zheng, X.; Luo, H. Materials and Methods of Biosensor Interfaces With Stability. *Front. Mater.* **2021**, *7*, 1–11, doi:10.3389/fmats.2020.583739.
2. Tzeng, Y.; Lin, B.Y. Silver SERS Adenine Sensors with a Very Low Detection Limit. *Biosensors* **2020**, *10*, doi:10.3390/BIOS10050053.
3. Bernat, A.; Samiwala, M.; Albo, J.; Jiang, X.; Rao, Q. Challenges in SERS-Based Pesticide Detection and Plausible Solutions. *J. Agric. Food Chem.* **2019**, doi:10.1021/acs.jafc.9b05077.
4. Wang, Y.; Li, P.; Lin, D.; Chen, J.; Zhang, Y.; Yang, L. Ethanol-Extraction SERS Strategy for Highly Sensitive Detection of Poisons in Oily Matrix. *Spectrochim. Acta - Part A Mol. Biomol. Spectrosc.* **2021**, *259*, 119883, doi:10.1016/j.saa.2021.119883.
5. Costas, C.; López-Puente, V.; Bodelón, G.; González-Bello, C.; Pérez-Juste, J.; Pastoriza-Santos, I.; Liz-Marzán, L.M. Using Surface Enhanced Raman Scattering to Analyze the Interactions of Protein Receptors with Bacterial Quorum Sensing Modulators. *ACS Nano* **2015**, *9*, 5567–5576, doi:10.1021/acsnano.5b01800.
6. Morton, S.M.; Jensen, L. Understanding the Molecule-Surface Chemical Coupling in SERS. *J. Am. Chem. Soc.* **2009**, *131*, 4090–4098, doi:10.1021/ja809143c.
7. Szaniawska, A.; Kudelski, A. Applications of Surface-Enhanced Raman Scattering in Biochemical and Medical Analysis. *Front. Chem.* **2021**, *9*, 296, doi:10.3389/fchem.2021.664134.
8. Fikiet, M.A.; Khandasammy, S.R.; Mistek, E.; Ahmed, Y.; Halámková, L.; Bueno, J.; Lednev, I.K. Surface Enhanced Raman Spectroscopy: A Review of Recent Applications in Forensic Science. *Spectrochim. Acta Part A Mol. Biomol. Spectrosc.* **2018**, *197*, 255–260, doi:10.1016/J.SAA.2018.02.046.
9. Halvorson, R.A.; Vikesland, P.J. Surface-Enhanced Raman Spectroscopy (SERS) for Environmental Analyses. *Environ. Sci. Technol.* **2010**, *44*, 7749–7755, doi:10.1021/es101228z.
10. Jiang, L.; Hassan, M.M.; Ali, S.; Li, H.; Sheng, R.; Chen, Q. Evolving Trends in SERS-Based Techniques for Food Quality and Safety: A Review. *Trends Food Sci. Technol.* **2021**, *112*, 225–240, doi:10.1016/J.TIFS.2021.04.006.
11. Khnykina, K.A.; Baranov, M.A.; Babaev, A.A.; Dubavik, A.Y.; Fedorov, A. V; Baranov, A. V; Bogdanov, K. V Comparison Study of Surface-Enhanced Raman Spectroscopy Substrates. *J. Phys. Conf. Ser.* **2021**, *1984*, 12020, doi:10.1088/1742-6596/1984/1/012020.
12. Mo, S.; Shao, X.; Chen, Y.; Cheng, Z. Increasing Entropy for Colloidal Stabilization. *Sci. Rep.* **2016**, *6*, 1–7, doi:10.1038/srep36836.
13. Shi, L.; Zhang, L.; Tian, Y. Rational Design of Surface-Enhanced

Raman Scattering Substrate for Highly Reproducible Analysis. *Anal. Sens.* **2022**, e202200064, doi:10.1002/anse.202200064.
14. Mikac, L.; Gotić, M.; Gebavi, H.; Ivanda, M. The Variety of Substrates for Surface-Enhanced Raman Spectroscopy. In Proceedings of the The 2017 IEEE 7th International Conference on Nanomaterials: Applications and Properties, NAP 2017; Institute of Electrical and Electronics Engineers Inc., December 12 2017; Vol. 2017-Janua.
15. Tite, T.; Chiticaru, E.A.; Burns, J.S.; Ioniţă, M. Impact of Nano-Morphology, Lattice Defects and Conductivity on the Performance of Graphene Based Electrochemical Biosensors. *J. Nanobiotechnology 2019 171* **2019**, *17*, 1–22, doi:10.1186/S12951-019-0535-6.
16. Sharafeldin, M.; Davis, J.J. Characterising the Biosensing Interface. *Anal. Chim. Acta* **2022**, *1216*, 339759, doi:10.1016/j.aca.2022.339759.
17. Xu, Y.; Hu, X.; Kundu, S.; Nag, A.; Afsarimanesh, N.; Sapra, S.; Mukhopadhyay, S.C.; Han, T. Silicon-Based Sensors for Biomedical Applications: A Review. *Sensors (Basel).* **2019**, *19*, doi:10.3390/S19132908.
18. Zhu, G.; Cheng, L.; Liu, G.; Zhu, L. Synthesis of Gold Nanoparticle Stabilized on Silicon Nanocrystal Containing Polymer Microspheres as Effective Surface-Enhanced Raman Scattering (SERS) Substrates. *Nanomaterials* **2020**, *10*, 1–9, doi:10.3390/nano10081501.
19. Cai, S.; Wu, C.; Yang, W.; Liang, W.; Yu, H.; Liu, L. Recent Advance in Surface Modification for Regulating Cell Adhesion and Behaviors. *Nanotechnol. Rev.* **2020**, *9*, 971–989, doi:10.1515/ntrev-2020-0076.
20. Ivanova, E.P.; Hasan, J.; Webb, H.K.; Gervinskas, G.; Juodkazis, S.; Truong, V.K.; Wu, A.H.F.; Lamb, R.N.; Baulin, V.A.; Watson, G.S.; et al. Bactericidal Activity of Black Silicon. *Nat. Commun.* **2013**, *4*, 1–7, doi:10.1038/ncomms3838.
21. Gervinskas, G.; Seniutinas, G.; Hartley, J.S.; Kandasamy, S.; Stoddart, P.R.; Fahim, N.F.; Juodkazis, S. Surface-Enhanced Raman Scattering Sensing on Black Silicon. *Ann. Phys.* **2013**, *525*, 907–914, doi:10.1002/andp.201300035.
22. Lin, B.W.; Tai, Y.H.; Lee, Y.C.; Xing, D.; Lin, H.C.; Yamahara, H.; Ho, Y.L.; Tabata, H.; Daiguji, H.; Delaunay, J.J. Aluminum-Black Silicon Plasmonic Nano-Eggs Structure for Deep-UV Surface-Enhanced Resonance Raman Spectroscopy. *Appl. Phys. Lett.* **2022**, *120*, 51102, doi:10.1063/5.0084907.
23. Cancer Available online: https://www.who.int/news-room/fact-sheets/detail/cancer (accessed on 5 May 2023).
24. Kalash, R.S.; Lakshmanan, V.K.; Cho, C.S.; Park, I.K. Theranostics. In *Biomaterials Nanoarchitectonics*; Elsevier Inc., 2016; pp. 197–215 ISBN 9780323371278.

25. Yang, N.; Li, H.; Cao, C.; Zhao, L.; Song, X.; Wang, W.; Xu, W.; Zhang, Y.; Chen, P.; Dong, X. Tumor Microenvironment-Activated Theranostic Nanoreactor for NIR-II Photoacoustic Imaging-Guided Tumor-Specific Photothermal Therapy. *Fundam. Res.* **2022**, doi:10.1016/j.fmre.2022.04.021.
26. Chen, Q.; Ke, H.; Dai, Z.; Liu, Z. Nanoscale Theranostics for Physical Stimulus-Responsive Cancer Therapies. *Biomaterials* **2015**, *73*, 214–230, doi:10.1016/j.biomaterials.2015.09.018.
27. Romanov, O.; Timoshchenko, I. Numerical Simulation of Photoacoustic Effect in One-Dimensional Carbon Nanostructures. *Nonlinear Phenom. Complex Syst.* **2022**, *25*, 341–348, doi:10.33581/1561-4085-2022-25-4-341-348.
28. Lan, J. Overview of Application of Nanomaterials in Medical Domain. *Contrast Media Mol. Imaging* **2022**, *2022*, doi:10.1155/2022/3507383.
29. Sim, S.; Wong, N.K. Nanotechnology and Its Use in Imaging and Drug Delivery (Review). *Biomed. Reports* **2021**, *14*, 1–9, doi:10.3892/br.2021.1418.
30. Chen, S.; Zhang, Q.; Hou, Y.; Zhang, J.; Liang, X.J. Nanomaterials in Medicine and Pharmaceuticals: Nanoscale Materials Developed with Less Toxicity and More Efficacy. *Eur. J. Nanomedicine* **2013**, *5*, 61–79, doi:10.1515/ejnm-2013-0003.
31. Shalaby, M.A.; Anwar, M.M.; Saeed, H. Nanomaterials for Application in Wound Healing: Current State-of-the-Art and Future Perspectives. *J. Polym. Res.* **2022**, *29*, 1–37, doi:10.1007/s10965-021-02870-x.
32. Barroso, A.; Mestre, H.; Ascenso, A.; Simões, S.; Reis, C. Nanomaterials in Wound Healing: From Material Sciences to Wound Healing Applications. *Nano Sel.* **2020**, *1*, 443–460, doi:10.1002/nano.202000055.
33. Abdollahiyan, P.; Oroojalian, F.; Mokhtarzadeh, A. The Triad of Nanotechnology, Cell Signalling, and Scaffold Implantation for the Successful Repair of Damaged Organs: An Overview on Soft-Tissue Engineering. *J. Control. Release* **2021**, *332*, 460–492, doi:10.1016/j.jconrel.2021.02.036.
34. Urie, R.; Ghosh, D.; Ridha, I.; Rege, K. Inorganic Nanomaterials for Soft Tissue Repair and Regeneration. *Annu. Rev. Biomed. Eng.* **2018**, *20*, 353–374, doi:10.1146/annurev-bioeng-071516-044457.
35. Garg, P.; Attri, P.; Sharma, R.; Chauhan, M.; Chaudhary, G.R. Advances and Perspective on Antimicrobial Nanomaterials for Biomedical Applications. *Front. Nanotechnol.* **2022**, *4*, 36, doi:10.3389/fnano.2022.898411.
36. Hochvaldová, L.; Večeřová, R.; Kolář, M.; Prucek, R.; Kvítek, L.; Lapčík, L.; Panáček, A. Antibacterial Nanomaterials: Upcoming Hope to Overcome Antibiotic Resistance Crisis. *Nanotechnol. Rev.*

2022, *11*, 1115–1142, doi:10.1515/ntrev-2022-0059.
37. Dahinden, C.A.; Fehr, J.; Hugli, T.E. Role of Cell Surface Contact in the Kinetics of Superoxide Production by Granulocytes. *J. Clin. Invest.* **1983**, *72*, 113–121, doi:10.1172/JCI110948.
38. Spillmann, C.M.; Lomakina, E.; Waugh, R.E. Neutrophil Adhesive Contact Dependence on Impingement Force. *Biophys. J.* **2004**, *87*, 4237–4245, doi:10.1529/biophysj.103.031773.
39. Hoffman, R.; Benz, E.J.; Silberstein, L.E.; Heslop, H.E.; Weitz, J.I.; Anastasi, J.; Salama, M.E.; Abutalib, S. *Hematology: Basic Principles and Practice*; Elsevier Inc., 2017; ISBN 9781455740413.
40. Chen, S.; Lewallen, M.; Xie, T. Adhesion in the Stem Cell Niche: Biological Roles and Regulation. *Dev.* 2013, *140*, 255–265.
41. Akhmanova, M.; Osidak, E.; Domogatsky, S.; Rodin, S.; Domogatskaya, A. Review Article Physical, Spatial, and Molecular Aspects of Extracellular Matrix of In Vivo Niches and Artificial Scaffolds Relevant to Stem Cells Research. **2015**, doi:10.1155/2015/167025.
42. Handorf, A.M.; Zhou, Y.; Halanski, M.A.; Li, W.J. Tissue Stiffness Dictates Development, Homeostasis, and Disease Progression. *Organogenesis* **2015**, *11*, 1–15, doi:10.1080/15476278.2015.1019687.
43. Xie, K.; Yang, Y.; Jiang, H. Controlling Cellular Volume via Mechanical and Physical Properties of Substrate. *Biophys. J.* **2018**, *114*, 675–687, doi:10.1016/j.bpj.2017.11.3785.
44. Sun, Y.; Liu, J.; Xu, Z.; Lin, X.; Zhang, X.; Li, L.; Li, Y. Matrix Stiffness Regulates Myocardial Differentiation of Human Umbilical Cord Mesenchymal Stem Cells. *Aging (Albany. NY).* **2021**, *13*, 2231–2250, doi:10.18632/AGING.202244.
45. Naganuma, T. The Relationship between Cell Adhesion Force Activation on Nano/Micro-Topographical Surfaces and Temporal Dependence of Cell Morphology. *Nanoscale* **2017**, *9*, 13171–13186, doi:10.1039/c7nr04785a.
46. Losero, E.; Jagannath, S.; Pezzoli, M.; Goblot, V.; Babashah, H.; Lashuel, H.A.; Galland, C.; Quack, N. Neuronal Growth on High-Aspect-Ratio Diamond Nanopillar Arrays for Biosensing Applications. *Sci. Reports 2023 131* **2022**, *13*, 1–12, doi:10.1038/s41598-023-32235-x.
47. Harjunpää, H.; Asens, M.L.; Guenther, C.; Fagerholm, S.C. Cell Adhesion Molecules and Their Roles and Regulation in the Immune and Tumor Microenvironment. *Front. Immunol.* **2019**, *10*, 1078, doi:10.3389/fimmu.2019.01078.
48. Wysotzki, P.; Sancho, A.; Gimsa, J.; Groll, J. A Comparative Analysis of Detachment Forces and Energies in Initial and Mature Cell-Material Interaction. *Colloids Surfaces B Biointerfaces* **2020**, *190*, 110894, doi:10.1016/j.colsurfb.2020.110894.

49. Han, S.B.; Kim, J.K.; Lee, G.; Kim, D.H. Mechanical Properties of Materials for Stem Cell Differentiation. *Adv. Biosyst.* **2020**, *4*, 2000247, doi:10.1002/adbi.202000247.
50. Boulnois, J.L. Photophysical Processes in Recent Medical Laser Developments: A Review. *Lasers Med. Sci.* **1986**, *1*, 47–66, doi:10.1007/BF02030737.
51. Smith, R.; Wright, K.L.; Ashton, L. Raman Spectroscopy: An Evolving Technique for Live Cell Studies. *Analyst* **2016**, *141*, 3590–3600, doi:10.1039/c6an00152a.
52. Downes, A.; Elfick, A. Raman Spectroscopy and Related Techniques in Biomedicine. *Sensors* 2010, *10*, 1871–1889.
53. Keiser, G. Light-Tissue Interactions. In *Biophotonics*; Springer Singapore, 2016; p. 345 ISBN 9789811009457.
54. Sato, H.; Ishigaki, M.; Taketani, A.; Andriana, B.B. Raman Spectroscopy and Its Use for Live Cell and Tissue Analysis. *Biomed. Spectrosc. Imaging* **2019**, *7*, 97–104, doi:10.3233/bsi-180184.
55. Notingher, I. Raman Spectroscopy Cell-Based Biosensors. *Sensors* **2007**, *7*, 1343–1358, doi:10.3390/s7081343.
56. Le Ru, E.C.; Etchegoin, P.G. A Quick Overview of Surface-Enhanced Raman Spectroscopy. In *Principles of Surface-Enhanced Raman Spectroscopy: and Related Plasmonic Effects*; Le Ru, E.C., Etchegoin, P.G., Eds.; Elsevier Science: Amsterdam, 2009; pp. 1–27.
57. Le Ru, E.C.; Etchegoin, P.G. Introduction to Plasmons and Plasmonics. In *Principles of Surface-Enhanced Raman Spectroscopy: and Related Plasmonic Effects*; 2009; pp. 29–120.
58. Dietzek, B.; Cialla, D.; Schmitt, M.; Popp, J. Introduction to the Fundamentals of Raman Spectroscopy. In *Confocal Raman Microscopy*; Toporski, J., Dieing, T., Hollricher, O., Eds.; Springer Series in Surface Sciences; Springer International Publishing: Cham, 2018; Vol. 66, pp. 47–68 ISBN 978-3-319-75378-2.
59. Long, D.A. Intensities in Raman Spectra I. A Bond Polarizability Theory. *Proc. R. Soc. London. Ser. A. Math. Phys. Sci.* **1953**, *217*, 203–221, doi:10.1098/rspa.1953.0057.
60. Le Ru, E.C.; Etchegoin, P.G. SERS Enhancement Factors and Related Topics. In *Principles of Surface-Enhanced Raman Spectroscopy: and Related Plasmonic Effects*; Le Ru, E.C., Etchegoin, P.G., Eds.; Elsevier Science: Amsterdam, 2009; pp. 185–264 ISBN 978-0444527790.
61. Jiang, L.; You, T.; Yin, P.; Shang, Y.; Zhang, D.; Guo, L.; Yang, S. Surface-Enhanced Raman Scattering Spectra of Adsorbates on Cu2O Nanospheres: Charge-Transfer and Electromagnetic Enhancement. *Nanoscale* **2013**, *5*, 2784–2789, doi:10.1039/c3nr33502j.
62. Rodríguez-Oliveros, R.; Paniagua-Domínguez, R.; Sánchez-Gil, J.A.; Macías, D. Plasmon Spectroscopy: Theoretical and Numerical Calculations, and Optimization Techniques. *Nanospectroscopy* **2016**,

1, 67–96, doi:10.1515/nansp-2015-0006.
63. Bhushan, B. *Encyclopedia of Nanotechnology*; Bhushan, B., Ed.; Springer Science and Business Media B.V., 2012; Vol. 50; ISBN 9789048197507.
64. Pérez-Jiménez, A.I.; Lyu, D.; Lu, Z.; Liu, G.; Ren, B. Surface-Enhanced Raman Spectroscopy: Benefits, Trade-Offs and Future Developments. *Chem. Sci.* **2020**, *11*, 4563–4577, doi:10.1039/d0sc00809e.
65. Mendoza Herrera, L.J.; Arboleda, D.M.; Schinca, D.C.; Scaffardi, L.B. Determination of Plasma Frequency, Damping Constant, and Size Distribution from the Complex Dielectric Function of Noble Metal Nanoparticles. *J. Appl. Phys.* **2014**, *116*, 233105, doi:10.1063/1.4904349.
66. Huang, K.J.; Qin, S.J.; Zhang, Z.P.; Ding, Z.; Bai, Z.C. Nonlocal and Size-Dependent Dielectric Function for Plasmonic Nanoparticles. *Appl. Sci.* **2019**, *9*, 3083, doi:10.3390/app9153083.
67. Rakić, A.D.; Djurišić, A.B.; Elazar, J.M.; Majewski, M.L. Optical Properties of Metallic Films for Vertical-Cavity Optoelectronic Devices. *Appl. Opt.* **1998**, *37*, 5271, doi:10.1364/ao.37.005271.
68. Polyanskiy, M.N. RefractiveIndex.INFO - Refractive Index Database Available online: https://refractiveindex.info/ (accessed on 2 June 2023).
69. Bohren, C.F.; Huffman, D.R. *Absorption and Scattering of Light by Small Particles*; Wiley, 1998; ISBN 9780471293408.
70. Ren, K.F.; Gréhan, G.; Gouesbet, G. Scattering of a Gaussian Beam by an Infinite Cylinder in the Framework of Generalized Lorenz–Mie Theory: Formulation and Numerical Results. *J. Opt. Soc. Am. A* **1997**, *14*, 3014, doi:10.1364/josaa.14.003014.
71. Gansen, A.; El Hachemi, M.; Belouettar, S.; Hassan, O.; Morgan, K. A 3D Unstructured Mesh FDTD Scheme for EM Modelling. *Arch. Comput. Methods Eng.* **2021**, *28*, 181–213, doi:10.1007/s11831-019-09395-z.
72. Lumerical Inc. Understanding Mesh Refinement and Conformal Mesh in FDTD Available online: https://optics.ansys.com/hc/en-us/articles/360034382594-Understanding-Mesh-Refinement-and-Conformal-Mesh-in-FDTD (accessed on 4 May 2023).
73. Jin, J.-M. *The Finite Element Method in Electromagnetics*; Jin, J.-M., Ed.; 3rd Editio.; Wiley-IEEE Press: Hoboken, 2014; ISBN 978-1-118-84198-3.
74. COMSOL.com Wave Optics Software for Analyzing Micro- and Nano-Optical Devices Available online: https://www.comsol.com/wave-optics-module (accessed on 26 April 2023).
75. Ansys Ansys Lumerical FDTD Simulation of Photonic Components Available online: https://www.ansys.com/products/photonics/fdtd

(accessed on 26 April 2023).
76. Cyrankiewicz, M.; Wybranowski, T.; Kruszewski, S. Study of SERS Efficiency of Metallic Colloidal Systems. *J. Phys. Conf. Ser.* **2007**, *79*, 012013, doi:10.1088/1742-6596/79/1/012013.
77. Hoang, V.T.; Tufa, L.T.; Lee, J.; Doan, M.Q.; Anh, N.H.; Tran, V.T.; Le, A.T. Tunable SERS Activity of Ag@Fe3O4 Core-Shell Nanoparticles: Effect of Shell Thickness on the Sensing Performance. *J. Alloys Compd.* **2023**, *933*, 167649, doi:10.1016/j.jallcom.2022.167649.
78. Tang, S.; Liu, H.; Wang, M.; Wang, S.; Wang, C.; Gu, C.; Zhao, Z.; Jiang, T.; Zhou, J. Further Enhancement of SERS Signals from Au@Ag@PSPAA Core–Shell Nanoparticles Surrounded by Ag Nanoplates. *Mater. Chem. Phys.* **2019**, *225*, 60–63, doi:10.1016/j.matchemphys.2018.12.040.
79. Yilmaz, A.; Yilmaz, M. Bimetallic Core–Shell Nanoparticles of Gold and Silver via Bioinspired Polydopamine Layer as Surface-Enhanced Raman Spectroscopy (SERS) Platform. *Nanomaterials* **2020**, *10*, 688, doi:10.3390/nano10040688.
80. Krajczewski, J.; Kudelski, A. Shell-Isolated Nanoparticle-Enhanced Raman Spectroscopy. *Front. Chem.* **2019**, *7*, 410, doi:10.3389/fchem.2019.00410.
81. Olson, L.G.; Lo, Y.S.; Beebe, T.P.; Harris, J.M. Characterization of Silane-Modified Immobilized Gold Colloids as a Substrate for Surface-Enhanced Raman Spectroscopy. *Anal. Chem.* **2001**, *73*, 4268–4276, doi:10.1021/ac000873b.
82. Dao, T.C.; Luong, T.Q.N. Fabrication of Uniform Arrays of Silver Nanoparticles on Silicon by Electrodeposition in Ethanol Solution and Their Use in SERS Detection of Difenoconazole Pesticide. *RSC Adv.* **2020**, *10*, 40940–40947, doi:10.1039/d0ra08060h.
83. Romo-Herrera, J.M.; Juarez-Moreno, K.; Guerrini, L.; Kang, Y.; Feliu, N.; Parak, W.J.; Alvarez-Puebla, R.A. Paper-Based Plasmonic Substrates as Surface-Enhanced Raman Scattering Spectroscopy Platforms for Cell Culture Applications. *Mater. Today Bio* **2021**, *11*, 100125, doi:10.1016/j.mtbio.2021.100125.
84. Rafiq, F.; Wang, N.; Li, K.; Hong, Z.; Cao, D.; Du, J.; Sun, Z. Au-NP-Decorated Cotton Swabs as a Facile SERS Substrate for Food-Safety-Related Molecule Detection. *ACS Omega* **2023**, *8*, 8541–8547, doi:10.1021/acsomega.2c07690.
85. Ma, X.; Xie, J.; Wang, Z.; Zhang, Y. Transparent and Flexible AuNSs/PDMS-Based SERS Substrates for in-Situ Detection of Pesticide Residues. *Spectrochim. Acta Part A Mol. Biomol. Spectrosc.* **2022**, *267*, 120542, doi:10.1016/j.saa.2021.120542.
86. Abu Hatab, N.A.; Oran, J.M.; Sepaniak, M.J. Surface-Enhanced Raman Spectroscopy Substrates Created via Electron Beam Lithography and Nanotransfer Printing. *ACS Nano* **2008**, *2*, 377–385,

doi:10.1021/nn7003487.
87. Wu, H.-Y.; Lin, H.-C.; Hung, G.-Y.; Tu, C.-S.; Liu, T.-Y.; Hong, C.-H.; Yu, G.; Hsu, J.-C. High Sensitivity SERS Substrate of a Few Nanometers Single-Layer Silver Thickness Fabricated by DC Magnetron Sputtering Technology. *Nanomaterials* **2022**, *12*, 2742, doi:10.3390/nano12162742.
88. Chu, F.; Yan, S.; Zheng, J.; Zhang, L.; Zhang, H.; Yu, K.; Sun, X.; Liu, A.; Huang, Y. A Simple Laser Ablation-Assisted Method for Fabrication of Superhydrophobic SERS Substrate on Teflon Film. *Nanoscale Res. Lett.* **2018**, *13*, 244, doi:10.1186/s11671-018-2658-3.
89. Chen, D.; Zhang, L.; Ning, P.; Yuan, H.; Zhang, Y.; Zhang, M.; Fu, T.; He, X. In-Situ Growth of Gold Nanoparticles on Electrospun Flexible Multilayered PVDF Nanofibers for SERS Sensing of Molecules and Bacteria. *Nano Res.* **2021**, *14*, 4885–4893, doi:10.1007/s12274-021-3530-9.
90. Mir-Simon, B.; Reche-Perez, I.; Guerrini, L.; Pazos-Perez, N.; Alvarez-Puebla, R.A. Universal One-Pot and Scalable Synthesis of SERS Encoded Nanoparticles. *Chem. Mater.* **2015**, *27*, 950–958, doi:10.1021/cm504251h.
91. Chirumamilla, A.; Moise, I.M.; Cai, Z.; Ding, F.; Jensen, K.B.; Wang, D.; Kristensen, P.K.; Jensen, L.R.; Fojan, P.; Popok, V.; et al. Lithography-Free Fabrication of Scalable 3D Nanopillars as Ultrasensitive SERS Substrates. *Appl. Mater. Today* **2023**, *31*, 101763, doi:10.1016/j.apmt.2023.101763.
92. Bai, S.; Serien, D.; Hu, A.; Sugioka, K. 3D Microfluidic Surface-Enhanced Raman Spectroscopy (SERS) Chips Fabricated by All-Femtosecond-Laser-Processing for Real-Time Sensing of Toxic Substances. *Adv. Funct. Mater.* **2018**, *28*, 1706262, doi:10.1002/adfm.201706262.
93. Liao, W.; Liu, K.; Chen, Y.; Hu, J.; Gan, Y. Au–Ag Bimetallic Nanoparticles Decorated Silicon Nanowires with Fixed and Dynamic Hot Spots for Ultrasensitive 3D SERS Sensing. *J. Alloys Compd.* **2021**, *868*, 159136, doi:10.1016/j.jallcom.2021.159136.
94. Seo, S.; Chang, T.-W.; Liu, G.L. 3D Plasmon Coupling Assisted Sers on Nanoparticle-Nanocup Array Hybrids. *Sci. Rep.* **2018**, *8*, 3002, doi:10.1038/s41598-018-19256-7.
95. Sun, H.; Gao, R.; Zhu, A.; Hua, Z.; Chen, L.; Wang, Y.; Zhang, Y. Surface-Enhanced Raman Scattering from Metal and Transition Metal Nano-Caped Arrays. *Superlattices Microstruct.* **2018**, *115*, 59–66, doi:10.1016/j.spmi.2018.01.020.
96. Chiou, A.H.; Wei, J.L.; Chen, S.H. Ag-Functionalized Si Nanowire Arrays Aligned Vertically for Sers Detection of Captured Heavy Metal Ions by Bsa. *Coatings* **2021**, *11*, 685, doi:10.3390/coatings11060685.
97. Wang, P.; Wu, L.; Lu, Z.; Li, Q.; Yin, W.; Ding, F.; Han, H. Gecko-

Inspired Nanotentacle Surface-Enhanced Raman Spectroscopy Substrate for Sampling and Reliable Detection of Pesticide Residues in Fruits and Vegetables. *Anal. Chem.* **2017**, *89*, 2424–2431, doi:10.1021/acs.analchem.6b04324.
98. Boginskaya, I.; Sedova, M.; Baburin, A.; Afanas'ev, K.; Zverev, A.; Echeistov, V.; Ryzhkov, V.; Rodionov, I.; Tonanaiskii, B.; Ryzhikov, I.; et al. SERS-Active Substrates Nanoengineering Based on e-Beam Evaporated Self-Assembled Silver Films. *Appl. Sci.* **2019**, *9*, 3988, doi:10.3390/app9193988.
99. Zhou, N.; Meng, G.; Huang, Z.; Zhang, X.; Zhu, C.; Ke, Y. Ag-Coated 3D Cu(OH)2 Nanowires on the Woven Copper Mesh as a Cost-Effective Surface-Enhanced Raman Scattering Substrate. *Surf. Coatings Technol.* **2021**, *415*, 127132, doi:10.1016/j.surfcoat.2021.127132.
100. La Porta, A.; Grzelczak, M.; Liz-Marzán, L.M. Gold Nanowire Forests for SERS Detection. *ChemistryOpen* **2014**, *3*, 146–151, doi:10.1002/open.201402009.
101. Abu Hatab, N.A.; Oran, J.M.; Sepaniak, M.J. Surface-Enhanced Raman Spectroscopy Substrates Created via Electron Beam Lithography and Nanotransfer Printing. *ACS Nano* **2008**, *2*, 377–385, doi:10.1021/nn7003487.
102. Salvador-Porroche, A.; Herrer, L.; Sangiao, S.; Philipp, P.; Cea, P.; De Teresa, J.M. High-Throughput Direct Writing of Metallic Micro- and Nano-Structures by Focused Ga+Beam Irradiation of Palladium Acetate Films. *ACS Appl. Mater. Interfaces* **2022**, *14*, 28211–28220, doi:10.1021/acsami.2c05218.
103. Kara, S.A.; Keffous, A.; Giovannozzi, A.M.; Rossi, A.M.; Cara, E.; D'Ortenzi, L.; Sparnacci, K.; Boarino, L.; Gabouze, N.; Soukane, S. Fabrication of Flexible Silicon Nanowires by Self-Assembled Metal Assisted Chemical Etching for Surface Enhanced Raman Spectroscopy. *RSC Adv.* **2016**, *6*, 93649–93659, doi:10.1039/c6ra20323j.
104. Chadha, U.; Bhardwaj, P.; Agarwal, R.; Rawat, P.; Agarwal, R.; Gupta, I.; Panjwani, M.; Singh, S.; Ahuja, C.; Selvaraj, S.K.; et al. Recent Progress and Growth in Biosensors Technology: A Critical Review. *J. Ind. Eng. Chem.* **2022**, *109*, 21–51, doi:10.1016/j.jiec.2022.02.010.
105. Lv, J.; Zhang, T.; Zhang, P.; Zhao, Y.; Li, S. Review Application of Nanostructured Black Silicon. *Nanoscale Res. Lett.* **2018**, *13*, 1–10, doi:10.1186/s11671-018-2523-4.
106. Yuan, H.C.; Yost, V.E.; Page, M.R.; Stradins, P.; Meier, D.L.; Branz, H.M. Efficient Black Silicon Solar Cell with a Density-Graded Nanoporous Surface: Optical Properties, Performance Limitations, and Design Rules. *Appl. Phys. Lett.* **2009**, *95*, 123501, doi:10.1063/1.3231438.

107. Sarkar, S.; Elsayed, A.A.; Nefzaoui, E.; Drevillon, J.; Basset, P.; Marty, F.; Anwar, M.; Yu, Y.; Zhao, J.; Yuan, X.; et al. NIR and MIR Absorption of Ultra-Black Silicon (UBS). Application to High Emissivity, All-Silicon, Light Source. In Proceedings of the The IEEE International Conference on Micro Electro Mechanical Systems (MEMS); Institute of Electrical and Electronics Engineers Inc., January 1 2019; Vol. 2019-Janua, pp. 860–862.
108. Lu, J.; Zhuang, W.; Yang, W.; Zhang, X.; Su, G.; Gong, X.; Yuan, J.; Sui, J.; Zhou, Y.; Zhang, G.; et al. Enhanced Absorption in the Wide Wavelength Range: Black Silicon Decorated with Few-Layer PtS2. *J. Phys. Chem. C* **2021**, *125*, 27335–27343, doi:10.1021/acs.jpcc.1c07114.
109. Wu, C.; Crouch, C.H.; Zhao, L.; Carey, J.E.; Younkin, R.; Levinson, J.A.; Mazur, E.; Farrell, R.M.; Gothoskar, P.; Karger, A. Near-Unity below-Band-Gap Absorption by Microstructured Silicon. *Appl. Phys. Lett.* **2001**, *78*, 1850–1852, doi:10.1063/1.1358846.
110. Wen, Z.; Shi, H.; Yue, S.; Li, M.; Zhang, Z.; Wang, R.; Song, Q.; Xu, Z.; Zhang, Z.; Hou, Y. Large-Scale Black Silicon Induced by Femtosecond Laser Assisted With Laser Cleaning. *Front. Phys.* **2022**, *10*, 235, doi:10.3389/fphy.2022.862605.
111. Zhong, H.; Ilyas, N.; Song, Y.; Li, W.; Jiang, Y. Enhanced Near-Infrared Absorber: Two-Step Fabricated Structured Black Silicon and Its Device Application. *Nanoscale Res. Lett.* **2018**, *13*, 1–8, doi:10.1186/s11671-018-2741-9.
112. Serpenguzel, A. Luminescence of Black Silicon. *J. Nanophotonics* **2008**, *2*, 021770, doi:10.1117/1.2896069.
113. Jansen, H.; de Boer, M.; Burger, J.; Legtenberg, R.; Elwenspoek, M. The Black Silicon Method II:The Effect of Mask Material and Loading on the Reactive Ion Etching of Deep Silicon Trenches. *Microelectron. Eng.* **1995**, *27*, 475–480, doi:10.1016/0167-9317(94)00149-O.
114. Cui, Z. *Nanofabrication: Principles, Capabilities and Limits: Second Edition*; Second Edi.; Springer International Publishing, 2017; ISBN 9783319393612.
115. Weigel, C.; Brokmann, U.; Hofmann, M.; Behrens, A.; Rädlein, E.; Hoffmann, M.; Strehle, S.; Sinzinger, S. Perspectives of Reactive Ion Etching of Silicate Glasses for Optical Microsystems. *J. Opt. Microsystems* **2021**, *1*, 1–22, doi:10.1117/1.jom.1.4.040901.
116. Tang, Y.H.; Lin, Y.H.; Chen, P.L.; Shiao, M.H.; Hsiao, C.N. Comparison of Optimised Conditions for Inductively Coupled Plasma-Reactive Ion Etching of Quartz Substrates and Its Optical Applications. *Micro Nano Lett.* **2014**, *9*, 395–398, doi:10.1049/mnl.2014.0093.
117. Peng, Y.; Cui, L.; Gao, J.; Jiang, S.; Wang, H.; Yu, B.; Qian, L. Fabrication of High-Performance Microfluidic SERS Substrates by

Metal-Assisted Chemical Etching of Silicon Scratches. *Surf. Topogr. Metrol. Prop.* **2022**, *10*, 035008, doi:10.1088/2051-672X/ac81dd.
118. Schmidt, M.S.; Hübner, J.; Boisen, A. Large Area Fabrication of Leaning Silicon Nanopillars for Surface Enhanced Raman Spectroscopy. *Adv. Mater.* **2012**, *24*, OP11–OP18, doi:10.1002/adma.201103496.
119. Fan, Z.; Cui, D.; Zhang, Z.; Zhao, Z.; Chen, H.; Fan, Y.; Li, P.; Zhang, Z.; Xue, C.; Yan, S. Recent Progress of Black Silicon: From Fabrications to Applications. *Nanomaterials* **2021**, *11*, 1–26, doi:10.3390/nano11010041.
120. Hoyer, P.; Theuer, M.; Beigang, R.; Kley, E.B. Terahertz Emission from Black Silicon. *Appl. Phys. Lett.* **2008**, *93*, 091106, doi:10.1063/1.2978096.
121. Wang, X.; Bhadra, C.M.; Yen Dang, T.H.; Buividas, R.; Wang, J.; Crawford, R.J.; Ivanova, E.P.; Juodkazis, S. A Bactericidal Microfluidic Device Constructed Using Nano-Textured Black Silicon. *RSC Adv.* **2016**, *6*, 26300–26306, doi:10.1039/c6ra03864f.
122. Singh, J.; Jadhav, S.; Avasthi, S.; Sen, P. Designing Photocatalytic Nanostructured Antibacterial Surfaces: Why Is Black Silica Better than Black Silicon? *ACS Appl. Mater. Interfaces* **2020**, *12*, 20202–20213, doi:10.1021/acsami.0c02854.
123. Bogue, R. Novel Infrared Detectors Based on Black Silicon. *Sens. Rev.* **2010**, *30*, 59–62, doi:10.1108/sr.2010.08730bab.001.
124. Hu, F.; Dai, X.-Y.; Zhou, Z.-Q.; Kong, X.-Y.; Sun, S.-L.; Zhang, R.-J.; Wang, S.-Y.; Lu, M.; Sun, J. Black Silicon Schottky Photodetector in Sub-Bandgap near-Infrared Regime. *Opt. Express* **2019**, *27*, 3161, doi:10.1364/oe.27.003161.
125. Liu, X.L.; Zhu, S.W.; Sun, H. Bin; Hu, Y.; Ma, S.X.; Ning, X.J.; Zhao, L.; Zhuang, J. "infinite Sensitivity" of Black Silicon Ammonia Sensor Achieved by Optical and Electric Dual Drives. *ACS Appl. Mater. Interfaces* **2018**, *10*, 5061–5071, doi:10.1021/acsami.7b16542.
126. Altug, H.; Oh, S.H.; Maier, S.A.; Homola, J. Advances and Applications of Nanophotonic Biosensors. *Nat. Nanotechnol.* **2022**, *17*, 5–16, doi:10.1038/s41565-021-01045-5.
127. Baia, M.; Astilean, S.; Iliescu, T. *Raman and SERS Investigations of Pharmaceuticals*; Springer Berlin Heidelberg, 2008; ISBN 9783540782827.
128. Deng, Y.L.; Juang, Y.J. Black Silicon SERS Substrate: Effect of Surface Morphology on SERS Detection and Application of Single Algal Cell Analysis. *Biosens. Bioelectron.* **2014**, *53*, 37–42, doi:10.1016/j.bios.2013.09.032.
129. Alhmoud, H.; Brodoceanu, D.; Elnathan, R.; Kraus, T.; Voelcker, N.H. A MACEing Silicon: Towards Single-Step Etching of Defined Porous Nanostructures for Biomedicine. *Prog. Mater. Sci.* **2021**, *116*,

100636, doi:10.1016/j.pmatsci.2019.100636.
130. Arafat, M.Y.; Islam, M.A.; Mahmood, A.W. Bin; Abdullah, F.; Nur-E-Alam, M.; Kiong, T.S.; Amin, N. Fabrication of Black Silicon via Metal-Assisted Chemical Etching—a Review. *Sustain.* **2021**, *13*, doi:10.3390/su131910766.
131. Sainiemi, L.; Jokinen, V.; Shah, A.; Shpak, M.; Aura, S.; Suvanto, P.; Franssila, S. Non-Reflecting Silicon and Polymer Surfaces by Plasma Etching and Replication. *Adv. Mater.* **2011**, *23*, 122–126, doi:10.1002/adma.201001810.
132. Chen, Y.; Kang, G.; Shah, A.; Pale, V.; Tian, Y.; Sun, Z.; Tittonen, I.; Honkanen, S.; Lipsanen, H. Improved SERS Intensity from Silver-Coated Black Silicon by Tuning Surface Plasmons. *Adv. Mater. Interfaces* **2014**, *1*, 1300008, doi:10.1002/admi.201300008.
133. Atteia, F.; Le Rouzo, J.; Berginc, G.; Simon, J.-J.; Escoubas, L. Black Silicon (BS) Using Room-Temperature Reactive Ion Etching (RT-RIE) for Interdigitated Back Contact (IBC) Silicon Solar Cells. In Proceedings of the SPIE 10913, Physics, Simulation, and Photonic Engineering of Photovoltaic Devices VIII; SPIE: San Francisco, February 27 2019; Vol. 10913, p. 29.
134. Fang, C.; Zhang, M. Nanoparticle-Based Theragnostics: Integrating Diagnostic and Therapeutic Potentials in Nanomedicine. *J. Control. Release* **2010**, *146*, 2–5, doi:10.1016/j.jconrel.2010.05.013.
135. Zhou, Y.; Fang, Y.; Ramasamy, R.P. Non-Covalent Functionalization of Carbon Nanotubes for Electrochemical Biosensor Development. *Sensors (Switzerland)* **2019**, *19*, doi:10.3390/s19020392.
136. Zhou, L.; Forman, H.J.; Ge, Y.; Lunec, J. Multi-Walled Carbon Nanotubes: A Cytotoxicity Study in Relation to Functionalization, Dose and Dispersion. *Toxicol. Vitr.* **2017**, *42*, 292–298, doi:10.1016/j.tiv.2017.04.027.
137. Anzar, N.; Hasan, R.; Tyagi, M.; Yadav, N.; Narang, J. Carbon Nanotube - A Review on Synthesis, Properties and Plethora of Applications in the Field of Biomedical Science. *Sensors Int.* **2020**, *1*, 100003, doi:10.1016/j.sintl.2020.100003.
138. Eatemadi, A.; Daraee, H.; Karimkhanloo, H.; Kouhi, M.; Zarghami, N.; Akbarzadeh, A.; Abasi, M.; Hanifehpour, Y.; Joo, S.W. Carbon Nanotubes: Properties, Synthesis, Purification, and Medical Applications. *Nanoscale Res. Lett.* **2014**, *9*, 1–13, doi:10.1186/1556-276X-9-393.
139. Saifuddin, N.; Raziah, A.Z.; Junizah, A.R. Carbon Nanotubes: A Review on Structure and Their Interaction with Proteins. *J. Chem.* **2013**, doi:10.1155/2013/676815.
140. Zare, H.; Ahmadi, S.; Ghasemi, A.; Ghanbari, M.; Rabiee, N.; Bagherzadeh, M.; Karimi, M.; Webster, T.J.; Hamblin, M.R.; Mostafavi, E. Carbon Nanotubes: Smart Drug/Gene Delivery Carriers. *Int. J. Nanomedicine* **2021**, *16*, 1681–1706,

doi:10.2147/IJN.S299448.
141. Zhang, W.; Zhang, Z.; Zhang, Y. The Application of Carbon Nanotubes in Target Drug Delivery Systems for Cancer Therapies. *Nanoscale Res. Lett.* **2011**, *6*, 1–22, doi:10.1186/1556-276X-6-555.
142. Golubewa, E.N.; Shuba, M. V.; Vasilieu, M. V.; Kulahava, T.A. Application of Raman Spectroscopy for Analysis of Carbon Nanotube Distribution in Living Cells. *J. Appl. Spectrosc.* **2019**, *85*, 1121–1127, doi:10.1007/s10812-019-00768-7.
143. Wei, X.; Tanaka, T.; Yomogida, Y.; Sato, N.; Saito, R.; Kataura, H. Experimental Determination of Excitonic Band Structures of Single-Walled Carbon Nanotubes Using Circular Dichroism Spectra. *Nat. Commun.* **2016**, *7*, 12899, doi:10.1038/ncomms12899.
144. Liang, C.; Diao, S.; Wang, C.; Gong, H.; Liu, T.; Hong, G.; Shi, X.; Dai, H.; Liu, Z. Tumor Metastasis Inhibition by Imaging-Guided Photothermal Therapy with Single-Walled Carbon Nanotubes. *Adv. Mater.* **2014**, *26*, 5646–5652, doi:10.1002/adma.201401825.
145. Ma, P.C.; Siddiqui, N.A.; Marom, G.; Kim, J.K. Dispersion and Functionalization of Carbon Nanotubes for Polymer-Based Nanocomposites: A Review. *Compos. Part A Appl. Sci. Manuf.* **2010**, *41*, 1345–1367, doi:10.1016/j.compositesa.2010.07.003.
146. Golubewa, L.N.; Kulahava, T.A.; Leonik, Y.S.; Shuba, M. V.; Semenkova, G.N. Application of Raman Spectroscopy for Studying the Mechanisms of Neutrophil Activation by Carbon Nanotubes. *J. Appl. Spectrosc.* **2021**, *88*, 77–84, doi:10.1007/s10812-021-01143-1.
147. Donaldson, K.; Aitken, R.; Tran, L.; Stone, V.; Duffin, R.; Forrest, G.; Alexander, A. Carbon Nanotubes: A Review of Their Properties in Relation to Pulmonary Toxicology and Workplace Safety. *Toxicol. Sci.* **2006**, *92*, 5–22, doi:10.1093/toxsci/kfj130.
148. Semberova, J.; De Paoli Lacerda, S.H.; Simakova, O.; Holada, K.; Gelderman, M.P.; Simak, J. Carbon Nanotubes Activate Blood Platelets by Inducing Extracellular Ca 2+ Influx Sensitive to Calcium Entry Inhibitors. *Nano Lett.* **2009**, *9*, 3312–3317, doi:10.1021/nl901603k.
149. Wang, J.; Sun, P.; Bao, Y.; Liu, J.; An, L. Cytotoxicity of Single-Walled Carbon Nanotubes on PC12 Cells. *Toxicol. Vitr.* **2011**, *25*, 242–250, doi:10.1016/j.tiv.2010.11.010.
150. Jiang, T.; Amadei, C.A.; Gou, N.; Lin, Y.; Lan, J.; Vecitis, C.D.; Gu, A.Z. Toxicity of Single-Walled Carbon Nanotubes (SWCNTs): Effect of Lengths, Functional Groups and Electronic Structures Revealed by a Quantitative Toxicogenomics Assay. *Environ. Sci. Nano* **2020**, *7*, 1348–1364, doi:10.1039/d0en00230e.
151. Ge, C.; Li, Y.; Yin, J.J.; Liu, Y.; Wang, L.; Zhao, Y.; Chen, C. The Contributions of Metal Impurities and Tube Structure to the Toxicity of Carbon Nanotube Materials. *NPG Asia Mater.* **2012**, *4*, e32–e32, doi:10.1038/am.2012.60.

152. Hou, P.X.; Liu, C.; Cheng, H.M. Purification of Carbon Nanotubes. *Carbon N. Y.* **2008**, *46*, 2003–2025, doi:10.1016/j.carbon.2008.09.009.
153. Huang, J.Q.; Zhang, Q.; Zhao, M.Q.; Wei, F. A Review of the Large-Scale Production of Carbon Nanotubes: The Practice of Nanoscale Process Engineering. *Chinese Sci. Bull.* **2012**, *57*, 157–166, doi:10.1007/S11434-011-4879-Z/METRICS.
154. Shuba, M. V.; Paddubskaya, A.G.; Kuzhir, P.P.; Maksimenko, S.A.; Ksenevich, V.K.; Niaura, G.; Seliuta, D.; Kasalynas, I.; Valusis, G. Soft Cutting of Single-Wall Carbon Nanotubes by Low Temperature Ultrasonication in a Mixture of Sulfuric and Nitric Acids. *Nanotechnology* **2012**, *23*, 9, doi:10.1088/0957-4484/23/49/495714.
155. Gong, F.; Liu, J.; Yang, J.; Qin, J.; Yang, Y.; Feng, T.; Liu, W.; Duong, H.M.; Papavassiliou, D. V.; Wu, M. Effective Thermal Transport Properties in Multiphase Biological Systems Containing Carbon Nanomaterials. *RSC Adv.* **2017**, *7*, 13615–13622, doi:10.1039/C6RA27768C.
156. Ding, Y.; Alias, H.; Wen, D.; Williams, R.A. Heat Transfer of Aqueous Suspensions of Carbon Nanotubes (CNT Nanofluids). *Int. J. Heat Mass Transf.* **2006**, *49*, 240–250, doi:10.1016/j.ijheatmasstransfer.2005.07.009.
157. Cui, X.; Wan, B.; Yang, Y.; Ren, X.; Guo, L.-H. Length Effects on the Dynamic Process of Cellular Uptake and Exocytosis of Single-Walled Carbon Nanotubes in Murine Macrophage Cells. *Sci. Rep.* **2017**, *7*, 1518, doi:10.1038/s41598-017-01746-9.
158. Roxbury, D.; Jena, P. V.; Shamay, Y.; Horoszko, C.P.; Heller, D.A. Cell Membrane Proteins Modulate the Carbon Nanotube Optical Bandgap via Surface Charge Accumulation. *ACS Nano* **2016**, *10*, 499–506, doi:10.1021/acsnano.5b05438.
159. Kotchey, G.P.; Zhao, Y.; Kagan, V.E.; Star, A. Peroxidase-Mediated Biodegradation of Carbon Nanotubes in Vitro and in Vivo. *Adv. Drug Deliv. Rev.* **2013**, *65*, 1921–1932, doi:10.1016/j.addr.2013.07.007.
160. Kagan, V.E.; Konduru, N. V.; Feng, W.; Allen, B.L.; Conroy, J.; Volkov, Y.; Vlasova, I.I.; Belikova, N.A.; Yanamala, N.; Kapralov, A.; et al. Carbon Nanotubes Degraded by Neutrophil Myeloperoxidase Induce Less Pulmonary Inflammation. *Nat. Nanotechnol.* **2010**, *5*, 354–359, doi:10.1038/nnano.2010.44.
161. Frangie, C.; Daher, J. Role of Myeloperoxidase in Inflammatioand Atherosclerosis (Review). *Biomed. Reports* **2022**, *16*, 1–11, doi:10.3892/br.2022.1536.
162. Shah, A.; Stenberg, P.; Karvonen, L.; Ali, R.; Honkanen, S.; Lipsanen, H.; Peyghambarian, N.; Kuittinen, M.; Svirko, Y.; Kaplas, T. Pyrolytic Carbon Coated Black Silicon. *Sci. Rep.* **2016**, *6*, 10–15, doi:10.1038/srep25922.
163. Laermer, F.; Urban, A. MEMS at Bosch – Si Plasma Etch Success

Story, History, Applications, and Products. *Plasma Process. Polym.* **2019**, *16*, 1800207, doi:10.1002/ppap.201800207.
164. Blauw, M.A.; Zijlstra, T.; van der Drift, E. Balancing the Etching and Passivation in Time-Multiplexed Deep Dry Etching of Silicon. *J. Vac. Sci. Technol. B Microelectron. Nanom. Struct.* **2001**, *19*, 2930, doi:10.1116/1.1415511.
165. Labelle, C.B.; Opila, R.; Kornblit, A. Plasma Deposition of Fluorocarbon Thin Films from C-C4F8 Using Pulsed and Continuous Rf Excitation. *J. Vac. Sci. Technol. A Vacuum, Surfaces, Film.* **2005**, *23*, 190–196, doi:10.1116/1.1830496.
166. Schneider, C.A.; Rasband, W.S.; Eliceiri, K.W. NIH Image to ImageJ: 25 Years of Image Analysis. *Nat. Methods* **2012**, *9*, 671–675, doi:10.1038/nmeth.2089.
167. Riveline, D.; Zamir, E.; Balaban, N.Q.; Schwarz, U.S.; Ishizaki, T.; Narumiya, S.; Kam, Z.; Geiger, B.; Bershadsky, A.D. Focal Contacts as Mechanosensors: Externally Applied Local Mechanical Force Induces Growth of Focal Contacts by an MDia1-Dependent and ROCK-Independent Mechanism. *J. Cell Biol.* **2001**, *153*, 1175–1185, doi:10.1083/jcb.153.6.1175.
168. Owen, G.R.; Meredith, D.O.; Ap Gwynn, I.; Richards, R.G.; Bongrand, P.; Curtis, A.S.G. Focal Adhesion Quantification - A New Assay of Material Biocompatibility?: Review. *Eur. Cells Mater.* 2005, *9*, 85–96.
169. Simitzi, C.; Stratakis, E.; Fotakis, C.; Athanassakis, I.; Ranella, A. Microconical Silicon Structures Influence NGF-Induced PC12 Cell Morphology. *J. Tissue Eng. Regen. Med.* **2015**, *9*, 424–434, doi:10.1002/term.1853.
170. Sun, C.; Zhang, S.; Wang, J.; Ge, F. Enhancement of SERS Performance Using Hydrophobic or Superhydrophobic Cotton Fabrics. *Surfaces and Interfaces* **2022**, *28*, 101616, doi:10.1016/j.surfin.2021.101616.
171. Capocefalo, A.; Mammucari, D.; Brasili, F.; Fasolato, C.; Bordi, F.; Postorino, P.; Domenici, F. Exploring the Potentiality of a SERS-Active PH Nano-Biosensor. *Front. Chem.* **2019**, *7*, 413, doi:10.3389/fchem.2019.00413.
172. Michota, A.; Bukowska, J. Surface-Enhanced Raman Scattering (SERS) of 4-Mercaptobenzoic Acid on Silver and Gold Substrates. *J. Raman Spectrosc.* **2003**, *34*, 21–25, doi:10.1002/jrs.928.
173. Xu, Y.; Wang, Y.; Chen, Y.; Yue, Y.; Jiang, J. Temperature Dependence of Raman Enhancement Induced by Au Nanorods Array. *Mater. Res. Express* **2018**, *5*, 065057, doi:10.1088/2053-1591/aabab9.
174. Ma, H.; Xu, L.; Tian, Y.; Jiao, A.; Zhang, M.; Li, S.; Chen, M. Design of a Thermally Stable and Highly Active SERS Optical Sensor for the Ultrasensitive Detection of Dye Molecules at High-

Temperature. *Opt. Mater. Express* **2021**, *11*, 2001, doi:10.1364/ome.430061.
175. Rycenga, M.; Wang, Z.; Gordon, E.; Cobley, C.M.; Schwartz, A.G.; Lo, C.S.; Xia, Y. Probing the Photothermal Effect of Gold-Based Nanocages with Surface-Enhanced Raman Scattering (SERS). *Angew. Chemie - Int. Ed.* **2009**, *48*, 9924–9927, doi:10.1002/anie.200904382.
176. Fontana, J.; Livenere, J.; Bezares, F.J.; Caldwell, J.D.; Rendell, R.; Ratna, B.R. Large Surface-Enhanced Raman Scattering from Self-Assembled Gold Nanosphere Monolayers. *Appl. Phys. Lett.* **2013**, *102*, 201606, doi:10.1063/1.4807659.
177. Chen, H.C.; Chen, C.H.; Hsu, C.S.; Chen, T.L.; Liao, M.Y.; Wang, C.C.; Tsai, C.F.; Chen, H.M. In Situ Creation of Surface-Enhanced Raman Scattering Active Au-Auo x Nanostructures through Electrochemical Process for Pigment Detection. *ACS Omega* **2018**, *3*, 16576–16584, doi:10.1021/acsomega.8b02677.
178. Wu, J.; Shi, W.; Chopra, N. Plasma Oxidation Kinetics of Gold Nanoparticles and Their Encapsulation in Graphene Shells by Chemical Vapor Deposition Growth. *J. Phys. Chem. C* **2012**, *116*, 12861–12874, doi:10.1021/jp301009f.
179. Lafuente, M.; Berenschot, E.J.W.; Tiggelaar, R.M.; Rodrigo, S.G.; Mallada, R.; Tas, N.R.; Pina, M.P. Attomolar SERS Detection of Organophosphorous Pesticides Using Silver Mirror–like Micro-Pyramids as Active Substrate. *Microchim. Acta* **2020**, *187*, 1–10, doi:10.1007/s00604-020-4216-9.
180. Golubewa, L.; Kulahava, T.; Timoshchenko, I.; Shuba, M.; Svirko, Y.; Kuzhir, P. Rapid and Delayed Effects of Single-Walled Carbon Nanotubes in Glioma Cells. *Nanotechnology* **2021**, *32*, 505103, doi:10.1088/1361-6528/ac28da.
181. Steiner, R. Laser-Tissue Interactions. In *Laser and IPL Technology in Dermatology and Aesthetic Medicine*; Raulin, C., Karsai, S., Eds.; Springer, Berlin, Heidelberg, 2011; pp. 1–419 ISBN 978-3-642-03437-4.
182. Schneckenburger, H.; Weber, P.; Wagner, M.; Schickinger, S.; Richter, V.; Bruns, T.; Strauss, W.S.L.; Wittig, R. Light Exposure and Cell Viability in Fluorescence Microscopy. *J. Microsc.* **2012**, *245*, 311–318, doi:10.1111/j.1365-2818.2011.03576.x.
183. Prats Mateu, B.; Harreither, E.; Schosserer, M.; Puxbaum, V.; Gludovacz, E.; Borth, N.; Gierlinger, N.; Grillari, J. Label-Free Live Cell Imaging by Confocal Raman Microscopy Identifies CHO Host and Producer Cell Lines. *Biotechnol. J.* **2017**, *12*, 1600037, doi:10.1002/biot.201600037.
184. Rajender, G.; Giri, P.K. Formation Mechanism of Graphene Quantum Dots and Their Edge State Conversion Probed by Photoluminescence and Raman Spectroscopy. *J. Mater. Chem. C*

2016, *4*, 10852–10865, doi:10.1039/c6tc03469a.
185. Das, R.; Parveen, S.; Bora, A.; Giri, P.K. Origin of High Photoluminescence Yield and High SERS Sensitivity of Nitrogen-Doped Graphene Quantum Dots. *Carbon N. Y.* **2020**, *160*, 273–286, doi:10.1016/j.carbon.2020.01.030.
186. Yogesh, G.K.; Shuaib, E.P.; Kalai Priya, A.; Rohini, P.; Anandhan, S.V.; Krishnan, U.M.; Kalyanavalli, V.; Shukla, S.; Sastikumar, D. Synthesis of Water-Soluble Fluorescent Carbon Nanoparticles (CNPs) from Nanosecond Pulsed Laser Ablation in Ethanol. *Opt. Laser Technol.* **2021**, *135*, 106717, doi:10.1016/j.optlastec.2020.106717.
187. Li, Y.; Zhao, Y.; Cheng, H.; Hu, Y.; Shi, G.; Dai, L.; Qu, L. Nitrogen-Doped Graphene Quantum Dots with Oxygen-Rich Functional Groups. *J. Am. Chem. Soc.* **2012**, *134*, 15–18, doi:10.1021/ja206030c.
188. Rajender, G.; Giri, P.K. Formation Mechanism of Graphene Quantum Dots and Their Edge State Conversion Probed by Photoluminescence and Raman Spectroscopy. *J. Mater. Chem. C* **2016**, *4*, 10852–10865, doi:10.1039/c6tc03469a.
189. Sigma-Aldrich Graphene Quantum Dots Aqua Green Luminescent Available online: https://www.sigmaaldrich.com/LT/en/product/aldrich/900712 (accessed on 6 June 2023).
190. Wu, J.; Wang, P.; Wang, F.; Fang, Y. Investigation of the Microstructures of Graphene Quantum Dots (GQDs) by Surface-Enhanced Raman Spectroscopy. *Nanomaterials* **2018**, *8*, doi:10.3390/nano8100864.
191. Yamini, D.; Devanand Venkatasubbu, G.; Kumar, J.; Ramakrishnan, V. Raman Scattering Studies on PEG Functionalized Hydroxyapatite Nanoparticles. *Spectrochim. Acta - Part A Mol. Biomol. Spectrosc.* **2014**, *117*, 299–303, doi:10.1016/j.saa.2013.07.064.
192. Matulaitiene, I.; Barkauskas, J.; Trusovas, R.; Račiukaitis, G.; Mažeikiene, R.; Eicher-Lorka, O.; Niaura, G. Potential Dependence of SERS Spectra of Reduced Graphene Oxide Adsorbed on Self-Assembled Monolayer at Gold Electrode. *Chem. Phys. Lett.* **2013**, *590*, 141–145, doi:10.1016/j.cplett.2013.10.068.

Before all the experiments with analytes and bio-probes, spectra of empty fabricated black silicon substrates were collected (see Figure A1). As it follows from a blue spectrum, some impurities are present even on freshly prepared and stored in N_2 atmosphere samples. Intensity of the bands, which originate from the impurities, increases after a 6h storage of the measured sample exposed to the external environment, as this condition allows more molecules distributed in the air to be adsorbed on the surface of a black silicon sputtered with gold (yellow spectrum in Figure A1). However, these trace impurities do not affect the SERS spectrum of 4-MBA SAM (red line in Figure A1).

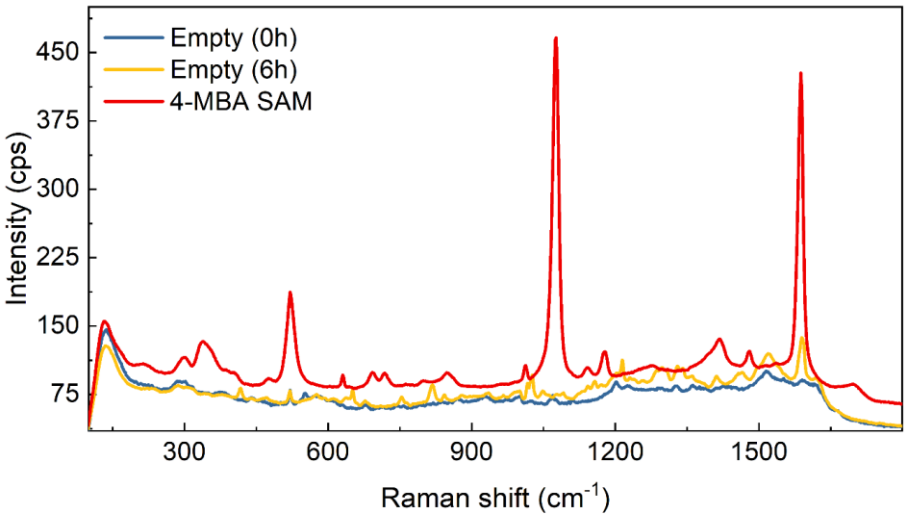

Figure A1. SERS spectra of cone-like black silicon sputtered with gold after 1 day of storage in N_2 atmosphere in hermetically closed package (blue line, "Empty (0h)"), the same sample but exposed to external laboratory environment for 6 h (yellow line, "Empty (6h)") and covered with 4-MBA SAM right after the black silicon sputtering (red line, "4-MBA SAM"). Intensity is given as counts per second.

Experimental determination of 4-MBA SERS spectral stability on the cone-like bSi/Au substrate over a longer time period was also performed (see Figure A2). Measurement of the SERS spectrum of 4-MBA SAM was repeated after 8 months and it was revealed tha both spectra (initial and after 8 months of storing in the air) were of the same intensities for the same samples, performed with identical conditions for SERS spectra collection.

However, there were some changes in the positions of the bands which indicate probable changes due to storage in air and the adsorption of some impurities, which due to their presence modify the way how 4-MBA molecules attache to the surface. Nevertheless, these changes do not affect the SERS substrate efficiency drastically.

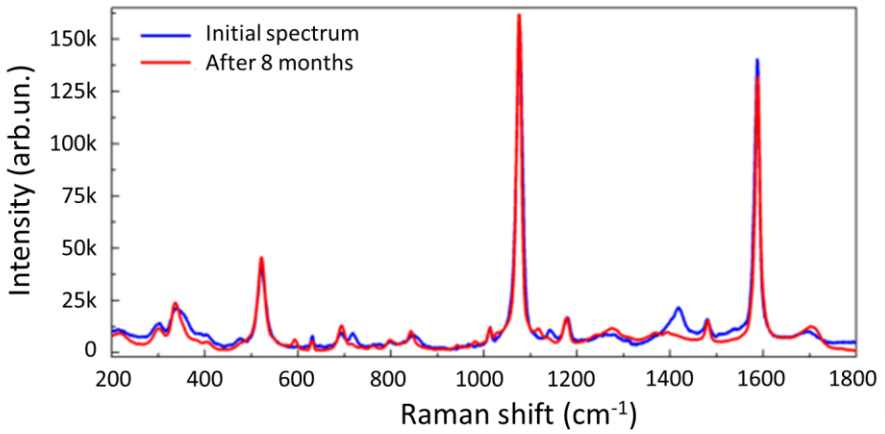

Figure A2. SERS spectra of 4-MBA SAM on the cone-like black silicon sputtered with gold at the time of substrate preparation (blue line) and after 8 months of storing the sample in air atmosphere (in a hermetical package).

The same type of experiment was performed for several simultaneously fabricated lace-like bSi/Au substrates, which were individually packed in plastic Petri dishes, wrapped with a parafilm to avoid accidental contamination, and stored under ambient conditions. These substrates were used to obtain 4-MBA SERS spectra after storage for 1–20 months with the same setup and measurement conditions. The results are summarized in Figure A3. Less than 5% decrease and 40% decrease of the intensities of two characteristic bands at 1076 and 1588 cm^{-1} in the 4-MBA SAM spectra was observed after 120 days and 20 months of storage, respectively. The growth of the intensity of the 2200 cm^{-1} band with time also indicates the increase in the adsorbed CO_2 molecules from the atmosphere.

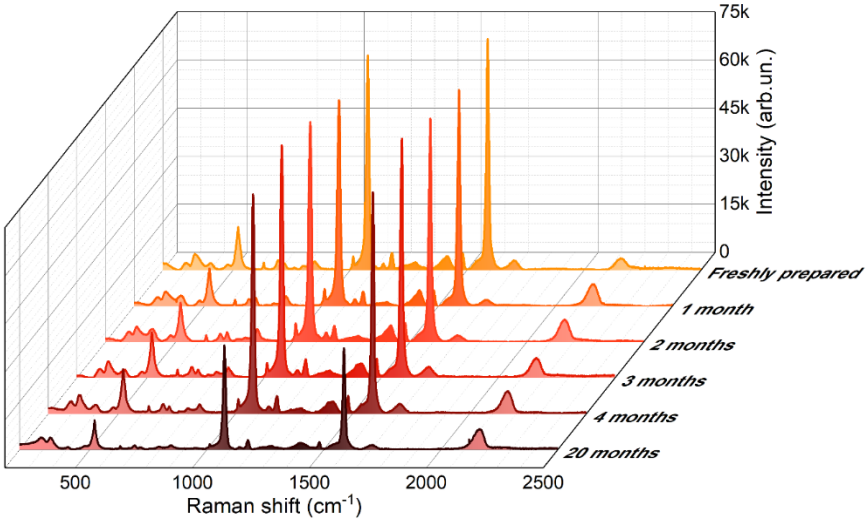

Figure A3. Storage stability of the bSi/Au substrate evaluated with 4-MBA as a probe analyte. Each SERS spectrum corresponds to a 4-MBA monolayer on the surface of freshly manufactured bSi/Au samples and bSi/Au samples stored for 1, 2, 3, 4, and 20 months. Adapted from **Paper (D)**.

SANTRAUKA

Įvadas

Medžiagotyros ir fotonikos mokslai yra svarbūs šiuolaikinėjebiomedicinoje, ir reikšmingai prisideda prie žmonių gerovės gerinimo ir darnaus žmonijos vystymosi. Tarpdisciplinini tyrim yra pasiūlomos naujos medžiagos su unikaliomis savybėmis, tinkamos biojutikliams, skirtiems atskirų ląstelių funkcinei būklei stebėti, ir vaistų, virusų ir bakterijų koncentracijai nustatyti.

Paprastai, "biojutiklio" sąvoka apima: (i) jutimo elementą, skirtą konkrečios analitės detektavimui arba dominančio fizikinio parametro vertės nustatymui; (ii) sąsają, užtikrinančią tinkamą darbo aplinką jutikliui; (iii) keitiklį, skirtą vienos rūšies informacijai paversti kita (pavyzdžiui, analitės molekulės cheminį ryšį su receptoriumi paversti elektros srove); ir (iv) signalo nuskaitymo, stiprinimo, apdorojimo ir analizės sistemą. Pagal fizikinį signalo konversijos mechanizmą biojojutikliai skirstomi į šiuos tipus: elektrocheminius, pjezoelektrinius, kalorimetrinius, šiluminius ir optinius [1]. Pastarasis tipas turi keletą privalumų, palyginti su kitais. Optinis metodas yra mažiausiai invaziškas, nes leidžia surinkti duomenis per nuotolį. Tuo būdu, įmanoma panaudoti, pavyzdžiui, jutiklio elektrines galimybes, norint nustatyti papildomas analizuojamos sistemos charakteristikas arba valdyti matavimo parametrus, tokius kaip temperatūra.

Paviršiumi sustiprintos Ramano sklaidos spektroskopija (SERS ang. k.) yra patikima optinė jutiklių technologija, tinkama aptikti mažas molekulių koncentracijas [2], pavyzdžiui, pesticidus [3] ir nuodus [4], [4], tirti sąveiką tarp molekulių [5] ir/arba tarp molekulių ir biojutiklio substrato [6]. Pastaruoju metu, SERS taikymų laukas prasiplėtė s nuo fundamentinių tyrimų iki praktinio panaudojimo biomedicinoje [7], kriminalistikoje [8], aplinkosaugoje [9] ir saugume [10]. SERS suteikia specifinę informaciją apie analitę, įskaitant jos struktūrą ir grynumą, o taip pat su aplinka susijusius pokyčius. Pagrindiniai fizikiniai SERS principai apsprendžia jo efektyvumą ir jautrumą net pavienos molekulės lygyje, tačiau praktikoje toks jautrumas sunkiai pasiekiamas dėl tam tikrų kliūčių, susijusių su substratų, skirtų Ramano signalo intensyvumui didinti, gamyba. Tauriųjų metalų nanodalelių, ypač sidabro (Ag), koloidai iš tiesų suteikia išskirtinį Ramano signalo stiprinimą, kai susidaro metalo nanodalelių ir analitės molekulių agregatai, pranokdami daugelį kitų analogų ir leidžia atlikti tyrimus pavienės molekulės lygmenyje. Tačiau stabilumas, atsikartojamumas ir rutininio naudojimo paprastumas [11] yra aukojamas dėl išskirtinio signalo stiprinimo: koloidiniai tirpalai yra nestabilūs [12] ir labai

jautrūs laikymo sąlygoms [13] (temperatūrai, neorganinių druskų priemaišoms, purtymui, tiesioginei šviesai ir kt.).

Kitas būdas gaminti SERS substratus yra imobilizuoti plazmonines nanodaleles ant nanostruktūrinių paviršių, nusodinant jas iš koloidinių tirpalų arba formuojant aukso [14] arba sidabro purškimo, garinimo ar cheminio nusodinimo būdu. Tai leidžia tolygų padengimą, didelius naudingus plotus, kontroliuoti karštų taškų tankį, bet Ramano signalo stiprinimas yra vidutiniškas, ir aušti gaminimo kaštai. Taigi, SERS substratų, stiprinančių Ramano signalo intensyvumą, projektavimas ir gamyba dažnai yra kompromisas tarp stabilumo, sąnaudų, patikimumo, homogeniškumo ir substrato dydžio iš vienos pusės ir efektyvumo bei Ramano signalo stiprinimo iš kitos pusės.

Medžiagos, skirtos biojutikliams, turi atitikti keletą funkcinių ir saugos reikalavimų [1]. Nesvarbu, koks yra galutinis tikslas (ar tai būtų biologinio jutimo sistema ar tam tikra struktūra įmontuota į žmogaus kūną), turi būti kontroliuojami: (i) substrato morfologija, (ii) fizikinės savybės (klampumas, standumas, poringumas ir kt.) [15], ir (iii) biocheminės savybės (cheminis stabilumas, biosuderinamumas, gimiringumas ir kt.) [16], kad būtų pasiektas aukštas jutimo našumas ir galimybė integruoti šią medžiagą į sudėtingesnius įrenginius. Dėl silicio mikroelektronikos dominavimo suderinamumas su silicio fotonika yra labai sveikintinas technologiniu požiūriu [17].

Silicis yra akivaizdžiausias kandidatas naudoti jį kaip biojutiklio substratą. Jis jau buvo naudojamas kaip substratas plazmoninėms tauriųjų metalų nanodalelėms [18]. Silicio paviršiaus mikrostruktūra gali suteikti medžiagai naujų optinių savybių, tokių kaip padidinta sugertis ir atspindžio slopinamas, o tai savo ruožtu gali būti panaudota nanoplazmoniniams taikymams, įskaitant SERS. Silicis su modifikuotu paviršiumi, sudarytu iš piramidžių, adatų, kūgių, skylių, stulpelių, kolonų ir kt., bendrai vadinamas „juoduoju siliciu“. Be padidėjusios šviesos sugerties, specifinė juodojo silicio paviršiaus morfologija, pagal analogiją su raštuotais paviršiais [19], gali prisidėti prie kryptingo ląstelių augimo *in vitro,* o taip pat žymiai padidinti efektyvų paviršiaus plotą, tinkamą karštųjų taškų susidarymui SERS atveju, ir tokiu būdu, gali padėti atsirasti daugybei analitės molekulių prijungimo vietų. Per pastaruosius dešimtmečius buvo atlikta keletas bandymų juodąjį silicį pritaikyti kaip SERS biojutiklį, tačiau jo praktinis panaudojimas susidūrė su tam tikromis kliūtimis. Pirma, buvo įrodyta, kad juodasis silicis yra biologiškai nesuderinamas ir pasižymi antibakterinėmis savybėmis [20]. Antra, tauriųjų metalų sluoksniai, kurių storis svyravo nuo 100 [21] iki daugiau nei 1000 nm [22], vargu ar leidžia gautus substratus laikyti pigiais, prieinamais ir plačiai naudojamais biojutikliais. Nepaisant to, juodasis silicis

vis dar kelia didelį susidomėjimą biologinių jutiklių srityje, nes visas šios medžiagos potencialas vis dar nėra iki galo ištirtas.

Biojutiklių tobulinimas yra įkvėptas žmonių sveikatos ir gerovės reikalavimų. Pasaulio sveikatos organizacijos duomenimis, vėžys yra viena iš pagrindinių žmonių mirties priežasčių visame pasaulyje, nes per pastaruosius metus viena iš šešių mirčių yra dėl šios ligos [23]. Teranostika yra vienas iš perspektyviausių vėžio nustatymo ir gydymo būdų, kai sujungiama diagnostika ir terapija viename konkrečiame nanoagente [24], galinčiame vizualizuoti vėžinį naviką ir jį sunaikinti. Sunaikinimas įvyksta, kai agentą aktyvuoja koks nors specifinis vidinis cheminis veiksnys (pvz., vėžinės ląstelės citoplazmos pH [25]) arba išorinis fizikinis poveikis, toks kaip ultragarsas, švitinimas ir kt. [26]). Šie nanoagentai turi būti veiksmingi ir saugūs bei po tam tikro veikimo laiko turi įvykti jų biologinis skaidymas ir tolesnis pašalinimas iš organizmo. Veiksmingų teranostinių metodų, pagrįstų tokių saugių nanoagentų naudojimu, sukūrimas, paremtas nustatytais jų biologinio skaidymo mechanizmais, užtikrins jų sėkmingą tolimesnį naudojimą.

Nebrangūs, patikimi ir įvairūs juodojo silicio biojutikliai veikiantys SERS principu būtų paklausūs praktinėje biomedicinoje. Jų taikymas galėtų būti nuo tikslaus mažų analičių koncentracijų nustatymo naudojant specifinius zondus iki gyvų ląstelių funkcijų analizės ir terapinio poveikio.

Disertacijos tikslas

Sukurti biologiškai suderinamą, nebrangų, stabilų, patikimą, vienalytį ir keičiamo dydžio juodo silicio substratą, tinkamą SERS jutikliams, keičiant jo paviršiaus geometriją, aukso plazmoninio sluoksnio storį ir vienalitiškumą, detektuoti nanomedžiagas, biomolekules ir gyvas ląsteles.

Disertacijos uždaviniai

Siekiant užsibrėžto tikslo, darbe buvo sprendžiami šie uždaviniai:

1. Nustatyti, kaip juodojo silicio substrato mikro ir nano struktūra, modifikuota keičiant ėsdinimo sąlygas ir padegta įvairiais 2D grafeno pagrindu nanostuktorizuotais paviršiais, veikia ląstelių augimą ir sukibimą, išsaugo ląstelių gyvybingumą.

2. Naudojant biologiškai suderinamą juodojo silicio substratą, padengtą plonu aukso pseudo sluoksniu, įvertinti jo SERS stiprinimo koeficientą, vienalytiškumą ir jautrumą analitei, taip pat įvertinti galimybę išgauti informacijos apie gliomos ląstelių biocheminę sudėtį.

3. Pasitelkus skaitmeninį modeliavimą nustatyti labiausiai tikėtiną elektrinio lauko stiprinimo mechanizmą; paaiškinti eksperimentiškai nustatytą SERS stiprinimo koeficientą, gautą su juoduoju siliciu, padegtu 50 nm storio aukso pseudosluoksniu; nustatyti juodojo silicio substrato morfologijos bei auksu padegto sluoksnio storio įtaką SERS signalo stiprumui.

4. Ištirti anglies pagrindu pagamintų nanomedžiagų sąveikos su vėžinėmis ir imuninėmis ląstelėmis mechanizmus bei nustatyti šių nanomedžiagų biodegradacijos mechanizmą po jų išsiskyrimo iš pažeistų ląstelių, naudojant juodojo silicio SERS substratą.

Ginamieji teiginiai

1. Juodojo silicio paviršiaus mikrostruktūra, nano ir mikro šiurkštumas yra lemiami gamybos proceso. Pagaminti kriogeniniu ICP-RIE būdu paviršiai yra hidrofiliniai, jų nanostruktūros yra kūgio formos, . Jie tinka gyvų ląstelių analizei. Pagaminti RT ICP-RIE būdu paviršiai yra hidrofobiniai ir su tankiomis, nėrinius primenančiomis, silicio nanostruktūromis. Jie tinka analitiniam naudojimui.

2. Kūgio formos juodojo silicio substrato paviršius, pagamintas kriogeniniu reaktyviųjų jonų ėsdinimo būdu ir padengtas 50-nm aukso pseudosluoksniu, turi 10^8 stiprinimo koeficientą ir yra tinkamas gyvų ląstelių tyrimui.

3. Silicio pagrindas su juodojo silicio/aukso struktūromis bei 3D erdviniu aukso nanostruktūrų pasiskirstymu suteikia SERS substratui smarkiai išreikštą optinį rezonansą 700–800 nm diapazone, kuris gali būti dar labiau pastumtas į raudoną spektro pusę, ploninant aukso pseudosluoksnį iki kelių dešimties nanometrų.

4. Vėžio ląsteles galima sunaikinti taikant fotoakustinį mechanizmą, kuris pagristas sąveika tarp pikosekundinės lazerinės spinduliuotės ir anglies nanomedžiagų aglomeratų, kurie vėliau, suaktyvėjus neutrofilams, yra biologiškai skaidomi hipochlorito sukelto mechanizmo, atskleisto naudojant SERS aktyvų juodojo silicio padegto aukso nanosluoksniu substratą.

Darbo naujumas ir aktualumas

Šio darbo metu buvo pagamintas biologiškai suderinamas juodojo silicio substratas ir pirmą kartą pritaikytas gyvų (nefiksuotų) ląstelių SERS analizei, išplečiant juodojo silicio taikymą biojutikliams. Toks juodojo silicio naudojimo išplėtimas biojutikliams buvo paremtas skaitmeninio modeliavimo rezultatais, iš kurių atrodė, kad juodas silicis, padengtas itin plonu aukso

sluoksniu, turėtų gerai stiprinti SERS signalą. Juodojo silicio substratai, padengti 10 nm storio aukso sluoksniu, yra gerokai pigesni gaminti, o silicio/aukso nanostruktūros pastumia plazmono rezonansą į NIR ir užtikrina signalo stiprinimą iki EF 10^6-10^8, pranokstant daugelį esamų SERS substratų. Atlikome eksperimentinį tyrimą, siekdami išbandyti šalto fototermoakustinio vėžio ląstelių naikinimo koncepciją fotoaktyvuojant SWCNT aglomeratų generuojamas akustines bangas, o tai patvirtina teorines prognozes. Šie duomenys sudaro prielaidas kurti naują teranostikos kryptį, susijusią su konkrečiais nanoagentais. Jų savybes reguliuoja ir lemia vėžinės ląstelės mikroaplinka, nanoagentai aktyvuojami NIR šviesa, kuri gali efektyviai sunaikinti naviką, išvengiant nepageidaujamos gretimų sveikų audinių hipertermijos. Naudodami juodojo silicio pagrindu sukurtą SERS substratą, atskleidėme struktūrinius pokyčius, atsirandančius anglies nanomedžiagose, kai jos sąveikauja su imuninės sistemos ląstelėmis. Pasiūlėme anglies nanomedžiagų biologinio skaidymo mechanizmą, kuriame dalyvauja hipochlorinė rūgštis , ir tuo būdų parodėme jų tinkamumą vėžio gydymui. Gauti rezultatai atveria kelią pereiti nuo sudėtingų ir brangių laboratorinių tyrimų prie plataus ir prieinamo SERS metodo taikymo praktikoje. Sukurtas pigus, bet stabilus, patikimas ir efektyvus juodojo silicio pagrindu pagamintas SERS substratas tinka įvairiems tikslams, pradedant nuo mažų analitės koncentracijos nustatymo iki anglies nanomedžiagų struktūros ir gyvų ląstelių funkcionavimo analizės.

Metodika

Trys juodojo silicio kartos buvo pagamintos naudojant (i) kriogeninį induktyviai susietą plazmos reaktyvųjį jonų ėsdinimą (ICP-RIE ang. k.), (ii) be kaukinį kambario temperatūros (RT ang. k.) ICP-RIE ir (iii) savaime užmaskuotą RT ICP-RIE. 10–80 nm storio aukso sluoksniai buvo nusodinami magnetrono.

Visi matavimai, susiję su skirtingų kartų juodojo silicio substratų SERS taikymu, buvo atlikti naudojant Ramano spektroskopiją ir Ramano lazerinę skenavimo mikroskopiją. Pagamintų medžiagų paviršiaus morfologijos analizei buvo naudojama skenuojanti elektroninė mikroskopija. Gyvų ląstelių tyrimai buvo atlikti naudojant plataus lauko fluorescencinę mikroskopiją, naudojant įvairius fluorescencinius dažus, nudažytus antikūnus ir kvantinius taškus, siekiant nustatyti specifinių ląstelių savybių ar funkcijų modifikaciją. Koherentinės ant-Stokso spektroskopijos (CARS ang. k.) vaizdavimo metodas buvo naudojamas gyvų ląstelių, sukaupusių SWCNT, vizualizavimui ir

stimuliavimui pikosekundiniais lazerio impulsais, sukėlusiais SWCNT aglomeratų fotoakustinį aktyvumą ir vėžio ląstelių sunaikinimą.

Diskusija ir išvados

1. Juodojo silicio substrato paviršius su nano- ir (arba) mikrostruktūra padengtas pirolitinės anglies (PyC ang. k.) plėvele arba grafeno nanosienelių agregatų plėvele, sudaryta iš grafeno dribsnių, orientuotų statmenai substrato paviršiaus, lemia ląstelių gyvybingumą, reguliuojant ląstelių sukibimą, plitimą ir morfologiją. **Kūgio formos juodojo silicio substratas**, pagamintas kriogeniniu ICP-RIE būdu, demonstruoja gerą biologinį suderinamumą, išsaugo ląstelių proliferacijos greitį, veleno formos morfologiją ir tarpląstelinių kontaktų formavimąsi, todėl yra perspektyvus naudoti biologinių jutiklių srityje. Kūgio pavidalo juodojo silicio padengimas PyC plėvele susilpnina ląstelių sukibimą su substrato paviršiumi ir, atitinkamai, proliferacijos greitį, tačiau nepaisant to tokia danga lieka ląstelėms nekenksminga ir gali būti naudojama be poli-l-lizino ar kitų biopolimerų, kontroliuojančių ląstelių adheziją. Į **nėrinius panašus juodasis silicis**, pagamintas RT ICP-RIE būdu, kaip ir padengtas grafeno nanosienelių agregatų sluoksniu yra labai hidrofobiškas ir biologiškai nesuderinamas dėl specifinio nano šiurkštumo ir aštrių kraštų. Nepaisant to, į nėrinius panašus juodas silicis gali būti taikomas analitiniams tikslams.

2. **Kūgio formos juodojo silicio substratas**, padengtas 80 nm aukso sluoksniu, yra tinkamas organinių molekulių ir gyvų ląstelių SERS, leidžia vizualizuoti būdingas nukleino rūgščių, baltymų ir lipidų juostas „pirštų antspaudų“ srityje, naudojant mažą sužadinimo intensyvumą ir trumpą kaupinimo laiką. Kūgio pavidalo juodojo silicio paviršius pasižymi dideliu jautrumu ir aukštu stiprinimo koeficientu (EF ang. k.) $EF = 10^8$ bei mažesniu nei 13% Ramano signalo santykiniu standartiniu nuokrypiu, kuris pasiekiamas tankiai paskirstant skirtingų formų aukso nanostruktūras tarp submikroninių įprastų silicio kūgių, tolygiai paskirstytus visame paviršiuje.

3. Baigtinių elementų metodu (FEM ang. k.) modeliuota plokščios bangos sąveika su įvairiomis kūgio formos aukso ir silicio/aukso nanostruktūromis, patvirtno eksperimentiškai gautą tokio tipo juodojo silicio stiprinimo koeficientą. FEM modeliavimas atskleidė lokalų paviršiaus plazmonų rezonanso buvimą NIR spektrinėje srityje kai kurioms analizuotoms struktūroms. Remiantis $|E|^4$ aproksimacija, skaitiniu būdu įvertintas modeliuojamų struktūrų elektromagnetinio lauko stiprinimas su NIR sužadinimu buvo 10^7, o dominuojančią įtaką turėjo tarpo tarp persidengiančių bi-sferų ir Si@Au dalelytės padidėjimas. Si@Au struktūrų

aukso sluoksnio storio mažėjimo ir atstumo padidėjimo tarp aukso nanodalelių modeliavimas parodė galimybę toliau sumažinti aukso sluoksnio storį ir padidinti silicio struktūras praktiškai neprarandant stiprinimo efektyvumo dirbant NIR diapazone. Ši teorinė prognozė buvo panaudota kuriant naujos kartos optimizuotą į nėrinius ir stulpus panašų juodą silicį, naudojant supaprastintą ICP-RIE technologiją su itin sumažintu aukso pseudo sluoksniu, rodančiu gerą SERS našumą.

4. Į nėrinius panašus juodas silicis su plonu auksiniu pseudosluoksniu, pagamintas RT ICP-RIE (10 min ėsdinimas), turi SERS EF = 10^6 . Pagaminti substratai yra vienalyčiai (su mažesniu nei 6% SERS signalo svyravimu 100 × 100 μm^2 plote) ir patvarūs, nes laikant šiuos substratus įprastoje aplinkoje SERS signalas sumažėja mažiau nei 3% per 1 mėnesį ir ne daugiau kaip 40% per 20 mėnesių. Nėrinius primenantis juodas silicis su plonu nanometriniu aukso pseudosluoksniu gali būti pakartotinai naudojamas po deguonies plazmos valymo. Po mažiausiai 10 valymo ciklu, Ramano signalo intensyvumas sumažėja per eilę. Juodojo silicio pakartotinis panaudojimas buvo parodytas tiek kovalentiškai jungiančioms molekulėms (4-MBA), tiek adsorbuotoms chemoterapinio vaisto doksorubicino molekulėms, kurios nesudaro kovalentinio ryšio su SERS paviršiumi. Juodojo silicio pagrindu pagaminti SERS substratai yra stabilūs, ir dėl to gali būti naudojami daug kartų, yra patikimi, ir ilgaamžiški. Jų gamyba nebrangi ir dėl to šio tipo nano-/mikrostruktūrines medžiagos yra perspektyvus įrankis atliekant įprastinius tyrimus įvairiose mokslo ir sveikatos priežiūros srityse.

5. Vienasieniai anglies nanovamzdeliai (SWCNT ang. k.) yra tinkamos nanomedžiagos veiksmingai vėžio diagnostikai ir terapijai. Veiksmingas SWCNT kaupimasis vėžio ląstelėse santykinai didelių konkglomeratų pavidalu leidžia vaizdinti vėžines ląsteles Ramano mikroskopu, taikant nuolatinį NIR lazerinį sužadinimą, ir šviesa sukeltą vėžio ląstelių sunaikinimą naudojant pikosekundinį lazerio spinduliuotę. Atskiri SWCNT, išsklaidyti tarpląstelinėje aplinkoje, nėra fotoakustiškai aktyvūs apšviečiant ta pačia pikosekundine lazerine spinduliuote. Tai apibrėžia metodo selektyvumą: sunaikinamos tik tos lasteles, kuriose, susikaupę SWCNT aglomeratai citoplazmoje dėl ląstelių endocitinio aktyvumo, o atskiri nanovamzdeliai, esantys tarpląstelinėje aplinkoje, nesukelia žalingo poveikio gretimiems skysčiams ir audiniams.

6. Modelinės anglies nanomedžiagos, grafeno kvantinių taškų (GQDs ang. k.), SERS analizė, atlikta panaudojus į nėrinius panašų juodojo silicio substratą, padengtą plonu aukso pseudosluoksniu, kartu su kitais spektroskopiniais metodais leido atskleisti anglies nanomedžiagų biologinio skaidymo mechanizmą. GQD sukelia neutrofilų, pirmosios eilės imuninės

sistemos gynybos ląstelių, aktyvavimą, kartu su mieloperoksidazės išsiskyrimu. Dėl to susidaro hipochloro rūgštis, daugiausia atidarius epoksido žiedą C – O – C, dėl to GQD struktūra sutrikdoma, susidaro per daug C=O jungčių ir pažeidžiama GQD anglies karkasas. Gauti rezultatai atskleidžia vėžio terapijoje naudojamų grafeno pagrindu pagamintų nanomedžiagų evoliuciją po gydymo procedūros, atskleidžia jų pašalinimo mechanizmą ir taip palaiko jų gyvybingumą. Šie duomenys parodo juodojo silicio SERS substratų efektyvumą sprendžiant praktinius biomedicinos srities klausimus.

Autoriaus indelis:

Didžiąją dalį eksperimentinių darbų, t.y. duomenų rinkimą ir jų analizę, mokslinių publikacijų rašymą atliko doktorantė. Visus tyrimus, su gyvomis ląstelėmis atliko doktorantė. Ramano matavimai atlikti FTMC Organinės chemijos skyriuje dalyvaujant Dr. Ievai Matulaitienei ir Alenai Klimovič. Juodojo silicio SEM atliko Dr. Algirdas Selskis dirbantis FTMC Medžiagų struktūrinės analizės skyriuje. Juodojo silicio bandiniai buvo pagaminti bendradarbiaujant su Rytų Suomijos universiteto Fotonikos mokslo centre (Joensuu, Suomija) kartu su Marina Fetisova ir Hamza Rehman. Fluorescencinės ir CARS mikroskopijos matavimai buvo atlikti kartu su dr. Danieliu Rutkausku ir dr. Andrejumi Dementjevu.

Apie autorių

Lena Golubewa gimė 1987 metais Minske, Baltarusijoje. 2005 metais ji baigė Minsko gimnaziją nr. 146 ir pradėjo mokytis Fizikos fakultete Baltarusijos valstybiniame universitete (Minskas, Baltarusija). 2010 metais ji įgijo bakalauro laipsnį (specialistė, 5 metų studijos) *cum Laude*, o 2011 metais – magistro laipsnį *cum Laude* biofizikoje. Po studijų dirbo jaunesniaja, o vėliau vyresniaja dėstytoja Baltarusijos valstybiniame universitete. Stažavosi Meksikoje (2 mėn. 2015 m.) bei JAV (1 mėn. 2016 m.) mokslinėse laboratorijose. 2019 metais ji pradėjo doktorantūros studijas Valstybiniame mokslinių tyrimų institute Fizinių ir technologijos mokslų centre.

LIST OF PUBLICATIONS

This thesis is based on the results that were published in the following peer reviewed scientific papers:

(A) **Golubewa, L.**; Rehman, H.; Kulahava, T.; Karpicz, R.; Baah, M.; Kaplas, T.; Shah, A.; Malykhin, S.; Obraztsov, A.; Rutkauskas, D.; Jankunec, M.; Matulaitienė, I.; Selskis, A.; Denisov, A.; Svirko, Y.; Kuzhir, P. Macro-, Micro-and Nano-Roughness of Carbon-Based Interface with the Living Cells: Towards a Versatile Bio-Sensing Platform. *Sensors* **2020**, *20* (18), 1–14. https://doi.org/10.3390/s20185028.

(B) **Golubewa, L.**; Karpicz, R.; Matulaitiene, I.; Selskis, A.; Rutkauskas, D.; Pushkarchuk, A.; Khlopina, T.; Michels, D.; Lyakhov, D.; Kulahava, T.; Shah, A.; Svirko, Y.; Kuzhir, P. Surface-Enhanced Raman Spectroscopy of Organic Molecules and Living Cells with Gold-Plated Black Silicon. *ACS Appl. Mater. Interfaces* **2020**, *12* (45), 50971–50984. https://doi.org/10.1021/acsami.0c13570.

(C) **Golubewa, L.**; Rehman, H.; Padrez, Y.; Basharin, A.; Sumit, S.; Timoshchenko, I.; Karpicz, R.; Svirko, Y.; Kuzhir, P. Black Silicon: Breaking through the Everlasting Cost vs. Effectivity Trade-Off for SERS Substrates. *Materials (Basel)*. **2023**, *16* (5), 1948. https://doi.org/10.3390/MA16051948.

(D) **Golubewa, L.**; Klimovich, A.; Timoshchenko, I.; Padrez, Y.; Fetisova, M.; Rehman, H.; Karvinen, P.; Selskis, A.; Adomavičiūtė-Grabusovė, S.; Matulaitienė, I.; Ramanavicius, A.; Karpicz, R.; Kulahava, T.; Svirko, Y.; Kuzhir, P. Stable and Reusable Lace-like Black Silicon Nanostructures Coated with Nanometer-Thick Gold Films for SERS-Based Sensing. *ACS Appl. Nano Mater.* **2023**, *6* (6), 4770−4781. https://doi.org/10.1021/acsanm.3c00281.

(E) **Golubewa, L.**; Timoshchenko, I.; Romanov, O.; Karpicz, R.; Kulahava, T.; Rutkauskas, D.; Shuba, M.; Dementjev, A.; Svirko, Y.; Kuzhir, P. Single-Walled Carbon Nanotubes as a Photo-Thermo-Acoustic Cancer Theranostic Agent: Theory and Proof of the Concept Experiment. *Sci. Rep.* **2020**, *10* (1), 22174. https://doi.org/10.1038/s41598-020-79238-6.

(F) **Golubewa, L.**; Kulahava, T.; Klimovich, A.; Rutkauskas, D.; Matulaitiene, I.; Karpicz, R.; Belko, N.; Mogilevtsev, D.; Kavalenka, A.; Fetisova, M.; Karvinen, P.; Svirko, Y.; Kuzhir, P. Visualizing Hypochlorous Acid Production by Human Neutrophils with

Fluorescent Graphene Quantum Dots. *Nanotechnology* **2022**, *33*, 15. https://doi.org/10.1088/1361-6528/ac3ce4.

The author contribution

Most of the experimental work, the collection and analysis of data, and the writing of research papers were performed by the PhD candidate. The studies involving the living cells were carried out completely by the PhD candidate. Numerical simulations of the interacion of electromagnetic waves with gold and silicon-gold nanostructures by FEM were performed entirily by the PhD candidate. Raman measurements were carried out with the participation of Dr. Ieva Matulaitene and PhD student Alena Klimovich at the Department of Organic Chemistry of FTMC. SEM of black silicon was performed by Dr. Algirdas Selskis at the Department of Structural Analysis of Materials of FTMC. The black silicon samples were fabricated in collaboration with the Center of Photonics Science, University of Eastern Finland (Joensuu, Finland) by Marina Fetisova and Hamza Rehman. Fluorescence and CARS microscopies were performed together with Dr. Danielis Rutkauskas and Dr. Andrej Dementiev.

Detailed description of the impact of the PhD candidate in each Paper is described below:

Paper A: Biocompatibility assay, cell viability assay, sample preparation, data analysis, paper writing, submission and referee‘s questions answering – **PhD candidate**. Fluorescence microscopy – Danielis Rutkauskas, **PhD candidate**. AFM – Marija Jankunec, **PhD candidate**. Black silicon and PyC fabrication – Rehman, Hamza; Baah, Marian; Kaplas, Tommy; Shah, Ali. Vertical graphene nanowalls fabrication – Malykhin, Sergei; Obraztsov, Alexander. SEM imaging – Algirdas Selskis. Raman measurements of PyC, GNWs, etc. – Hamza Rehman, Ieva Matulaitienė. Supervision, funding, manuscript editing and finalizing – Tatsiana Kulahava, Yuri Svirko, Polina Kuzhir, Renata Karpicz, Andrei Denisov.

Paper B: Experimental data accumulation, data analysis and interpretation, computational electromagnetics, living cell assay, paper writing, paper submission and referee‘s questions answering – **PhD candidate**. Raman and SERS measurements – **PhD candidate**, Ieva Matulaitienė. Fluorescence measurements – Danielis Rutkauskas, **PhD candidate**. SEM imaging – Algirdas Selskis. Black silicon fabrication – Ali Shah. DFT simulations – Aliaksandr Pushkarchuk, Tatsiana Khlopina, Dominik Michels, Dmitry Lyakhov. Supervision, funding, manuscript editing

and finalizing – Tatsiana Kulahava, Yuri Svirko, Polina Kuzhir, Renata Karpicz.

Paper C: Data acquisition – **PhD candidate**, Hamza Rehman. Black silicon fabrication – Hamza Rehman, Sumit Sumit. Data analysis and interpretation – **PhD candidate**, Yaraslau Padrez, Hamza Rehman, Igor Timoshchenko. Simulations – Aleksey Basharin, Polina Kuzhir. Paper drafting – **PhD candidate**, Yaraslau Padrez, Hamza Rehman. Paper submission and editing – **PhD candidate**. Supervision, funding, manuscript editing and finalizing – Tatsiana Kulahava, Yuri Svirko, Polina Kuzhir, Renata Karpicz.

Paper D: Experimental study, Raman and SERS measurements – **PhD candidate**, Aliona Klimovich. Data analysis and interpretation paper writing, paper submission and referee‘s questions answering – **PhD candidate**. Spectral data analysis and statistical studies **PhD candidate**, Igor Timoshchenko, Yaraslau Padrez. Black silicon fabrication – Marina Fetisova, Hamza Rehman, Petri Karvinen. 2D Raman mapping (VU) – Ieva Matulaitienė, Sonata Adomavičiūtė-Grabusove. SEM imaging – Algirdas Selskis. Supervision, funding, manuscript editing and finalizing – Arunas Ramanavicius, Renata Karpicz, Tatsiana Kulahava, Yuri Svirko, Polina Kuzhir.

Paper E: Raman measurements (performed with NanoFinder HE confocal micro-Raman system, BSU, Physics Faculty) – **PhD candidate**. SWCNT-DNA complexes preparation – **PhD candidate**, Mikhail Shuba. All living cell studies – **PhD candidate**. Photo-acoustic theory and simulations – Igor Timoshchenko, Oleg Romanov. Data analysis, paper writing, submission – **PhD candidate**, Igor Timoshchenko. CARS measurements – Andrej Dementijev. Fluorescence microscopy – Danielis Rutkauskas. Supervision, funding, manuscript editing and finalizing – Tatsiana Kulahava, Yuri Svirko, Polina Kuzhir, Renata Karpicz.

Paper F: Experimental data accumulation, data analysis and interpretation, computational electromagnetics, living cell assay, paper writing, paper submission and referee‘s questions answering – **PhD candidate**. Living cell assays – **PhD candidate**, Alena Kavalenka. Fluorescence microscopy assays – **PhD candidate**, Danielis Rutkauskas. ATR-FTIR, Raman and SERS measurements – **PhD candidate**, Aliona klimovich, Ieva Matulaitienė. Black silicon fabrication – Marina Fetisova, Petri Karvinen. Nikita Belko, Dmitry Mogilevtsev – paper editing. Supervision, funding, manuscript editing and finalizing – Tatsiana Kulahava, Yuri Svirko, Polina Kuzhir, Renata Karpicz.

Scientific publications that were not included in the thesis:

(1) **Golubewa, L.**; Kulahava, T.; Kunitskaya, Y.; Bulai, P.; Shuba, M.; Karpicz, R. Enhancement of Single-Walled Carbon Nanotube Accumulation in Glioma Cells Exposed to Low-Strength Electric Field: Promising Approach in Cancer Nanotherapy. *Biochem. Biophys. Res. Commun.* **2020**, *529* (3), 647–651. https://doi.org/10.1016/j.bbrc.2020.06.100.

(2) Chelnokova, I.; **Golubewa, L.**; Starodubtseva, M.; Kulahava, T.; Kunitskaya, Y.; Bulai, P.; Starodubtsev, I.; Kharin, Y.; Shuba, M. Effect of Single-Walled Carbon Nanotubes on the Structural, Physical, and Mechanical Properties of Rat Glial Cell Surface. *J. Nanoparticle Res.* **2020**, *22*, 144, doi:10.1007/s11051-020-04856-0.

(3) **Golubewa, L.**; Kulahava, T.; Leonik, Y.; Shuba, M.; Semenkova, G. Application of Raman Spectroscopy for Studying the Mechanisms of Neutrophil Activation by Carbon Nanotubes. *J. Appl. Spectrosc.* **2021**, *88*, 77–84, doi:10.1007/s10812-021-01143-1.

(4) **Golubewa, L.**; Kulahava, T.; Timoshchenko, I.; Shuba, M.; Svirko, Y.; Kuzhir, P. Rapid and Delayed Effects of Single-Walled Carbon Nanotubes in Glioma Cells. *Nanotechnology* **2021**, *32* (50), 505103. https://doi.org/10.1088/1361-6528/ac28da.

(5) Padrez, Y.; **Golubewa, L.**; Kulahava, T.; Vladimirskaja, T.; Semenkova, G.; Adzerikho, I.; Yatsevich, O.; Amaegberi, N.; Karpicz, R.; Svirko, Y.; Kuzhir, P.; Rutkauskas, D. Quantitative and Qualitative Analysis of Pulmonary Arterial Hypertension Fibrosis Using Wide-Field Second Harmonic Generation Microscopy. *Sci. Reports* **2022**, *12* (1), 1–11. https://doi.org/10.1038/s41598-022-11473-5.

(6) Rehman, H.; **Golubewa, L.**; Basharin, A.; Urbanovic, A.; Lähderanta, E.; Soboleva, E.; Matulaitiene, I.; Jankunec, M.; Svirko, Y.; Kuzhir, P. Fragmented Graphene Synthesized on Dielectric Substrate for THz Applications. *Nanotechnology* **2022**, *33* (39), 395703. https://doi.org/10.1088/1361-6528/ac7403.

(7) **Golubewa, L.**; Padrez, Y.; Malykhin, S.; Kulahava, T.; Shamova, E.; Timoshchenko, I.; Franckevicius, M.; Selskis, A.; Karpicz, R.; Obraztsov, A.; Svirko, Y.; Kuzhir, P. All-Optical Thermometry with NV and SiV Color Centers in Biocompatible Diamond Microneedles. *Adv. Opt. Mater.* **2022**, *10* (15), 2200631. https://doi.org/10.1002/adom.202200631.

(8) Belko, N.; **Golubewa, L.**; Chizhevsky, V.; Karuseichyk, S.; Filimonenko, D.; Jankunec, M.; Rehman, H.; Kulahava, T.; Kuzhir, P.;

Mogilevtsev, D. Hysteresis and Stochastic Fluorescence by Aggregated Ensembles of Graphene Quantum Dots. *J. Phys. Chem. C* **2022**, *126* (25), 10469–10477. https://doi.org/10.1021/acs.jpcc.2c02472.

(9) Padrez, Y.; **Golubewa, L.**; Bahdanava, A.; Jankunec, M.; Matulaitiene, I.; Semenov, D.; Karpicz, R.; Kulahava, T.; Svirko, Y.; Kuzhir, P. Nanodiamond Surface as a Photoluminescent pH Sensor. *Nanotechnology* **2023**, 34 (19), 195702. https://doi.org/10.1088/1361-6528/acb94b.

The results of the thesis were presented at the following conferences:

1. Advanced Materials and Technologies 2020, the 22nd International Conference – School, Palanga, Lithuania, 24-28 August 2020. Poster Presentation: "Black Silicon as an Effective Substrate for Surface-Enhanced Raman Spectroscopy of Organic Molecules and Living Cells".
2. Apropos 17, Vilnius, Lithuania, 30 September – 1 October 2020, Oral Presentation: "Raman Spectroscopic Investigation of Multi-Walled Carbon Nanotubes Mediated Neutrophil Activation".
3. FizTech-2020, Vilnius, Lithuania, 22-23 October 2020. Poster Presentation: "Black Silicon Based Substrate for Surface-Enhanced Raman Spectroscopy of Living Cells". *Awarded as the best Poster Presentation.*
4. Chemistry & Chemical Technology, Vilnius, Lithuania, 24 September 2021. Poster presentation: "Graphene Quantum Dots as Promising Nanostructures for Studying Redox Processes in Neutrophils".
5. FizTech, Vilnius, Lithuania, 20-21 October 2021. Oral presentation: "Gold-coated Black Silicon-Based SERS-Substrate as a Robust and Versatile Bio-Sensing Platform".
6. Advanced Materials and Technologies 2021, the 23rd International Conference – School 23-27 August 2021, Palanga, Lithuania. Poster presentation: "Black Silicon-Based SERS-Active Substrates for Doxorubicin Concentration Determination".
7. DiSetCom Mid-Term Meeting (hybrid participance), Grant agreement ID: 823728, 30 September – 1 October 2021, Finland. Oral presentation: "Interaction of Fluorescent Graphene Quantum Dots with Living Cells: Towards Biosafety, Specific Sensing and Bioimaging".
8. The 16th International conference on nanostructured materials Nano-2022, Seville, Spain, 6-10 June 2022. Oral presentation: "Black Silicon-Based

SERS-Active Substrates for Nanomaterial Characterization and Drug Detection".

9. Hanseatic Workshop on "Exciton Dynamics and Spectroscopy", 24-26 August 2022, Vilnius, Lithuania. Poster presentation: "Single-Walled Carbon Nanotubes for Photo-Thermo-Acoustic Destruction of Cancer Cells".
10. The 8th Workshop on Nanocarbon Photonics and Optoelectronics (NPO2022) Huhmari, Polvijärvi, Finland, 31 July – 5 August 2022. Oral presentation: "Structure Analysis of Carbon Nanomaterials Using Black Silicon-Based SERS Substrate".
11. FizTech-2022, 18-19 October 2022, Vilnius, Lithuania. Oral presentation: "Analysis of Doxorubicin/Graphene Quantum Dot Complex Formation Using Black Silicon-Based SERS Substrate". *Awarded as the best Oral Presentation.*
12. The Annual Scientific Conference of FTMC, 1-2 March 2023, FTMC, Vilnius, Lithuania. Oral presentation: "Black Silicon Covered with Nanometer-Thick Gold Layer for Surface Enhanced Raman Scattering Spectroscopy".

About the author:

Lena was born in Minsk, Belarus. In 2005 she finished Minsk Gymnasium 146 and entered the Faculty of Physics of Belarusian State University (Minsk, Belarus). In 2010 she got Bachelor degree (specialist, 5-year study) cum Laude and in 2011 – Master degree cum Laude in biophysics. Beginning from 2011, she worked as a junior and then a senior lecturer at the Department of Higher Mathematics and Mathematical Physics, Faculty of Physics, Belarusian State University. During the work in BSU, she interned in scientific laboratories in Mexico (2 months in 2015) and in the USA (1 month in 2016). In 2019 she started her PhD studies at the State research institute Center for Physical Sciences and Technology.

COPIES OF PUBLICATIONS

sensors

MDPI

Article

Macro-, Micro- and Nano-Roughness of Carbon-Based Interface with the Living Cells: Towards a Versatile Bio-Sensing Platform

Lena Golubewa [1,2], Hamza Rehman [3], Tatsiana Kulahava [2,4], Renata Karpicz [1], Marian Baah [3], Tommy Kaplas [3], Ali Shah [5], Sergei Malykhin [3,6,7], Alexander Obraztsov [3,7], Danielis Rutkauskas [1], Marija Jankunec [8], Ieva Matulaitienė [1], Algirdas Selskis [1], Andrei Denisov [4,9], Yuri Svirko [3] and Polina Kuzhir [2,3,*]

1 Center for Physical Sciences and Technology, Sauletekio Ave. 3, LT-10257 Vilnius, Lithuania; lena.golubewa@ftmc.lt (L.G.); renata.karpicz@ftmc.lt (R.K.); danielis@ar.fi.lt (D.R.); ieva.matulaitiene@ftmc.lt (I.M.); algirdas.selskis@ftmc.lt (A.S.)
2 Institute for Nuclear Problems, Belarusian State University, Bobruiskaya 11, 220030 Minsk, Belarus; tatyana_kulagova@tut.by
3 Institute of Photonics, University of Eastern Finland, Yliopistokatu 2, FI-80100 Joensuu, Finland; hamzar@uef.fi (H.R.); marian.baah@uef.fi (M.B.); tommi.kaplas@gmail.com (T.K.); sergeim@uef.fi (S.M.); alexander.obraztsov@uef.fi (A.O.); yuri.svirko@uef.fi (Y.S.)
4 Department of Biophysics, Belarusian State University, Nezavisimosti Ave. 4, 220030 Minsk, Belarus; denisov@bsu.by
5 Department of Micro and Nanosciences, Aalto University, FI-00076 Espoo, P.O. Box 13500, Finland; ali.shah07@outlook.com
6 Division of Solid State Physics, Lebedev Physical Institute of the Russian Academy of Sciences, Leninskiy Prospekt 53, 119991 Moscow, Russia
7 Department of Physics, Lomonosov Moscow State University, Leninskie gory 1–2, 119991 Moscow, Russia
8 Institute of Biochemistry, Life Sciences Center, Vilnius University, Sauletekio Ave. 7, LT-10257 Vilnius, Lithuania; marija.jankunec@gmc.vu.lt
9 Institute of Physiology of the National Academy of Sciences of Belarus, Minsk, Belarus, 28 Akademichnaya Str., BY-220072 Minsk, Belarus
* Correspondence: polina.kuzhir@uef.fi

Received: 30 July 2020; Accepted: 2 September 2020; Published: 4 September 2020

Abstract: Integration of living cells with nonbiological surfaces (substrates) of sensors, scaffolds, and implants implies severe restrictions on the interface quality and properties, which broadly cover all elements of the interaction between the living and artificial systems (materials, surface modifications, drug-eluting coatings, etc.). Substrate materials must support cellular viability, preserve sterility, and at the same time allow real-time analysis and control of cellular activity. We have compared new substrates based on graphene and pyrolytic carbon (PyC) for the cultivation of living cells. These are PyC films of nanometer thickness deposited on SiO_2 and black silicon and graphene nanowall films composed of graphene flakes oriented perpendicular to the Si substrate. The structure, morphology, and interface properties of these substrates are analyzed in terms of their biocompatibility. The PyC demonstrates interface biocompatibility, promising for controlling cell proliferation and directional intercellular contact formation while as-grown graphene walls possess high hydrophobicity and poor biocompatibility. By performing experiments with C6 glioma cells we discovered that PyC is a cell-friendly coating that can be used without poly-L-lysine or other biopolymers for controlling cell adhesion. Thus, the opportunity to easily control the physical/chemical properties and nanotopography makes the PyC films a perfect candidate for the development of biosensors and 3D bioscaffolds.

Keywords: pyrolytic carbon; graphene; graphene nanowalls; black silicon; glioma cells; biocompatibility

1. Introduction

The importance of cell–surface contact for the living cell functioning has been known for decades. For example, for granulocytes, surface contact regulates the production of superoxide which is one of the milestones in immune response [1]. Similarly, neutrophils recruitment for the host defense via the inflammatory response is also initiated by cell adhesion and eventual migration through the vascular wall [2], and platelet activation and aggregation during blood vessel injury in the arterial circuit is triggered through the interaction of immobilized vWF with GPIb receptors after adhesion [3]. Extrinsic signals from the stem cell niche regulate neural stem/progenitor cells self-renewal [4] and the time course of neural stem cell fate determination [5]. Binding of the cell to the extracellular matrix and other cells connecting them with the surroundings play a crucial role in stem cell development including proliferation, differentiation, and migration, involved in organism repair processes. Thus, tuning the cell–surface interaction has tremendous potential in treating various disorders and injuries.

Cell–surface interactions and signaling events are two closely related processes. Among the main characteristics of the substrate responsible for its interaction with cells are (i) physical properties (stiffness, viscoelasticity, porosity, etc.), (ii) morphology (scaffold dimensionality (2D or 3D); thickness; area, shape, microscale topography of cell adhesion surface and nanotopography), and (iii) biochemical characteristics (affinity, the specificity of epitope interaction with cell receptors, nonaffinity domains, supramolecular organization, etc.) [6].

All these factors should be taken into account when integrating new materials in biosensors, scaffolds, implants, etc. toward cell or tissue regulation and engineering. Unfavorable reactions due to tissue scar [7] and unstable mechanical and electrical properties of silicon, which is conventionally used in the implants for the monitoring and regeneration of neurons, for instance, fuel the search for a viable alternative among both newly developed and traditional materials. The key requirements for the material to be met are biocompatibility, the possibility of using them as scaffolds for 3D cell growth (for tissue reconstruction), and the potential for biosensing platforms. Finding such materials, which should provide ample opportunities for the development of effective biocompatible sensing systems for monitoring cell activity, implies an analysis of surface properties and revealing the correlation between specific surface parameters and cell functional state.

Along with self-assembled monolayers and covalently bound peptides [8,9], carbon nanomaterials are being considered as a very promising candidate in the cultivation of living cells [10–12] and tissue engineering. Their advantageous—for bio-engineering—properties are the following: (i) they do not trigger unwanted reactions being injected into the tissue, (ii) they prevent blood clotting and exhibit good durability, (iii) they are robust and wear-resistant [13]. For instance, carbon nanotube-layered substrates are biocompatible and efficient in inducing stem cell differentiation, specifically to neurons [14], promoting neurite outgrowth and enhancing synaptogenesis [15] and consequential development of neuronal network [16].

Graphene promotes the growth and differentiation of stem cells into neurons offering a very attractive strategy for the treatment of neuronal injuries [17]. It has been also found that coating surfaces with graphene results in the acceleration—in comparison with bare surfaces—of stem cell growth [18]. Pristine graphene offers better electrical conductivity and further enhances the electric field of the cell; therefore, it is promising for cell culture and regeneration [19].

Three-dimensional (3D) graphene foam synthesized by chemical vapor deposition (CVD), which is biocompatible and shows no toxicity whatsoever, can be used as a conductive scaffold for neural stem cells [20]. The ripples and wrinkles on the surface of 3D graphene foams facilitate better interlocking of the cell with substrate stimulating proliferation and assisting the neural cell differentiation.

It is important to ensure the growth and functioning of cells on such surfaces of sensors. This biocompatible approach allows fulfilling the effective pharmacological screening and the modeling of various forms of various diseases in vitro, such as ischemia, trauma, stroke, epilepsy, Alzheimer's disease, cancer, etc. [21]. On the other hand, microelectrode sensors are used for implantation into the structures of the central nervous system for registration and modulation of physiological processes in vivo. When electrodes are implanted into the brain, an acute reaction is initially observed at the point of contact between the brain tissue and the microelectrode material [22].

Our study was performed with astrocyte-like glioma cells. We concentrate on the creation of the biointerface of carbon nanomaterials and glioma cells to analyze the possibility of directed cell growth without using poly-L-lysine or other biopolymers for controlling cell adhesion. In this paper, we report on the biocompatibility of the surfaces based on graphene nanowalls (GNW) [23] and pyrolytic carbon (PyC) [24]. The GNW film comprises self-assembled graphene flakes with few nanometers thicknesses, which are vertically oriented to the substrate and have the lateral size of a few microns [25]. The PyC film is composed of graphene flakes predominantly parallel to the substrate, which have the lateral size of a few nanometers and are embedded into the amorphous carbon matrix [26].

PyC implants have been already used in human bodies suffering from arthritis, and no side effects have been experienced by the trial subjects [27]. Properties of PyC mostly depend on its synthesis conditions [28]. The combination of prominent electrical properties with relatively good optical characteristics [24], high thermal conductivity [29], and high chemical wear resistance and durability [30] make PyC film a promising coating material for a very broad spectrum of applications, including optical and electrical sensors, lab-on-a-chip schemes, scaffolds, implants, and almost in any device that must function stably in biological environments. Successful efforts have been already made in the creation of patterned PyC and tetrahedral amorphous carbon thin films for biocompatible surfaces [31]. Nevertheless, the question of the effect of surface roughness, as well as its nano and microstructuring on the adhesion of cells to the surface and the rate of their division, remains poorly understood.

Here, we investigated the influence of carbon synthesis conditions and the template/substrate properties on the final bioscaffold biocompatibility. By using different configurations of carbon-based interfaces including GNW on Si wafer, PyC on SiO_2, and PyC-coated black silicon (bSi) we demonstrate that biocompatibility is strongly influenced by the substrate morphology. We show how the micro- and nanostructuring of carbon substrate affects the cell growth and adhesion and prove that the graphene and PyC can control the cell growth and adhesion.

2. Materials and Methods

2.1. Substrate Synthesis

2.1.1. Black Silicon (bSi)

BSi refers to silicon surfaces covered by a layer of "needle" or "pyramidal"-like nano- or microstructures that suppress reflection and enhance the scattering and absorption of light [32,33]. The details of bSi fabrication can be found elsewhere [34]. Briefly, the fabrication of bSi was carried out with an Oxford Instruments Plasmalab system 100-ICP180 which has a double plasma source that allows for the independent control over density and directionality of ions. The plasma is created at a pressure of 13.3 Pa within the temperature range from −150 to 400 °C. Tall bSi pyramid-like structures were obtained at a pressure of 10 mTorr with an SF6 flow rate of 40 sccm, O_2 flow of 18 sccm at −110 °C for 7 min, followed by 7 min of etching.

2.1.2. PyC on SiO_2 and PyC on bSi

PyC deposition on various surfaces might have some limitations, because the coefficient of thermal expansion (CTE) of the coating and the substrate must be similar. Otherwise high-temperature

deposition of PyC on the substrate with the too different CTE from that of PyC will lead to dimensional interferences at room temperature and stresses generation, which will compromise PyC adherence [35]. However, the deposition of PyC on bSi and SiO_2 overcomes this problem as CTE for Si, SiO_2, and PyC is 0.54×10^{-6} K^{-1}, 0.55×10^{-6} $K^{-1,}$ and 0.29×10^{-6} K^{-1} [36], respectively. Moreover, direct deposition and PyC films of different thickness stability were demonstrated in [24].

For this particular study, the PyC films were deposited via CVD on the SiO_2 or bSi substrates. The CVD chamber was sealed with the sample substrate inside, and H_2 was injected for 2 h at a flow rate of 20 sccm and 100 Pa pressure to clean the substrates. Next, the pumping out was stopped and by flowing the H_2, the chamber pressure was increased to approximately 1 kPa. Then, the H_2 flow was stopped, and the CVD chamber was heated to 700 °C in a static H_2 environment. With H_2 already inside, CH_4 was injected into the chamber at 30 and 50 sccm, allowing the chamber pressure to reach approximately 2.44 kPa. The chamber was further heated to 1100 °C at a rate of 10 °C/min. During the procedure, there was no active flow of gasses and the entire process was performed in static conditions. After resting for 5 min, the chamber was cooled down to 700 °C at a rate of 5 °C/min. Then, the CH_4-H_2 mixture was pumped out, replaced with H_2 (20 sccm) at 1 kPa, and allowed to cool overnight. The dependence of the PyC film thickness on CVD synthesis conditions (CH_4 to H_2 concentration ratio, time, and temperature of synthesis) was specified in [26].

The optical properties of PyC films were previously investigated, and major features and characteristics of PyC are reported in [28]. In particular, it was shown that the dielectric permittivity of the PyC films deposited on the silica substrate is quite similar to those obtained for graphite and graphene, allowing the broadcasting of all applications of graphene as a material for optical biosensors on PyC films.

2.1.3. Graphene Nanowalls (GNW)

The GNW films were deposited on a silicon substrate by a plasma-assisted CVD process. CH_4–H_2 mixture with a methane concentration of about 6.5% was activated by DC discharge. The deposition process was carried out within the temperature range from 850 to 1100 °C at 9.6 kPa for about 45 min [37]. In the deposited films, the multilayer graphene flakes of nanometer thickness with atomic layers oriented predominantly along a normal to Si substrate surface, while their lateral size (along substrate surface) and height (along normal to the substrate surface) are of a few microns. Both EDX and electrochemical analysis of graphene nanowalls carried out in [38] did not reveal the presence of any elements other than C (nanowalls themselves), Si (substrate), and O (oxygen on the sample due to exposure to air). The amount of impurities was 0.05–0.06 wt.%, which is less than the minimum detectable by an EDX value of 2000 ppm.

2.2. Structural and Morphological Characterization

2.2.1. Scanning Electron Microscopy (SEM)

SEM micrographs of investigated samples were obtained by a Helios NanoLab 650 microscope (FEI, Netherlands, 2011) with a Schottky type field emission electron source. The cathode current was 25 pA at the tilt angle of 57°. The PyC on SiO_2 samples was coated with chromium to improve the image quality and prevent the overcharging on the surface. The thickness of the PyC layer on SiO_2 and bSi was determined from the lateral cleavage of the sample from SEM images. PyC has a clearly visible interface with a semiconductor/dielectric. Using the built-in SEM software, the thickness of the PyC film was determined at 10 different points, and then the mean value and standard deviation were calculated.

2.2.2. Atomic Force Microscopy (AFM)

AFM imaging was carried out in a tapping mode on a Dimension Icon (Bruker, Santa Barbara, CA, USA) scanning probe microscope system at room temperature (20 ± 0.5 °C) using silicon AFM

probes Multi75AI-G (BudgetSensors, Sofia, Bulgaria), for relatively rough surfaces of bSi with PyC and bSi, and Tap300AI-G (BudgetSensors, Sofia, Bulgaria) for smoother surfaces of PyC on SiO_2. The scans were performed at a 512 pixel or higher resolution with a scan rate of 0.3–0.5 Hz. The imaged area was 2×2 μm. AFM measurements were carried out in at least three replicates.

Roughness parameters were calculated using the Build-In Software NanoScope Analysis version 1.90 (Bruker). According to the NanoScope Analysis 1.90 Manual, the Image R_q is defined as the Root mean square average of height deviations taken from the mean image data plane and can be presented in the following form:

$$R_q = \sqrt{\frac{\sum Z_i^2}{N}} \quad (1)$$

Image R_{max} is the maximum vertical distance between the highest and lowest data points in the image following the planefit. Image Surface Area Difference is the difference between the surface area of the substrate and the area of its projection on the plane.

2.2.3. Raman Spectroscopy

Raman measurements were performed using a Raman spectrometer/microscope inVia (Renishaw, UK). Spectra were analyzed with the custom WIRE software. A 785 nm near-infrared (NIR) laser source was used for all the samples. Objective magnification was 50×. The grating was with 1200 grooves/mm. The power at the sample was adjusted to 1 mW. The exposure time was 10 s, and the spectra were accumulated 3 times in one point to obtain a better signal-to-noise ratio. At least three different points were measured for each sample. The intensity units were counts per second.

2.3. Cell Culture Growth and Visualization

2.3.1. Cell Culture

ATCC C6 (ATCC® CCL-107™) rat glioma cells, obtained from ATCC, LGC Standards, Ogrodowa 27/29, Kielpin, Poland, were used in all experiments. Cells were grown in DMEM/F12 medium (Gibco, Grand Island, NY, USA) supplemented with 10% fetal bovine serum (Sigma Chemical Co., St. Louis, MO, USA) and 80 μg/mL gentamicin sulfate (Belmedpreparaty, Belarus) in 100% humidity at 37 °C in 5% CO_2 atmosphere. In the log-phase cells were trypsinized, centrifuged, and 10^5 cells were seeded in standard 3.5 cm plastic Standard Nunc™ Cell Culture Petri dishes with investigated substrates (bSi, bSi with PyC, SiO_2-PyC (2 types) and GNW) placed on the Petri dish bottom. None of the sample surfaces were treated with poly-L-lysine for additional improvement of cell adhesion to the substrate. Cells were cultured for 3 days. For the measurements, the growth medium was replaced with Hepes buffer solution (pH 7.2) of the following content (in mmol/L): NaCl—131, KCl—5, $MgSO_4$—1.3, $CaCl_2$—1.3, Hepes—20, $C_6H_{12}O_6$—5.

2.3.2. Fluorescence Microscopy

Cell visualization was performed using DNA-staining fluorescent dye propidium iodide (Sigma-Aldrich, Germany). Before each measurement, substrates with cells on them were washed twice with Hepes buffer solution, fixed with ice-cold methanol for 30 min at 4 °C. Then substrates with cells were washed twice in Hepes buffer solution for 10 min each time and once with deionized water. During the measurements, water was replaced with 10^{-6} mol/L propidium iodide solution in Hepes buffer. The excitation wavelength was 532 nm and the emission maximum was 617 nm. The imaged area was 200×200 μm.

2.3.3. Data Analysis

Measurements of average surface area, occupied by cells during their growth on different substrates (confluence), as well as morphological features analysis were performed using specific built-in functions

of the open-source software ImageJ (version 1.51J8). For confluence determination, 7–10 fluorescent images (200 × 200 μm) were analyzed.

The results are expressed as the means ± standard deviations or means ± confidence intervals. Statistical analysis for 7–10 independent samples was conducted using the one-way ANOVA ($p < 0.05$); the statistical significance of the results was analyzed by an unpaired two-tailed Student's *t*-test using Microsoft Office Excel 2010 (Microsoft Corporation, Redmond, Washington, DC, USA) and STATISTICA 6.0 (StatSoft Inc., Tulsa, Oklahoma, OK, USA). Statistical significance is indicated in the table footnote.

3. Results

To characterize the fabricated samples, we employed AFM and SEM imaging (Figure 1). The statistical results of AFM data analysis are summarized in Table 1.

Figure 1b,h show the SEM images of the PyC films of (42 ± 11) nm and (19 ± 7) nm thickness, respectively, deposited on SiO_2. For simplicity, we dubbed samples "PyC (40 nm)" and "PyC (20 nm)", respectively. One can observe that both films are uniform over the substrate, even though from the comparison of the AFM images in Figure 1a,c, it appears that the 40 nm thick film exhibits a grainy structure. The analysis of the AFM data summarized in Table 1 shows that the 20 nm thick PyC film (R_q = 0.9 ± 0.2 nm) was much smoother than the 40 nm thick PyC film (R_q = 2.9 ± 1.3 nm). This can be seen from Figure 1i,c which show the thicknesses of the film as a function of the lateral coordinate. It is worth noting that the 40 nm thick film was much denser than its 20 nm counterpart, which had rather scarce high amplitude peaks.

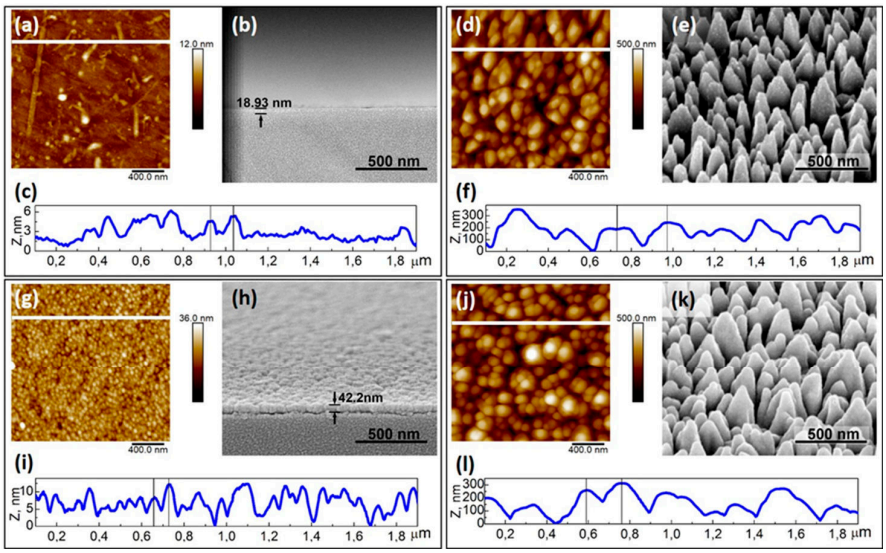

Figure 1. Typical two-dimensional AFM and SEM surface images of PyC of 20 nm (**a**,**b**) and 40 nm thickness (**g**,**h**) on SiO_2, bSi (**d**,**e**), PyC of 20 nm on bSi (**j**,**k**), respectively. PyC layer is marked with arrows (**b**,**h**); (**c**,**f**,**i**,**l**) cross-sectional profiles of PyC (20 nm), bSi, PyC (40 nm), PyC (20 nm) on bSi from (**a**,**d**,**g**,**j**) AFM images, respectively. The cross-sectional profiles are marked with a white line on the AFM images (**a**,**d**,**g**,**j**).

BSi consisted of pyramid-like silicon structures that were randomly distributed through the substrate surface as shown in Figure 1d,e. Figure 1j,k show the bSi coated with a 20 nm thick PyC film. One can observe from Figure 1e,k that a pyramid-like surface structure of the bSi endured PyC film

deposition, even though the apex curvature of the pyramids increased resulting in a much smoother surface. Such a smoothing of the bSi after deposition of the 20 nm thick PyC film is quantitatively described by the decrease in the roughness from 81 ± 12 nm to 75 ± 9 nm (see Table 1). The difference between the maximum and minimum points of the tip position R_{max} also increased after depositing the PyC film. Nevertheless, statistical analysis of two independent datasets (bSi and bSi with PyC) does not allow us to suggest that differences between these datasets are statistically significant.

Table 1. Macroscopic and microscopic roughness of PyC (40 nm), PyC (20 nm) on SiO_2, PyC (20 nm) on bSi and bSi (AFM images analysis).

Parameter	PyC (20 nm) on SiO_2	PyC (40 nm) on SiO_2	bSi	PyC (20 nm) on bSi
Surface Area Difference, %	0.3 ± 0.2	2.9 ± 2.5	136 ± 7	139 ± 9
Image R_q, nm	0.9 ± 0.2	2.9 ± 1.3	81 ± 12	75 ± 9
Image R_{max}, nm	11.2 ± 2.6	42 ± 19	499 ± 12	508 ± 37

Data are presented as the means ± CIs (p = 0.95, n = 10).

In contrast to the PyC, the nanoscale roughness of the GNW film, which consisted of graphene flakes oriented perpendicular to the silicon substrate, was suppressed. In the SEM image of the GNW film surface presented in Figure 2, one can observe that GNWs formed "bushes" of 20 µm in diameter. They were distributed fairly evenly over the entire surface of the substrate (see Figure 2a) and were composed of vertically oriented multilayer graphene flakes (Figure 2b).

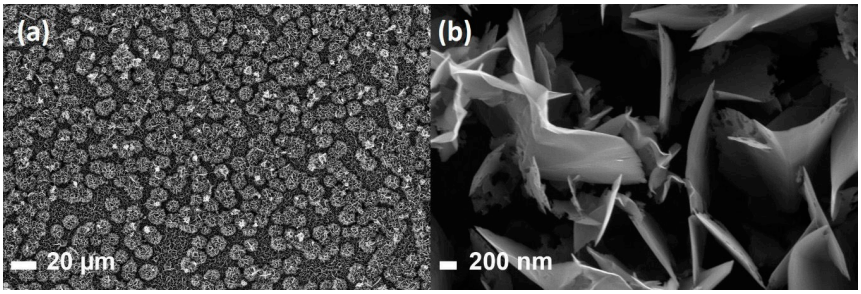

Figure 2. SEM images of graphene nanowalls; (**b**) the enlarged image of the area of "bushes" made of graphene sheets in (**a**).

Raman spectra of the PyC and GNW films are presented in Figure 3, while positions of the D and G peaks are summarized in Table 2. The Raman peaks of the 40 nm thick PyC film were approximately 7 cm^{-1} red-shifted to those of the 20 nm thick PyC film due to an increase in the internal stress in the thicker film [39]. This is because the composition of the pyrolytic carbon film does not depend on its thickness [40]: it comprises the graphene flakes embedded into the amorphous graphene matrix. Since the chemical conditions for the synthesis of the PyC films of different thicknesses were equivalent, the difference in the positions of the peaks caused by surface functionalization, which could occur during the synthesis process, was not expected. Following the theoretical estimations [41], peak displacement is most likely a result of mechanical stresses. Such a conclusion is supported by the fact that there was no shift in the position of the G-mode in the Raman spectrum of the PyC deposited onto SiO_2 and bSi.

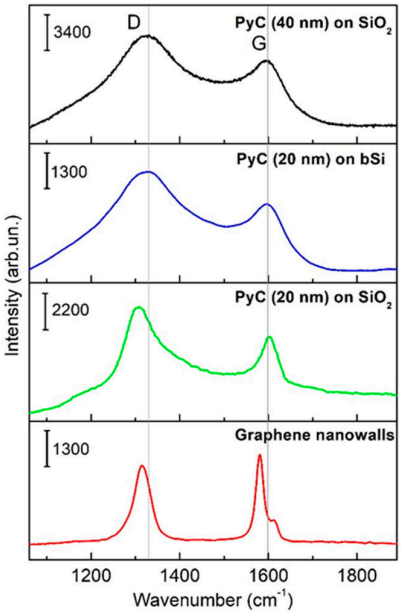

Figure 3. Raman spectra of PyC (40 nm) on SiO_2, PyC (20 nm) on SiO_2, PyC (20 nm) on bSi, and graphene nanowalls. λ_{ex} = 785 nm. Presented spectra are average spectra from triplicates. All scales are marked with corresponding scale bars on each individual spectrum.

Table 2. Raman spectra characteristic modes of carbon multilayered materials deposited on different substrates.

Mode	PyC (40 nm) on SiO_2	PyC (20 nm) on SiO_2	PyC (20 nm) on bSi	GNWs on Flat Si
D mode, cm^{-1}	1322.6 ± 2.1	1307.2 ± 1.3	1322.2 ± 2.2	1314.7 ± 3.1
G mode, cm^{-1}	1595.2 ± 1.8	1602.1 ± 3.4	1595.2 ± 2.6	1580.8 ± 4.7

Data are presented as the means ± SDs of three independent measurements.

Affinity and biocompatibility of the fabricated substrates to living cells were analyzed in terms of average area occupied by cells in culture (confluence), average cell number, the average area per one cell, and morphological features of cells grown on the substrates. The results of the cell morphology analysis on fluorescent images of glioma cells fixed on the substrates (Figure 4) are summarized in Table 3. One can observe from Figure 4a,b that bSi biocompatibility was very similar to standard plastic used for cell culture, even though its surface structure differed from that of the plastic. Cells occupied comparable areas (68.9 ± 28.2% confluence for bSi vs. 63.3 ± 10.3% for plastic) and were spindle-shaped, with numerous processes. At the same time, bSi demonstrated enhanced cell proliferation: on bSi, the number of cells was almost two times larger (53.8 ± 15.2 cells per area for bSi vs. 36.0 ± 3.7 for plastic). Increased proliferation also led to an increase in cell growth density, reducing the area per each cell two times, as can be seen from Table 3.

Thus, rat C6 glioma cells, grown on the bSi as a substrate, demonstrated strong adhesion to the surface, a higher division rate than that obtained on the plastic of the tissue culture-treated dishes. Cells also preserved their usual morphology.

The PyC layer deposition on the bSi modified the adhesive properties of the surface: cell–surface contact became weaker, and as a consequence, the division rate decreased (Figure 4c). Cell confluence

was only 20.7 ± 4.6% vs. 63.3 ± 10.3% in the control and 68.9 ± 28.2% on bSi. However, the surface remained biocompatible, cells preserved their usual morphology, were elongated, spindle-shaped, and with long processes. Their dimensional parameters also remained very similar to the control, even though the percentage of the area per each cell on the PyC on bSi was 80% of the percentage of the area per cell on the plastic (see Table 3).

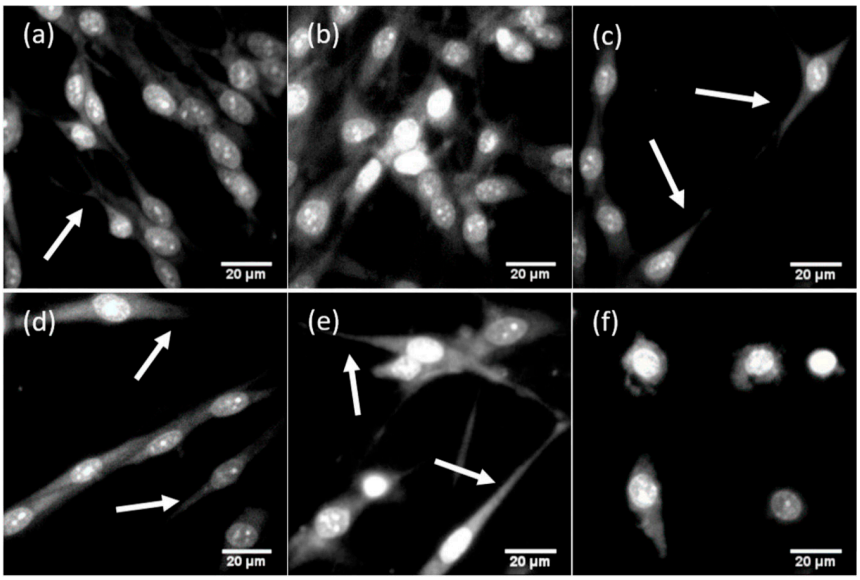

Figure 4. Typical fluorescent images of glioma cells grown on substrates with different roughnesses. Glioma cells were grown on (**a**) plastic (as a control); (**b**) bSi; (**c**) PyC (20 nm) on bSi; (**d**) PyC (20 nm) on SiO_2; (**e**) PyC (40 nm) on SiO_2; (**f**) graphene nanowalls. Long processes are marked with arrows. Cells were stained with propidium iodide. Image size 115 × 115 µm.

Table 3. Cell confluence and morphological features of cells grown onto different substrates.

Parameter	Plastic	PyC (20 nm) on SiO_2	PyC (40 nm) on SiO_2	bSi	PyC (20 nm) on bSi	Graphene Nanowalls
Area occupied by cells, %	63.3 ± 10.3	33.7 ± 7.1 *	55.1 ± 10.3	68.9 ± 28.2	# 20.7 ± 4.6 *	11.6 ± 5.1 *
Area occupied by cells, µm^2	25310 ± 4131	13475 ± 2848 *	22052 ± 4124	27570 ± 11261	# 8271 ± 1855 *	4652 ± 2047 *
Average cell number per 200 × 200 µm area	36.0 ± 3.7	15.6 ± 1.1 *	25.2 ± 2.6 *	53.8 ± 15.2 ***	## 13.0 ± 0.7 *	7.3 ± 0.4 *
Area per cell, %	1.8 ± 0.3	2.2 ± 0.1 **	2.2 ± 0.1 **	1.3 ± 0.3 ***	1.6 ± 0.1	1.6 ± 0.1
Area per cell, µm^2	703 ± 115	864 ± 183 **	875 ± 164 **	513 ± 209 ***	636 ± 143	637 ± 280
Cell morphology characteristics	Elongated, spindle-shaped, 2–3 long processes, numerous intercellular contacts	Elongated, spindle-shaped, 2–3 long thin processes, few intercellular contacts	Elongated, spindle-shaped, 2–3 long thin processes, few intercellular contacts	Spindle-shaped, rounded, many middle-sized processes, many intercellular contacts	Elongated, spindle-shaped, 2–3 long thin processes, few intercellular contacts	Rounded, no processes or short wide processes, no intercellular contacts

Data are presented as the means ± SDs. The statistical significance of the results was analyzed by an unpaired *t*-test (* $p < 0.001$, ** $p < 0.01$, *** $p < 0.05$ vs. sample on plastic, # $p < 0.05$, ## $p < 0.001$ vs. sample on bSi).

A similar effect was observed for PyC of different thicknesses, deposited on flat quartz. Data are shown in Figure 4d,e and Table 3. For cells grown on PyC with a 20 nm thickness, the cell division rate was 2.3 times lower than in the control sample; cell confluence was 33.7 ± 7.1%, indicating lower proliferation. However, in the case of 40 nm PyC on SiO_2 as a substrate, an increase in confluence and cell proliferation was observed, but still, it was lower than in the control sample. It is worth noting that neither 20 nm PyC nor 40 nm PyC modified the area per cell (%) parameter, and for rat C6 glioma cells, it remained approximately 2 for both PyC on SiO_2 and the control samples. Moreover, the PyC layer on bSi increased this parameter from 1.3 ± 0.3 for bSi to 1.6 ± 0.1 for bSi with PyC, indicating that PyC does not modify cell morphology.

In the air, the bSi surface was covered by a 30–80 Å thick SiO_2 layer. This oxide layer resulted in the positive surface charge at the interface, which improved the adhesion of cells to the surface because the outer surface of the cell membrane was negatively charged due to phosphate groups of the phospholipid bilayer. However, the deposition of highly conductive PyC led to a decrease in cell adhesion, as we observed for all our samples.

Vertical GNW on the Si wafer was associated with a further roughness decrease to nanoscale (thickness of the surface prominences oriented to the cell is defined by the graphene wall thickness). This led to a significant loss in cell adhesion and very poor biocompatibility, as shown in Figure 4e. Moreover, the distance between the GNW exceeded several microns. Cells lost long processes, did not form intercellular contacts, stayed round-shaped, and thus, lost the ability of effective cell division. This is the result of the high hydrophobicity of GNW [42]. Another effect reducing cell adhesion on GNW films may be related to the presence on their surface of needle-like species elongating above the flakes [23].

The cell–surface contact was provided by focal adhesions responsible for sensing environmental conditions. These specific protein complexes include transmembrane integrin molecules, associated with many cytoplasmic proteins regulating actin cytoskeleton dynamics, cell movement, and attachment [43]. Focal adhesions include "dot"-like or point contacts of 200–500 nm in the active edge of the cell, and elongated "dash" contacts of 2–10 μm in length and 0.5 μm in width, partially located under the nucleus [44]. These dimensional parameters of focal adhesion are critical in cell-surface contact formation as it strongly correlates with the interspike distance. Cell attachment is promoted by textures of low- and intermediate-roughness. It is inhibited by the increase in the interspike distance to 4.5 μm [45]. As seen from Figure 1, the distance between the surface prominences varied from approximately 70 nm for PyC on SiO_2 (Figure 1c,i) to approximately 260 nm for bSi and PyC on bSi (Figure 1b,l). Under such conditions, the cells successfully spread over the substrate, as they could establish the next focal adhesion contact with surface prominences in any direction. At the same time, the thickness of GNW was less than the minimal required size of the focal adhesion contact of 200–500 nm. Therefore, it did not provide cells with the area for attachment, and the growth of the C6 glioma cells on such substrate was impeded. Thus, all fabricated surfaces except GNW met the requirements of dimensionality of surface texture roughness necessary for focal adhesions.

Poly-L-lysine, traditionally used for the improvement of cell adhesion to the growth surface, is a dielectric material, and like most biopolymers, has its own refractive index different from water, creates an uneven layer on the surface of the substrate, which significantly reduces the quality of signal transmission from the cell to the sensor electrodes, and degrades the quality of the optical images of cells introducing additional distortions into registered spectral characteristics of cells. PyC has significant advantages over the poly-L-lysine layer because this material can be directly used in the production of conductive–insulating surfaces for biosensors. Even though the PyC synthesis conditions require high temperature, which undoubtedly prohibits the use of classical optical glasses as a substrate, PyC can be successfully synthesized on quartz. It makes it possible to use these substrates with PyC for all types of NUV, visible, and NIR spectroscopies, as well as to transfer synthetized PyC to any other substrate, even flexible, for example, polydimethylsiloxane. In this case, any designed contact scheme can be created on the PyC by lithographic methods. All this becomes possible due to

the unique electrical and optical properties of PyC, as well as the good biocompatibility and adhesive properties demonstrated in this study.

4. Conclusions

Special attention should be paid to macro-, micro- and nanoroughness of the materials that are intended to be used as functional substrates for biosensing/bioregulation platforms.

We demonstrate that GNW being roughly perpendicular to the Si substrate as well as PyC films of different thicknesses used in combination with microstructured surfaces (SiO_2 and bSi) of different topography may provide both cell adhesion and proliferation promotion or arrest.

Rat C6 glioma cells strongly adhere to the bSi as a substrate. Cells are of spindle shape which corresponds to their usual morphology. The PyC layer on the bSi modifies the adhesive properties of the surface and smooths the bSi nanostructures. The cell–surface contact becomes weaker, and as a consequence, the division rate decreases. At the same time, the surface remains biocompatible (even without poly-L-lysine or other biopolymers commonly used for cell growth), providing the opportunity for the fine-tuning of cell growth speed.

To summarize, macro-, micro- and nanoscale roughness plays a crucial role in the process of cell adhesion to the biosensor surface. The combination of macroscopic and microscopic bSi roughness as well as surface charge distribution results in sufficient biocompatibility. In terms of adhesive properties, bSi can be compared to special plastics used for the cultivation of brain cells. BSi surface modification with PyC leads to decreased cell adhesion to the surface. This was observed both for PyC on bSi and PyC of different thicknesses on plain SiO_2 substrates. Such PyC effect may be due to the fact that the PyC shields electric charges located on the surface and mimics nanoscale roughness. This will be used in the future for directed cell growth and intercellular contact formation for cells grown on 3D scaffolds covered with PyC. Further lowering the dimension of the surface roughness to nanoscale using vertical GNW-covered Si wafers demonstrates poor biocompatibility. The latter preparation can thus be used for the formation of superhydrophobic tracks for directed neuron network formation. The regulation of cell adhesion by changing roughness and the selective biocompatibility of investigated materials allow them to be applied further for the development of sensor platforms. The sensory properties of such platforms will be determined by the unique optical and electrical properties of the carbon-based materials.

Author Contributions: Conceptualization, P.K., Y.S., R.K., T.K. (Tatsiana Kulahava), A.D., and L.G.; methodology, L.G., H.R., M.B., T.K. (Tommy Kaplas), A.S. (Ali Shah), S.M., A.O., D.R., M.J., I.M., A.S. (Algirdas Selskis), and Y.S.; investigation, L.G., H.R., S.M., D.R., M.J., I.M., A.D., and A.S. (Algirdas Selskis); data curation, L.G., H.R., Y.S., T.K. (Tatsiana Kulahava), R.K., and P.K.; writing—original draft preparation, L.G., H.R.; writing—review and editing, T.K. (Tatsiana Kulahava), R.K., D.R., A.O., P.K., and Y.S.; supervision, T.K. (Tatsiana Kulahava), R.K., P.K., and Y.S. All authors have read and agreed to the published version of the manuscript.

Funding: This work was financially supported by Horizon 2020 RISE DiSeTCom Project 823728 (associated with Graphene Flagship), the Academy of Finland Flagship Programme projects nos. 320166 and 298298, joint project no. S-LB-19-4 from the Research Council of Lithuania Foundation, and the Belarusian Republican Foundation for Fundamental Research (BRFFR) project F19LITG-003. PK is supported by Horizon 2020 IF TURANDOT project 836816. SM and AO are also grateful for support from the Russian Foundation for Basic Research project 18-29-19071.

Conflicts of Interest: The authors declare no conflict of interest.

References

1. Dahinden, C.A.; Fehr, J.; Hugli, T.E. Role of Cell Surface Contact in the Kinetics of Superoxide Production by Granulocytes. *J. Clin. Investig.* **1983**, *72*, 113–121. [CrossRef] [PubMed]
2. Spillmann, C.M.; Lomakina, E.; Waugh, R.E. Neutrophil Adhesive Contact Dependence on Impingement Force. *Biophys. J.* **2004**, *87*, 4237–4245. [CrossRef] [PubMed]
3. Hoffman, R.; Benz, E.J.; Silberstein, L.E.; Heslop, H.E.; Weitz, J.I.; Anastasi, J.; Salama, M.E.; Abutalib, S. *Hematology: Basic Principles and Practice*; Elsevier Inc.: Amsterdam, The Netherlands, 2017. [CrossRef]

4. Chen, S.; Lewallen, M.; Xie, T. Adhesion in the Stem Cell Niche: Biological Roles and Regulation. Development (Cambridge). *Development* **2013**, *140*, 255–265. [CrossRef]
5. Bian, S. Cell Adhesion Molecules in Neural Stem Cell and Stem Cell—Based Therapy for Neural Disorders. In *Neural Stem Cells—New Perspectives*; InTech: London, UK, 2013. [CrossRef]
6. Akhmanova, M.; Osidak, E.; Domogatsky, S.; Rodin, S.; Domogatskaya, A. Review Article Physical, Spatial, and Molecular Aspects of Extracellular Matrix of In Vivo Niches and Artificial Scaffolds Relevant to Stem Cells Research. *Stem Cells Int.* **2015**, *2015*, 167025. [CrossRef] [PubMed]
7. Bahrami, S.; Baheiraei, N.; Mohseni, M.; Razavi, M.; Ghaderi, A.; Azizi, B.; Rabiee, N.; Karimi, M. Three-Dimensional Graphene Foam as a Conductive Scaffold for Cardiac Tissue Engineering. *J. Biomater. Appl.* **2019**, *34*, 74–85. [CrossRef]
8. Costa, F.; Carvalho, I.F.; Montelaro, R.C.; Gomes, P.; Martins, M.C. Covalent immobilization of antimicrobial peptides (AMPs) onto biomaterial surfaces. *Acta Biomater.* **2011**, *7*, 1431–1440. [CrossRef]
9. Krutty, J.D.; Schmitt, S.K.; Gopalan, P.; Murphy, W.L. Surface functionalization and dynamics of polymeric cell culture substrates. *Curr. Opin. Biotechnol.* **2016**, *40*, 164–169. [CrossRef]
10. Liao, C.; Li, Y.; Tjong, S.C. Graphene Nanomaterials: Synthesis, Biocompatibility, and Cytotoxicity. *Int. J. Mol. Sci.* **2018**, *19*, 3564. [CrossRef]
11. Jeong, J.T.; Choi, M.K.; Sim, Y.; Lim, J.T.; Kim, G.S.; Seong, M.J.; Hyung, J.H.; Kim, K.S.; Umar, A.; Lee, S.K. Effect of Graphene Oxide Ratio on the Cell Adhesion and Growth Behavior on a Graphene Oxide-Coated Silicon Substrate. *Sci. Rep.* **2016**, *6*. [CrossRef]
12. Syama, S.; Mohanan, P.V. Comprehensive Application of Graphene: Emphasis on Biomedical Concerns. *Nano-Micro Lett.* **2019**, *11*, 1–31. [CrossRef]
13. Turon Teixidor, G.; Gorkin, R.A.; Tripathi, P.P.; Bisht, G.S.; Kulkarni, M.; Maiti, T.K.; Battacharyya, T.K.; Subramaniam, J.R.; Sharma, A.; Park, B.Y.; et al. Carbon Microelectromechanical Systems as a Substratum for Cell Growth. *Biomed. Mater.* **2008**, *3*. [CrossRef] [PubMed]
14. Das, K.; Madhusoodan, A.; Mili, B.; Kumar, A.; Saxena, A.C.; Kumar, K.; Sarkar, M.; Singh, P.; Srivastava, S.; Bag, S. Functionalized Carbon Nanotubes as Suitable Scaffold Materials for Proliferation and Differentiation of Canine Mesenchymal Stem Cells. *Int. J. Nanomed.* **2017**, *12*, 3235–3252. [CrossRef] [PubMed]
15. Jin, G.Z.; Kim, M.; Shin, U.S.; Kim, H.W. Neurite Outgrowth of Dorsal Root Ganglia Neurons Is Enhanced on Aligned Nanofibrous Biopolymer Scaffold with Carbon Nanotube Coating. *Neurosci. Lett.* **2011**, *501*, 10–14. [CrossRef]
16. Fabbro, A.; Bosi, S.; Ballerini, L.; Prato, M. Carbon Nanotubes: Artificial Nanomaterials to Engineer Single Neurons and Neuronal Networks. *ACS Chem. Neurosci.* **2012**, *3*, 611–618. [CrossRef] [PubMed]
17. Bei, H.P.; Yang, Y.; Zhang, Q.; Tian, Y.; Luo, X.; Yang, M.; Zhao, X. Graphene-Based Nanocomposites for Neural Tissue Engineering. *Molecules* **2019**, *24*, 658. [CrossRef] [PubMed]
18. Menaa, F.; Abdelghani, A.; Menaa, B. Graphene Nanomaterials as Biocompatible and Conductive Scaffolds for Stem Cells: Impact for Tissue Engineering and Regenerative Medicine. *J. Tissue Eng. Regen. Med.* **2015**, *9*, 1321–1338. [CrossRef]
19. Ryu, S.; Kim, B.S. Culture of Neural Cells and Stem Cells on Graphene. *Tissue Eng. Regen. Med.* **2013**, *10*, 39–46. [CrossRef]
20. Li, N.; Zhang, Q.; Gao, S.; Song, Q.; Huang, R.; Wang, L.; Liu, L.; Dai, J.; Tang, M.; Cheng, G. Three-Dimensional Graphene Foam as a Biocompatible and Conductive Scaffold for Neural Stem Cells. *Sci. Rep.* **2013**, *3*. [CrossRef]
21. Mofazzal Jahromi, M.A.; Abdoli, A.; Rahmanian, M.; Bardania, H.; Bayandori, M.; Moosavi Basri, S.M.; Kalbasi, A.; Aref, A.R.; Karimi, M.; Hamblin, M.R. Microfluidic Brain-on-a-Chip: Perspectives for Mimicking Neural System Disorders. *Mol. Neurobiol.* **2019**, *56*, 8489–8512. [CrossRef]
22. Lotti, F.; Ranieri, F.; Vadalà, G.; Zollo, L.; Di Pino, G. Invasive Intraneural Interfaces: Foreign Body Reaction Issues. Frontiers in Neuroscience. *Front. Media* **2017**, *11*, 497. [CrossRef]
23. Kleshch, V.I.; Vasilyeva, E.A.; Lyashenko, S.A.; Obronov, I.V.; Tyurnina, A.V.; Obraztsov, A.N. Surface Structure and Field Emission Properties of Few-Layer Graphene Flakes. *Phys. Status Solidi Basic Res.* **2011**, *248*, 2623–2626. [CrossRef]
24. Kaplas, T.; Svirko, Y. Direct Deposition of Semitransparent Conducting Pyrolytic Carbon Films. *J. Nanophotonics* **2012**, *6*, 061703. [CrossRef]

25. Hiramatsu, M.; Kondo, H.; Hori, M. Graphene Nanowalls. In *New Progress on Graphene Research*; InTech: London, UK, 2013. [CrossRef]
26. Batrakov, K.; Kuzhir, P.; Maksimenko, S.; Paddubskaya, A.; Voronovich, S. Enhanced Microwave Shielding Effectiveness of Ultrathin Pyrolytic Carbon Films. *Appl. Phys. Lett.* **2013**, *103*, 73117. [CrossRef]
27. Cook, S.D.; Beckenbaugh, R.D.; Redondo, J.; Popich, L.S.; Klawitter, J.J.; Linscheid, R.L. Long-Term Follow-up of Pyrolytic Carbon Metacarpophalangeal Implants. *J. Bone Jt. Surg. Ser. A* **1999**, *81*, 635–648. [CrossRef] [PubMed]
28. Dovbeshko, G.I.; Romanyuk, V.R.; Pidgirnyi, D.V.; Cherepanov, V.V.; Andreev, E.O.; Levin, V.M.; Kuzhir, P.P.; Kaplas, T.; Svirko, Y.P. Optical Properties of Pyrolytic Carbon Films Versus Graphite and Graphene. *Nanoscale Res. Lett.* **2015**, *10*. [CrossRef]
29. Graham, A.P.; Schindler, G.; Duesberg, G.S.; Lutz, T.; Weber, W. An Investigation of the Electrical Properties of Pyrolytic Carbon in Reduced Dimensions: Vias and Wires. *J. Appl. Phys.* **2010**, *107*, 114316. [CrossRef]
30. McEvoy, N.; Peltekis, N.; Kumar, S.; Rezvani, E.; Nolan, H.; Keeley, G.P.; Blau, W.J.; Duesberg, G.S. Synthesis and Analysis of Thin Conducting Pyrolytic Carbon Films. *Carbon* **2012**, *50*, 1216–1226. [CrossRef]
31. Heikkinen, J.J.; Peltola, E.; Wester, N.; Koskinen, J.; Laurila, T.; Franssila, S.; Jokinen, V. Fabrication of Micro- and Nanopillars from Pyrolytic Carbon and Tetrahedral Amorphous Carbon. *Micromachines* **2019**, *10*, 510. [CrossRef]
32. Shah, A.; Stenberg, P.; Karvonen, L.; Ali, R.; Honkanen, S.; Lipsanen, H.; Peyghambarian, N.; Kuittinen, M.; Svirko, Y.; Kaplas, T. Pyrolytic Carbon Coated Black Silicon. *Sci. Rep.* **2016**, *6*, 1–6. [CrossRef]
33. Ozturk, S.; Kayabasi, E.; Kucukdogan, N.; Ayakdas, O. Progress in Applications of Black Silicon. *Most Recent Stud. Sci. Art* **2018**, *2*, 1866–1882.
34. Sainiemi, L.; Jokinen, V.; Shah, A.; Shpak, M.; Aura, S.; Suvanto, P.; Franssila, S. Non-Reflecting Silicon and Polymer Surfaces by Plasma Etching and Replication. *Adv. Mater.* **2011**, *23*, 122–126. [CrossRef] [PubMed]
35. Hassler, M. Other commonly used biomedical coatings: Pyrolytic carbon coatings. *Coat. Biomed. Appl.* **2012**, 75–105. [CrossRef]
36. Zhang, W.; Li, A.; Reznik, B.; Deutschmann, O. Thermal expansion of pyrolytic carbon with various textures, ZAMM Zeitschrift Fur Angew. *Math. Mech.* **2013**, *93*, 338–345. [CrossRef]
37. Obraztsov, A.N.; Pavlovsky, I.Y.; Volkov, A.P.; Petrov, A.S.; Petrov, V.I.; Rakova, E.V.; Roddatis, V.V. Electron Field Emission and Structural Properties of Carbon Chemically Vapor-Deposited Films. *Diam. Relat. Mater.* **1999**, *8*, 814–819. [CrossRef]
38. Magdesieva, T.V.; Shvets, P.V.; Nikitin, O.M.; Obraztsova, E.A.; Tuyakova, F.T.; Sergeyev, V.G.; Khokhlov, A.R.; Obraztsov, A.N. Electrochemical characterization of mesoporous nanographite films. *Carbon* **2016**, *105*, 96–102. [CrossRef]
39. Childres, I.; Jauregui, L.A.; Park, W.; Caoa, H.; Chena, Y.P. Raman Spectroscopy of Graphene and Related Materials. In *New Developments in Photon and Materials Research*; Nova Science Publishers: Hauppauge, NY, USA, 2013; pp. 403–418.
40. Baryshevsky, V.; Belous, N.; Gurinovich, A.; Gurnevich, E.; Kuzhir, P.; Maksimenko, S.; Molchanov, P.; Shuba, M.; Roddatis, V.; Kaplas, T.; et al. Study of nanometric thin pyrolytic carbon films for explosive, electron emission cathode in high-voltage planar diode. In *Thin Solid Films*; Elsevier: Amsterdam, The Netherlands, 2015; pp. 107–111. [CrossRef]
41. Lambin, P. Graphene as a prototypical model for two-dimensional continuous mechanics. *Appl. Sci.* **2017**, *7*, 830. [CrossRef]
42. Samanta, T.; Biswas, R.; Banerjee, S.; Bagchi, B. Study of Distance Dependence of Hydrophobic Force between Two Graphene-like Walls and a Signature of Pressure Induced Structure Formation in the Confined Water. *J. Chem. Phys.* **2018**, *149*. [CrossRef]
43. Riveline, D.; Zamir, E.; Balaban, N.Q.; Schwarz, U.S.; Ishizaki, T.; Narumiya, S.; Kam, Z.; Geiger, B.; Bershadsky, A.D. Focal Contacts as Mechanosensors: Externally Applied Local Mechanical Force Induces Growth of Focal Contacts by an MDia1-Dependent and ROCK-Independent Mechanism. *J. Cell Biol.* **2001**, *153*, 1175–1185. [CrossRef]

44. Owen, G.R.; Meredith, D.O.; Ap Gwynn, I.; Richards, R.G.; Bongrand, P.; Curtis, A.S.G. Focal Adhesion Quantification—A New Assay of Material Biocompatibility? *Rev. Eur. Cells Mater. AO Res. Inst. Davos* **2005**, 85–96. [CrossRef]
45. Simitzi, C.; Stratakis, E.; Fotakis, C.; Athanassakis, I.; Ranella, A. Microconical Silicon Structures Influence NGF-Induced PC12 Cell Morphology. *J. Tissue Eng. Regen. Med.* **2015**, *9*, 424–434. [CrossRef]

ACS APPLIED MATERIALS & INTERFACES

www.acsami.org Research Article

Surface-Enhanced Raman Spectroscopy of Organic Molecules and Living Cells with Gold-Plated Black Silicon

Lena Golubewa,* Renata Karpicz, Ieva Matulaitiene, Algirdas Selskis, Danielis Rutkauskas, Aliaksandr Pushkarchuk, Tatsiana Khlopina, Dominik Michels, Dmitry Lyakhov, Tatsiana Kulahava, Ali Shah, Yuri Svirko, and Polina Kuzhir

Cite This: *ACS Appl. Mater. Interfaces* 2020, 12, 50971−50984 Read Online

ACCESS | Metrics & More | Article Recommendations | Supporting Information

ABSTRACT: Black silicon (bSi) refers to an etched silicon surface comprising arrays of microcones that effectively suppress reflection from UV to near-infrared (NIR) while simultaneously enhancing the scattering and absorption of light. This makes bSi covered with a nm-thin layer of plasmonic metal, i.e., gold, an attractive substrate material for sensing of bio-macromolecules and living cells using surface-enhanced Raman spectroscopy (SERS). The performed Raman measurements accompanied with finite element numerical simulation and density functional theory analysis revealed that at the 785 nm excitation wavelength, the SERS enhancement factor of the bSi/Au substrate is as high as 10^8 due to a combination of electromagnetic and chemical mechanisms. This finding makes the SERS-active bSi/Au substrate suitable for detecting trace amounts of organic molecules. We demonstrate the outstanding performance of this substrate by highly sensitive and specific detection of a small organic molecule of 4-mercaptobenzoic acid and living C6 rat glioma cell nucleic acids/proteins/lipids. Specifically, the bSi/Au SERS-active substrate offers a unique opportunity to investigate the living cells' malignant transformation using characteristic protein disulfide Raman bands as a marker. Our findings evidence that bSi/Au provides a pathway to the highly sensitive and selective, scalable, and low-cost substrate for lab-on-a-chip SERS biosensors that can be integrated into silicon-based photonics devices.

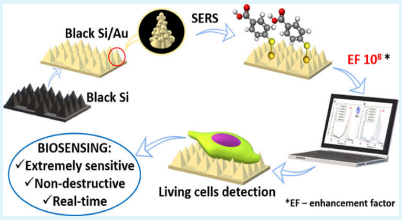

KEYWORDS: *Black silicon, surface-enhanced Raman spectroscopy, enhancement factor, DFT, small organic molecules, living cells*

INTRODUCTION

Curing neurodegenerative diseases and stem cell therapies require effective biosensors for real-time *in vivo* controlling and monitoring the growth and functional activity of the cells. Materials used for biosensor systems must provide cellular viability and stable functional state, preserve sterility, and preferably be compatible with silicon photonics to address the lab-on-a-chip technological flow.[1]

Raman spectroscopy is actively implemented in biosensing[2] partially because it can use NIR radiation, which is less damaging for biological tissues providing deeper − in comparison with VIS light − tissue penetration.[3] In addition, detecting NIR radiation does not require any specific sample preparation keeping the object unaltered.[4] The sensitivity and specificity of Raman measurements can be drastically improved by using substrates enabling surface-enhanced Raman scattering spectroscopy (SERS). This technique allows one to detect low biomolecule concentration[5−7] changes in cell metabolism[8] or cell viability,[9] discriminate individual vesicles,[10] and to real-time control biochemical changes[11−13] by using so-called SERS-active substrates, which are conventionally based on noble metal (Au, Ag, Cu) nanostructures.[14−16] They allow enhancement of the Raman signal due to the surface plasmon resonance, associated with the collective motion of the conductive electrons in the vicinity of "hot spots" at high curvature metal structures.[17] This makes the SERS signal very sensitive to the substrate morphology[18] and requires fabrication techniques providing fine control over the geometry and size of nanostructures/hot spots,[19] which should be uniformly distributed over the entire substrate to be employed for biosensing.

Although SERS-active substrates based on metal micro- and nanostructures deposited on glass are widely available on the market,[20] their performance is often limited by the low curvature of metal nanoparticles and/or small surface density of the hot spots, which do not allow analytes' detection at concentrations at the ppb level.[21] To improve the sensitivity, we suggest employing in SERS substrates based on black

Received: July 28, 2020
Accepted: October 14, 2020
Published: October 27, 2020

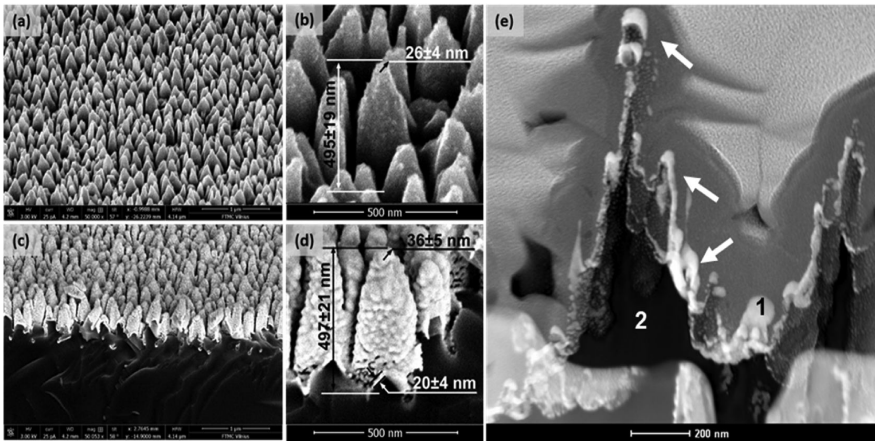

Figure 1. SEM images of bSi (a,b) and bSi/Au (c,d) substrates; (e) TEM image of the silicon cone covered by a 25−50 nm-thick gold layer. Gold structures on the bSi substrate are marked with arrows. The white color corresponds to Au components (1), and the dark gray area corresponds to Si (2).

silicon (bSi), which was proposed in 1997 to increase absorbance and suppress reflectivity of silicon[22] by forming cone-shaped structures of micrometer height over the sample surface.[23] These properties made bSi a versatile material for various applications, such as solar cells,[24] THz emission sources,[25] microfluidic devices,[26] chemical[27] and biological sensors,[28] antibacterial surfaces,[29,30] etc.

BSi forms a functional platform for the fabrication of SERS-active substrates because the apexes of the high-curvature cone-like structures can serve as active sites for electromagnetic field (E-field) enhancement. Its performance in SERS has been demonstrated with a high-intensity 532 nm laser by detecting individual algal cells (*Chlorella vulgaris*)[31] on bSi substrates covered with a 200−400 nm-thick gold layer.[31,32] Unfortunately, the hundreds-nm-thick Au film smooths out the curvature of the bSi cones suppressing significantly the Raman signal enhancement.

In vivo bSi-based SERS biosensing challenges the excitation of the Raman signal with low-power NIR lasers; i.e., the decrease of laser power and increase of the enhancement factor (EF) are needed. The latter implies decreasing the thickness of the gold layer to be deposited on bSi and increasing the number of hot spots at needles' apexes.

The electromagnetic field enhancement at the metal surface may originate from the electromagnetic (EM) and chemical (CM) mechanisms.[33] The EM mechanism occurs when the analyte molecule is situated in the close vicinity of the hot spots on the substrate surface. Since the induced dipole moment of the molecule is proportional to the electric field, it drastically increases at the plasmon resonance. Moreover, the electromagnetic wave emitted by the analyte at the shifted frequency also enhances due to the plasmonic effect. As a result, the Raman signal is proportional to the fourth power of the local field enhancement factor (EF).[34]

The chemical (also referred to as the charge transfer) mechanism occurs when the studied substance forms chemical bonds with the substrate material. These bonds lead to the increase of the polarizability and, as a consequence, the intensity of Raman scattering.

Understanding of the mechanisms of E-field enhancement in the bSi/Au system will make it possible to predict the EF, which also depends on the morphology of the bSi surface (cone height and base diameter, the density of the cones) and the gold layer thickness.

In this paper, we propose effective, noninvasive, label-free, high-speed SERS detection of trace amounts of small organic molecules and living rat C6 glioma cells utilizing bSi covered with a 25−50 nm gold layer. Using the finite elements method (FEM) and density functional theory (DFT), we also perform numerical modeling and theoretical analysis of the SERS signal of organic molecules/cells deposited on the bSi/Au substrate and reveal the contributions of EM and CM mechanisms to the E-field enhancement. The obtained results allow us to reveal the optimal morphology and composition of the bSi/Au SERS-active substrate for *in vivo* biosensing of trace amounts of biomolecules and living cells.

RESULTS AND DISCUSSION

Experimental Results. Scanning electron microscope (SEM) images of bSi and bSi/Au are presented in Figure 1a−d. Figure 1e shows the transmission electron microscopy (TEM) image of an individual silicon cone covered with the golden layer. One can observe that the substrates consist of vertically oriented quasi-regular cone-like structures. The height and base diameter of cones comprising a bare bSi substrate are 495 ± 19 and 221 ± 24 nm, respectively, while the apex curvature radius is 26 ± 4 nm (Figure 1b). On the bSi/Au substrates, the height of the cones is 497 ± 21 nm and an apex curvature radius is 36 ± 5 nm. It is worth noting that the roughness of the gold layer is as high as 10−50 nm (Figure 1d) due to nanoscale irregularities and nanoroughness of the bSi cones. The average thickness of the deposited gold layer was 25−50 nm. The Au semispheres on the bSi substrate vary in size and separation distance. For this reason, we analyzed the distribution of the particle sizes from the SEM image of the

https://dx.doi.org/10.1021/acsami.0c13570
ACS Appl. Mater. Interfaces 2020, 12, 50971−50984

SiO_2/Au surface. The SEM image of the SiO_2/Au is presented in Figure S1. This surface was obtained under the same conditions as the surface of bSi/Au but is much easier for analysis. It consists of the hemisphere structures; their diameter distribution is presented in Figure S1b. As the conditions were the same both for bSi and SiO_2, we used the SiO_2/Au SEM image to obtain the nanoparticle size distribution assuming that the Au structures on the SiO_2 and bSi would be very similar. Since hemispheres with diameters in the range of 40 to 60 nm (almost 70% of all hemispheres) give the major contribution to the SERS enhancement, for further simulations, we assumed that the studied nanoparticles have a diameter of 50 nm.

The effective surface area of the bSi substrate is about 2.4 times larger than that of the flat SiO_2 substrate, which was confirmed by the AFM method earlier.[35] The presence of semispherical structures on an inclined lateral surface does not allow the cantilever to correctly repeat the surface profile and introduces additional errors in measurements. However, assuming that Au roughness on the flat SiO_2 and on the conical Si surface is of the same order of magnitude (the conditions of Au deposition were the same), it will add the same multiplier to the values of both surface areas, and thus, the bSi/Au to SiO_2/Au surface ratio could be estimated to be also about 2.4.

To quantitatively evaluate the performance of the bSi/Au SERS-active substrate, we employ the 4-mercaptobenzoic acid (4-MBA) molecule with a well-known Raman spectrum. When 4-MBA molecules are deposited on the gold-plated substrate, the nearest to the substrate molecules form covalent bonds with gold through S−H groups. That is, by washing the sample in the ethanol, one can remove the nonbonded molecules and obtain a monolayer of 4-MBA molecules covalently bonded to the substrate.

The Raman spectra of the 4-MBA molecule monolayer deposited on SiO_2/Au and bSi/Au substrates are presented in Figure 2a,c, respectively. Under the same measurement conditions (10 μW, 30 s accumulation time), 4-MBA bands are not detectable when the molecule monolayer is deposited on the plane SiO_2/Au substrate, while these bands are clearly resolved for the 4-MBA monolayer deposited on the bSi/Au surface. All observed bands are in good correspondence with the Raman spectrum of the bulk 4-MBA (Figure 2b) described elsewhere.[33,36]

It is worth noting that the S−H stretching mode of 4-MBA at about 2570 cm^{-1}, typical for a Raman spectrum of bulk 4-MBA, is absent in the Raman spectrum of the monolayer (data are not shown) because this resonance is suppressed by the covalent bond, in which the S−H group forms with the gold layer.

The enhancement factor of the SERS-active bSi/Au substrate can be found from the following equation[37]

$$EF = \frac{I_{bSi/Au}/N_{bSi/Au}}{I_{bulk}/N_{bulk}} \quad (1)$$

where $I_{bSi/Au}$ ($N_{bSi/Au}$) and I_{bulk} (N_{bulk}) are Raman intensities (numbers of irradiated molecules) of the 4-MBA monolayer on the bSi/Au substrate and bulk 4-MBA on the SiO_2 substrate obtained at the same laser power and accumulation time, respectively. In our experimental conditions, the laser spot area on the bSi/Au substrate was 1.28 μm^2; however, atomic force microscopy measurements indicated that the effective surface

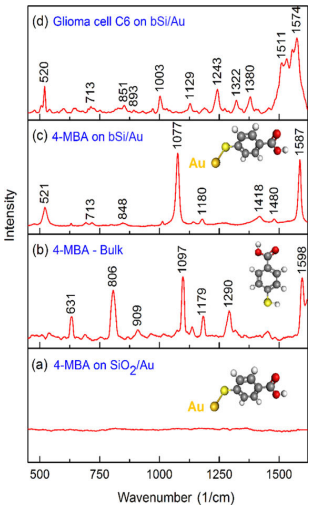

Figure 2. Comparison of the Raman spectra of the 4-MBA monolayer on the SiO_2/Au smooth substrate (a), of bulk 4-MBA (b), and SERS spectra of 4-MBA (c) and living rat glioma cell (d) on the bSi/Au substrate. The spectrum of a living cell was recorded in aqueous Hepes-buffer solution. The buffer spectrum was subtracted from the living cell Raman spectrum. The excitation wavelength is 785 nm.

area of the bSi/Au substrate is 2.4 times larger; i.e., it is equal to 3.07 μm^2. That is, at a surface density of 0.5 nmol/cm^2,[37] the number of adsorbed molecules on the bSi/Au substrate is $N_{bSi/Au} = 9.2 \times 10^6$. Since the penetration depth of the laser radiation into the bulk 4-MBA sample is about 10 μm and the molecular density is 1.5 g/cm^3, the number of molecules in the irradiated volume is $N_{bulk} = 7.5 \times 10^{10}$. Therefore, at the measured intensity ratio of $I_{bSi/Au}/I_{bulk} = 2.3 \times 10^5$ for the ν_{12} (a_1) aromatic ring breathing mode at 1077 cm^{-1}, eq 1 gives a SERS enhancement factor of EF ≈ 2×10^8.

From the top-down SEM images of the bSi/Au substrate (see Figure 3a), one can see very good structural uniformity of the substrate. This suggests that bSi/Au substrates exhibit good SERS signal uniformity over large areas. In Figure 3b, SERS mapping of the substrates with the 4-MBA monolayer in three randomly selected 10 × 10 μm areas with 1 μm resolution is performed. Images are reconstructed using a 1077 cm^{-1} band in the 4-MBA SERS spectrum. Equal SERS-signal intensities indicate very good uniformity over the whole sample area.

Experimental determination of 4-MBA SERS spectral stability on the bSi/Au substrate over a long time period was performed (see Figure S2). Measurement of the SERS spectrum of 4-MBA molecules was repeated after 8 months. Both spectra (initial and after 8 months of storing in the air) demonstrate the same intensities for the same samples, performed with identical conditions for SERS spectrum registration. Some changes in the positions of the bands indicate probable changes due to storage in air (strengthening of the C=O band (1706 cm^{-1})); however, these changes do not affect the SERS substrate efficiency. Moreover, the data presented in Figure S3 indicate that the bSi/Au substrate

https://dx.doi.org/10.1021/acsami.0c13570
ACS Appl. Mater. Interfaces 2020, 12, 50971−50984

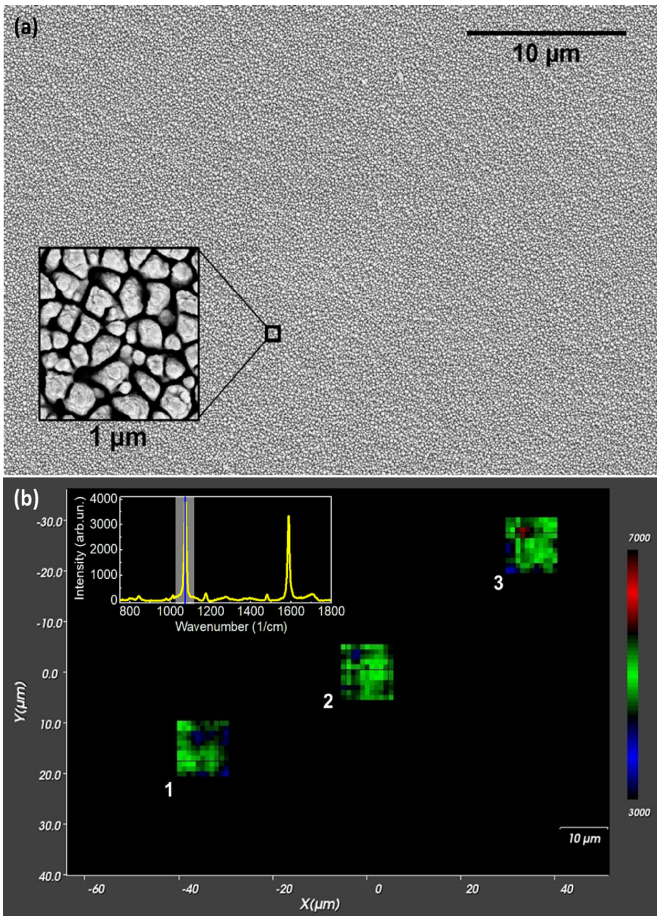

Figure 3. Uniformity of the bSi/Au SERS substrate. (a) Top-down SEM image of the bSi/Au substrate; the inset gives 1 × 1 μm area. (b) Map of the background-corrected Raman intensity. 1077 cm^{-1} C−S stretch vibration peak; a 50× objective (NA 1.0) was used. The map resolution is 1 μm. 1, 2, 3 − separate 10 × 10 μm maps taken randomly from a 75 × 115 μm area. The inset gives a SERS spectrum of the 4-MBA monolayer from 1 × 1 μm pixel.

provides a possibility to obtain the SERS spectrum of the 4-MBA molecule with extremely low laser power (two spectra for comparison − 0.5 mW and 1 μW).

SERS-active substrates (for instance, Ag-capped Si nanopillar systems[38]) are often hydrophobic, which limits their use for the detection of organic molecules, cellular structures, or the cells themselves in aqueous media. The hydrophobicity of these structures is a consequence of the nanostructured nature of the substrate. In contrast, bSi substrates exhibit very nice adhesive properties, similar to the commercially provided tissue-treated plastics for cell culture.[39] Due to a combination of micro- and nanoroughnesses, bSi substrates are hydrophilic (see Figure S4). Water-drop hydrophilicity assay of bSi/Au and plastic (Nunc)) and therefore biocompatible. Hydrophilicity, adhesion, and SERS activity provide a tremendous advantage of the bSi/Au substrates over the existing ones in biochemical, biological, and biomedical applications, which implies working in aqueous environments.

The large enhancement factor allows us to employ the bSi/Au SERS-active substrate for the detection of the living C6 rat glioma cells. Using the propidium iodide (PI) assay, it was shown that the cells on the bSi/Au substrate were viable, preserved their usual morphology, and formed a good monolayer (see Figure S5).

Measurements of a living cell are complicated by continuous cell "movement" due to the dynamics of biochemical reactions taking place inside the cell and due to the constant medium convective flow, which cannot be fully avoided despite the low laser power and relatively short signal accumulation time. These factors led to some changes in SERS spectral band

https://dx.doi.org/10.1021/acsami.0c13570
ACS Appl. Mater. Interfaces 2020, 12, 50971−50984

intensities demonstrating high dynamics of intracellular processes. For instance, one can observe from Figure 4 that

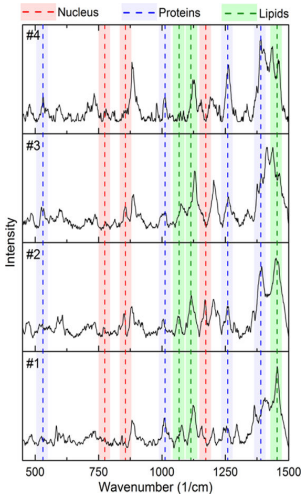

Figure 4. SERS spectra of a living rat glioma cell on the bSi/Au substrate, measured at one point in 1 min intervals. Specific markers indicate the intensity changes of some characteristic bands.

the intensity of the CH_3 symmetric stretch band at 1380 cm^{-1} varies slightly from measurement to measurement due to the density fluctuations in the vicinity of the hot spots on the bSi/Au substrate. Thus, the cellular activity imposes stringent requirements on biosensors' substrates being developed for biosensors. These include a uniform and dense hot spot distribution and a high enhancement factor that will enable real-time monitoring of the cell activity with high accuracy and about one micron spatial resolution.

In the present study, we investigate the living cells by averaging the five separate Raman spectra measured at the same point. The typical averaged spectrum of a living rat glioma cell C6 on the bSi/Au substrate is presented in Figure 2d. Similar to the 4-MBA monolayer (see Figure 2a), we do not observe Raman bands of living cells seeded on the reference SiO_2/Au substrate.

Specific bands of bio-macromolecules of C6 glioma cells, detected in the "fingerprint" spectral region, are grouped and summarized in Table 1. Averaging makes Raman spectra poorly suited to identifying specific molecules in living cells such as specific proteins or lipids,[40] but they can serve to detect relative concentration changes of biomolecules. By using the bSi/Au substrate, we managed to resolve the characteristic bands of nucleic acids, proteins, and lipids. This makes it possible to distinguish between normal and cancerous cells by taking into account the higher relative content of nucleic acids specific to malignant cell transformation.[41,42] Specifically, relatively high intensities of 787 (U, C, T, O−P−O symmetric stretch), 827 (O−P−O), and 1322 and 1574 cm^{-1} (A, G) bands indicate the high content of nucleic acids characteristic for cancer cells; strong bands at 1243, 1273, and 1288 cm^{-1} correspond to the bands of Amide III giving information on the secondary structure of proteins (1243 for the β-sheet and 1288 for the α-helix); high intensities of 506, 520, and 540 cm^{-1} reveal high content of proteins with disulfide bonds enriched with cysteine. The main intracellular function of such proteins in cells is the participation in redox reactions and regulation of intracellular balance between oxidants and reductants. One of the key players in the redox balance in cells is the glutathione/glutathione-disulfide (GSH/GSSG) ratio. It has been shown[43] that a decreased GSH/GSSG ratio (increased GSSG fraction) is the key factor in cancer progression. Thus, bSi/Au SERS-active substrates offer unique opportunity to investigate the cell malignant transformation using characteristic protein disulfide Raman bands as a marker.

Nevertheless, we should admit that the SERS effect depends on the distance, and therefore, it is really possible to obtain SERS signals only from the attached to the substrate part of the cell. The bSi/Au substrate is biocompatible and exhibits nice adhesive properties (as it was demonstrated previously). It was shown that the cell/substrate distance varies from 10 to 80 nm[44] for most parts of the cells and 25 ± 10 nm for peripheral lamellipodia.[45] This explains the fact that the majority of detected lines belong to lipid structures (see Table 1); nevertheless, proteins and DNA from the adjacent to the membrane organelles are also observed.

The SERS spectrum of C6 glioma cells does not exhibit strong lines of Amide I, but nevertheless, it is supposed that there is some weak impact of the α-helix at ∼1645 cm^{-1} in the whole spectrum. Amide I is very active and useful for IR measurements as these bands are strong, but in Raman, Amide I is not so significant and even was shown to be suppressed in SERS and TERS of protein specimens.[46] Moreover, due to the distance dependence of the signal enhancement in SERS spectra, we obtain information mainly on the cell membrane, which is closely located to the SERS substrate, and some structures adjacent to the membrane. Thus, the protein impact on the SERS signal is visualized by Amide III, which is more active in Raman, and there is no overlap with the bands of lipids and nuclear structures.

Finite Elements Method: Electromagnetic Enhancement Contribution to SERS. We performed 3D FEM modeling of the interaction of the light wave propagating along the substrate normal to the cone-like Si structures covered by the 20−50 nm-thick gold layer. By analyzing the SEM and TEM images, we found that the gold layer can be presented as an ensemble of spheres, bi-spheres, and dumbbell-like particles having a different orientation from the cone axis (see Figure 5). We also took into account that nanoparticles may have different sizes and compositions.

We assume that the nanoparticles were irradiated with a plane electromagnetic wave and consider the complex refractive indices of nanoparticles' materials to be dependent on the wavelength. Au dielectric properties in the optical and (IR) frequency ranges were simulated by COMSOL Multiphysics via the Drude model taking into account the experimental data presented elsewhere[47] and the fact that the wavelength of the incident radiation is much larger than the characteristic nanoparticle mean size and golden layer thickness. The bSi/Au cone edge was modeled by a spherical particle of the core−shell Si@Au type. From SEM images presented in Figure 1 we reveal that the radius of the Si core and thickness of the gold shell varies in the 36−44 and 13−21 nm ranges, respectively.

https://dx.doi.org/10.1021/acsami.0c13570
ACS Appl. Mater. Interfaces 2020, 12, 50971−50984

Table 1. Major Peak Location in a "Fingerprint" Region of Raman Spectra of Main Bio-Macromolecules, SERS Spectrum of C6 Rat Glioma Cells, and Their Assignments (Raman Spectral Band Locations and Their Assignments Are Taken from Elsewhere[40])

	Raman spectrum peak location (cm^{-1})	SERS spectrum peak location (cm^{-1}) for C6 rat glioma cells	peak assignments
nucleic acids	723−728	727	C−N head group in adenine
	763	768	pyrimidines (cytosine, thymine, uracil)
	782−792	787	uracil, cytosine, thymine ring breathing; O−P−O symmetric stretch
	813	817	RNA, A-type DNA
	828	827	O−P−O
	898	894	adenine, nucleotide backbone
	1084−1095	1088, 1097	PO2 stretch
	1173−1180	1180, 1188	cytosine, guanine, adenine
	1304−1342	1322, 1342	adenine, guanine
	1487	1484	guanine, adenine
	1510	1509	adenine
	1578	1574	guanine, adenine
proteins	500−550	506, 520, 540	disulfide S−S stretch (conformation dependent)
	755−760	753	Trp ring br.
	850−855	852	Pro C−C stretch (collagen); tyrosine ring br.
	935−937	930	Pro C−C stretch (collagen); C−C backbone stretch (α-helix)
	1000−1006	1003	Phe symmetric ring br.
	1014	1018	Trp symmetric ring br.
	1030−1033	1032	Phe C−H in-plane bend
	1066; 1080−1083; 1125−1128	1069, 1128	C−N stretch
	1155−1158	1155	C−C/C−N stretch
	1225−1280	1243, 1273, 1288	Amide III (random coil 1225−1240; β-pleated sheet 1240−1260; α-helix 1260−1300)
	1600−1610	1600, 1610	Phe, Tyr C=C in-plane bending
lipids	719	714	CN + C (choline)
	955−975	953, 961, 972	CH_3 deformations
	1030−1130	1042, 1110	skeletal C−C stretches (*cis* 1030−1040; chain *trans* 1055−1066; chain random 1080−1085; chain 1092−1098; *trans* 1127)
	1365−1380	1380	CH_3 symmetric stretch
	1440−1460	1437, 1457	CH_2 scissors

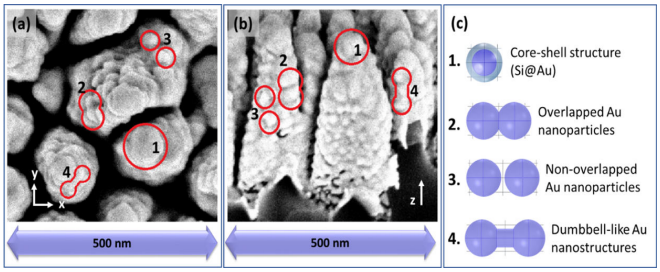

Figure 5. (a) Top-view SEM image of bSi/Au showing horizontally (perpendicular to the wave vector $\vec{k}$) oriented bi-spheres and dumbbell-like particles; (b) side-view SEM image of bSi/Au showing vertically (along the wave vector $\vec{k}$) oriented bi-spheres and dumbbell-like particles; (c) elementary nanostructures selected for numerical simulation of the E-field enhancement.

The numerical simulation showed that there are three absorption bands (see Figure 6). The band in the NIR region dominates having the central wavelength depending on the Si core radius and Au shell thickness. The bigger the Si core radius, the higher the absorption cross section, and the longer the central wavelength (Figure 6a). The decrease of the Au layer thickness also leads to the red-shift of the absorption band, but the absorption cross section maximum decreases (Figure 6b).

Simulation results strongly support the hypothesis that in the red−NIR spectrum region, the absorption resonance of a gold bi-sphere depends not only on the distance between the sphere centers and nanogap sizes but also on the orientation of the pair with respect to the EM wave propagation direction (Figure 7). If bi-spheres are oriented along the wave vector $\vec{k}$ of the EM wave, then there is a strong NIR absorption band, which is absent in the individual Au nanospheres. The red absorption maximum arises from the nanogaps in bi-sphere

https://dx.doi.org/10.1021/acsami.0c13570
ACS Appl. Mater. Interfaces 2020, 12, 50971−50984

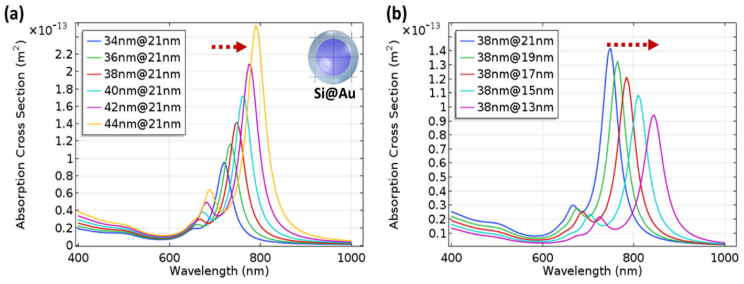

Figure 6. Absorption cross section as a function of wavelength simulated for a Si@Au spherical nanoparticle. (a) Changing the Si-core radius from 34 to 44 nm at a Au-shell thickness of 21 nm, (b) changing the Au-shell thickness from 13 to 21 nm at a Si-core radius of 38 nm.

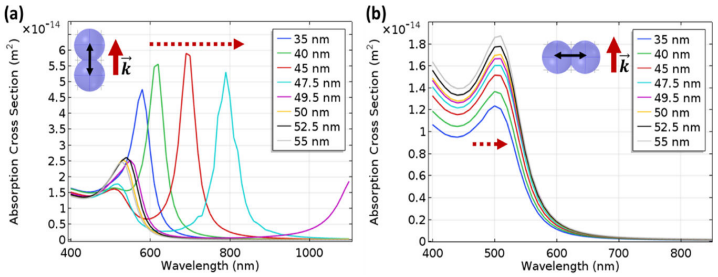

Figure 7. Absorption cross section as a function of the wavelength of the Au bi-spheres (r = 25 nm) having distances between the sphere centers from 35 (overlapped spheres) to 55 nm (nonoverlapped spheres). The electromagnetic wave propagates (a) along with and (b) perpendicular to the bi-sphere axis.

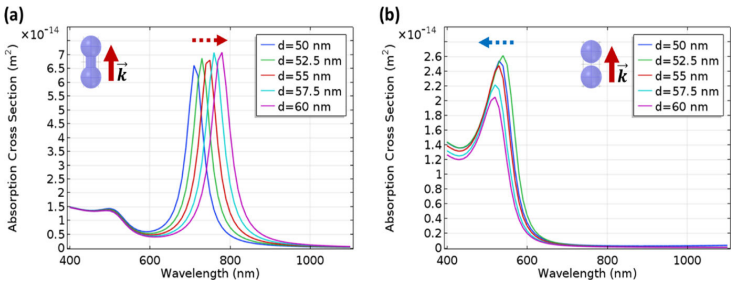

Figure 8. Absorption cross section as a function of wavelength, simulated for (a) Au dumbbell-like nanoparticle (r = 25 nm) and (b) Au bi-spheres with different distances between the sphere centers. The electromagnetic wave propagates along the bi-sphere axis; d is the distance between the sphere centers.

structures and is red-shifted with the increase of the distance between the spheres (Figure 7a).

If the bi-sphere axis is oriented perpendicular to $\vec{k}$ (i.e., horizontally), then a green resonance peak characteristic to gold nanostructures appears. The central position of this band "floats" in the 500−515 nm range when the distance between the centers of spheres changes; however, there is no absorption resonance in the red or NIR spectrum range (Figure 7b).

The system of nonoverlapped Au spheres was further modified into a dumbbell-like structure, which models well the Au droplets on the Au layer. A bridge between the two spheres led to the appearance of an additional absorption peak, which red-shifts with the increase of the distance between the spheres (Figure 8a) and disappears for nonoverlapped Au spheres (Figure 8b). For nonoverlapped Au spheres, the "green" absorption maximum blue-shifts with the increase in the distance between the sphere centers (Figure 8b) approaching the plasmon resonance of the individual Au nanoparticle at 560 nm.

Figure 9 presents the numerical simulation of the E-field enhancement in nanostructures having an absorption maximum at 785 nm. For the Si@Au (44 nm@21 nm) nanoparticle with an absorption maximum of 785 nm, the E-field enhancement on the outer Au surface is as high as 20

https://dx.doi.org/10.1021/acsami.0c13570
ACS Appl. Mater. Interfaces 2020, 12, 50971−50984

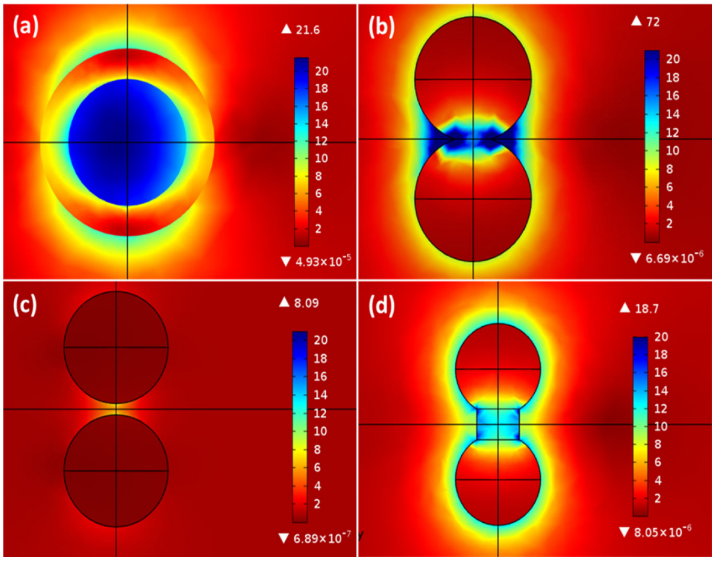

Figure 9. E-field enhancement maps at an irradiation wavelength of 785. (a) Si@Au (44 nm@21 nm), (b) Au bi-sphere (r = 25 nm, distance 47.5 nm), (c) Au bi-sphere (r = 25 nm, distance 55 nm), (d) dumbbell-like structure (r_0 = 13.5 nm). Triangle-up and triangle-down are maximum and minimum values of the E-field enhancement, respectively.

(Figure 9a) giving EF ≈ 1.6 × 10^5. In the overlapped Au nanospheres (Figure 9b), there exists a 70-fold E-field enhancement in the nanogaps between the overlapped spheres (EF ≈ 2.4 × 10^7). E-field enhancement on the sphere surface gives an EF equal to approximately 10^4–10^5. For non-overlapped Au spheres, the E-field enhancement occurs only in the gap between the spheres with an EF of the order of 10^4 (Figure 9c). However, for the refined model on the Au dumbbell structure, E-field enhancement occurs over the whole structure surface, but the most significant E-field enhancement in the space between is as high as 10^5 (Figure 9d).

Based on the results of FEM simulations and their comparison with the experimental measurements of 4-MBA SERS spectra, we may conclude that the SERS-active bSi/Au substrate is very efficient for detecting biological objects as it allows using an NIR laser source for sample irradiation and provides extremely high E-field enhancement. The major mechanism in Raman signal enhancement is the localized surface plasmon resonance (LSPR). Simulation results indicate that the EF due to localized surface plasmon resonance reaches a value of 10^4–10^7, while the experimentally obtained value of the EF is 10^8 (expecting the remaining contribution of CM).

BSi/Au possesses a significant advantage over the conventional plane SERS-active surfaces with Au hot spots because it enables confining the living cells and biomolecules into a 3D enclosure surrounded with the hot spots. For Au nanoparticles with an average diameter of 50 nm, LSPR should appear for 500–530 nm excitation. This statement is proven both by the existing data and our simulation results (see Figure 7). In our experiments, we used a 785 nm laser for excitation, and thus, LSPR did not take place. Living cell sample measurement was provided for only 30 s with a 785 nm laser (this excitation wavelength is not resonant to lots of living cell components such as proteins, DNA, and RNA, as 532 nm;[48] however, its application is favorable as it is not damaging to cells and tissues and can provide nondestructive analysis). This time period and laser power were not enough to obtain a living cell Raman spectrum with an acceptable signal-to-noise ratio on flat SiO_2/Au. However, due to the increase of the bSi/Au absorption cross section in the NIR region, the observation of the living cell SERS spectrum on them becomes possible. Moreover, the predominantly vertical orientation of the gold bi-spheres and dumbbells (see SEM images in Figure 2) on the Si cone surface allows one to obtain an excellent enhancement of the Raman signal by employing plasmon resonance situated in the red and NIR region.

DFT Modeling: Chemical Enhancement Contribution to SERS. To evaluate the enhancement of the SERS signal via the CM mechanism, we employed DFT analysis by studying the equilibrium geometry, electronic structure, and Raman spectra of the 4-MBA molecule and the complex 4-MBA/Au. Simulated Raman and SERS spectra in comparison with experimentally obtained ones as well as optimized geometries of the 4-MBA molecule and 4-MBA/Au (insets) are presented in Figure 10. The simulated spectra display good agreement with the experimental results. Peak assignment of the main characteristic bands in the simulated and experimental Raman spectra of 4-MBA molecules and SERS spectra of 4-MBA/Au complexes are summarized in Table 2. The charge transfer (CT) mechanism is a short-range effect caused by the chemical interaction between the adsorbed molecule and the metal or semiconductor surface.[49] It was shown that the CT process leads to the symmetrical mode enhancement in general,

https://dx.doi.org/10.1021/acsami.0c13570
ACS Appl. Mater. Interfaces 2020, 12, 50971–50984

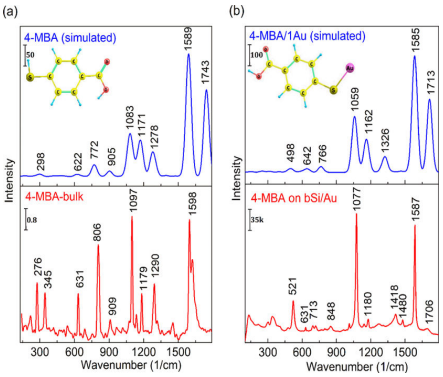

Figure 10. Simulated and experimental Raman spectra of 4-MBA molecules (a) and SERS spectra of 4-MBA/Au complexes (b) with optimized geometries of 4-MBA molecule and 4-MBA/Au complex (insets in panels (a) and (b), respectively). Intensity is presented in arbitrary units as a scale bar. Simulated vibrational bands were fitted with the Gaussian profile with a bandwidth of 30 cm^{-1}.

whereas the modes involving the vibrational coordinates, which are relaxed by the electronically excited state, would be enhanced preferably.[50] In our experiments, we observe a significant increase in ν_{12} (a_1) aromatic ring breathing mode (1077 cm^{-1}) and ν_{8a} (a_1) totally symmetric ν C−C (a_1) (1587 cm^{-1}) intensities, which is well confirmed by DFT simulations, considering the chemical mechanism (molecule adsorption on the Au surface, charge transfer) impact on the Raman signal enhancement. Nevertheless, the DFT simulation results allow us to conclude that the CT process contributes to the signal enhancement by no more than 1 order of magnitude (supporting the primary contribution of the EM mechanism as follows from FEM modeling and comparison of both contributions with the experimental observations). It has been demonstrated elsewhere[51] that for a 4-aminothiophenol molecule (it differs from 4-MBA with one functional group) adsorbed on the Au nanorings, the 1075 cm^{-1} enhancement is observed only for excitation with the 785 nm laser and has pure EM origin. In our study, enhancement of the 1075 and 1585 cm^{-1} bands was of the same order (EF ~10^8), which allows us to conclude that the contribution of the CT mechanism to SERS enhancement of molecules adsorbed on the bSi/Au surface is negligible. Thus, when excited by a 785 nm laser, the electromagnetic mechanism of surface-enhanced Raman spectra dominates.

4-MBA molecules were covalently bonded to the Au surface. It is confirmed by the appearance of a 220 cm^{-1} band of Au−S and the absence of a 2565 cm^{-1} band of S−H (see Figure S3). According to the procedure of the molecular monolayer formation and data presented elsewhere,[52] we suppose the vertical configuration of the molecules on the bSi/Au substrate. The 4-MBA molecule flat orientation to the surface could be identified by strong out-of-plane γ(CCC) vibration of the aromatic ring. In the SERS spectrum of 4-MBA molecules on the bSi/Au surface, this band at 713 cm^{-1} responsible for γ(CCC) as well as 848 cm^{-1} corresponding to $\beta(COO^-)$ practically vanishes, while 1706 cm^{-1} corresponding to C=O stretching vibrations of nondissociated COOH groups is present. These experimental data are in good agreement with the results of DFT calculations (no γ(CCC) and $\beta(COO^-)$ bands, while C=O at 1713 cm^{-1} is present (see Table 2 and Figure 10), and confirm the vertical orientation of the 4-MBA molecules on the bSi/Au substrate.[52]

The appearance of a band at 848 cm^{-1}, assigned to the COO^- stretching mode, in the SERS spectrum likely indicates that some 4-MBA molecules are deprotonated. The pK_a of 4-MBA is 4.2 for free 4-MBA and 5.6 for the covalent bond to gold nanoparticles.[36] At pH 7, 4-MBA is totally deprotonated[53] as ethanol pH is 7.33. During the sample drying procedure in the presence of humid air, the 4-MBA molecule protonates via hydration. However, a small part of it has remained deprotonated, as we observe due to the 848 cm^{-1} band.

CONCLUSIONS

Detection of single organic molecules and living cells with high throughput, speed, and resolution is a very challenging biosensing task. In creating a SERS-active biosensor platform, one should aim in using NIR light for excitation and low power values to prevent possible living cell damage and minimizing the signal accumulation time to acquire accurate information on dynamic biochemical and biophysical processes in living cells. Special attention must also be paid to the quality of the surfaces used for SERS of living cells as hot spot density and EF must satisfy the requirements of uniformity, sensitivity resistance to external influences, and easy low-cost reproducibility on an industrial scale.

We propose a new SERS-active platform for detection of not only trace amounts of small organic molecules but also living cells. The developed bSi/Au substrate ensures high sensitivity by exploring nanoscale roughness of submicron regular cone structures evenly distributed over the entire surface. The increased effective surface area at dense and homogeneous hot spot distribution allows us to obtain an EF of about 10^8. It is worth adding that the proposed SERS-active substrate requires only a 25−50 nm gold layer instead of 100−400 nm conventionally used for SiO_2-based substrates, thus significantly reducing production costs.

The performed numerical FEM simulation confirmed the strong enhancement of the local field at the bSi/Au surface and revealed that the outstanding performance of the bSi/Au substrate originates mostly from the EM mechanism of SERS. Moreover, we demonstrate that the dominating vertical orientation of the gold bi-spheres and dumbbells along bSi/Au cones is crucial for achieving the high efficiency of the substrate in the NIR spectral range. DFT analysis exhibits a relatively small contribution of CM to the SERS activity of bSi/Au, at the level of 1 order of the EF magnitude vs 7 orders coming from the electromagnetic enhancement.

Implementation of the bSi/Au substrate for living C6 rat glioma cell analysis made it possible to visualize the characteristic bands of nucleic acids, proteins, and lipids in the "fingerprint" SERS spectrum region with low excitation intensities and short accumulation time. Moreover, we demonstrated that the bSi/Au substrate has tremendous potential for the real-time cellular dynamics SERS observations. Thus, the bSi/Au substrates may be easily fabricated on a large scale using existing well-developed techniques, with the tune control of specific surface parameters, providing efficient Raman signal enhancement, stability, and reproducibility.

We demonstrate that covering of bSi with up to 50 nm-thick golden layer leads to the formation of specific size-geometry

https://dx.doi.org/10.1021/acsami.0c13570
ACS Appl. Mater. Interfaces 2020, 12, 50971−50984

Table 2. Peak Assignment of the Main Characteristic Bands (Colored Boxes) in the Simulated and Experimental Raman Spectra of 4-MBA Molecules and SERS Spectra of 4-MBA/Au Complexes[a,33,36,49,54−56]

4-MBA {exp.} (cm^{-1})	4-MBA {theor.} (cm^{-1})	4-MBA on bSi/Au {exp.^{SERS}} (cm^{-1})	4-MBA/Au {theor.^{SERS}} (cm^{-1})	Peak assignment
–	–	521	498	ν(CS) [36,54] δ(COOH) deformation
631	622	631	642	ν_{6b} [36] +δ(COOH) deformation
–	–	693	–	γ(CH) out-of-plane [54]
–	–	713	–	ν_{4b} + γ(CCC) out-of-plane [36,54]
806	772	–	766	ν_{10a} [36] in-plane aromatic ring breathing mode +-COH deformation
–	–	848	–	β(COO^-) [36]
909	905	–	–	β(SH) [36]
–	–	1013	–	in-plane ring breathing, b_2 [36,49,54]
1097	1083	1077	1059	ν_{12} (a_1) in-plane aromatic ring breathing mode + ν(CS), a_1 [33,49,54,55,56]
–	–	1142	–	ν_{15} (b_2) δ(CH) deformation [33,54,56]
1179	1171	1180	1162	ν_9 (a_1) δ(CH) deformation [33,36,49,55,56]
1290	1278	–	–	ν_3 [36]
–	–	–	1326	δ(OH) deformation δ(C-Ar) deformation
–	–	1418	–	ν (COO^-) stretching mode [33,36,49]
–	–	1480	–	ν(CC) + γ(CH) [54,55]
1598	1589	1587	1585	ν_{8a} (a_1) totally symmetric aromatic ring vibration [33,36,49,54,55,56]
–	1743	1706	1713	ν (C=O) stretching mode

[a]The vibrational modes are as follows: ν − stretching, β − bending, δ − deformation, γ − out-of-plane deformation.

hot spots to enhance the bSi-for-SERS selectivity and sensitivity.

Applying these bSi/Au substrates for SERS biochemical change detection overcomes the limitations of other biosensing platforms and provides precise information on the biochemistry of cell behavior, cell−substrate contact, and metabolism. BSi/Au can be implemented for high-throughput screening due to outstanding bSi-for-SERS sensitivity and ease of use. Proposed bSi/Au substrate production fully meets the specified requirements for effective SERS of living cells and allows the scalable production of the low-cost SERS-active hydrophilic substrates of outstanding quality and reproducibility.

METHODS

Materials and Substrate Preparation. The silicon used in the experiment was lightly p-doped, 0.5-mm thick silicon wafers. BSi was formed in a cryogenic, inductively coupled plasma reactive ion etcher as reported elsewhere.[57,58] As a plain reference substrate, quartz slides (SiO_2) were used.

Before the vacuum deposition of gold, the substrates were rinsed with ethanol for 10 min, washed in deionized water, and dried in a dry stream of N_2. The Au films were deposited on the bSi and SiO_2 substrates using a Quorum Q150T ES Plus-Turbomolecular pumped coater. Sputtering parameters for targets were as follows: Au, sputter current 50 mA, sputter time 120 s, argon pressure 2 mBar.

Before surface coating with testing molecules or cells, the bSi/Au and SiO_2/Au substrates were held in a N_2 atmosphere to prevent undesirable absorption of impurity molecules by these substrates. Both bSi/Au and SiO_2/Au slides were incubated in the 4-mercaptobenzoic acid (4-MBA, $HSC_6H_4CO_2H$; Sigma, USA) solution at a final concentration of 5×10^{-3} mol/L for 4 h to provide the molecular monolayer formation on the gold-covered surface of the SiO_2 slides and bSi through the −SH group. Then all samples were washed with ethanol flow for 10 min to remove trace amounts of 4-MBA molecules not bound to the surface, dried with N_2, and kept in hermetically closed containers before SERS measurements. For SERS of living cells, the prepared bSi/Au and SiO_2/Au substrates were additionally sterilized at 110 °C for 2 h and then in full sterility placed in plastic Petri dishes in cell culture medium DMEM/F12.

https://dx.doi.org/10.1021/acsami.0c13570
ACS Appl. Mater. Interfaces 2020, 12, 50971−50984

Cell Culture. ATCC C6 (ATCC CCL-107) rat glioma cells were obtained from ATCC, LGC Standards, Ogrodowa 27/29, Kielpin, Poland, and used in all experiments. A DMEM/F12 medium (Gibco) supplemented with 10% fetal bovine serum (Sigma) and 80 μg/mL gentamycin sulfate (Belmedpreparaty, Belarus) was used for cell growth. C6 glioma cells were held in 100% humidity at 37 °C in a 5% CO_2 atmosphere. In the log-phase, cells were trypsinized and centrifuged at 1500 rpm, and 10^5 cells were seeded in standard 3.5 cm plastic Petri dishes with bSi/Au or SiO_2/Au slides placed on the Petri dish bottom. Cells were cultured for 3 days, and all measurements were conducted at 70% cell confluence. To exclude undesirable SERS signals from growth medium components during measurements, it was replaced with Hepes buffer solution (pH 7.2) of the following content (in mmol/L): NaCl − 131, KCl − 5, $MgSO_4$ − 1.3, $CaCl_2$ − 1.3, Hepes − 20, $C_6H_{12}O_6$ − 5.

Fluorescence Microscopy. Fluorescence images were recorded using a fluorescence microscope built around an inverted biological Nikon Eclipse Ti-U with a 40× CFI S Plan Fluor ELWD air objective and operated in the wide-field epi-illumination mode. The excitation source was a 532 nm CW DPSS laser (Crystalaser). The excitation spot diameter was about 200 μm. The laser power after the objective was 60 μW. The excitation laser was focused into the back focal plane of the objective with a 600 mm focal distance achromatic doublet and directed into the objective by a 50/50 beam splitter. The resulting fluorescence was filtered off the excitation light with a long-pass filter (HQ545LP, Chroma) and imaged with an EMCCD (DU-897E-CS0-UVB, Andor). The camera EM gain was 150, the integration time was 0.1 s, and each image was an average of 20 frames.

Cell Viability Detection. Viability determination was performed via the propidium iodide (PI) assay. PI is a cell membrane nonpenetrating fluorescent dye, which becomes strongly fluorescent only if it penetrates the cell membrane and intercalates in DNA molecules. Cells on the bSi/Au substrate were washed twice with Hepes-buffer, and fluorescence measurements were conducted in Hepes-buffer containing 10^{-6} M PI.

The cell death control study was performed by cell permeabilization and fixation with ice-cold ethanol: the cell culture medium was removed, cells on the bSi/Au substrates were gently washed with Hepes-buffer, and the sample was immersed in ice-cold ethanol and stored at 4 °C for 30 min. Then the sample was washed twice with Hepes-buffer and once with distilled water. Measurements were conducted in a medium containing 10^{-6} M PI.

SEM, TEM, and Image Processing. Scanning electron microscopy (SEM) micrographs of investigated samples were obtained using a Helios NanoLab 650 model microscope, manufactured by FEI. Analysis of bSi and bSi/Au was performed with a nominal beam voltage of 3 kV. Transmission electron microscopy (TEM) was performed with a transmission electron microscope Tecnai G2 F20 X-TWIN (FEI, Netherlands, 2011) with the Schottky type field emission electron source.

The bSi surface dimensions were tracked and analyzed manually by open-source software ImageJ (https://imagej.nih.gov/ij/). Surface dimensions are presented as mean ± SD.

SERS. Raman spectral measurements were obtained using an inVia confocal microscopic Raman system (Renishaw) with the 785 nm beam of the diode laser used as the excitation source. The laser power at the samples was restricted to 10 μW for 4-MBA observations (air objective 50×) and 10 mW for living cell spectral detection. Such a power increase for living cells is associated with the measurement conditions and intended to overcome power dissipation and signal loss: living cells were investigated in Petri dishes with 0.5 cm of liquid Hepes-buffer solution above the cells, causing some radiation absorption by water in NIR, and with air objective 20×. An excitation wavelength of 785 nm belongs to the tissue optical window and is not damaging to cells and tissues. Irradiation of living cells with wavelengths of 488 and 514.5 nm with only 5 mW laser power leads to cell overheating and death, but 115 mW power of 785 nm irradiation for more than 1 h does not influence cell viability.[39] The exposure time was 10 s, and the spectra were collected three times to obtain a better signal-to-noise ratio. The intensity was estimated as counts per second. For spectral graphical presentation, simple baseline correction was performed.

Electromagnetic Enhancement Mechanism (EM) Simulation. For evaluation of the localized surface plasmon resonance impact on Raman signal enhancement, Au and Si/Au nanostructure models were designed using FEM-based COMSOL Multiphysics 5.5 software. The simulation domain is composed of a nanostructure with experimentally obtained geometry with an air domain surrounded by a perfectly matched layer. The wavelength-dependent optical properties such as the absorption cross section were simulated. The substrate was excluded from the simulation to reduce computation time. Moreover, the influence of the substrate of the considered Au plasmonic structures is the higher-order effect, and the aim of the simulations was to show the general tendency and to explain the observed SERS enhancement.

Chemical Mechanism (CM) Simulation. The equilibrium geometry, electronic structure, and Raman spectra of the complex 4-MBA/Au, which simulated 4-MBA adsorption on Au, and 4-MBA molecule were simulated using nonempirical density functional theory (DFT). The calculations were carried out with the B3LYP exchange-correlation functional and mixed basis sets using computational chemistry software package Gaussian 16, Revision B.01 for structure optimization and Raman spectral simulation of 4-MBA adsorption on Au. The basis sets for H, C, O, and S atoms were aug-cc-pvdz,[59] which included the polarization function and diffuse functions to all four kinds of atoms. For the Au atom, the valence electrons and the inner shell electrons were described by the LANL2DZ basis set and the corresponding relativistic effective core potentials, respectively.[60] The chemical enhancement (CM) mechanism in SERS spectra involves the formation of new electronic states due to charge transfer (CT) or adsorbate−substrate bonding interactions.[61] The B3LYP functional has the problems with resolving long-range CT processes.[62] For this reason, in order to take into account the CT effect CAM-B3LYP and B3LYP-D3 functionals were used. These functionals provide a more accurate asymptotic behavior for CT transitions. The CAM-B3LYP functional[63] is based on the long-range correction of the exchange potential[64,65] and used the Coulomb-attenuating method (CAM). B3LYP-D3 denotes a calculation with the usual B3LYP functional and a D3 dispersion correction energy term. In this method developed by Grimme, the DFT-Dispersion method appends to the base functional a scaled, damped, and fitted leading term to the dispersion energy series.[66] Thus, in Raman spectral simulations, the DFT/CAM-B3LYP/aug-cc-pvdz/LANL2DZ and DFT/ B3LYP-D3/aug-cc-pvdz/LANL2DZ levels of theory were applied. In our calculations, a scaling factor of 0.97 was used.[67]

For the investigation of the adsorption behavior of 4-MBA on gold nanostructures, a model proposed elsewhere[68] was used, supposing 4-MBA molecule adsorption on one Au atom through the S atom with a parallel orientation. Consideration of more Au atoms during the formation of a complex with a 4-MBA molecule significantly complicates the vibration spectral calculations. Thus, only the Au atom was used in simulations, and as the mass of the Au atom is relatively large, this makes the approximation reasonable.[68]

■ ASSOCIATED CONTENT

Supporting Information

The Supporting Information is available free of charge at https://pubs.acs.org/doi/10.1021/acsami.0c13570.

Determination of the semisphere diameters; SERS-response quality control: time-dependence; laser power range test for the SERS-response; hydrophilic properties of bSi/Au and plastic Petri dish comparison; glioma cells on substrate viability determination (PDF)

https://dx.doi.org/10.1021/acsami.0c13570
ACS Appl. Mater. Interfaces 2020, 12, 50971−50984

AUTHOR INFORMATION

Corresponding Author

Lena Golubewa − *Center for Physical Sciences and Technology, Vilnius LT-10257, Lithuania; Institute for Nuclear Problems, Belarusian State University, Minsk 220006, Belarus;* orcid.org/0000-0003-2125-6366; Email: lena.golubewa@ftmc.lt

Authors

Renata Karpicz − *Center for Physical Sciences and Technology, Vilnius LT-10257, Lithuania;* orcid.org/0000-0001-5884-4538

Ieva Matulaitiene − *Center for Physical Sciences and Technology, Vilnius LT-10257, Lithuania*

Algirdas Selskis − *Center for Physical Sciences and Technology, Vilnius LT-10257, Lithuania*

Danielis Rutkauskas − *Center for Physical Sciences and Technology, Vilnius LT-10257, Lithuania*

Aliaksandr Pushkarchuk − *Institute of Physical Organic Chemistry, National Academy of Sciences of Belarus, Minsk 220072, Belarus; Institute for Nuclear Problems, Belarusian State University, Minsk 220006, Belarus*

Tatsiana Khlopina − *Institute for Nuclear Problems, Belarusian State University, Minsk 220006, Belarus*

Dominik Michels − *Computer, Electrical and Mathematical Science and Engineering Division, 4700 King Abdullah University of Science and Technology, Thuwal 23955-6900, Saudi Arabia*

Dmitry Lyakhov − *Computer, Electrical and Mathematical Science and Engineering Division, 4700 King Abdullah University of Science and Technology, Thuwal 23955-6900, Saudi Arabia*

Tatsiana Kulahava − *Institute for Nuclear Problems, Belarusian State University, Minsk 220006, Belarus*

Ali Shah − *Department of Micro and Nanosciences, Aalto University, Espoo FI-00076, Finland*

Yuri Svirko − *Institute of Photonics, University of Eastern Finland, Joensuu FI-80100, Finland;* orcid.org/0000-0002-2927-6233

Polina Kuzhir − *Institute of Photonics, University of Eastern Finland, Joensuu FI-80100, Finland; Institute for Nuclear Problems, Belarusian State University, Minsk 220006, Belarus;* orcid.org/0000-0003-3689-0837

Complete contact information is available at: https://pubs.acs.org/10.1021/acsami.0c13570

Notes

The authors declare no competing financial interest.

ACKNOWLEDGMENTS

This work was supported by Horizon 2020 RISE DiSeTCom Project 823728, the Academy of Finland (Flagship Programme, Photonics Research and Innovation (PREIN), no 320166, and projects nos 298298 and 334370), joint project no. S-LB-19-4 from the Research Council of Lithuania Foundation, and the Belarusian Republican Foundation for Fundamental Research (BRFFR) project F19LITG-003. P.K. is supported by Horizon 2020 IF TURANDOT project 836816. D.M. and D.L. are supported by KAUST baseline funding. The authors are grateful to Dr. Martynas Skapas and Mr. Martynas Talaikis (Center for Physical Sciences and Technology, Vilnius, Lithuania) for assistance in TEM and Raman measurements, respectively, and to Alesia Paddubskaya (Institute for Nuclear Problems, Belarusian State University, Minsk, Belarus) for valuable discussions and interest to the work.

ABBREVIATIONS

UV, ultraviolet
NIR, near infrared
SERS, surface-enhanced Raman spectroscopy
bSi, black silicon
EF, enhancement factor
E-field, electromagnetic field
EM, electromagnetic mechanism
CM, chemical mechanism
CT, charge transfer
FEM, finite elements method
DFT, density functional theory
SEM, scanning electron microscopy
TEM, transmission electron microscopy
4-MBA, 4-mercaptobenzoic acid
LSPR, localized surface plasmon resonance
GSH, glutathione in the reduced state
GSSG, glutathione in the oxidized state

REFERENCES

(1) Bhalla, N.; Jolly, P.; Formisano, N.; Estrela, P. Introduction to Biosensors. *Essays Biochem.* **2016**, *60*, 1−8.

(2) Sato, H.; Ishigaki, M.; Taketani, A.; Andriana, B. B. Raman Spectroscopy and Its Use for Live Cell and Tissue Analysis. *Biomed. Spectrosc. Imaging* **2019**, *7*, 97−104.

(3) Smith, R.; Wright, K. L.; Ashton, L. Raman Spectroscopy: An Evolving Technique for Live Cell Studies. *Analyst* **2016**, *141*, 3590−3600.

(4) Notingher, I. Raman Spectroscopy Cell-Based Biosensors. *Sensors* **2007**, *7*, 1343−1358.

(5) Cialla, D.; Pollok, S.; Steinbrücker, C.; Weber, K.; Popp, J. SERS-Based Detection of Biomolecules. *NANO* **2014**, *3*, 383−411.

(6) Jia, M.; Li, S.; Zang, L.; Lu, X.; Zhang, H. Analysis of Biomolecules Based on the Surface Enhanced Raman Spectroscopy. *Nanomaterials* **2018**, *8*, 730.

(7) Xu, F.; Ma, F.; Ding, Z.; Xiao, L.; Zhang, X.; Lu, Q.; Lu, G.; Kaplan, D. L. SERS Substrate with Silk Nanoribbons as Interlayer Template. *ACS Appl. Mater. Interfaces* **2019**, *11*, 42896−42903.

(8) Han, G.; Liu, R.; Han, M. Y.; Jiang, C.; Wang, J.; Du, S.; Liu, B.; Zhang, Z. Label-Free Surface-Enhanced Raman Scattering Imaging to Monitor the Metabolism of Antitumor Drug 6-Mercaptopurine in Living Cells. *Anal. Chem.* **2014**, *86*, 11503−11507.

(9) Veloso, A. B.; Longo, J. P. F.; Muehlmann, L. A.; Tollstadius, B. F.; Souza, P. E. N.; Azevedo, R. B.; Morais, P. C.; Da Silva, S. W. SERS Investigation of Cancer Cells Treated with PDT: Quantification of Cell Survival and Follow-Up. *Sci. Rep.* **2017**, *7*, 7175.

(10) Fraire, J. C.; Stremersch, S.; Bouckaert, D.; Monteyne, T.; De Beer, T.; Wuytens, P.; De Rycke, R.; Skirtach, A. G.; Raemdonck, K.; De Smedt, S.; Braeckmans, K. Improved Label-Free Identification of Individual Exosome-like Vesicles with Au@Ag Nanoparticles as SERS Substrate. *ACS Appl. Mater. Interfaces* **2019**, *11*, 39424−39435.

(11) Panikkanvalappil, S. R.; Hira, S. M.; El-Sayed, M. A. Elucidation of Ultraviolet Radiation-Induced Cell Responses and Intracellular Biomolecular Dynamics in Mammalian Cells Using Surface-Enhanced Raman Spectroscopy. *Chem. Sci.* **2016**, *7*, 1133−1141.

(12) Leong, S. X.; Koh, L. K.; Koh, C. S. L.; Phan-Quang, G. C.; Lee, H. K.; Ling, X. Y. In Situ Differentiation of Multiplex Noncovalent Interactions Using SERS and Chemometrics. *ACS Appl. Mater. Interfaces* **2020**, *12*, 33421−33427.

(13) Kim, S.; Kim, T. G.; Lee, S. H.; Kim, W.; Bang, A.; Moon, S. W.; Song, J.; Shin, J. H.; Yu, J. S.; Choi, S. Label-Free Surface-

Enhanced Raman Spectroscopy Biosensor for On-Site Breast Cancer Detection Using Human Tears. *ACS Appl. Mater. Interfaces* **2020**, *12*, 7897−7904.
(14) Park, M.; Hwang, C. S. H.; Jeong, K. H. Nanoplasmonic Alloy of Au/Ag Nanocomposites on Paper Substrate for Biosensing Applications. *ACS Appl. Mater. Interfaces* **2018**, *10*, 290−295.
(15) Mei, R.; Wang, Y.; Yu, Q.; Yin, Y.; Zhao, R.; Chen, L. Gold Nanorod Array-Bridged Internal-Standard SERS Tags: From Ultrasensitivity to Multifunctionality. *ACS Appl. Mater. Interfaces* **2020**, *12*, 2059−2066.
(16) Tan, Y.; Gu, J.; Xu, W.; Chen, Z.; Liu, D.; Liu, Q.; Zhang, D. Reduction of CuO Butterfly Wing Scales Generates Cu SERS Substrates for DNA Base Detection. *ACS Appl. Mater. Interfaces* **2013**, *5*, 9878−9882.
(17) Sitjar, J.; Liao, J.-D.; Lee, H.; Liu, B. H.; Fu, W.-e. SERS-Active Substrate with Collective Amplification Design for Trace Analysis of Pesticides. *Nanomaterials* **2019**, *9*, 1−12.
(18) Shiohara, A.; Wang, Y.; Liz-Marzán, L. M. Recent Approaches toward Creation of Hot Spots for SERS Detection. *J. Photochem. Photobiol., C* **2014**, *21*, 2−25.
(19) Yao, X.; Jiang, S.; Luo, S.; Liu, B. W.; Huang, T. X.; Hu, S.; Zhu, J.; Wang, X.; Ren, B. Uniform Periodic Bowtie SERS Substrate with Narrow Nanogaps Obtained by Monitored Pulsed Electrodeposition. *ACS Appl. Mater. Interfaces* **2020**, *12*, 36505−36512.
(20) Hajduková, N.; Procházka, M.; Štěpánek, J.; Špírková, M. Chemically Reduced and Laser-Ablated Gold Nanoparticles Immobilized to Silanized Glass Plates: Preparation, Characterization and SERS Spectral Testing. *Colloids Surf., A* **2007**, *301*, 264−270.
(21) Fan, M.; Andrade, G. F. S.; Brolo, A. G. A Review on the Fabrication of Substrates for Surface Enhanced Raman Spectroscopy and Their Applications in Analytical Chemistry. *Anal. Chim. Acta.* **2011**, 7−25.
(22) Serpenguzel, A. Luminescence of Black Silicon. *J. Nanophotonics* **2008**, *2*, No. 021770.
(23) Ozturk, S.; Kayabasi, E.; Kucukdogan, N.; Ayakdas, O. Progress in Applications of Black Silicon. *Most Recent Stud. Sci. Art* **2018**, *2*, 1866−1882.
(24) Hsu, C. H.; Wu, J. R.; Lu, Y. T.; Flood, D. J.; Barron, A. R.; Chen, L. C. Fabrication and Characteristics of Black Silicon for Solar Cell Applications: An Overview. *Mater. Sci. Semicond. Proc.* **2014**, *25*, 2−17.
(25) Hoyer, P.; Theuer, M.; Beigang, R.; Kley, E. B. Terahertz Emission from Black Silicon. *Appl. Phys. Lett.* **2008**, *93*, No. 091106.
(26) Wang, X.; Bhadra, C. M.; Yen Dang, T. H.; Buividas, R.; Wang, J.; Crawford, R. J.; Ivanova, E. P.; Juodkazis, S. A Bactericidal Microfluidic Device Constructed Using Nano-Textured Black Silicon. *RSC Adv.* **2016**, *6*, 26300−26306.
(27) Liu, X. L.; Zhu, S. W.; Sun, H. B.; Hu, Y.; Ma, S. X.; Ning, X. J.; Zhao, L.; Zhuang, J. "infinite Sensitivity" of Black Silicon Ammonia Sensor Achieved by Optical and Electric Dual Drives. *ACS Appl. Mater. Interfaces* **2018**, *10*, 5061−5071.
(28) Mironenko, A. Y.; Tutov, M. V.; Sergeev, A. A.; Mitsai, E. V.; Ustinov, A. Y.; Zhizhchenko, A. Y.; Linklater, D. P.; Bratskaya, S. Y.; Juodkazis, S.; Kuchmizhak, A. A. Ultratrace Nitroaromatic Vapor Detection via Surface-Enhanced Fluorescence on Carbazole-Terminated Black Silicon. *ACS Sensors* **2019**, *4*, 2879−2884.
(29) Ivanova, E. P.; Hasan, J.; Webb, H. K.; Gervinskas, G.; Juodkazis, S.; Truong, V. K.; Wu, A. H. F.; Lamb, R. N.; Baulin, V. A.; Watson, G. S.; Watson, J. A.; Mainwaring, D. E.; Crawford, R. J. Bactericidal Activity of Black Silicon. *Nat. Commun.* **2013**, *4*, 1−7.
(30) Singh, J.; Jadhav, S.; Avasthi, S.; Sen, P. Designing Photocatalytic Nanostructured Antibacterial Surfaces: Why Is Black Silica Better than Black Silicon? *ACS Appl. Mater. Interfaces* **2020**, *12*, 20202−20213.
(31) Deng, Y. L.; Juang, Y. J. Black Silicon SERS Substrate: Effect of Surface Morphology on SERS Detection and Application of Single Algal Cell Analysis. *Biosens. Bioelectron.* **2014**, *53*, 37−42.
(32) Gervinskas, G.; Seniutinas, G.; Hartley, J. S.; Kandasamy, S.; Stoddart, P. R.; Fahim, N. F.; Juodkazis, S. Surface-Enhanced Raman Scattering Sensing on Black Silicon. *Ann. Phys.* **2013**, *525*, 907−914.
(33) Jiang, L.; You, T.; Yin, P.; Shang, Y.; Zhang, D.; Guo, L.; Yang, S. Surface-Enhanced Raman Scattering Spectra of Adsorbates on Cu2O Nanospheres: Charge-Transfer and Electromagnetic Enhancement. *Nanoscale* **2013**, *5*, 2784−2789.
(34) Le Ru, E. C.; Etchegoin, P. G. *Principles of Surface-Enhanced Raman Spectroscopy*; Elsevier, 2009. DOI: 10.1016/B978-0-444-52779-0.X0001-3.
(35) Golubewa, L.; Rehman, H.; Kulahava, T.; Karpicz, R.; Baah, M.; Kaplas, T.; Shah, A.; Malykhin, S.; Obraztsov, A.; Rutkauskas, D.; Jankunec, M.; Matulaitiene, I.; Selskis, A.; Denisov, A.; Svirko, Y.; Kuzhir, P. Macro-, Micro-and Nano-Roughness of Carbon-Based Interface with the Living Cells: Towards a Versatile Bio-Sensing Platform. *Sensors* **2020**, *20*, 1−14.
(36) Capocefalo, A.; Mammucari, D.; Brasili, F.; Fasolato, C.; Bordi, F.; Postorino, P.; Domenici, F. Exploring the Potentiality of a SERS-Active PH Nano-Biosensor. *Front. Chem.* **2019**, *7*, 1−11.
(37) Orendorff, C. J.; Gole, A.; Sau, T. K.; Murphy, C. J. Surface-Enhanced Raman Spectroscopy of Self-Assembled Monolayers: Sandwich Architecture and Nanoparticle Shape Dependence. *Anal. Chem.* **2005**, *77*, 3261−3266.
(38) Wu, K.; Rindzevicius, T.; Schmidt, M. S.; Mogensen, K. B.; Xiao, S.; Boisen, A. Plasmon Resonances of Ag Capped Si Nanopillars Fabricated Using Mask-Less Lithography. *Opt. Express* **2015**, *23*, 12965.
(39) Downes, A.; Elfick, A. Raman Spectroscopy and Related Techniques in Biomedicine. *Sensors* **2010**, *10*, 1871−1889.
(40) Shipp, D. W.; Sinjab, F.; Notingher, I. Raman Spectroscopy: Techniques and Applications in the Life Sciences. *Adv. Opt. Photonics* **2017**, *9*, 315.
(41) Zimmermann, A. Nucleus, Nuclear Structure, and Nuclear Functional Changes in Liver Cancer. *In Tumors and Tumor-Like Lesions of the Hepatobiliary Tract;* Springer International Publishing, 2017; pp. 3043−3069. DOI: 10.1007/978-3-319-26956-6_169.
(42) Abramczyk, H.; Surmacki, J.; Kopeć, M.; Olejnik, A. K.; Lubecka-Pietruszewska, K.; Fabianowska-Majewska, K. The Role of Lipid Droplets and Adipocytes in Cancer. Raman Imaging of Cell Cultures: MCF10A, MCF7, and MDA-MB-231 Compared to Adipocytes in Cancerous Human Breast Tissue. *Analyst* **2015**, *140*, 2224−2235.
(43) Desideri, E.; Ciccarone, F.; Ciriolo, M. R. Targeting Glutathione Metabolism: Partner in Crime in Anticancer Therapy. *Nutrients* **2019**, *11*, 1926.
(44) Kreysing, E.; Hassani, H.; Hampe, N.; Offenhäusser, A. Nanometer-Resolved Mapping of Cell-Substrate Distances of Contracting Cardiomyocytes Using Surface Plasmon Resonance Microscopy. *ACS Nano* **2018**, *12*, 8934−8942.
(45) Giebel, K. F.; Bechinger, C.; Herminghaus, S.; Riedel, M.; Leiderer, P.; Weiland, U.; Bastmeyer, M. Imaging of Cell/Substrate Contacts of Living Cells with Surface Plasmon Resonance Microscopy. *Biophys. J.* **1999**, *76*, 509−516.
(46) Kurouski, D.; Postiglione, T.; Deckert-Gaudig, T.; Deckert, V.; Lednev, I. K. Amide i Vibrational Mode Suppression in Surface (SERS) and Tip (TERS) Enhanced Raman Spectra of Protein Specimens. *Analyst* **2013**, *138*, 1665−1673.
(47) Rakić, A. D.; Djurišić, A. B.; Elazar, J. M.; Majewski, M. L. Optical Properties of Metallic Films for Vertical-Cavity Optoelectronic Devices. *Appl. Opt.* **1998**, *37*, 5271−5283.
(48) Brozek-Pluska, B.; Miazek, K.; Musiał, J.; Kordek, R. Label-Free Diagnostics and Cancer Surgery Raman Spectra Guidance for the Human Colon at Different Excitation Wavelengths. *RSC Adv.* **2019**, *9*, 40445−40454.
(49) Zhang, X. Y.; Han, D.; Pang, Z.; Sun, Y.; Wang, Y.; Zhang, Y.; Yang, J.; Chen, L. Charge Transfer in an Ordered Ag/Cu2S/4-MBA System Based on Surface-Enhanced Raman Scattering. *J. Phys. Chem. C* **2018**, *122*, 5599−5605.

(50) Brolo, A. G.; Irish, D. E.; Smith, B. D. Applications of Surface Enhanced Raman Scattering to the Study of Metal-Adsorbate Interactions. *J. Mol. Struct.* **1997**, *405*, 29−44.
(51) Ye, J.; Hutchison, J. A.; Uji-i, H.; Hofkens, J.; Lagae, L.; Maes, G.; Borghs, G.; Van Dorpe, P. Excitation Wavelength Dependent Surface Enhanced Raman Scattering of 4-Aminothiophenol on Gold Nanorings. *Nanoscale* **2012**, *4*, 1606.
(52) Michota, A.; Bukowska, J. Surface-Enhanced Raman Scattering (SERS) of 4-Mercaptobenzoic Acid on Silver and Gold Substrates. *J. Raman Spectrosc.* **2003**, *34*, 21−25.
(53) Phan, H. T.; Haes, A. J. Impacts of PH and Intermolecular Interactions on Surface-Enhanced Raman Scattering Chemical Enhancements. *J. Phys. Chem. C* **2018**, *122*, 14846−14856.
(54) Chen, L.; Sun, H.; Zhao, Y.; Zhang, Y.; Wang, Y.; Liu, Y.; Zhang, X.; Jiang, Y.; Hua, Z.; Yang, J. Plasmonic-Induced SERS Enhancement of Shell-Dependent Ag@Cu2O Core-Shell Nanoparticles. *RSC Adv.* **2017**, *7*, 16553−16560.
(55) Zhu, S.; Fan, C.; Wang, J.; He, J.; Liang, E.; Chao, M. Realization of High Sensitive SERS Substrates with One-Pot Fabrication of Ag-Fe3O4 Nanocomposites. *J. Colloid Interface Sci.* **2015**, *438*, 116−121.
(56) Yang, L.; Jiang, X.; Ruan, W.; Yang, J.; Zhao, B.; Xu, W.; Lombardi, J. R. Charge-Transfer-Induced Surface-Enhanced Raman Scattering on Ag-TiO_2 Nanocomposites. *J. Phys. Chem. C* **2009**, *113*, 16226−16231.
(57) Sainiemi, L.; Jokinen, V.; Shah, A.; Shpak, M.; Aura, S.; Suvanto, P.; Franssila, S. Non-Reflecting Silicon and Polymer Surfaces by Plasma Etching and Replication. *Adv. Mater.* **2011**, *23*, 122−126.
(58) Shah, A.; Stenberg, P.; Karvonen, L.; Ali, R.; Honkanen, S.; Lipsanen, H.; Peyghambarian, N.; Kuittinen, M.; Svirko, Y.; Kaplas, T. Pyrolytic Carbon Coated Black Silicon. *Sci. Rep.* **2016**, *6*, 25922.
(59) Wilson, A. K.; Van Mourik, T.; Dunning, T. H. Gaussian Basis Sets for Use in Correlated Molecular Calculations. VI. Sextuple Zeta Correlation Consistent Basis Sets for Boron through Neon. *J. Mol. Struct. Theochem.* **1996**, *388*, 339−349.
(60) Hay, P. J.; Wadt, W. R. Ab Initio Effective Core Potentials for Molecular Calculations. Potentials for K to Au Including the Outermost Core Orbitale. *J. Chem. Phys.* **1985**, *82*, 299−310.
(61) Ho, C. H.; Lee, S. SERS and DFT Investigation of the Adsorption Behavior of 4-Mercaptobenzoic Acid on Silver Colloids. *Colloids Surf., A.* **2015**, *474*, 29−35.
(62) Dreuw, A.; Head-Gordon, M. Single-Reference Ab Initio Methods for the Calculation of Excited States of Large Molecules. *Chem. Rev.* **2005**, 4009−4037.
(63) Yanai, T.; Tew, D. P.; Handy, N. C. A New Hybrid Exchange-Correlation Functional Using the Coulomb-Attenuating Method (CAM-B3LYP). *Chem. Phys. Lett.* **2004**, *393*, 51−57.
(64) Tawada, Y.; Tsuneda, T.; Yanagisawa, S.; Yanai, T.; Hirao, K. A Long-Range-Corrected Time-Dependent Density Functional Theory. *J. Chem. Phys.* **2004**, *120*, 8425−8433.
(65) Becke, A. D. Density-Functional Thermochemistry. III. The Role of Exact Exchange. *J. Chem. Phys.* **1993**, *98*, 5648−5652.
(66) Grimme, S.; Ehrlich, S.; Goerigk, L. Effect of the Damping Function in Dispersion Corrected Density Functional Theory. *J. Comput. Chem.* **2011**, *32*, 1456−1465.
(67) Russell, D. J., III *NIST Computational Chemistry Comparison and Benchmark Database*; https://cccbdb.nist.gov/intro.asp (accessed Sep 26, 2020).
(68) Ma, W. Q.; Fang, Y.; Hao, G. L.; Wang, W. G. Adsorption Behaviors of 4-Mercaptobenzoic Acid on Silver and Gold Films. *Chin. J. Chem. Phys.* **2010**, *23*, 659−663.

https://dx.doi.org/10.1021/acsami.0c13570
ACS Appl. Mater. Interfaces 2020, 12, 50971−50984

materials

MDPI

Article

Black Silicon: Breaking through the Everlasting Cost vs. Effectivity Trade-Off for SERS Substrates

Lena Golubewa [1,2], Hamza Rehman [2], Yaraslau Padrez [1], Alexey Basharin [2], Sumit Sumit [2], Igor Timoshchenko [1], Renata Karpicz [1], Yuri Svirko [2] and Polina Kuzhir [2,*]

[1] Department of Molecular Compound Physics, State Research Institute Center for Physical Sciences and Technology, Sauletekio Av. 3, 10257 Vilnius, Lithuania
[2] Department of Physics and Mathematics, Center for Photonics Sciences, University of Eastern Finland, Yliopistokatu 7, 80101 Joensuu, Finland
* Correspondence: polina.kuzhir@uef.fi

Abstract: Black silicon (bSi) is a highly absorptive material in the UV-vis and NIR spectral range. Photon trapping ability makes noble metal plated bSi attractive for fabrication of surface enhanced Raman spectroscopy (SERS) substrates. By using a cost-effective room temperature reactive ion etching method, we designed and fabricated the bSi surface profile, which provides the maximum Raman signal enhancement under NIR excitation when a nanometrically-thin gold layer is deposited. The proposed bSi substrates are reliable, uniform, low cost and effective for SERS-based detection of analytes, making these materials essential for medicine, forensics and environmental monitoring. Numerical simulation revealed that painting bSi with a defected gold layer resulted in an increase in the plasmonic hot spots, and a substantial increase in the absorption cross-section in the NIR range.

Keywords: black silicon; surface-enhanced Raman spectroscopy; surface plasmon resonance; nanostructures; etching

Citation: Golubewa, L.; Rehman, H.; Padrez, Y.; Basharin, A.; Sumit, S.; Timoshchenko, I.; Karpicz, R.; Svirko, Y.; Kuzhir, P. Black Silicon: Breaking through the Everlasting Cost vs. Effectivity Trade-Off for SERS Substrates. *Materials* **2023**, *16*, 1948. https://doi.org/10.3390/ma16051948

Academic Editors: Hsiang-Chen Chui and Rui Li

Received: 31 December 2022
Revised: 22 February 2023
Accepted: 26 February 2023
Published: 27 February 2023

1. Introduction

Silicon is the most widely used electronics and photonics semiconducting material. Although a polished silicon possesses a high reflectivity in the ultraviolet (UV) [1], visible (vis) and near infrared (NIR) range [2], the micro-structuring of silicon may make it remarkably absorptive [3–5]. As a result, the micro-structured silicon surface acquires a deep black color, and it is often referred to as "black silicon" (bSi).

Having been discovered accidentally, bSi was initially considered an unwanted side-product [6]; however, nowadays it is undergoing a rebirth because of new opportunities it opens in a number of applications. The surface of bSi may comprise of various shapes and geometries, including needles, pyramids, cones, pillars, holes, columns, etc., which enhance absorption and suppress light scattering [7] via effective light trapping [8]. The suppression of specular reflectance and enhancement of absorbance can be described in terms of the structural defects in the Si lattice or impurities (specifically sulfur) which appear during surface micro-structuring [7]. These defects and impurities create IR absorbing states in the band gap and are also responsible for the trapping of photoexcited carriers (for flat silicon, the band gap is 1.07 eV) [9]. The absorbance caused by these defects is enhanced by multiple reflections between the microstructures of bSi, which, in turn, suppresses specular reflection and increases absorbance.

The significant increase in absorbance in UV-vis and NIR spectral ranges by bSi, compared to bulk silicon, spans the applications of bSi to many areas, including solar cells [10,11], photo-electrocatalysis [12,13], visible light and NIR sensors [9,14]. Moreover, there is also a trend to replace indium gallium arsenide and germanium in commercial NIR photodetectors [15] with bSi because it is cost-effective and enables integration of the photodetectors into a silicon platform.

The high absorptive properties of bSi in a wide spectral range are also beneficial for nanoplasmonic applications, including surface enhanced Raman spectroscopy (SERS) [16], which employs the enhancement of the light field in the vicinity of the metal surface, where the eigenfrequency of the electron ensemble match the light frequency. If the molecules of the analyte are situated in the vicinity of the interface between the metal plasmonic particle and the environment, the surface plasmon resonance (SPR) results in an increase in the Raman scattering cross-section by several orders of magnitude, allowing one to detect trace amounts of molecules adsorbed onto the interface [17,18]. When using bSi as a supporting material for the formation of plasmonic nanostructures, significant UV-vis–NIR absorption and the phenomenon of light-trapping by the micro- and nano-structured surface of bSi may drastically increase the local electromagnetic field enhancement on the metal–environment interface. This, in its turn, will cause the increase in the Raman signal of the adsorbed molecules of the analyte.

The SERS approach is a reliable method for detecting low concentrations of molecules [19], investigating molecule–molecule [20] or molecule–surface [21] interactions, investigating living cells functions [22] and detecting pesticides [23] and poisons [24], which obviously extends its applications from fundamental science to practice, including biomedicine, forensics, environment, security, etc. However, obtaining very specific information from analytes in the form of a 'fingerprint' vibrational spectra, SERS exhibits some drawbacks, which significantly reduce its applications in real life. Namely, SERS substrate fabrication always presents a trade-off between stability, cost, efficiency, reliability, uniformity, density of hot-spots and scalability. Commonly used approaches for SERS substrate fabrication are based either on colloidal solutions of noble metal nanoparticles or nanostructured surfaces of noble metal slabs and films. The former usually give significant enhancement of Raman intensity; however, they are non-stable [25], storage condition-dependent [26], inconvenient in routine use [27], require immobilization on the flat surface for measuring [28], poorly reproducible and non-uniform [27,28]. The latter allows one to control the density of hot spots and to be fabricated in large areas, but they are expensive and give rather limited signal enhancement.

Pronounced surface micro-structuring of bSi in combination with exceptional absorbance may serve as a regular, stable and highly uniform support for plasmonic nanostructures, ensuring a strong Raman signal enhancement. However, strong dependence of SPR on the geometry of plasmonic structures [29–31] and their three-dimensional organization implies bSi profile control.

Nano- and micro-structured bSi can be fabricated by metal-assisted chemical etching, femtosecond laser assisted fabrication [8,32], laser chemical etching [7], wet chemical etching and reactive ion etching (RIE) [33]. The latter is the most suitable option when aiming for uniform surface structure coverage over large areas. The RIE system uses a plasma source consisting of highly reactive ion species, and when they bombard the sample, a chemical reaction takes place that selectively erodes away the sample surface [34].

In the present study, we fabricate bSi by using room temperature (RT) Inductively Coupled Plasma (ICP) RIE in such a way that the created surface profile supports a gold plasmonic layer of a thickness as low as almost ten nanometers with distributed cracks that still provides satisfactory Raman signal enhancement. Fabrication by RT ICP-RIE, instead of cryogenic ICP-RIE, and an extremely reduced defected gold layer allowed for a significant reduction in the cost of obtaining the bSi-based substrates. We developed the 'recipe' for fabrication of bSi substrates by supporting SERS signal enhancement at the NIR (785 nm) excitation, which meets biomedical application requirements and does not lead to overheating and thermal damage of the analyte that may occur at the vis-range excitation [35–37]. Moreover, uniformity of vertically aligned hot spots on bSi microstructures and the opportunity to control their spatial distribution over large areas open the way towards the detection of extremely low amounts of molecules, though the integration of the signal obtained from the whole substrate area has uniform signal enhancement. We show that bSi based SERS substrates provide a breakthrough in the

trade-off between cost and efficiency, making this an important step towards a simple, effective, low-cost and reliable sensing technique.

2. Materials and Methods

Single side polished 2"x 275 ± 25 µm p-doped Si <100> wafer with bulk resistivity of 1–30 Ohm·cm was used for the fabrication of black silicon SERS substrates. To ensure that the surface impurities of the substrate did not affect the fabrication process, the wafers were pre-cleaned with acetone and isopropyl alcohol in an ultrasonic bath at 60 W/20 °C for 10 min and 5 min, respectively. To further ensure that there were no left-over dirt particles, the wafers were oxygen plasma treated for 2 min at 20 sccm flow rate and at a radio frequency (RF) power of 150 W, using Plasma-Etch (PE-50, Plasma Etch Inc.; Carson City, NV, USA).

To obtain bSi with different surface profiles suitable for SERS and to optimize the procedure of bSi fabrication and gold coating, the Bosch etching process was used [38,39]. This cost efficient and relatively fast method allows one to obtain uniformly distributed high aspect ratio relief features. Through the cyclic Bosch process, we can obtain self-masked black silicon structures within a single RIE system under controlled environmental conditions.

The process consists of the following two steps: (i) formation of plasma-polymerized fluorocarbon islands from C_4F_8 gas [40] serving as a mask, and (ii) etching using SF_6/O_2 gas combination. For the deposition stage, ICP is employed in addition to RIE. This step allows producing high density plasma with low ion bombardment energy at lower pressures needed for micro-masking. Helium backside cooling was used to keep the temperature of the wafer controlled. The deposition/etching parameters used for bSi fabrication are presented in Table 1. The time of etching stage varied in the range of 18–30 min to reveal its influence on the bSi surface geometrical features. Morphological analysis was performed using Zeiss LEO 1550 scanning electron microscope (SEM). All presented images were obtained at 5 kV acceleration voltage using the InLens detector. The SEM images of bSi samples etched at different times are presented in Figure 1. The sizes of related bSi geometrical features are summarized in Table 2. All dimensional characteristics were extracted from SEM images using open-source ImageJ software.

Table 1. Deposition/etching parameters for bSi fabrication.

	Gasses	Flow (sccm)	Time (min)	RF (W)	ICP (W)	Pressure (mTorr)	DC Bias (V)	Temperature (°C)	He-Backside Cooling (sccm)
Deposition	C_4F_8/SF_6	40:1	1	20	295	20	100	20	5
Etching	SF_6/O_2	10:9	18–30	30	0	30	100	20	10

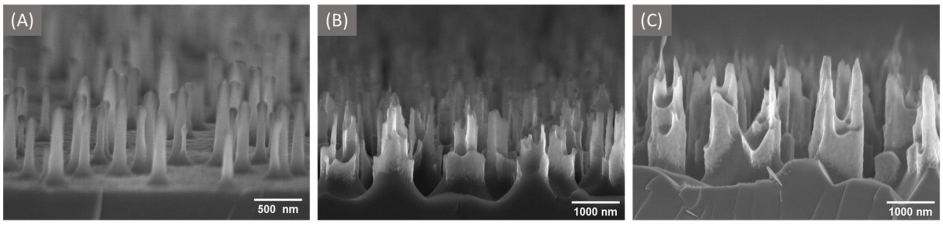

Figure 1. The micro-structured silicon surface obtained at the etching time of (**A**) 18 min, (**B**) 25 min, (**C**) 30 min.

Table 2. Geometrical parameters of structures covering the Si substrate at different etching times.

Etching Time (min)	Height (nm)	Apex Thickness (nm)	Base Thickness (nm)	Pillars Density, pcs/μm^2
				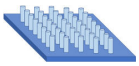
18	639 ± 126	112 ± 21	110 ± 32	4.33
25	1625 ± 298	125 ± 36	638 ± 155	1.12
30	2217 ± 433	144 ± 63	832 ± 377	0.56

The next step was bSi coating with the gold layer using Q300T Plus magnetron sputter (Quorum Technologies Ltd.; Lewes, UK) at a pressure of 0.001 mbar and sputter current of 80 mA. The bSi samples that were etched at different times and had different surface areas were covered with a layer of gold under the same conditions for which 25 nm of gold on a flat SiO_2 substrate occurs. Hereinafter, bSi sputtered with Au are labeled as bSi18, bSi25 and bSi30, related to their etching times of 18, 25 and 30 min, respectively.

Further, the bSi/Au substrates were treated with N_2 to protect them from undesired adsorption on their surface before coating them with the analyte. Quartz slides were sputtered with gold (SiO_2/Au) under the same conditions as bSi substrates, to be used for comparison.

Measurements for all fabricated SiO_2/Au and bSi/Au substrates were performed under the same conditions. The substrates were incubated for 4 h in a solution of 4-mercaptobenzoic acid (4-MBA, $HSC_6H_4CO_2H$; Sigma; Saint Louis, MO, USA) of a concentration of 0.005 mol/L in ethanol to facilitate the formation of a molecular monolayer on the gold surface of these substrates, through the -SH group. After that, all the samples were washed with ethanol for 10 min so that unbounded 4-MBA molecules were removed. The samples were dried with N_2 before proceeding with Raman measurements.

Raman and SERS measurements of 4-MBA (bulk) and 4-MBA self-assembled monolayers (SAM) on SiO_2/Au and bSi/Au, respectively, were performed by inVia (Renishaw, UK) Raman spectrometer. Two excitation lasers were used, with wavelengths of 785 nm and 514 nm, delivering 5 mW and 3 mW, respectively, on the sample surface at an exposure time of 10 s. The grating 1200 line/mm and a microscope air objective of ×50 magnification, NA 0.75 were utilized. The intensity was recorded as counts per second, and simple baseline correction was performed for better spectral graphical representation. Spectra were collected from at least three points on the sample and then averaged.

To evaluate structural uniformity of the substrates, SERS mapping was performed over an area of 10 × 10 μm^2 with 1 μm spatial resolution at 785 nm excitation wavelength, delivering 0.3 mW on the sample surface for an exposure time equal to 5 s.

3. Experimental Results

Sputtering of the bSi samples with gold resulted in the formation of plasmonic nanostructures of various shapes. Typical silicon-gold structures are presented in Figure 2. Gold nanostructure parameters (thickness, shape, uniformity) are summarized in Table 3. The more developed surface of samples bSi25 and bSi30 contributed to the formation of an almost two-times thinner layer of gold, compared to sample bSi18. The gold layer is non-continuous in all samples; however, some differences between the samples are revealed. In bSi18, the area in the pillar base proximity remains uncovered, but the gold layer is uniform and dense between the rarely distributed thin pillars. In contrast, in case of bSi25 and bSi30, the pillars and their close vicinities are covered by a somewhat-uniform gold pattern, while the interpillar areas are not gold painted (see Figure 2B,D,F). As a result, the Si band is always present in the Raman and SERS spectra, collected from the surfaces.

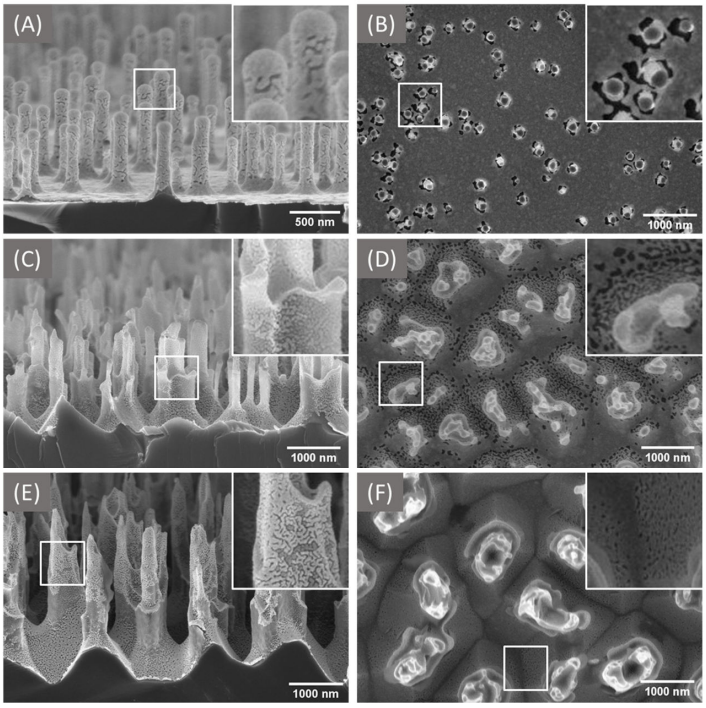

Figure 2. SEM side- and top-view images of the bSi18 (**A**,**B**), bSi25 (**C**,**D**), bSi30 (**E**,**F**), sputtered with Au. Inset images (**B**–**F**) are 800 × 800 nm and (**A**) is 400 × 400 nm.

Table 3. Parameters of the structures and surfaces of the bSi.

Sample	Thickness of Au Layer (nm)	Type of Geometry	Area Uncovered with Au (%)
bSi18	25 ± 5	Cylindrical pillars	8.24 (98 μm^2 was analyzed)
bSi25	14 ± 5	Cylindrical pillars on stump	9.03 (49 μm^2 was analyzed)
bSi30	13 ± 4	Spiked mountains	Difficult to analyze. Very mosaic structure

This peculiarity of the bSi-based SERS substrates can be employed to determine the concentrations of reagents in solutions. The Raman signal from Si serves as a reference to normalize the SERS signal of the detected molecules at hot spots, in terms of their non-uniform distribution over the surface [41]. The pillars in all three samples are densely covered with gold nanoparticles, which may serve as hot spots for SERS (see Figure 1A,C,E and corresponding inset).

In all three analyzed cases, bSi/Au substrates comprise quasi-cylindrical 'pillars' covered with defected gold (enriched with crucks or 'plasmonic holes'), which might be beneficial for substantial SERS enhancement.

To evaluate the efficiency of the fabricated substrates for SERS applications, we used 4-MBA as a standard test molecule [42]. It exhibits a characteristic Raman spectrum (see Figure 3) and may form a self-assembled monolayer (SAM) of molecules on the surfaces covered with gold, through the formation of covalent bonding S-Au [43]. This process is

easily monitored in Raman and SERS spectra as the band 2570 cm^{-1} arising from -SH in 4-MBA disappears in the spectrum of SAM and a new band associated with S-Au at 257 cm^{-1} appears [44]. To reveal the effect of bSi structures in the enhancements of the Raman signal intensity, we used quartz slides sputtered with gold under equivalent conditions, as a reference. The spectrum of SAM of 4-MBA on the SiO_2/Au obtained at 785 nm excitation is presented in Figure 3. The gold nanostructures formed on the flat SiO_2 surface gave no Raman intensity enhancement, as no characteristic 4-MBA bands were detected except the Raman spectrum of SiO_2 substrate itself.

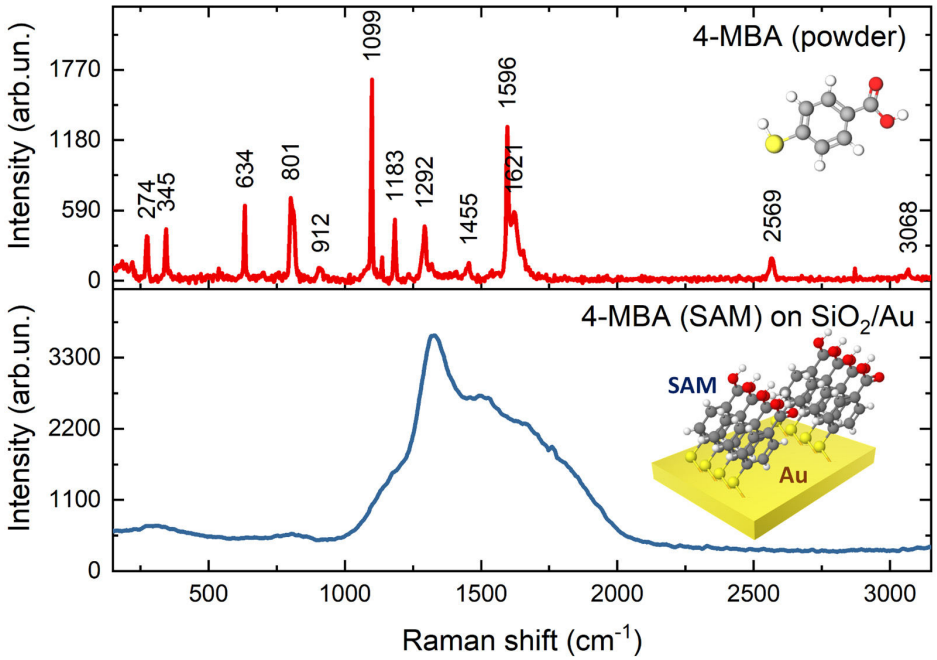

Figure 3. Raman spectra of 4-MBA powder and SAM of 4-MBA molecules on SiO_2/Au. Measurements were performed at the following conditions: λ_{ex} = 785 nm, laser power = 3 mW, accumulation time = 10 s. 4-MBA composition: Gray—carbon atoms, red—oxygen atoms, yellow—sulfur atom, white—hydrogen atoms.

In contrast to the SiO_2/Au substrate with SAM of 4-MBA, all bSi/Au substrates provided the enhancement of 4-MBA Raman signal. The enhancement of Raman signal occurs when the excitation wavelength coincides with the wavelength of surface plasmons. The bSi/Au substrates with 4-MBA SAMs were analyzed under 514 nm and 785 nm excitation. No resonances were detected for 514 nm excitation, while for the excitation at 785 nm, significant Raman signal enhancement was obtained (see Figure 4A,B for 514 nm and 785 nm excitation, respectively). The characteristic bands in SERS spectra of 4-MBA on bSi/Au substrates and their assignments are summarized in Table 4.

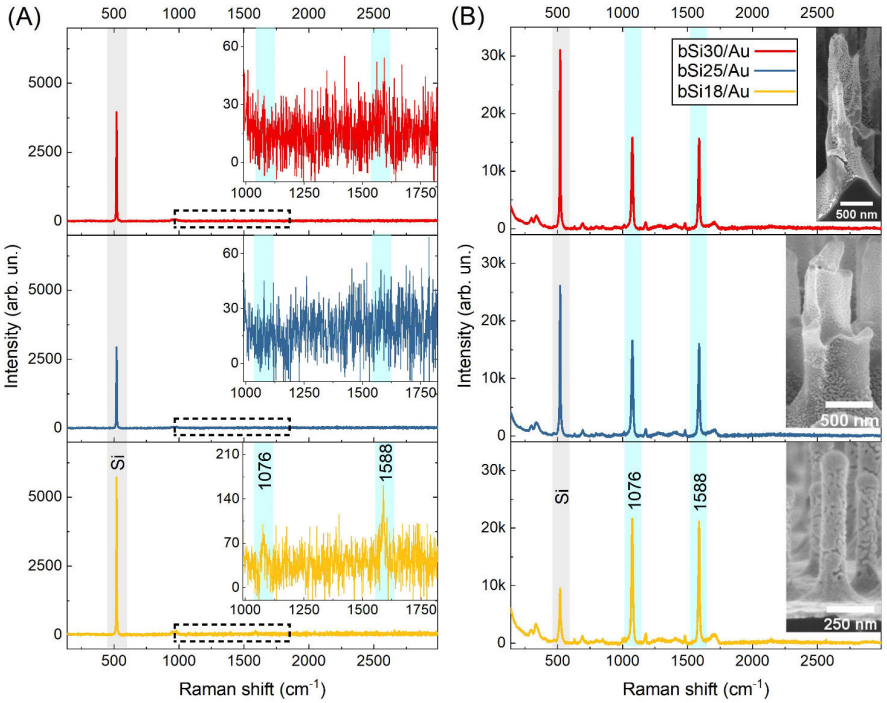

Figure 4. SERS spectra of 4-MBA on (**A**) 514 nm (10 s, 5 mW) and (**B**) 785 nm (10 s, 3 mW) excitation wavelengths on bSi/Au samples.

Table 4. Assignment of the characteristic bands of both Raman spectra of bulk 4-MBA and SERS spectra of SAM of 4-MBA on bSi18/Au [45,46].

4-MBA Bulk (cm^{-1})	4-MBA on bSi18/Au (cm^{-1})	Peak Assignments
	257 (w)	ν(Au-S)
–	520 (m)	Si (E_{2g} mode)
634 (m) #	632 (w)	ν_{6b} + δ(COOH) deformation
–	691 (m)	γ(CH) out of plane
801 (m)	–	ν_{10a} in-plane aromatic ring breathing mode + -COH deformation
–	848 (w)	β(COO^-)
912 (w)	–	β(SH)
1099 (s)	1076 (s)	$\nu_{12}(a_1)$ in-plane aromatic ring breathing mode + ν(CS)
1183 (m)	1182 (w)	$\nu_9(a_1)$ + δ(CH) deformation
1292 (m)	–	ν_3
1455 (w)	1481 (w)	ν(CC) + γ(CH)
1596 (s)	1588 (s)	$\nu_{8a}(a_1)$ totally symmetric aromatic ring vibration
1621 (m)	–	ν(C=O), ν(OC) + δ(HOC)
–	1706 (m)	ν(C=O), COOH are hydrogen bonded [46]
2569 (m)	–	ν(SH) stretching mode

The vibrational modes are as follows: ν—stretching; β—bending; δ—deformation; γ—out of plane deformation. (w), (m) and (s) indicate 'weak', 'medium' and 'strong' bands in the spectra, respectively.

The obtained experimental results are in good agreement with the simulations performed in [45]. The maximum of the absorption cross-section for Si@Au core@shell structures, with characteristic dimensions of 68–88 nm diameter for Si core and 21 nm thickness of the gold shell, is around 780–800 nm, and thinning of the gold layer results in the red shift of the absorption cross-section of nanostructures of this type. These structures correspond to the bSi apex with a gold cap for all bSi samples in our experiments. Moreover, it was demonstrated in [45] that vertical alignment of the groups of gold nanostructures with diameters of 50 nm, which are overlapped with each other and form dumbbell-like structures, have weakly pronounced absorption cross-section maxima of around 500–520 nm and intense absorption cross-section maxima in the NIR range (600–1000 nm). These simulations explain the high 4-MBA SERS signal of molecular monolayers on all the bSi/Au substrates under the 785 nm excitation and support insignificant but observable SERS spectra of 4-MBA molecules detected with 514 nm excitation from bSi18. As it follows from the parameters of the gold layer summarized in Table 3 and simulation results [45], only semi-spheres with a radius of 25 nm exhibit satisfactory absorption at 500–520 nm, which can provide SERS signal enhancement. The decrease in the gold layer thickness, which occurred for the samples bSi25 and bSi30 due to their more developed surface and larger cone-like structures, led to no SERS signal enhancement at 514 nm excitation. However, the vertical alignment of gold nanostructures and silicon core provided bSi25 and bSi30 with efficiency in NIR (see Figure 4).

The substrates were tested for the uniformity of the SERS signal enhancement. All studied bSi substrates are characterized by quite uniform SERS intensity distributions, and the standard deviations for the 1588 cm^{-1} band intensity of 4-MBA molecules were 6.1%, 5.2% and 4.3% (see Figure 5). However, the bSi18 substrate, due to the circumstances described above, provides significantly larger SERS signal enhancement.

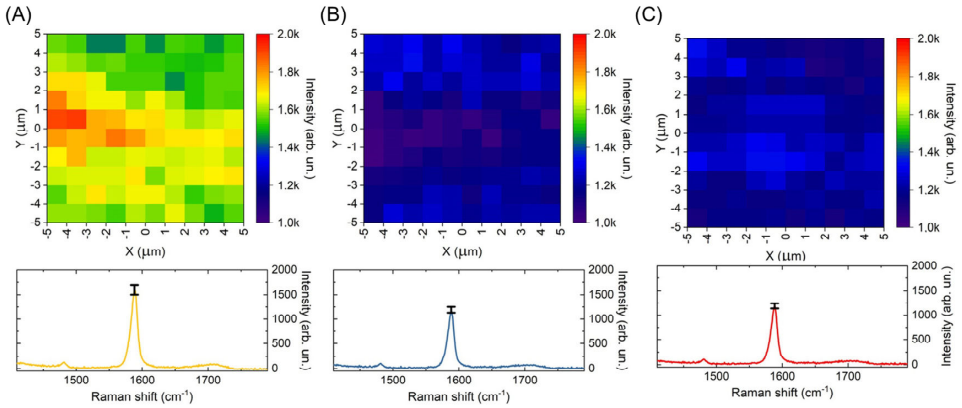

Figure 5. Spatial distributions of SERS signal on 1588 cm^{-1} for 4-MBA on (**A**) bSi18/Au, (**B**) bSi25/Au and (**C**) bSi30/Au samples.

4. Numerical Simulation

Along with the Si@Au core@shell structures responsible for SERS enhancement in the NIR range, cracks in the thin gold layer covering the silicon pillars (see Figure 2) may give rise to a strong enhancement of the local electric field, due to plasmon hot spots localized on the cracks' edges. The light absorption of bSi/Au substrates comprising bSi quasi-cylindrical 'pillars' covered with a defected (i.e., enriched with plasmonic hot spots) gold layer was studied by averaging the light scattered over the pilar surface. The scattering cross-section of a pillar illuminated by a plane wave along the pillar axis and the

polarization in a perpendicular direction to this axis can be described in terms of the dipole moments of hot spots randomly distributed on its surface as the following [47,48]:

$$\sigma = \frac{{k_0}^4}{6\pi{\varepsilon_0}^2|E_0|^2}\left|\sum_i p_i\right|^2 \quad (1)$$

where p_i is the dipole moment of the ith hot spot, summation is carried out over all hot spots on the pillar, and E_0 and k_0 are amplitude and wave number of the incident wave, respectively.

One can observe from Figure 6 that cracks in the gold layer increase the pillar absorption cross-section in the near-IR spectral range, i.e., plasmon hot spots provide up to one order of a magnitude enhancement for the gold-plated pillar at wavelengths longer than 800 nm. However, for all types of bSi geometries, in the visual part of the spectrum, the absorption cross-section of pillars covered with a perfect gold layer slightly exceeds that of the pillars having cracks in the gold coating. By comparing the data, one can see that a decrease in the gold layer thickness from 25 nm to 13 nm can be compensated by the larger size of the pillars (bSi25 and bSi30 geometries in Figure 6).

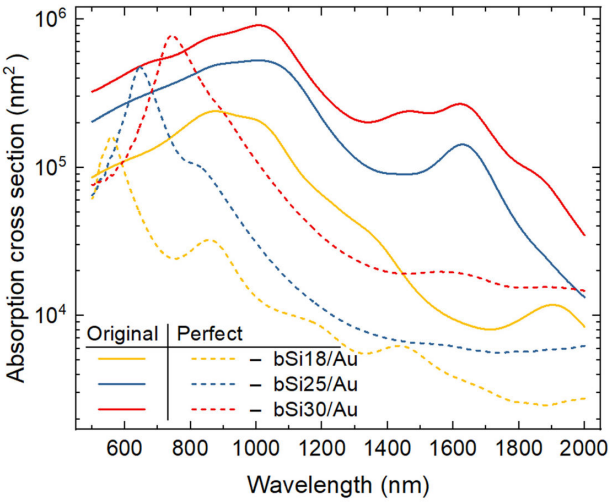

Figure 6. Absorption cross-section of individual pillars of bSi18, bSi25 and bSi30 geometry (taken from Table 3), either coated with perfect gold layer without cracks (perfect, dashed lines) or by defected gold-comprising cracks (original, solid lines).

The electric field distribution along the surface of the gold painted pillars were obtained using Comsol Multiphysics by using parameters (pillar size, distance between pillars, gold thickness and crack size) we observed in the experiment (see Table 3). By considering different distributions of the hot spots over a pillar surface, we calculated the absorption cross-section of an individual pillar. The absorbance of the whole bSi surface was obtained by using periodic boundary conditions. The values and dispersion law of silicon refraction index and extinction coefficient were taken from [49].

Figure 7 shows absorbance of an array of gold covered silicon pillars with different distributions of cracks. One can see that in the wavelength range 800–2000 nm, the covering of bSi with a defected gold layer increases the absorbance because of local field enhancement at the gold layer defects. Specifically, in the NIR spectral range, the absorbance of bSi

covered with cracked gold is 4–8 times higher than that of samples comprising an array of smooth bSi/Au pillars.

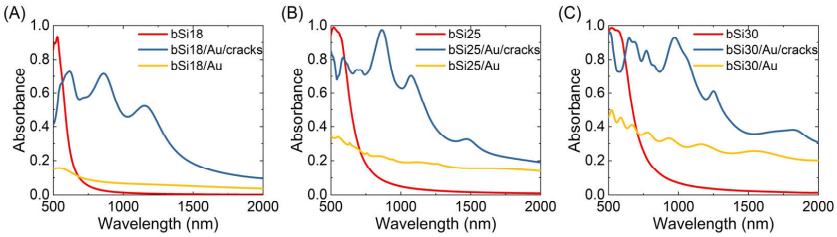

Figure 7. Calculated absorbance spectra for array of pillars of bare, covered with continuous and cracked gold layer bSi of the following three different geometries: bSi18 (**A**), bSi25 (**B**) and bSi30 (**C**). Geometrical parameters are taken from Table 3. Silicon refractive index, n, and extinction coefficient, k, were taken in the intervals 4–3.46 and 0.03–4.2 $\times$ 10^{-8}, respectively, for the wavelengths 500–2000 nm [49] in the simulations.

For all samples, in the vicinity of the reflection suppression 'threshold' wavelength (500–750 nm), the measured reflectivity was 30–35% higher than those obtained by numerical simulation. Such a discrepancy originates from the uncontrollable doping of silicon in the course of RIE [50] that was not taken into account in the numerical simulation, aiming at a qualitative rather than quantitative description of the reflectance spectra.

5. Discussion

Both numerical and experimental results demonstrate that sputtering with very a thin (approx. 10 nm) but cracked gold layer allows one to achieve stronger—in comparison with 'pyramidal' bSi [45]—enhancement of the Raman signal. Importantly, silicon outperforms cheaper glass materials as a plasmonic nanostructures support because the etch rate of glass is very low and is only 1/40th of the Si etch rate with fluorine radicals [51]. This makes micro-structuring of glass by ICR-RIE much more complex and time-consuming than bSi fabrication. Glasses are inhomogeneous, both chemically and structurally, and this inhomogeneity significantly complicates 3D or even 2D patterning, while the charging effects, which accompany the etching process of dielectrics, may drastically influence the reaction progress.

In terms of the choice of fabrication method, RT ICP-RIE also outperforms other techniques, including MACE, which requires using gold (Au), silver (Ag), aluminum (Al), copper (Cu) and nickel (Ni) catalysts [52]. In the one-step MACE process, metal on the surface emerges from the etching aqueous solutions, containing metal nitrates, while in the two-step MACE process, metals are physically deposited on the silicon surface before the chemical etching step [53]. After the etching step, a metal catalyst moves inside the Si wafer and locates itself at the bottom of silicon structures (deep in the pore), preventing formation of the 3D distribution of hot spots. However, such a 3D arrangement of the plasmonic hot spots on the bSi surface increases (in comparison with 2D distribution) the probability for the molecules of the analyte to meet a hot spot, thus significantly improving the sensitivity. Moreover, we demonstrate that cracks in the gold layer and gaps between the deposited gold islands provide significant enhancement of the Raman signal.

To sum up, we demonstrated that bSi offers the cheapest, most efficient, and reliable SERS substrate. The cost reduction was achieved by (i) the use of RT ICP-RIE instead of more complex and expensive cryogenic ICP-RIE, and (ii) the reduction in gold layer thickness. Until very recently, all the proposed SERS substrate fabrication techniques were based on very thick noble metal layers. For instance, in [54], the Ag layer thickness was 150 nm to achieve satisfactory Raman signal. In [55], the authors used a 100 nm thick layer

of gold (RT ICP-RIE), in [56], the gold layer thickness was even larger and amounted to 400 nm (cryo-ICP-RIE), and in [57], the thickness of the deposited aluminum layer was around 1000 nm (ICP-RIE, temperature not stated). However, when the noble metal layer is of hundreds of nanometers, the 3D packaging of plasmonic nanostructures does not occur. Black silicon only serves as a supporting material for 2D nanoparticle distribution, so that the substrate could be replaced by another, easy to manufacture rough material. In the bSi structures fabricated and analyzed in this study, the geometry of the bSi is used to provide efficient Raman signal enhancement in full.

6. Conclusions

We fabricated the black Si substrate with the controllable surface profile covered in a ten nanometers thick gold layer. The SERS measurements with 4-MBA revealed that the fabricated substrates allow one to obtain satisfactory Raman signal enhancement with excellent spatial uniformity (less than 6% signal intensity variation over a 20×20 μm^2 area) at the NIR excitation. The obtained results indicate that bSi can be employed for scalable fabrication of affordable SERS substrates, which may become a stable, simple and reliable consumable material in laboratory routine, providing relatively high sensitivity at low cost.

Numerical simulation was performed to calculate the absorbance of bSi/Au samples by considering the geometrical features of silicon pillars and non-perfect coverage with gold. According to modeling results, for all geometries of bSi surface relief, we observed a substantial increase in the NIR absorption cross-section of individual bSi pillars covered with the defected gold, in which cracks work as plasmonic hot spots. For more developed bSi surfaces (e.g., bSi25 and bSi30 in Table 3), even the sputtering of the structure with very thin, <15 nm, but cracked gold allows us to achieve strong Raman signal due to significant enhancement of the local field in the vicinity of the densely distributed hot spots.

Author Contributions: Conceptualization and design of the experimental study, P.K. and L.G.; data acquisition, L.G., H.R. and S.S.; black silicon substrate fabrication, H.R. and S.S.; data analysis and interpretation, L.G., Y.P., H.R., I.T. and R.K.; absorption theory and simulations, A.B. and L.G.; paper drafting, L.G., H.R. and Y.P.; paper revision, editing and final version preparation, L.G., R.K., P.K. and Y.S. All authors have read and agreed to the published version of the manuscript.

Funding: The study was accomplished with the financial support of Academy of Finland (Flagship Programme PREIN, decision 320166, and grant 343393), Horizon 2020 RISE DiSeTCom (Project No. 823728) and Horizon Europe FLORIN (Project No. 101086142).

Institutional Review Board Statement: Not applicable.

Informed Consent Statement: Not applicable.

Data Availability Statement: Data are available from the correspondent author by reasonable request.

Acknowledgments: The authors are grateful to Isaac Otto from the University of Eastern Finland for the SEM measurements.

Conflicts of Interest: The authors declare no conflict of interest.

References

1. Lv, J.; Zhang, T.; Zhang, P.; Zhao, Y.; Li, S. Review Application of Nanostructured Black Silicon. *Nanoscale Res. Lett.* **2018**, *13*, 110. [CrossRef] [PubMed]
2. Yuan, H.C.; Yost, V.E.; Page, M.R.; Stradins, P.; Meier, D.L.; Branz, H.M. Efficient Black Silicon Solar Cell with a Density-Graded Nanoporous Surface: Optical Properties, Performance Limitations, and Design Rules. *Appl. Phys. Lett.* **2009**, *95*, 123501. [CrossRef]
3. Lu, J.; Zhuang, W.; Yang, W.; Zhang, X.; Su, G.; Gong, X.; Yuan, J.; Sui, J.; Zhou, Y.; Zhang, G.; et al. Enhanced Absorption in the Wide Wavelength Range: Black Silicon Decorated with Few-Layer PtS2. *J. Phys. Chem. C* **2021**, *125*, 27335–27343. [CrossRef]
4. Sarkar, S.; Elsayed, A.A.; Nefzaoui, E.; Drevillon, J.; Basset, P.; Marty, F.; Anwar, M.; Yu, Y.; Zhao, J.; Yuan, X.; et al. NIR and MIR Absorption of Ultra-Black Silicon (UBS). Application to High Emissivity, All-Silicon, Light Source. In Proceedings of the IEEE International Conference on Micro Electro Mechanical Systems (MEMS), Virtual, 25–29 January 2019; Institute of Electrical and Electronics Engineers Inc.: Piscataway, NJ, USA, 2019; Volume 2019, pp. 860–862.

5. Zhang, P.; Li, S.; Liu, C.; Wei, X.; Wu, Z.; Jiang, Y.; Chen, Z. Near-Infrared Optical Absorption Enhanced in Black Silicon via Ag Nanoparticle-Induced Localized Surface Plasmon. *Nanoscale Res. Lett.* **2014**, *9*, 519. [CrossRef] [PubMed]
6. Fan, Z.; Cui, D.; Zhang, Z.; Zhao, Z.; Chen, H.; Fan, Y.; Li, P.; Zhang, Z.; Xue, C.; Yan, S. Recent Progress of Black Silicon: From Fabrications to Applications. *Nanomaterials* **2021**, *11*, 41. [CrossRef] [PubMed]
7. Wu, C.; Crouch, C.H.; Zhao, L.; Carey, J.E.; Younkin, R.; Levinson, J.A.; Mazur, E.; Farrell, R.M.; Gothoskar, P.; Karger, A. Near-Unity below-Band-Gap Absorption by Microstructured Silicon. *Appl. Phys. Lett.* **2001**, *78*, 1850–1852. [CrossRef]
8. Wen, Z.; Shi, H.; Yue, S.; Li, M.; Zhang, Z.; Wang, R.; Song, Q.; Xu, Z.; Zhang, Z.; Hou, Y. Large-Scale Black Silicon Induced by Femtosecond Laser Assisted With Laser Cleaning. *Front. Phys.* **2022**, *10*, 235. [CrossRef]
9. Zhong, H.; Ilyas, N.; Song, Y.; Li, W.; Jiang, Y. Enhanced Near-Infrared Absorber: Two-Step Fabricated Structured Black Silicon and Its Device Application. *Nanoscale Res. Lett.* **2018**, *13*, 316. [CrossRef]
10. Chai, J.Y.H.; Wong, B.T.; Juodkazis, S. Black-Silicon-Assisted Photovoltaic Cells for Better Conversion Efficiencies: A Review on Recent Research and Development Efforts. *Mater. Today Energy* **2020**, *18*, 100539. [CrossRef]
11. Ali, M.; Zhou, F.; Chen, K.; Kotzur, C.; Xiao, C.; Bourgeois, L.; Zhang, X.; MacFarlane, D.R. Nanostructured Photoelectrochemical Solar Cell for Nitrogen Reduction Using Plasmon-Enhanced Black Silicon. *Nat. Commun.* **2016**, *7*, 11335. [CrossRef]
12. Oh, K.; Joanny, L.; Gouttefangeas, F.; Fabre, B.; Dorcet, V.; Lassalle-Kaiser, B.; Vacher, A.; Mériadec, C.; Ababou-Girard, S.; Loget, G. Black Silicon Photoanodes Entirely Prepared with Abundant Materials by Low-Cost Wet Methods. *ACS Appl. Energy Mater.* **2019**, *2*, 1006–1010. [CrossRef]
13. Jian, J.X.; Liao, J.X.; Zhou, M.H.; Yao, M.M.; Chen, Y.J.; Liang, X.W.; Liu, C.P.; Tong, Q.X. Enhanced Photoelectrochemical Water Splitting of Black Silicon Photoanode with PH-Dependent Copper-Bipyridine Catalysts. *Chem.—A Eur. J.* **2022**, *28*, e202201520. [CrossRef] [PubMed]
14. Bogue, R. Novel Infrared Detectors Based on Black Silicon. *Sens. Rev.* **2010**, *30*, 59–62. [CrossRef]
15. Hu, F.; Dai, X.-Y.; Zhou, Z.-Q.; Kong, X.-Y.; Sun, S.-L.; Zhang, R.-J.; Wang, S.-Y.; Lu, M.; Sun, J. Black Silicon Schottky Photodetector in Sub-Bandgap near-Infrared Regime. *Opt. Express* **2019**, *27*, 3161. [CrossRef] [PubMed]
16. Bodelón, G.; Montes-García, V.; Pérez-Juste, J.; Pastoriza-Santos, I. Surface-Enhanced Raman Scattering Spectroscopy for Label-Free Analysis of *P. aeruginosa* Quorum Sensing. *Front. Cell Infect. Microbiol.* **2018**, *8*, 143. [CrossRef] [PubMed]
17. Pérez-Jiménez, A.I.; Lyu, D.; Lu, Z.; Liu, G.; Ren, B. Surface-Enhanced Raman Spectroscopy: Benefits, Trade-Offs and Future Developments. *Chem. Sci.* **2020**, *11*, 4563–4577. [CrossRef]
18. Wang, J.; Lin, W.; Cao, E.; Xu, X.; Liang, W.; Zhang, X. Surface Plasmon Resonance Sensors on Raman and Fluorescence Spectroscopy. *Sensors* **2017**, *17*, 2719. [CrossRef]
19. Tzeng, Y.; Lin, B.Y. Silver SERS Adenine Sensors with a Very Low Detection Limit. *Biosensors* **2020**, *10*, 53. [CrossRef]
20. Costas, C.; López-Puente, V.; Bodelón, G.; González-Bello, C.; Pérez-Juste, J.; Pastoriza-Santos, I.; Liz-Marzán, L.M. Using Surface Enhanced Raman Scattering to Analyze the Interactions of Protein Receptors with Bacterial Quorum Sensing Modulators. *ACS Nano* **2015**, *9*, 5567–5576. [CrossRef]
21. Morton, S.M.; Jensen, L. Understanding the Molecule-Surface Chemical Coupling in SERS. *J. Am. Chem. Soc.* **2009**, *131*, 4090–4098. [CrossRef]
22. Kneipp, J. SERS for Sensing and Imaging in Live Cells. In *Principles and Clinical Diagnostic Applications of Surface-Enhanced Raman Spectroscopy*; Elsevier: Amsterdam, The Netherlands, 2021; pp. 303–325. ISBN 9780128211212.
23. Bernat, A.; Samiwala, M.; Albo, J.; Jiang, X.; Rao, Q. Challenges in SERS-Based Pesticide Detection and Plausible Solutions. *J. Agric. Food Chem.* **2019**, *67*, 12341–12347. [CrossRef]
24. Wang, Y.; Li, P.; Lin, D.; Chen, J.; Zhang, Y.; Yang, L. Ethanol-Extraction SERS Strategy for Highly Sensitive Detection of Poisons in Oily Matrix. *Spectrochim. Acta—Part A Mol. Biomol. Spectrosc.* **2021**, *259*, 119883. [CrossRef] [PubMed]
25. Mo, S.; Shao, X.; Chen, Y.; Cheng, Z. Increasing Entropy for Colloidal Stabilization. *Sci. Rep.* **2016**, *6*, 36836. [CrossRef]
26. Shi, L.; Zhang, L.; Tian, Y. Rational Design of Surface-Enhanced Raman Scattering Substrate for Highly Reproducible Analysis. *Anal. Sens.* **2022**, *2022*, e202200064. [CrossRef]
27. Khnykina, K.A.; Baranov, M.A.; Babaev, A.A.; Dubavik, A.Y.; Fedorov, A.V.; Baranov, A.V.; Bogdanov, K.V. Comparison Study of Surface-Enhanced Raman Spectroscopy Substrates. *J. Phys. Conf. Ser.* **2021**, *1984*, 12020. [CrossRef]
28. Mikac, L.; Gotić, M.; Gebavi, H.; Ivanda, M. The Variety of Substrates for Surface-Enhanced Raman Spectroscopy. In Proceedings of the 2017 IEEE 7th International Conference on Nanomaterials: Applications & Properties, (NAP 2017), Odessa, Ukraine, 10–15 September 2017. [CrossRef]
29. Guo, R.; Hakala, T.K.; Törmä, P. Geometry Dependence of Surface Lattice Resonances in Plasmonic Nanoparticle Arrays. *Phys. Rev. B* **2017**, *95*, 155423. [CrossRef]
30. Juluri, B.K.; Zheng, Y.B.; Ahmed, D.; Jensen, L.; Huang, T.J. Effects of Geometry and Composition on Charge-Induced Plasmonic Shifts in Gold Nanoparticles. *J. Phys. Chem. C* **2008**, *112*, 7309–7317. [CrossRef]
31. Du, C.; Yang, W.; Peng, S.; Shi, D. Optimal Geometry Parameter for Plasmonic Sensitivities of Individual Au Nanopoarticle Sensors. *Phys. Chem. Chem. Phys.* **2019**, *21*, 7654–7660. [CrossRef]
32. Serpenguzel, A. Luminescence of Black Silicon. *J. Nanophoton.* **2008**, *2*, 021770. [CrossRef]
33. Jansen, H.; de Boer, M.; Burger, J.; Legtenberg, R.; Elwenspoek, M. The Black Silicon Method II:The Effect of Mask Material and Loading on the Reactive Ion Etching of Deep Silicon Trenches. *Microelectron. Eng.* **1995**, *27*, 475–480. [CrossRef]

34. Cui, Z. *Nanofabrication: Principles, Capabilities and Limits*, 2nd ed.; Springer International Publishing: Cham, Switzerland, 2017; ISBN 9783319393612.
35. Lawrence, K.P.; Douki, T.; Sarkany, R.P.E.; Acker, S.; Herzog, B.; Young, A.R. The UV/Visible Radiation Boundary Region (385–405 Nm) Damages Skin Cells and Induces "Dark" Cyclobutane Pyrimidine Dimers in Human Skin in Vivo. *Sci. Rep.* **2018**, *8*, 12722. [CrossRef] [PubMed]
36. Godley, B.F.; Shamsi, F.A.; Liang, F.Q.; Jarrett, S.G.; Davies, S.; Boulton, M. Blue Light Induces Mitochondrial DNA Damage and Free Radical Production in Epithelial Cells. *J. Biol. Chem.* **2005**, *280*, 21061–21066. [CrossRef] [PubMed]
37. Yuan, X.; Song, Y.; Song, Y.; Xu, J.; Wu, Y.; Glidle, A.; Cusack, M.; Ijaz, U.Z.; Cooper, J.M.; Huang, W.E.; et al. Effect of Laser Irradiation on Cell Function and Its Implications in Raman Spectroscopy. *Appl. Environ. Microbiol.* **2018**, *84*, 8. [CrossRef]
38. Laermer, F.; Urban, A. MEMS at Bosch—Si Plasma Etch Success Story, History, Applications, and Products. *Plasma Process. Polym.* **2019**, *16*, 1800207. [CrossRef]
39. Blauw, M.A.; Zijlstra, T.; van der Drift, E. Balancing the Etching and Passivation in Time-Multiplexed Deep Dry Etching of Silicon. *J. Vac. Sci. Technol. B Microelectron. Nanom. Struct.* **2001**, *19*, 2930. [CrossRef]
40. Labelle, C.B.; Opila, R.; Kornblit, A. Plasma Deposition of Fluorocarbon Thin Films from C-C4F8 Using Pulsed and Continuous Rf Excitation. *J. Vac. Sci. Technol. A Vacuum Surfaces Film.* **2005**, *23*, 190–196. [CrossRef]
41. Fu, H.; Bao, H.; Zhang, H.; Zhao, Q.; Zhou, L.; Zhu, S.; Wei, Y.; Li, Y.; Cai, W. Quantitative Surface-Enhanced Raman Spectroscopy for Field Detections Based on Structurally Homogeneous Silver-Coated Silicon Nanocone Arrays. *ACS Omega* **2021**, *6*, 18928–18938. [CrossRef]
42. Ho, C.H.; Lee, S. SERS and DFT Investigation of the Adsorption Behavior of 4-Mercaptobenzoic Acid on Silver Colloids. *Colloids Surfaces A Physicochem. Eng. Asp.* **2015**, *474*, 29–35. [CrossRef]
43. Barriet, D.; Yam, C.M.; Shmakova, O.E.; Jamison, A.C.; Lee, T.R. 4-Mercaptophenylboronic Acid SAMs on Gold: Comparison with SAMs Derived from Thiophenol, 4-Mercaptophenol, and 4-Mercaptobenzoic Acid. *Langmuir* **2007**, *23*, 8866–8875. [CrossRef]
44. Mhlanga, N.; Ntho, T.A. A Theoretical Study of 4-Mercaptobenzoic Acid Assembled on Ag for Surface-Enhanced Raman Scattering Applications. *Mater. Today Commun.* **2021**, *26*, 101698. [CrossRef]
45. Golubewa, L.; Karpicz, R.; Matulaitiene, I.; Selskis, A.; Rutkauskas, D.; Pushkarchuk, A.; Khlopina, T.; Michels, D.; Lyakhov, D.; Kulahava, T.; et al. Surface-Enhanced Raman Spectroscopy of Organic Molecules and Living Cells with Gold-Plated Black Silicon. *ACS Appl. Mater. Interfaces* **2020**, *12*, 50971–50984. [CrossRef] [PubMed]
46. Michota, A.; Bukowska, J. Surface-Enhanced Raman Scattering (SERS) of 4-Mercaptobenzoic Acid on Silver and Gold Substrates. *J. Raman Spectrosc.* **2003**, *34*, 21–25. [CrossRef]
47. Klyuchnik, A.V.; Kurganov, S.Y.; Lozovik, Y.E. Plasmons at a Hole in a Screen. *Phys. Solid State* **2003**, *45*, 1793–1797. [CrossRef]
48. Rytov, S.M.; Kravtsov, Y.A.; Tatarskii, V.I. *Wave Propagation through Random Media, Principles of Statistical Radiophysics 4*; Springer: Berlin/Heidelberg, Germany, 1978; ISBN 9783642726842.
49. Schinke, C.; Christian Peest, P.; Schmidt, J.; Brendel, R.; Bothe, K.; Vogt, M.R.; Kröger, I.; Winter, S.; Schirmacher, A.; Lim, S.; et al. Uncertainty Analysis for the Coefficient of Band-to-Band Absorption of Crystalline Silicon. *AIP Adv.* **2015**, *5*, 067168. [CrossRef]
50. Lin, Y.J.; Chu, Y.L. Effect of Reactive Ion Etching-Induced Defects on the Surface Band Bending of Heavily Mg-Doped p -Type GaN. *J. Appl. Phys.* **2005**, *97*, 104904. [CrossRef]
51. Weigel, C.; Brokmann, U.; Hofmann, M.; Behrens, A.; Rädlein, E.; Hoffmann, M.; Strehle, S.; Sinzinger, S. Perspectives of Reactive Ion Etching of Silicate Glasses for Optical Microsystems. *J. Opt. Microsystems* **2021**, *1*, 040901. [CrossRef]
52. Alhmoud, H.; Brodoceanu, D.; Elnathan, R.; Kraus, T.; Voelcker, N.H. A MACEing Silicon: Towards Single-Step Etching of Defined Porous Nanostructures for Biomedicine. *Prog. Mater. Sci.* **2021**, *116*, 100636. [CrossRef]
53. Arafat, M.Y.; Islam, M.A.; Mahmood, A.W.B.; Abdullah, F.; Nur-E-Alam, M.; Kiong, T.S.; Amin, N. Fabrication of Black Silicon via Metal-Assisted Chemical Etching—A Review. *Sustainability* **2021**, *13*, 766. [CrossRef]
54. Kim, H.J.; Kim, B.; Lee, D.; Lee, B.-H.; Cho, C. Fabrication of Surface-Enhanced Raman Scattering Substrate Using Black Silicon Layer Manufactured through Reactive Ion Etching. *J. Sens. Sci. Technol.* **2021**, *30*, 267–272. [CrossRef]
55. Gervinskas, G.; Seniutinas, G.; Hartley, J.S.; Kandasamy, S.; Stoddart, P.R.; Fahim, N.F.; Juodkazis, S. Surface-Enhanced Raman Scattering Sensing on Black Silicon. *Ann. Phys.* **2013**, *525*, 907–914. [CrossRef]
56. Deng, Y.L.; Juang, Y.J. Black Silicon SERS Substrate: Effect of Surface Morphology on SERS Detection and Application of Single Algal Cell Analysis. *Biosens. Bioelectron.* **2014**, *53*, 37–42. [CrossRef] [PubMed]
57. Lin, B.W.; Tai, Y.H.; Lee, Y.C.; Xing, D.; Lin, H.C.; Yamahara, H.; Ho, Y.L.; Tabata, H.; Daiguji, H.; Delaunay, J.J. Aluminum-Black Silicon Plasmonic Nano-Eggs Structure for Deep-UV Surface-Enhanced Resonance Raman Spectroscopy. *Appl. Phys. Lett.* **2022**, *120*, 51102. [CrossRef]

ACS APPLIED NANO MATERIALS

www.acsanm.org Article

Stable and Reusable Lace-like Black Silicon Nanostructures Coated with Nanometer-Thick Gold Films for SERS-Based Sensing

Lena Golubewa,* Aliona Klimovich, Igor Timoshchenko, Yaraslau Padrez, Marina Fetisova, Hamza Rehman, Petri Karvinen, Algirdas Selskis, Sonata Adomavičiūtė-Grabusovė, Ieva Matulaitienė, Arunas Ramanavicius, Renata Karpicz, Tatsiana Kulahava, Yuri Svirko, and Polina Kuzhir

Cite This: *ACS Appl. Nano Mater.* 2023, 6, 4770−4781 Read Online

ACCESS | Metrics & More | Article Recommendations | Supporting Information

ABSTRACT: We propose a simple, fast, and low-cost method for producing Au-coated black Si-based SERS-active substrates with a proven enhancement factor of 10^6. Room temperature reactive ion etching of silicon wafer followed by nanometer-thin gold sputtering allows the formation of a highly developed lace-type Si surface covered with homogeneously distributed gold islands. The mosaic structure of deposited gold allows the use of Au-uncovered Si domains for Raman peak intensity normalization. The fabricated SERS substrates have prominent uniformity (with less than 6% SERS signal variations over large areas, 100 × 100 μm^2). It has been found that the storage of SERS-active substrates in an ambient environment reduces the SERS signal by less than 3% in 1 month and not more than 40% in 20 months. We showed that Au-coated black Si-based SERS-active substrates can be reused after oxygen plasma cleaning and developed relevant protocols for removing covalently bonded and electrostatically attached molecules. Experiments revealed that the Raman signal of 4-MBA molecules covalently bonded to the Au coating measured after the 10th cycle was just 4 times lower than that observed for the virgin substrate. A case study of the reusability of the black Si-based substrate was conducted for the subsequent detection of 10^{-5} M doxorubicin, a widely used anticancer drug, after the reuse cycle. The obtained SERS spectra of doxorubicin were highly reproducible. We demonstrated that the fabricated substrate permits not only qualitative but also quantitative monitoring of analytes and is suitable for the determination of concentrations of doxorubicin in the range of 10^{-9}−10^{-4} M. Reusable, stable, reliable, durable, low-cost Au-coated black Si-based SERS-active substrates are promising tools for routine laboratory research in different areas of science and healthcare.

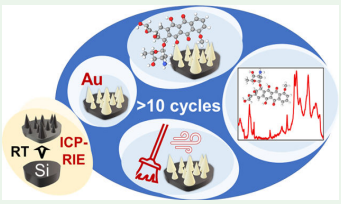

KEYWORDS: *black silicon, nanoroughness, surface-enhanced Raman spectroscopy, reusability, long-term stability, surface plasmon, doxorubicin*

1. INTRODUCTION

Surface-enhanced Raman spectroscopy (SERS) technique relies on the enhancement of the electric field occurring when the frequency of an excitation beam coincides with the eigenfrequency of an ensemble of conduction electrons in a metallic nanostructured substrate.[1,2] Experimentally obtained enhancement factors that vary from 10^4 to 10^{11}[3−5] allow one to employ SERS to detect molecules with an extremely low Raman scattering cross-section of 10^{-31} cm^2/sr[6] and to reduce the detectable concentration of an analyte down to 10^{-11}−10^{-6} M[7−9] and even to attomolar values.[10]

SERS is widely recognized as one of the most efficient analytical techniques in organic chemistry and biochemistry. However, the implementation of SERS in practice still suffers from several limitations. Among the crucial ones are (i) the intrinsic inhomogeneity of SERS substrates, which results in a variation of the Raman signal over the substrate surface at a low concentration of the analyte, (ii) rather limited opportunities for quantitative analysis, (iii) poor long-term stability and thereby short exploitation time of SERS substrates, and (iv) their disposability.

Among systems commonly used for SERS are nanoparticles of copper/silver/gold stabilized in colloidal solutions. Even though colloidal solutions of noble metals exhibit very good enhancement of the Raman signal, their performance in SERS may be hampered by temperature variations and contamination with inorganic salts.[11] The latter may lead to agglomeration of the metal nanoparticles, making the substrate no longer suitable for SERS.

Sacrificing the high enhancement, but greatly benefiting in repeatability, surfaces with immobilized noble metal nano-

Received: January 18, 2023
Accepted: February 28, 2023
Published: March 9, 2023

particles,[12−14] or metal-capped structured arrays[15] and nanowires,[16] Au-coated flexible polymer "fingers",[17] are increasingly used in laboratory practice. However, their fabrication techniques, such as electron-beam lithography,[18−21] focused ion-beam lithography,[22] and metal-assisted chemical etching,[23] are often multistep, complex, and not cost-efficient, leaving room for the development of new approaches for cheap and scalable SERS substrate production.

In the search for SERS substrates, silicon has attracted special attention because silicon platforms of modern electronics open avenues for the development of the lab-on-chip approach. There are several methods of using silicon materials as precursors for SERS-active substrates. In ref 24, e-beam lithography is used to modify self-assembled monolayers of 3-(4-nitrophenoxy)-propyltrimethoxysilane on Si/SiO_2 surfaces to push the assembly of citrate-passivated gold nanoparticles in distinct locations, creating patterned immobilization of Au NPs. Peng et al. applied metal-assisted chemical etching for the formation of micro-/nano-nested structures in Si with further Au deposition[25] for the fabrication of a SERS microfluidic platform with a satisfactory EF of around 10^6 and a prominent long-term stability of around 120 days. The fabrication approach of Si nanopillars capped with noble metals by the silicon plasma-etching method, omitting the lithographic step,[5] resulted in the low-cost production of nanopillar arrays, providing significant enhancement (10^{11}) and sensitivity.

However, there is always a trade-off among sensitivity, reproducibility, cost, stability (mechanical, operational, and durable), and reusability. As the laboratory routine usually involves multiple repeated experiments, the use of disposable SERS substrates leads to a corresponding multiplication of the resources needed. Cost and resource reduction can be achieved by developing large-scale and long-living substrates along with relevant methods for their reuse.

To address these challenges, we fabricated three-dimensional (3D) lace-type structures with a highly developed surface area over a 2 in. Si wafer using inductively coupled plasma reactive ion etching (ICP-RIE) technique at room temperature. These structures show a remarkably low reflectivity in the visual and near-IR spectral range[26] belonging to a class of artificial materials referred to as black silicon (bSi). The bSi obtained at room temperature appears to be more 'porous' and micro-rough[27] than that fabricated at cryogenic temperatures, where precise control of the bSi surface shape, micropillar sidewall orientation, and roughness can be achieved via competing etching and passivation processes.[28,29] The porosity of the bSi fabricated at room temperature allows one to increase the effective surface area and to achieve a higher—in comparison with regular micropillars—plasmonic "hotspot" surface density with the same amount of sputtered gold. In comparison with recently proposed gold−bSi structures,[30,31] which contain 100−600 nm thick gold layers, we significantly reduce the amount of gold needed by creating a mosaic distribution of plasmonic hemispheres on the rich Si relief having a quasiperiodic lace-like structure. Moreover, the enhanced nanoroughness of the bSi surface enables plasmonic core−shell Si-Au nanostructures,[32] rendering the buffer layer (e.g., Ti thin film), conventionally used to improve the adhesion of plasmonic nanoparticles, unnecessary.[29]

Analysis of the reliability, durability, stability, and reusability of Au-coated black Si-based SERS-active (bSi/Au) substrates reveals the beneficial "lace-type" bSi and mosaic gold geometries. Moreover, these "lace and mosaic" bSi/Au structures are much easier to manufacture, not requiring cryogenic conditions and being low cost due to the significant reduction in gold consumption. In addition, the stable Raman signal from the silicon underlying a very thin Au layer could be applied for precise calibration of peak intensities in the measured SERS spectra of analyte molecules, supporting capabilities of using such substrates not only for qualitative but also for quantitative analyte monitoring.

We suppose that the proposed simple methods of bSi/Au substrate fabrication and reuse, along with their applicability for monitoring trace amounts of molecules and their concentration determination, form a bridge for the translation of the SERS method from individual research laboratories for mass routine use in analytical research in many areas of biochemical and medical diagnostics, forensics, etc.

2. METHODS AND MATERIALS

2.1. Materials and Reagents. A silicon ⟨100⟩ oriented wafer (p-type) with 1−20 Ω·cm (Si-Mat, Germany) was used for SERS substrate fabrication.

Analytical grade 4-mercaptobenzoic acid (4-MBA, Sigma Aldrich, Germany), ethanol (EtOH, >99.9%, Sigma Aldrich, Germany), and doxorubicin hydrochloride (DOX, Sigma Aldrich, Germany) were used throughout the experiments.

2.2. bSi/Au Fabrication. A 2-inch silicon wafer was etched using one-step mask-free inductively coupled plasma reactive ion-etching technique. The plasma etching was carried out in a PlasmaLab80 system (Oxford Instruments plc, UK). A two-gas mixture of SF_6 and O_2 with flow rates of 10 and 9 sccm, respectively, was used in the etching process. Dry anisotropic silicon etching was conducted for 10 min at 30 mTorr chamber pressure and an RF power of 15 W as well as 200 W ICP power. The cooling system temperature was set to 20 °C. Before the etching experiments, the silicon wafer was cleaned by oxygen plasma for 2 min.

Gold deposition was carried out by magnetron sputtering for 80 s on top of the bSi substrates covered with a native oxide layer using the gold target (TARGET GOLD, 99.99%, 57 mm, 91017-AU, CAS 7440-57-5) purchased from Electron Microscopy Sciences (Hatfield, PA 19440). BSi/Au substrates sputtered simultaneously under the same conditions were stored in individual Petri dishes under normal ambient conditions for a period of up to 20 months, and each sample was analyzed immediately after the synthesis and after 1, 2, 3, 4, and 20 months of storage. The bSi/Au synthesis is schematically shown in Figure 1.

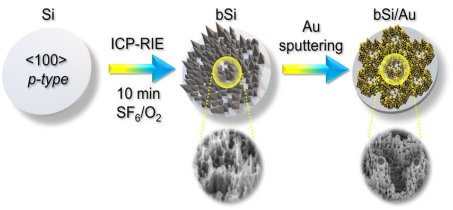

Figure 1. Steps of bSi/Au SERS substrate synthesis.

To evaluate the SERS performance of the fabricated bSi/Au substrates, we compare them with those obtained by the alternative cryogenic ICP-RIE technique.[28,32] The surface morphology of the latter substrates is characterized by well-defined cone-like shapes. Correspondingly, the substrates covered with gold after magnetron sputtering for 80 and 120 s will be hereafter referred to as bSi/Au(conical) and bSi/Au*(conical).

https://doi.org/10.1021/acsanm.3c00281
ACS Appl. Nano Mater. 2023, 6, 4770−4781

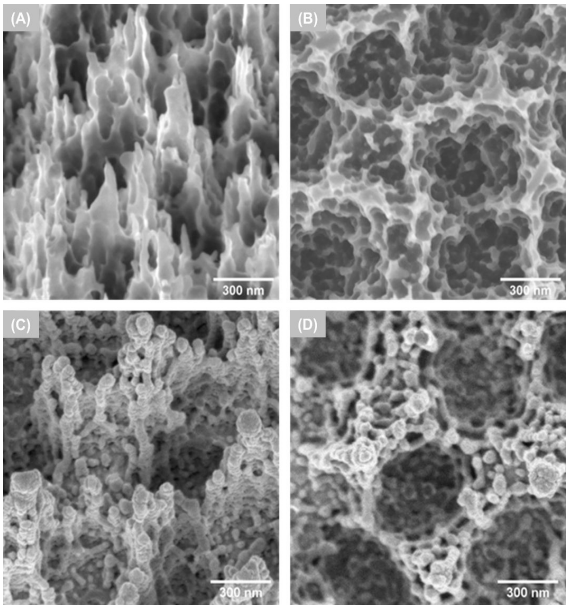

Figure 2. SEM micrographs of bSi (A, B) and bSi sputtered with gold (C, D): angle-side (A, C) and top−bottom (B, D) views.

2.3. Scanning Electron Microscopy (SEM) and Image Processing. SEM images of bSi and bSi sputtered with gold were obtained using a Helios NanoLab 650 (FEI) microscope. Analysis of bSi and bSi/Au was performed at a nominal beam voltage of 3 kV.

The bSi surface analysis was carried out using open-source software ImageJ.[33] SEM images with a total area of 5.5 μm^2 were analyzed. Six hundred and thirty-nine gold structures were identified from the images and ranged using Beeswarm plot statistics in OriginPro21 (OriginLab Corporation, USA). Quantitative evaluation of the effective bSi surface area was performed in Wolfram Mathematica 12 (Wolfram Research, Inc.). Side-view SEM micrographs were used to estimate the roughness of the bSi.

2.4. Raman and SERS Spectroscopy of 4-MBA. For SERS measurements, bSi/Au, bSi/Au(conical), and bSi/Au*(conical) substrates were incubated in 4-MBA solution of 1.0 mM concentration (in ethanol) for 4 h to allow the formation of a self-assembled monolayer (SAM) of 4-MBA molecules. Thereafter, each substrate was washed in a flow of ethanol to remove excess 4-MBA molecules and then rinsed in ultrapure water, dried in a laminar N_2 flow, and used for measurements.

The Raman spectra were recorded using RamanFlex 400 (PerkinElmer, Inc.), equipped with a near-infrared 785 nm laser delivering 100 mW at the sample (maximum) and a high-sensitivity open-electrode CCD detector (air-cooled, operated at −50 °C). All Raman and SERS spectra were collected from at least three points of the sample surface and then averaged. The laser power on the sample was adjusted to 16.8 mW, and the illumination time was 300 s in all measurements except when analyzing the effect of the employed laser power and exposure time on the spectra of 4-MBA SAM on the bSi/Au substrate.

To evaluate the effect of the laser power and exposure time on the spectra of 4-MBA SAM on the bSi/Au substrate, the laser power was varied from 3.8 to 90.9 mW with a step of 4.6 mW and the accumulation time was linearly changed from 1 to 60 s.

The uniformity of the hotspot distribution was estimated with a laser-scanning MonoVista CRS+ Raman microscope system (S&I GmbH, Germany) equipped with a liquid-nitrogen-cooled CCD detector. Raman spectra were collected using a 785 nm wavelength emitting laser as an excitation source. An Olympus 50 × /0.8 NA objective was used for the excitation and collection of Raman spectra. The spectrometer was calibrated using a fundamental vibrational band at 520.7 cm^{-1} of a silicon wafer. The power delivered to the sample was adjusted to 48.5 μW. An area of 100 × 100 μm on bSi/Au samples with 4-MBA SAM was scanned with 1 μm step, and the accumulation time was 1 s.

2.5. EF Calculation. The enhancement factor (EF) was estimated by the following equation[34]

$$\mathrm{EF} = \frac{I_{\mathrm{bSi/Au}}}{N_{\mathrm{bSi/Au}}} \times \frac{N_{\mathrm{NR}}}{I_{\mathrm{NR}}} \tag{1}$$

where $I_{\mathrm{bSi/Au}}$ and I_{NR} are intensities of the SERS and normal Raman bands, and $N_{\mathrm{bSi/Au}}$ and N_{NR} are the numbers of molecules in 4-MBA SAM on the bSi/Au substrate and 4-MBA on the flat silicon surface, respectively.

2.6. Oxygen Plasma Cleaning of bSi/Au Substrates. Removal of the molecules attached to the bSi/Au substrate was carried out using oxygen plasma treatment. An oxygen plasma etching device built in Super Cool Sputter Coater Leica EM SCD050 (Leica Microsystems GmbH, Germany) was used for sample cleaning. bSi/Au substrates with a SAM of 4-MBA were placed in the load-lock chamber of a vacuum system. The parameters were set as follows: pressure 0.1 mbar and current 48 mA. The duration of oxygen plasma treatment was determined experimentally and corresponded to a >99% decrease in the intensities of the 1076 and 1588 cm^{-1} bands. Afterward, the substrates were washed with deionized water and ethanol, dried in N_2 laminar flow, transferred to individual Petri dishes, and stored under ambient conditions before the next cycle of bSi/Au substrate reuse.

https://doi.org/10.1021/acsanm.3c00281
ACS Appl. Nano Mater. 2023, 6, 4770−4781

3. RESULTS AND DISCUSSION

3.1. bSi/Au Surface Characterization. SEM images of the obtained bSi/Au substrate are presented in Figure 2. The surface morphology is characterized by vertically standing, thin, lace-like, sharp-edged structures (Figure 2A), with an average height of around 1 μm and a base of 100−200 nm. These plates form wells with an average diameter of 500 nm (Figure 2B), the inner surface of which is also covered with rock-like structures with sharp peaks with high apex curvature, but their dimensions are much smaller and are around 10−100 nm. These various micro−nano structures are responsible for the very low light reflection in the visible and near-infrared (NIR) ranges and appear completely black to the naked eye.[26] The synthesized bSi demonstrates high absorption in the range of 200−900 nm (see Figure S1, Supporting Information). Numerous micro−nano structures comprising bSi surfaces create light traps that drastically increase the absorbance. This light-trapping ability of bSi in the vis−NIR range also drastically contributes to the excitation of the collective electron oscillations in the deposited gold particles, the phenomenon responsible for the high enhancement of the Raman signal in SERS.[35]

The fabrication process allowed us to obtain large-scale bSi substrates with structures uniformly distributed over a 2 in. Si wafer (see Figure S2, Supporting Information).

The micro−nano-structured bSi was then sputtered with gold to obtain plasmonic structures densely distributed over the bSi. SEM micrographs of bSi/Au are presented in Figure 2C,D. Side walls of vertically oriented Si plates are covered with gold hemispheres of sizes (diameters) from 4 to 16 nm (10.8 nm on average), while the sharp apexes of these plates serve as nuclei for spherical NP formation of sizes from 16 to 60 nm (34.6 nm on average). Also, in some cases, spherical NPs grew to sizes from 60 to 195 nm (109.7 nm on average) (see Figure S3, Supporting Information). The essential differences between these bSi/Au structures and bSi/Au (conic) substrates[30−32] are the significantly reduced Au deposition, which resulted in a very thin gold layer (tens versus hundreds of nanometers) and the presence of gold-free zones, which, as it will be shown below, can be used for independent signal normalization and quantitative determination of the concentration of the studied substances.

3.2. bSi/Au Enhancement Factor Calculation. To evaluate the effectiveness of the bSi/Au substrate for SERS, 4-mercaptobenzoic acid (4-MBA) was used as a test molecule. 4-MBA is widely utilized as a standard because its molecules form a self-assembled monolayer of well-known surface density and Raman spectrum.[36−38] BSi/Au substrates were incubated with 4-MBA as described in the Methods and Materials Section, which resulted in the formation of covalent bonding of 4-MBA through the thiol group with gold, with the creation of a S−Au bond.

SERS spectra of 4-MBA on the bSi/Au and SiO_2/Au substrates and the Raman spectrum of bulk 4-MBA are presented in Figure 3. bSi/Au substrates display a significant Raman intensity increase as compared with the SiO_2 substrate with nanostructured gold deposited on it. The assignment of characteristic bands of 4-MBA is presented in Table S1 (Supporting Information). As shown in Figure 3, several bands of 4-MBA molecules are significantly enhanced according to the surface selection rules:[39] 1076 cm^{-1} ν_{12} (a_1) aromatic ring breathing mode and 1587 cm^{-1} totally symmetric aromatic

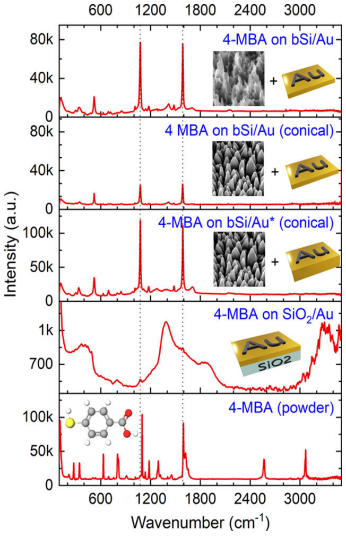

Figure 3. Raman spectrum of 4-MBA powder (bottom) and SERS spectra of 4-MBA on SiO_2/Au, bSi/Au* (conical),[32] bSi/Au (conical), and bSi/Au substrates (from bottom to top, respectively). *30% thicker gold layer sputtered on the surface of bSi than in other cases (bSi/Au (conical) and bSi/Au).

ring vibration (ν_{8a}). The intensive band in the Raman spectrum of bulk 4-MBA at 2570 cm^{-1}, which arises from the S−H stretching in 4-MBA, disappears in the SERS spectrum of 4-MBA on the bSi/Au substrate, while a new band around 260 cm^{-1} appears, indicating the breakage of the S−H bond in the 4-MBA molecule and the formation of a S−Au covalent bond[36,39] and the 4-MBA self-assembled monolayer. A band at 521 cm^{-1} associated with Si is also present in the recorded spectra, as a thin mosaic cover of irregular nanoscale gold islands does not eliminate this band.

Bands associated with the carboxylic moiety of the 4-MBA molecule are present in the spectrum of the 4-MBA SAM on the bSi/Au substrate: the bands at 849 and 1417 cm^{-1} correspond to bending $\beta(COO^-)$ and stretching $\nu(COO^-)$ vibrations and indicate the presence of deprotonated carboxylic groups, and the band at 1702 cm^{-1} arising from $\nu(C{=}O)$ indicates the presence of protonated carboxylic groups.[39] The normalized intensity of the $\nu(COO^-)$ band to ν_{8a} is often used to determine the pH value as this ratio increases with the growth of the deprotonation level of 4-MBA molecules.[40] However, in dried samples of bSi/Au with 4-MBA, the presence of $\beta(COO^-)$ and $\nu(COO^-)$ vibrations in the SAM more likely indicates the direct interaction of COO^- groups with the metal surface, which forces the flat orientation of the aromatic ring of 4-MBA molecules.[38] This assumption is supported by the appearance of γ(CCC) out-of-plane ring vibrations at 718 cm^{-1}[39] and a weak aromatic ν(CH) stretching band at 3074 cm^{-1} in SERS (see Table S1, Supporting Information), which weaken for flat-oriented aromatic rings due to surface selection rules.

It is worth noting that there are no characteristic signs of the decarboxylation process, which is caused by the interaction of

https://doi.org/10.1021/acsanm.3c00281
ACS Appl. Nano Mater. 2023, 6, 4770−4781

4-MBA molecules with plasmonic active surfaces and may be a result of the excessive surface irradiation and subsequent heating along with molecular degradation.[41] Decarboxylation is indicated by the appearance of two new peaks at 996 and 1019 cm^{-1} associated with benzene monosubstituted thiophenol.[38] In the case of the 4-MBA SAM on the bSi/Au substrate, no decarboxylation occurs, as only the 1012 cm^{-1} band assigned to ring deformations is present in the SERS spectra.

We compared the Raman signal enhancement for bSi/Au and bSi/Au (conical) substrates. The morphology of the latter substrate, which was described in ref 32. is dominant, with mostly smooth conical structures of 500 nm height and 200 nm base. From the fabrication point of view, the principal difference between these bSi/Au and bSi/Au (conical) substrates is that a transition from the cryogenic ICP-RIE to room temperature (RT) ICP-RIE occurred, which simplified and reduced the cost of fabrication of bSi and, at the same time, resulted in a more developed surface area (so-called lace-like bSi structures appeared). As it follows from Figure 3, cone-like silicon structures of bSi/Au* (conical) provide significant Raman signal enhancement. However, a reduction in the gold layer thickness by 30% leads to a decrease in the intensity by 4.6 times. The deposition of a gold layer of the same reduced thickness on the lace-type bSi with sharp lace-like structures gives a 3 times more intensive signal than bSi/Au (conical) with the same gold layer thickness (see Figure 3). This significant increase is due to the more developed surface area, which enables a larger number of hotspots. It is also important to note that either overlapping of nearby gold nanoparticles or the formation of vertically oriented dumbbell-like structures of the characteristic sizes obtained under the employed conditions of gold deposition (10.8 nm for side walls of Si plates and 34.6−109.7 nm for apex caps), as well as their vertical ordering on plates of bSi of the considered profile, also significantly contribute to the incidence of the plasmon resonance frequency of the substrate under consideration in the near-IR region, as previously demonstrated in ref 32. As a result, a successful combination of the profile of the supporting substrate and the appropriate size and orientation of the systems of gold nanoparticles allows one to consider the produced substrate as an effective material for sensitive SERS-based analyte detection using NIR excitation, which is extremely important for biomedical and biochemical tasks due to the safety of NIR irradiation as compared with UV light.

Further, the enhancement factor of the bSi/Au substrate was calculated using eq 1 (Methods and Materials) for the band at 1076 cm^{-1}, with reference to the Raman spectra of 4-MBA on the Si wafer. The effective surface area of the synthesized bSi sputtered with gold was calculated from SEM micrographs and is at least 20 times larger than that of bSi/Au (conical) substrates (based on estimations presented in Section 5, Supporting Information). The EF of the bSi/Au substrate was estimated to be around 1.1×10^6; calculations are given in the same section of the Supporting Information.

Enhancement of the Raman signal in SERS occurs through two possible mechanisms: electromagnetic (EM) and chemical (CM). These two mechanisms could be realized together or separately. The EM mechanism is based on the phenomenon of plasmon resonance and occurs when the frequency of the exciting radiation coincides with the frequency of collective oscillations of delocalized conducting electrons (or surface plasmons, SPs), which creates an electromagnetic field on the metal nanostructure/dielectric interface. The EM mechanism has the largest impact on signal enhancement (up to 10^{11}),[42] while CM manifests only a 10^0−10^3 times intensity increase[43] due to the charge-transfer (CT) process.[44] The calculated EF for BSi/Au has a magnitude of 10^6, indicating that the major impact on the SERS signal comes from the EM mechanism. However, CT could not be excluded as its possibility was demonstrated previously in ref 32 by DFT simulations for similar structures.

As it follows from a comparison of the obtained EF with the EF calculated for the bSi/Au* (conical) substrate,[32] there is a 2 order difference in EFs (10^6 for bSi/Au vs 10^8 for the foregoing bSi/Au* (conical)), while the intensity values of the 1076 cm^{-1} band of 4-MBA molecules for both substrates are of the same order, specifically I_{SERS} (on bSi/Au lace-like) ≈2/3 I_{SERS}(on bSi/Au* (conical)). This apparent inconsistency can be explained as follows. EF is calculated per molecule and strongly depends on the Au layer thickness, while measured intensities are determined by the joint contribution of irradiated molecules, the number of which is strongly dependent on the surface area available for molecular attachment, the hotspot density, and the E-field enhancement. Thus, a decrease in Au layer thickness leads to a decrease in the electromagnetic field enhancement, and an increase in the adsorbed molecules leads to a decrease in the I_{SERS}/N_{SERS} multiplier in Formula 1, and all of these result in a decrease of 2 orders in EF (as it is calculated per molecule) in comparison with the EF of bSi/Au* (conical). On the other hand, in the case of the detected spectra when the signal is provided by the additive impact of molecules trapped in the laser beam, due to the increased hotspot density and still satisfactory EM enhancement, the measurements of both bSi/Au and bSi/Au* (conical) provide comparable intensity values. This outcome is an obvious advantage of the bSi/Au substrate, described in the present study, as it is much cheaper and easier to fabricate than its foregoer bSi/Au* (conical).

The EF, demonstrated by micro-nano-structured bSi/Au substrates, is comparable to that reported for various SERS-active nanostructures, such as gold,[45] silver,[46] or gold−silver core−shell nanorods,[47] nanostars,[48] nanoflowers,[49] etc. Although it is lower than that for Ag-aligned[50] or semiconducting 15%-Mo-Ta_2O_5[51] nanorods (10^6 vs 10^8 and 10^7, respectively), bSi/Au has the significant advantage of being fabricated by the simple, fast, and low-cost RT-ICP-RIE technique. Moreover, the spontaneous formation of regular silicon lace-like structures with nanoroughness, which serve as precursors for the hotspots, excludes the most complex and time-consuming stage of large-scale fabrication of uniform and homogeneous substrates—the immobilization of nanostructures on a carrier surface (for example, quartz). The nanorough lace-like shape of the bSi/Au substrate also makes it very similar in geometry to needle-shaped regular nanostructured arrays, which were successfully applied for the SERS-based detection of SARS-CoV-2 virus[52] with extremely high affinity, where human angiotensin-converting-enzyme 2-functionalized gold needles served as effective virus traps. This similarity in geometry may expand the application of bSi/Au to the most urgent and vital areas of bioresearch and allow further consideration of the bSi/Au SERS substrate as a solution when emergencies, such as the coronavirus pandemic, require fast, large-scale, low-cost, and effective actions.

3.3. bSi/Au Responsivity, Photothermal Effect (PTE), and Heating Limitations. To estimate the possible substrate heating that might affect the efficiency of the proposed SERS

https://doi.org/10.1021/acsanm.3c00281
ACS Appl. Nano Mater. 2023, 6, 4770−4781

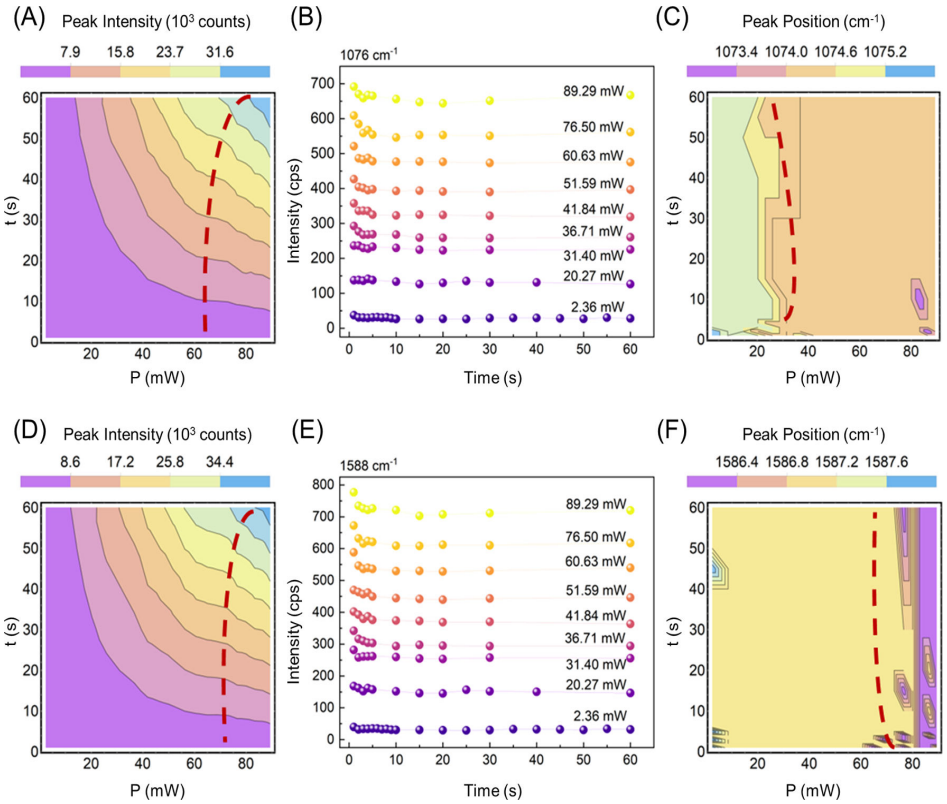

Figure 4. Evaluation of the photothermal effect on characteristic bands in SERS spectra of 4-MBA SAM on the bSi/Au substrate. SERS peak intensities of 1076 (A) and 1588 cm^{-1} (D); dynamic curves of intensities (in cps) obtained for 1076 cm^{-1} (B) and 1588 cm^{-1} (E) bands; the dependencies of the peak positions of 1076 cm^{-1} (C) and 1588 cm^{-1} (F) bands on the laser power and time of exposure of the probed 4-MBA molecules to excitation irradiation. The excitation wavelength is 785 nm. Ranges on the false color maps that correspond to photothermally affected and unaffected spectral characteristics are separated by red dashed lines.

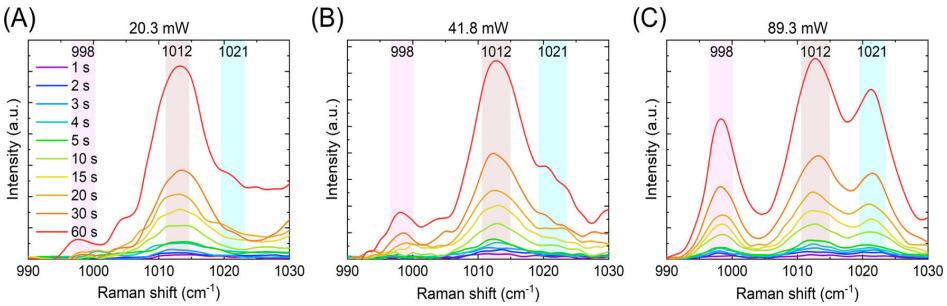

Figure 5. SERS spectra of a 4-MBA monolayer on bSi/Au in the range of 990−1030 cm^{-1}. The exposure time varies from 1 to 60 s. The excitation powers are (A) 20.3, (B) 41.8, and (C) 89.3 mW.

substrates, the SERS spectra of a 4-MBA monolayer on bSi/Au were obtained, varying the laser power from 3.8 to 90.9 mW and sample exposure time from 1 to 60 s. Variation of the intensities at 1076 and 1588 cm^{-1} and their shifts are presented in Figure 4. The bSi/Au substrate provides a detectable signal already at 1 s of exposure with 3.6 mW laser

https://doi.org/10.1021/acsanm.3c00281
ACS Appl. Nano Mater. 2023, 6, 4770−4781

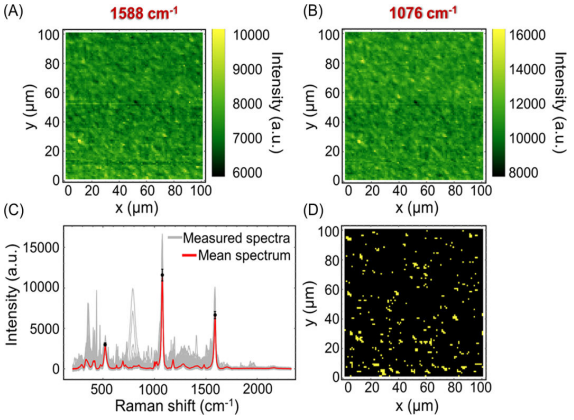

Figure 6. Two-dimensional (2D) distribution of the peak intensities at 1076 (A) and 1586 cm^{-1} (B) of SERS spectra of the 4-MBA monolayer deposited on top of the bSi/Au substrate. (C) 4-MBA SERS spectra from the whole scanned area of 100 × 100 μm^2 (shown in gray color); an orange spectrum corresponds to the mean SERS spectrum of 4-MBA. (D) Spatial distribution of accidental impurities. Measurement parameters: λ_{ex} = 785 nm, exposure time is 1s, laser power is 0.05 mW, scanning step is 1 μm, 50× objective.

power, and it reaches values suitable for analysis after 7 s of irradiation at 13 mW laser power. An intensity vs time SERS signal profiling revealed a slight decrease in SERS measured at both 1076 and 1588 cm^{-1} when the total energy imparted to the sample reaches 70 mW × 20 s = 1.4 J (see Figure 4A,D).

Local heating of gold plasmonic nanostructures may negatively affect the EF, lead to a decrease in the SERS signal,[53,54] and cause photothermal damage to the analyte, resulting in its degradation.[55] Figure 4B and E show the dynamics of the 1076 and 1588 cm^{-1} band intensities (in cps) in the SERS spectra of the 4-MBA SAM at different laser powers and exposure times of the probed molecules to irradiation at λ_{ex} = 785 nm. As can be noticed from the dynamic curves, there is no significant decrease in the SERS intensity under a wide range of experimental conditions, and only at laser powers exceeding 31.4 mW, a decrease of less than 10% in the intensity occurs. The results indicate that in contrast to, e.g., Mo-doped Ta_2O_5 semiconductor SERS substrates,[51] for which photoinduced degradation is non-negligible and could not be ignored as 5 mW and 60 s irradiation of 10^{-6} M methyl violet with a 532 nm laser causes approx. 30% intensity loss, bSi/Au SERS substrates could be used in wider time and laser power scales. The peak shift dependence on the laser intensity detected in Figure 4C,F may also correspond to the possible sample damage due to the high laser intensities, which was not detected using SERS intensities of the most intensive bands (1076 and 1588 cm^{-1}).

Analysis of the 990−1030 cm^{-1} range also reveals the PTE in 4-MBA SAM on the bSi/Au surface. Bands at 996 and 1021 cm^{-1}, which are associated with monosubstituted benzene derivatives (out-of-plane and in-plane ring deformations, respectively[56]), appear at the excitation power of 41.8 mW and exposure time of 20 s (see Figure 5). As mentioned above, the appearance of monosubstituted benzene derivatives indicates that the decarboxylation of the 4-MBA molecule occurs. The loss of the carboxylic group is caused by the plasmon-derived "hot" electron transfer from the metal to the absorbed molecules because of the plasmon excitation and is promoted by substrate heating. The obtained results allow assuming the upper limit for the total energy delivered to the analyte, avoiding the PTE, to be close to 1.0 J.

3.4. bSi/Au Substrate Uniformity. Evaluation of the bSi/Au SERS-substrate uniformity in terms of signal enhancement was performed by laser-scanning confocal Raman microscopy. False color maps of the distribution of intensities of 1076 and 1588 cm^{-1} bands are presented in Figure 6A,C, respectively. Relative standard deviations for both peak intensities were 0.06, and the medians almost completely coincide in magnitude with the mean values (see Table S2, Supporting Information). These parameters indicate very good uniformity of the substrate and a high density of hotspots (scanning step was 1 μm) across the analyzed area of 100 × 100 μm^2. However, in addition to the spectra of the analyzed analyte (4-MBA), spectra of impurities were detected, which were present on the substrate because of preparatory manipulations and/or came from the environment during the measurement itself (the gray spectra in Figure 6C). Additional statistical analyses showed that the number of "impurity" spectra was 434 out of 10201 (4%) (Figure S5, Supporting Information), impurities are distributed randomly and evenly over the substrate (see Figure 6D), and they can be easily identified and excluded from further analysis, significantly increasing the accuracy of the research.

3.5. Long-Term Stability of the bSi/Au SERS Substrate and its Reusability. Several simultaneously fabricated bSi/Au substrates were individually packed in plastic Petri dishes, wrapped with a parafilm to avoid accidental contamination, and stored under ambient conditions. These substrates were used to obtain 4-MBA SERS spectra after storage for 1−20 months in the same measurement setup. The results are summarized in Figure 7. The intensity of two characteristic bands at 1076 and 1588 cm^{-1} in the 4-MBA spectra decreased by less than 5% after 120 days and by 40% after 20 months of storage.

SERS spectra are collected from the molecules in the proximity of the bSi/Au surface. This is the main barrier to reusing the substrate, as physically or chemically adsorbed molecules are hardly eliminated. Remaining residues may

https://doi.org/10.1021/acsanm.3c00281
ACS Appl. Nano Mater. 2023, 6, 4770−4781

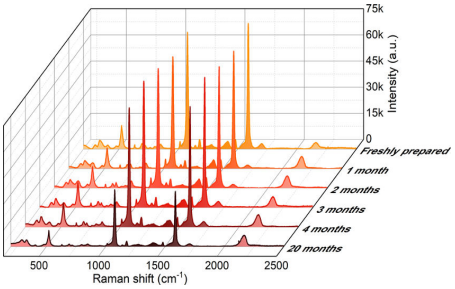

Figure 7. Storage stability of the bSi/Au substrate evaluated with 4-MBA as a probe analyte. Each SERS spectrum corresponds to a 4-MBA monolayer on the surface of freshly manufactured bSi/Au samples and bSi/Au samples stored for 1, 2, 3, 4, and 20 months.

decrease the effective area accessible for analyte molecules and yield signals that will interfere with the signal from the analyte; moreover, the cleaning procedure itself may damage the hotspots, decreasing the effectiveness of SERS spectra detection.

To reuse the bSi/Au substrate, mild oxygen plasma cleaning at room temperature was chosen as a surface refreshing procedure due to its wide accessibility in laboratories. A decrease in the intensity of the most intense bands of 4-MBA at 1076 and 1588 cm^{-1} by more than 99% was chosen as a determining criterion for whether the bSi/Au surface was free of the analyte molecule. It was estimated that 35 min in oxygen plasma is enough for residue elimination from the bSi/Au substrate (see Figure S6, Supporting Information), and after rinsing the substrate in deionized water and drying, it can be reused. The recycling of the substrate leads to a 4-MBA signal decrease and an increase in the intensity of the band centered at 560 cm^{-1} and assigned to ν(Au-O) formation due to the oxygen plasma effect (see Figure 8A).[57] To estimate the degree of EF decrease, the intensities of the 1076 and 1588 cm^{-1} bands were normalized with respect to the intensity of the 520 cm^{-1} band of silicon for each cycle of reuse. The intensity of the 520 cm^{-1} band remains constant over the whole area of the bSi/Au substrate (see Table S2, Supporting Information). As it does not change during the cleaning of the substrate with oxygen plasma, it is convenient to use this band as a reference to exclude possible laser intensity fluctuations in different experiments.

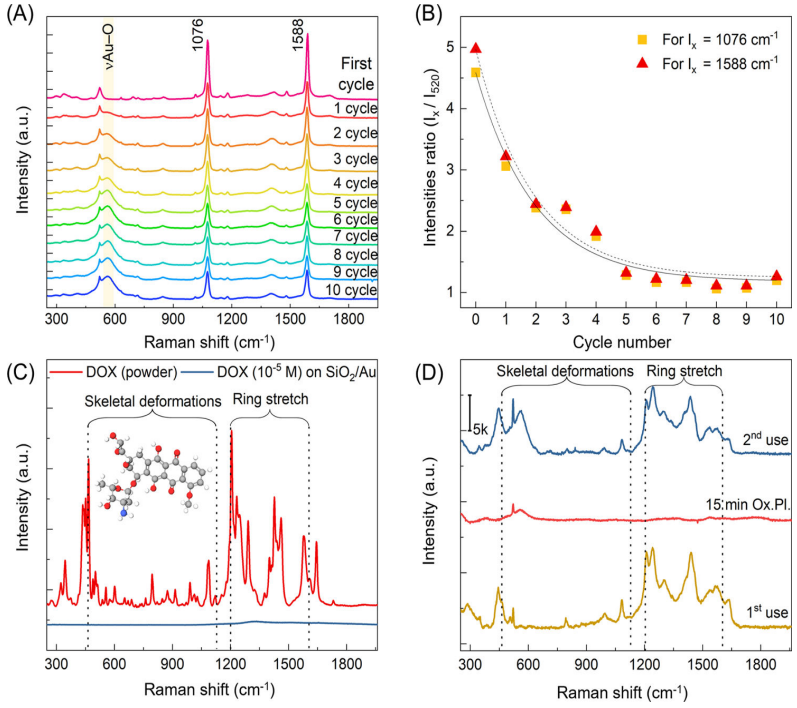

Figure 8. Versatility of the bSi/Au substrate reuse demonstrated for (A, B) covalently bonded molecules of 4-MBA and (C, D) noncovalently bonded molecules of DOX. (A) SERS spectra of 4-MBA on the bSi/Au substrate over 10 reusability cycles; (B) dependence of the 1076 and 1588 to 521 cm^{-1} intensity ratios on the number of reuse cycles; (C) Raman spectrum of DOX (powder) and SERS spectrum of 10^{-5} M of DOX on SiO_2/Au; (D) SERS spectrum of 10^{-5} M of DOX on bSi/Au substrate before oxygen plasma cleaning (mustard line), spectra of bSi/Au substrate after 15 min of oxygen plasma treatment (red line), and SERS spectrum of 10^{-5} M DOX on the reused bSi/Au substrate (blue line).

https://doi.org/10.1021/acsanm.3c00281
ACS Appl. Nano Mater. 2023, 6, 4770−4781

As it follows from Figure 8B, the intensity ratios decrease 5 times after the fifth cycle of reuse; however, the EF as compared with SiO_2/Au remains acceptable for analyte detection and analysis. Moreover, the high uniformity of hotspot distribution allows the accumulation and further integration of the SERS signal from large-scale areas, which is of even higher importance than EF for detecting trace amounts of analytes.[10]

3.6. Evaluation of Doxorubicin Concentration with the bSi/Au SERS Substrate. The bSi/Au substrate has been proven to be suitable also for the detection of molecules that do not form covalent bonds with it. BSi/Au was applied to detect the spectrum of the anticancer drug doxorubicin (DOX).[58] DOX causes many side effects, such as heart damage (cardiotoxicity), cardiomyopathy, and heart failure.[59,60] Therefore, control of the DOX concentration in the blood plasma during chemotherapy is important to minimize the possible harm to the patient during treatment.

DOX has a characteristic Raman spectrum; however, it is challenging to detect low concentrations of DOX in water solutions (Raman spectra of DOX powder and 10^{-5} M DOX solution are shown in Figure 8C). This obstacle can be overcome by the SERS approach, allowing the detection of DOX at concentrations of 1.0 nM to 0.1 mM (see Figure 9).

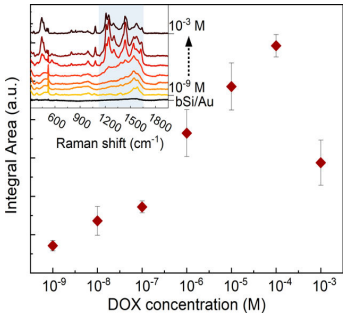

Figure 9. Calibration plot for the determination of DOX concentration by the bSi/Au substrate. Inset: SERS spectra of DOX at different concentrations (1.0 nM to 1.0 mM).

SERS spectra of a 10^{-5} M DOX solution are presented in Figure 8D (mustard line). Because of the low intensities of the R−H stretching range around 3000 cm^{-1}, data are presented for the fingerprint region of 300−1800 cm^{-1}. Characteristic vibrational frequencies of DOX are marked in the Raman and SERS spectra in Figure 8C,D; major band assignments are presented in Table S3 (Supporting Information).

The spectra of DOX were obtained from three different points with minor intensity fluctuations detected. The range 1150−1700 cm^{-1} corresponds to the ring stretch,[61] and the areas under the spectra in this range were used to obtain the concentration calibration curve (see Figure 9). Violation of the monotonicity of the calibration curve at DOX concentrations >10^{-3} M is associated with two factors: (i) agglomeration of DOX molecules at high concentrations leading to changes in the spectrum; (ii) decay of the SERS signal with an increase in the distance from the plasmonic structures due to the formation of several layers of analyte molecules. Thus, the DOX concentration range detectable with bSi is between 10^{-9} and 10^{-4} M.

To regenerate the bSi/Au surface before the next measurement, it is sufficient to treat the surface with oxygen plasma for 15 min to completely remove all adsorbed DOX molecules. During continuous multiple SERS-based measurements of DOX by the bSi/Au substrate, the same intensities of spectrum bands are observed (see Figure 8D), although the ν(Au-O) band is detected and should be considered when reusing the bSi/Au substrate during continuous measurements.

4. CONCLUSIONS

Analytical application of SERS substrates implies long-term stability and reusability. The majority of the manufactured substrates are disposable. Therefore, they can be stored only for a short period of time because of the aggregation and precipitation of colloidal nanoparticles in solutions due to their extreme sensitivity to storage conditions,[62] external environment, and/or impurities, due to the oxidation of metal nanoparticles, predominantly Ag and Au, immobilized on the supporting substrate,[63] or because of the mechanical fragility of the structures supporting nanoparticles, such as silicon nanowires,[23] and the irreversible collapse and agglomeration of plasmonic noble metal "caps" at the ends of flexible nanopillars[5,64] caused by surface tension upon contact with the analyte.

In the present study, we propose a simple one-step production of bSi with an extremely high effective surface area by room-temperature ICP-RIE technique. The sharp vertically oriented lace-like silicon plates create favorable conditions for the growth of gold nanostructures, which are similar in shape to overlapping hemispheres of 4−16 nm sizes on the side walls of blades and spherical nanoparticles of around 34.6 nm on the apex of cones with several extralarge particles of average size around 109.7 nm. The created structures demonstrate high Raman signal enhancement with excitation in the NIR region (785 nm), with an EF of around 10^6. A significant advantage of the produced bSi is the reduced thickness of the gold layer as compared with other gold-based structures used in SERS-based analyses.[30,31] The high surface density of vertically aligned gold nanostructures ensures the shift of the absorption cross-section to the NIR range and the high magnitude of electromagnetic field enhancement, as demonstrated in several studies.[32,65]

The bSi/Au substrate is characterized by the high reproducibility of the results and low signal variation within 6% over a 100 × 100 μm^2 area. Substrate storage in the air atmosphere and under normal ambient conditions results in less than 3% signal decrease over 4 months and around 40% decrease over 20 months of storage, which is, according to our knowledge, the longest term of SERS substrate storage, which offers good SERS signal enhancement. Along with this, the produced substrates can be reused. Substrate treatment with oxygen plasma, commonly available in most laboratories, allows one to get rid of the layer of molecules attached to the surface and retains the properties of the structures to enhance significantly the Raman signal from the analyte when the substrate is reused during continuous measurements. The number of reuse cycles exceeds 10. As proof of the concept, the SERS substrate was applied to detect the chemotherapeutic drug, DOX, and it was determined that DOX concentrations can be determined in the range of 1.0 nM to 0.1 mM. The developed bSi/Au surface recycling procedure preserved the

https://doi.org/10.1021/acsanm.3c00281
ACS Appl. Nano Mater. 2023, 6, 4770−4781

sensitivity of the substrate toward DOX with similar sensitivity as no observable SERS signal decrease was registered. Moreover, such a thin gold layer (tens of nanometers) deposited on the highly developed surface of bSi does not eliminate the first-order Si Raman band in the SERS spectra of analytes, and this can be used for independent Raman signal normalization at the silicon line and thereby allows quantitative determination of the concentration of the studied substances.

Summarizing, the type of bSi proposed in this study is easily producible on a large scale as the nano-microstructure-based morphology can significantly reduce the cost because much lower amounts of noble metal (gold) are required for the formation of plasmonic structures. The bSi/Au substrate provides a significant signal enhancement upon excitation in the near-IR range with a reproducible, stable, and uniform signal. bSi/Au is a highly sensitive SERS substrate, which can be repeatedly used to detect trace amounts of analytes and can be effectively used to assess the concentration of analytes in aqueous media, for example, organics-based medicinal compounds. All of the above open the way for the mass application of bSi/Au SERS substrates in many fields of science, allowing their commercialization and wide use as a routine technique that does not require high costs, compliance with special (sterile, for example) conditions, and complex sample preparation.

■ ASSOCIATED CONTENT

Supporting Information

The Supporting Information is available free of charge at https://pubs.acs.org/doi/10.1021/acsanm.3c00281.

Black silicon absorbance; large-scale uniformity and regularity of bSi structures; evaluation of gold nanoparticle size distribution; vibrational frequencies of 4-MBA in the Raman and SERS spectra; EF and effective surface area estimation; uniformity of the SERS signal over a 100 × 100 μm^2 area and substrate contamination; estimation of the parameters for oxygen plasma removal of the 4-MBA molecules attached to the substrate; typical vibrational frequencies of DOX water solution (PDF)

■ AUTHOR INFORMATION

Corresponding Author

Lena Golubewa − *Department of Molecular Compound Physics, State Research Institute Center for Physical Sciences and Technology, Vilnius LT-10257, Lithuania; Department of Physics and Mathematics, Center for Photonics Sciences, University of Eastern Finland, Joensuu FI-80101, Finland;* orcid.org/0000-0003-2125-6366; Email: lena.golubewa@ftmc.lt

Authors

Aliona Klimovich − *Department of Organic Chemistry, State Research Institute Center for Physical Sciences and Technology, Vilnius LT-10257, Lithuania;* orcid.org/0000-0002-4015-3517

Igor Timoshchenko − *Department of Molecular Compound Physics, State Research Institute Center for Physical Sciences and Technology, Vilnius LT-10257, Lithuania*

Yaraslau Padrez − *Department of Molecular Compound Physics, State Research Institute Center for Physical Sciences and Technology, Vilnius LT-10257, Lithuania;* orcid.org/0000-0003-0852-6579

Marina Fetisova − *Department of Physics and Mathematics, Center for Photonics Sciences, University of Eastern Finland, Joensuu FI-80101, Finland;* orcid.org/0000-0002-7531-3891

Hamza Rehman − *Department of Physics and Mathematics, Center for Photonics Sciences, University of Eastern Finland, Joensuu FI-80101, Finland*

Petri Karvinen − *Department of Physics and Mathematics, Center for Photonics Sciences, University of Eastern Finland, Joensuu FI-80101, Finland*

Algirdas Selskis − *Department of Characterization of Materials Structure, State Research Institute Center for Physical Sciences and Technology, Vilnius LT-10257, Lithuania*

Sonata Adomavičiūtė-Grabusovė − *Institute of Chemical Physics, Vilnius University, Vilnius LT-10222, Lithuania*

Ieva Matulaitienė − *Department of Organic Chemistry, State Research Institute Center for Physical Sciences and Technology, Vilnius LT-10257, Lithuania*

Arunas Ramanavicius − *Department of Physical Chemistry, Vilnius University, Vilnius LT-03225, Lithuania;* orcid.org/0000-0002-0885-3556

Renata Karpicz − *Department of Molecular Compound Physics, State Research Institute Center for Physical Sciences and Technology, Vilnius LT-10257, Lithuania;* orcid.org/0000-0001-5884-4538

Tatsiana Kulahava − *Department of Molecular Compound Physics, State Research Institute Center for Physical Sciences and Technology, Vilnius LT-10257, Lithuania*

Yuri Svirko − *Department of Physics and Mathematics, Center for Photonics Sciences, University of Eastern Finland, Joensuu FI-80101, Finland;* orcid.org/0000-0002-2927-6233

Polina Kuzhir − *Department of Physics and Mathematics, Center for Photonics Sciences, University of Eastern Finland, Joensuu FI-80101, Finland;* orcid.org/0000-0003-3689-0837

Complete contact information is available at: https://pubs.acs.org/10.1021/acsanm.3c00281

Author Contributions

L.G., T.K., R.K., and P.K. worked out the concept of the research. L.G. and A.K. conceived and designed the experimental study and performed the Raman and SERS measurements. M.F., H.R., and P.Ka. synthesized black silicon substrates. I.M. and S.A.-G. performed 2D Raman mapping. Spectral data analysis and statistical studies were carried out by L.G., A.K., I.T., and Y.P. Scanning electron microscopy was performed by A.S. The manuscript was written by L.G. and A.K. Manuscript review and editing were performed by A.R., R.K., T.K., Y.S., and P.K. All authors have approved the final version of the manuscript.

Notes

The authors declare no competing financial interest.

■ ACKNOWLEDGMENTS

This study was accomplished with the financial support of the Academy of Finland (Flagship Programme PREIN, decision 320166), Horizon 2020 RISE DiSeTCom (Project No. 823728), and Horizon Europe FLORIN (Project No. 101086142).

REFERENCES

(1) Mosier-Boss, P. A. Review of SERS Substrates for Chemical Sensing. *Nanomaterials* **2017**, *7*, No. 142.

(2) Kahraman, M.; Mullen, E. R.; Korkmaz, A.; Wachsmann-Hogiu, S. Fundamentals and Applications of SERS-Based Bioanalytical Sensing. *Nanophotonics* **2017**, *6*, 831−852.

(3) Heeg, S.; Mueller, N. S.; Wasserroth, S.; Kusch, P.; Reich, S. Experimental Tests of Surface-Enhanced Raman Scattering: Moving beyond the Electromagnetic Enhancement Theory. *J. Raman Spectrosc.* **2021**, *52*, 310−322.

(4) He, S.; Chua, J.; Tan, E. K. M.; Kah, J. C. Y. Optimizing the SERS Enhancement of a Facile Gold Nanostar Immobilized Paper-Based SERS Substrate. *RSC Adv.* **2017**, *7*, 16264−16272.

(5) Schmidt, M. S.; Hübner, J.; Boisen, A. Large Area Fabrication of Leaning Silicon Nanopillars for Surface Enhanced Raman Spectroscopy. *Adv. Mater.* **2012**, *24*, OP11−OP18.

(6) Pérez-Jiménez, A. I.; Lyu, D.; Lu, Z.; Liu, G.; Ren, B. Surface-Enhanced Raman Spectroscopy: Benefits, Trade-Offs and Future Developments. *Chem. Sci.* **2020**, *11*, 4563−4577.

(7) Neri, G.; Fazio, E.; Mineo, P. G.; Scala, A.; Piperno, A. SERS Sensing Properties of New Graphene/Gold Nanocomposite. *Nanomaterials* **2019**, *9*, 1236.

(8) Liu, C. Y.; Ram, R.; Kolaru, R. B.; Jana, A. S.; Sadhu, A. S.; Chu, C. S.; Lin, Y. N.; Pal, B. N.; Chang, S. H.; Biring, S. Ingenious Fabrication of Ag-Filled Porous Anodic Alumina Films as Powerful SERS Substrates for Efficient Detection of Biological and Organic Molecules. *Biosensors* **2022**, *12*, 807.

(9) Nguyen, T. Van.; Vu, D. C.; Pham, T. S.; Bui, H.; Pham, T. B.; Hoang, T. H. C.; Pham, V. H.; Pham, V. H. Quasi-3D-Structured Surface-Enhanced Raman Scattering Substrates Based on Silver Nanoparticles/Mesoporous Silicon Hybrid. *Phys. Status Solidi Appl. Mater. Sci.* **2022**, *219*, No. 2200128.

(10) Lafuente, M.; Berenschot, E. J. W.; Tiggelaar, R. M.; Rodrigo, S. G.; Mallada, R.; Tas, N. R.; Pina, M. P. Attomolar SERS Detection of Organophosphorous Pesticides Using Silver Mirror−like Micro-Pyramids as Active Substrate. *Microchim. Acta* **2020**, *187*, No. 247.

(11) Zhou, X. X.; Liu, R.; Hao, L. T.; Liu, J. F. Identification of Polystyrene Nanoplastics Using Surface Enhanced Raman Spectroscopy. *Talanta* **2021**, *221*, No. 121552.

(12) Ambroziak, R.; Krajczewski, J.; Pisarek, M.; Kudelski, A. Immobilization of Cubic Silver Plasmonic Nanoparticles on TiO2Nanotubes, Reducing the Coffee Ring Effect in Surface-Enhanced Raman Spectroscopy Applications. *ACS Omega* **2020**, *5*, 13963−13972.

(13) Ou, Y.; Wang, L. Y.; Zhu, L. W.; Wan, L. S.; Xu, Z. K. In-Situ Immobilization of Silver Nanoparticles on Self-Assembled Honeycomb-Patterned Films Enables Surface-Enhanced Raman Scattering (SERS) Substrates. *J. Phys. Chem. C* **2014**, *118*, 11478−11484.

(14) Chiang, C. Y.; Liu, T. Y.; Su, Y. A.; Wu, C. H.; Cheng, Y. W.; Cheng, H. W.; Jeng, R. J. Au Nanoparticles Immobilized on Honeycomb-like Polymeric Films for Surface-Enhanced Raman Scattering (SERS) Detection. *Polymers* **2017**, *9*, 93.

(15) Sun, H.; Gao, R.; Zhu, A.; Hua, Z.; Chen, L.; Wang, Y.; Zhang, Y. Surface-Enhanced Raman Scattering from Metal and Transition Metal Nano-Caped Arrays. *Superlattices Microstruct.* **2018**, *115*, 59−66.

(16) Chiou, A. H.; Wei, J. L.; Chen, S. H. Ag-Functionalized Si Nanowire Arrays Aligned Vertically for Sers Detection of Captured Heavy Metal Ions by Bsa. *Coatings* **2021**, *11*, 685.

(17) Wang, P.; Wu, L.; Lu, Z.; Li, Q.; Yin, W.; Ding, F.; Han, H. Gecko-Inspired Nanotentacle Surface-Enhanced Raman Spectroscopy Substrate for Sampling and Reliable Detection of Pesticide Residues in Fruits and Vegetables. *Anal. Chem.* **2017**, *89*, 2424−2431.

(18) Boginskaya, I.; Sedova, M.; Baburin, A.; Afanas'ev, K.; Zverev, A.; Echeistov, V.; Ryzhkov, V.; Rodionov, I.; Tonanaiskii, B.; Ryzhikov, I.; Lagarkov, A. SERS-Active Substrates Nanoengineering Based on e-Beam Evaporated Self-Assembled Silver Films. *Appl. Sci.* **2019**, *9*, 3988.

(19) Zhou, N.; Meng, G.; Huang, Z.; Zhang, X.; Zhu, C.; Ke, Y. Ag-Coated 3D Cu(OH)2 Nanowires on the Woven Copper Mesh as a Cost-Effective Surface-Enhanced Raman Scattering Substrate. *Surf. Coatings Technol.* **2021**, *415*, No. 127132.

(20) La Porta, A.; Grzelczak, M.; Liz-Marzán, L. M. Gold Nanowire Forests for SERS Detection. *ChemistryOpen* **2014**, *3*, 146−151.

(21) Abu Hatab, N. A.; Oran, J. M.; Sepaniak, M. J. Surface-Enhanced Raman Spectroscopy Substrates Created via Electron Beam Lithography and Nanotransfer Printing. *ACS Nano* **2008**, *2*, 377−385.

(22) Salvador-Porroche, A.; Herrer, L.; Sangiao, S.; Philipp, P.; Cea, P.; De Teresa, J. M. High-Throughput Direct Writing of Metallic Micro- and Nano-Structures by Focused Ga+Beam Irradiation of Palladium Acetate Films. *ACS Appl. Mater. Interfaces* **2022**, *14*, 28211−28220.

(23) Kara, S. A.; Keffous, A.; Giovannozzi, A. M.; Rossi, A. M.; Cara, E.; D'Ortenzi, L.; Sparnacci, K.; Boarino, L.; Gabouze, N.; Soukane, S. Fabrication of Flexible Silicon Nanowires by Self-Assembled Metal Assisted Chemical Etching for Surface Enhanced Raman Spectroscopy. *RSC Adv.* **2016**, *6*, 93649−93659.

(24) Mendes, P. M.; Jacke, S.; Critchley, K.; Plaza, J.; Chen, Y.; Nikitin, K.; Palmer, R. E.; Preece, J. A.; Evans, S. D.; Fitzmaurice, D. Gold Nanoparticle Patterning of Silicon Wafers Using Chemical E-Beam Lithography. *Langmuir* **2004**, *20*, 3766−3768.

(25) Peng, Y.; Cui, L.; Gao, J.; Jiang, S.; Wang, H.; Yu, B.; Qian, L. Fabrication of High-Performance Microfluidic SERS Substrates by Metal-Assisted Chemical Etching of Silicon Scratches. *Surf. Topogr. Metrol. Prop.* **2022**, *10*, No. 035008.

(26) Fan, Z.; Cui, D.; Zhang, Z.; Zhao, Z.; Chen, H.; Fan, Y.; Li, P.; Zhang, Z.; Xue, C.; Yan, S. Recent Progress of Black Silicon: From Fabrications to Applications. *Nanomaterials* **2021**, *11*, No. 41.

(27) Atteia, F.; Le Rouzo, J.; Berginc, G.; Simon, J.-J.; Escoubas, L. *Black Silicon (BS) Using Room-Temperature Reactive Ion Etching (RT-RIE) for Interdigitated Back Contact (IBC) Silicon Solar Cells* SPIE, 2019; Vol. *10913*, p 29 DOI: 10.1117/12.2509326.

(28) Sainiemi, L.; Jokinen, V.; Shah, A.; Shpak, M.; Aura, S.; Suvanto, P.; Franssila, S. Non-Reflecting Silicon and Polymer Surfaces by Plasma Etching and Replication. *Adv. Mater.* **2011**, *23*, 122−126.

(29) Chen, Y.; Kang, G.; Shah, A.; Pale, V.; Tian, Y.; Sun, Z.; Tittonen, I.; Honkanen, S.; Lipsanen, H. Improved SERS Intensity from Silver-Coated Black Silicon by Tuning Surface Plasmons. *Adv. Mater. Interfaces* **2014**, *1*, No. 1300008.

(30) Seniutinas, G.; Gervinskas, G.; Verma, R.; Gupta, B. D.; Lapierre, F.; Stoddart, P. R.; Clark, F.; McArthur, S. L.; Juodkazis, S. Versatile SERS Sensing Based on Black Silicon. *Opt. Express* **2015**, *23*, 6763.

(31) Deng, Y. L.; Juang, Y. J. Black Silicon SERS Substrate: Effect of Surface Morphology on SERS Detection and Application of Single Algal Cell Analysis. *Biosens. Bioelectron.* **2014**, *53*, 37−42.

(32) Golubewa, L.; Karpicz, R.; Matulaitiene, I.; Selskis, A.; Rutkauskas, D.; Pushkarchuk, A.; Khlopina, T.; Michels, D.; Lyakhov, D.; Kulahava, T.; Shah, A.; Svirko, Y.; Kuzhir, P. Surface-Enhanced Raman Spectroscopy of Organic Molecules and Living Cells with Gold-Plated Black Silicon. *ACS Appl. Mater. Interfaces* **2020**, *12*, 50971−50984.

(33) Schneider, C. A.; Rasband, W. S.; Eliceiri, K. W. NIH Image to ImageJ: 25 Years of Image Analysis. *Nat. Methods* **2012**, *9*, 671−675.

(34) Orendorff, C. J.; Gole, A.; Sau, T. K.; Murphy, C. J. Surface-Enhanced Raman Spectroscopy of Self-Assembled Monolayers: Sandwich Architecture and Nanoparticle Shape Dependence. *Anal. Chem.* **2005**, *77*, 3261−3266.

(35) Prochazka, M. *Surface-Enhanced Raman Spectroscopy*; Biological and Medical Physics, Biomedical Engineering; Springer International Publishing: Cham, 2016. DOI: 10.1007/978-3-319-23992-7.

(36) Jiang, L.; You, T.; Yin, P.; Shang, Y.; Zhang, D.; Guo, L.; Yang, S. Surface-Enhanced Raman Scattering Spectra of Adsorbates on Cu2O Nanospheres: Charge-Transfer and Electromagnetic Enhancement. *Nanoscale* **2013**, *5*, 2784−2789.

(37) Pham, X. H.; Hahm, E.; Huynh, K. H.; Son, B. S.; Kim, H. M.; Jeong, D. H.; Jun, B. H. 4-Mercaptobenzoic Acid Labeled Gold-Silver-

Alloy-Embedded Silica Nanoparticles as an Internal Standard Containing Nanostructures for Sensitive Quantitative Thiram Detection. *Int. J. Mol. Sci.* **2019**, *20*, 4841.
(38) Michota, A.; Bukowska, J. Surface-Enhanced Raman Scattering (SERS) of 4-Mercaptobenzoic Acid on Silver and Gold Substrates. *J. Raman Spectrosc.* **2003**, *34*, 21−25.
(39) Capocefalo, A.; Mammucari, D.; Brasili, F.; Fasolato, C.; Bordi, F.; Postorino, P.; Domenici, F. Exploring the Potentiality of a SERS-Active PH Nano-Biosensor. *Front. Chem.* **2019**, *7*, 413.
(40) Scarpitti, B. T.; Morrison, A. M.; Buyanova, M.; Schultz, Z. D. Comparison of 4-Mercaptobenzoic Acid Surface-Enhanced Raman Spectroscopy-Based Methods for PH Determination in Cells. *Appl. Spectrosc.* **2020**, *74*, 1423−1432.
(41) Zong, Y.; Guo, Q.; Xu, M.; Yuan, Y.; Gu, R.; Yao, J. Plasmon-Induced Decarboxylation of Mercaptobenzoic Acid on Nanoparticle Film Monitored by Surface-Enhanced Raman Spectroscopy. *RSC Adv.* **2014**, *4*, 31810−31816.
(42) Schatz, G. C.; Young, M. A.; Duyne, R. P. Electromagnetic Mechanism of SERS. In *Surface-Enhanced Raman Scattering*; Springer: Berlin Heidelberg, 2006; pp 19−45 DOI: 10.1007/3-540-33567-6_2.
(43) Valley, N.; Greeneltch, N.; Van Duyne, R. P.; Schatz, G. C. A Look at the Origin and Magnitude of the Chemical Contribution to the Enhancement Mechanism of Surface-Enhanced Raman Spectroscopy (SERS): Theory and Experiment. *J. Phys. Chem. Lett.* **2013**, *4*, 2599−2604.
(44) Cong, S.; Liu, X.; Jiang, Y.; Zhang, W.; Zhao, Z. Surface Enhanced Raman Scattering Revealed by Interfacial Charge-Transfer Transitions. *Innov.* **2020**, *1*, No. 100051.
(45) Das, G. M.; Managò, S.; Mangini, M.; De Luca, A. C. Biosensing Using Sers Active Gold Nanostructures. *Nanomaterials* **2021**, *11*, 2679.
(46) Ankamwar, B.; Sur, U. K.; Das, P. SERS Study of Bacteria Using Biosynthesized Silver Nanoparticles as the SERS Substrate. *Anal. Methods* **2016**, *8*, 2335−2340.
(47) Khlebtsov, B. N.; Khanadeev, V. A.; Burov, A. M.; Khlebtsov, N. G. A New Type of SERS Tags: Au@Ag Core/Shell Nanorods with Embedded Aromatic Molecules. *Nanotechnologies Russ.* **2017**, *12*, 495−507.
(48) Ma, W.; Sun, M.; Xu, L.; Wang, L.; Kuang, H.; Xu, C. A SERS Active Gold Nanostar Dimer for Mercury Ion Detection. *Chem. Commun.* **2013**, *49*, 4989−4991.
(49) Xie, J.; Zhang, Q.; Lee, J. Y.; Wang, D. I. C. The Synthesis of SERS-Active Gold Nanoflower Tags for in Vivo Applications. *ACS Nano* **2008**, *2*, 2473−2480.
(50) Chaney, S. B.; Shanmukh, S.; Dluhy, R. A.; Zhao, Y. P. Aligned Silver Nanorod Arrays Produce High Sensitivity Surface-Enhanced Raman Spectroscopy Substrates. *Appl. Phys. Lett.* **2005**, *87*, No. 031908.
(51) Yang, L.; Peng, Y.; Yang, Y.; Liu, J.; Huang, H.; Yu, B.; Zhao, J.; Lu, Y.; Huang, Z.; Li, Z.; Lombardi, J. R. A Novel Ultra-Sensitive Semiconductor SERS Substrate Boosted by the Coupled Resonance Effect. *Adv. Sci.* **2019**, *6*, No. 1900310.
(52) Yang, Y.; Peng, Y.; Lin, C.; Long, L.; Hu, J.; He, J.; Zeng, H.; Huang, Z.; Li, Z. Y.; Tanemura, M.; Shi, J.; Lombardi, J. R.; Luo, X. Human ACE2-Functionalized Gold "Virus-Trap" Nanostructures for Accurate Capture of SARS-CoV-2 and Single-Virus SERS Detection. *Nano-Micro Lett.* **2021**, *13*, No. 109.
(53) Xu, Y.; Wang, Y.; Chen, Y.; Yue, Y.; Jiang, J. Temperature Dependence of Raman Enhancement Induced by Au Nanorods Array. *Mater. Res. Express* **2018**, *5*, No. 065057.
(54) Ma, H.; Xu, L.; Tian, Y.; Jiao, A.; Zhang, M.; Li, S.; Chen, M. Design of a Thermally Stable and Highly Active SERS Optical Sensor for the Ultrasensitive Detection of Dye Molecules at High-Temperature. *Opt. Mater. Express* **2021**, *11*, 2001.
(55) Rycenga, M.; Wang, Z.; Gordon, E.; Cobley, C. M.; Schwartz, A. G.; Lo, C. S.; Xia, Y. Probing the Photothermal Effect of Gold-Based Nanocages with Surface-Enhanced Raman Scattering (SERS). *Angew. Chem., Int. Ed.* **2009**, *48*, 9924−9927.
(56) Fontana, J.; Livenere, J.; Bezares, F. J.; Caldwell, J. D.; Rendell, R.; Ratna, B. R. Large Surface-Enhanced Raman Scattering from Self-Assembled Gold Nanosphere Monolayers. *Appl. Phys. Lett.* **2013**, *102*, No. 201606.
(57) Chen, H. C.; Chen, C. H.; Hsu, C. S.; Chen, T. L.; Liao, M. Y.; Wang, C. C.; Tsai, C. F.; Chen, H. M. In Situ Creation of Surface-Enhanced Raman Scattering Active Au-Auo x Nanostructures through Electrochemical Process for Pigment Detection. *ACS Omega* **2018**, *3*, 16576−16584.
(58) Sritharan, S.; Sivalingam, N. A Comprehensive Review on Time-Tested Anticancer Drug Doxorubicin. *Life Sci.* **2021**, *278*, No. 119527.
(59) Mitry, M. A.; Edwards, J. G. Doxorubicin Induced Heart Failure: Phenotype and Molecular Mechanisms. *IJC Hear. Vasc.* **2016**, *10*, 17−24.
(60) Swain, S. M.; Whaley, F. S.; Ewer, M. S. Congestive Heart Failure in Patients Treated with Doxorubicin: A Retrospective Analysis of Three Trials. *Cancer* **2003**, *97*, 2869−2879.
(61) Gautier, J.; Munnier, E.; Douziech-Eyrolles, L.; Paillard, A.; Dubois, P.; Chourpa, I. SERS Spectroscopic Approach to Study Doxorubicin Complexes with Fe 2+ Ions and Drug Release from SPION-Based Nanocarriers. *Analyst* **2013**, *138*, 7354−7361.
(62) Mei, R.; Wang, Y.; Yu, Q.; Yin, Y.; Zhao, R.; Chen, L. Gold Nanorod Array-Bridged Internal-Standard SERS Tags: From Ultra-sensitivity to Multifunctionality. *ACS Appl. Mater. Interfaces* **2020**, *12*, 2059−2066.
(63) Alamri, M.; Sakidja, R.; Goul, R.; Ghopry, S.; Wu, J. Z. Plasmonic Au Nanoparticles on 2D MoS2/Graphene van Der Waals Heterostructures for High-Sensitivity Surface-Enhanced Raman Spectroscopy. *ACS Appl. Nano Mater.* **2019**, *2*, 1412−1420.
(64) Hu, M.; Ou, F. S.; Wu, W.; Naumov, I.; Li, X.; Bratkovsky, A. M.; Williams, R. S.; Li, Z. Gold Nanofingers for Molecule Trapping and Detection. *J. Am. Chem. Soc.* **2010**, *132*, 12820−12822.
(65) Liu, Y.; Kim, M.; Cho, S. H.; Jung, Y. S. Vertically Aligned Nanostructures for a Reliable and Ultrasensitive SERS-Active Platform: Fabrication and Engineering Strategies. *Nano Today* **2021**, *37*, No. 101063.

NOTE ADDED AFTER ASAP PUBLICATION

This paper was published on March 9, 2023. Due to production error, one of the findings was mischaracterized in the Abstract. The corrected version was reposted on March 13, 2023.

https://doi.org/10.1021/acsanm.3c00281
ACS Appl. Nano Mater. 2023, 6, 4770−4781

scientific reports

Check for updates

OPEN

Single-walled carbon nanotubes as a photo-thermo-acoustic cancer theranostic agent: theory and proof of the concept experiment

L. Golubewa[1,2✉], I. Timoshchenko[3], O. Romanov[3], R. Karpicz[1], T. Kulahava[2,3], D. Rutkauskas[1], M. Shuba[2,4], A. Dementjev[1], Yu. Svirko[5] & P. Kuzhir[2,5]

Theranostics is the emerging field of medicine that uniquely combines diagnostic techniques and active agents to diagnose and treat medical conditions simultaneously or sequentially. Finding a theranostic agent capable to cure the affected cells and being safe for the healthy ones is the key for successful treatment. Here, we demonstrate that agglomerated single-walled carbon nanotubes (SWCNTs) are promising theranostic agent that enables photo-activated 'cold' destruction of the cancer cells keeping their environment alive. The absorption of picosecond pulses by SWCNT agglomerates results in the mechanical (due to photoacoustic effect) rather than photothermal cancer cell destruction, which was visualized by micro-Raman and ultrafast near-infrared CARS. The developed theoretical model allows us to distinguish photothermal, photoacoustic, and photothermoacoustic regimes of the cancer cell destruction, and also to optimize SWCNT-based theranostics recipe.

Lasers are widely used in biomedicine because the irradiation of living cells and tissues with coherent light beams may result in a variety of effects. Among the most examined ones are wound healing, tissue coagulation and vaporization, tissue ablation, and necrosis[1]. However, for the tissue embedded with micro- or nanoparticles (NPs) having the sharp absorption lines in the so-called therapeutic window of 650–1350 nm[2], one can employ photothermal[3], photothermoacoustic[4], and photoacoustic[5] effects for treatment. Owing to their ability to target tumor tissue, as well as their capacity to be manipulated by light, NPs are perfectly suitable for theranostic cancer screening, staging, and treatment[6,7] using light in the near-infrared (NIR) tissue transparency window[2].

Photothermal effect (or hyperthermia) is observed when light absorption in NPs results in local overheating of the surrounding tissue[8] that can lead to protein denaturation, cell membrane lysis, and cell death. Although the temperature needed to destroy cancer cells in vitro is as high as 70–80°C[9], even lower temperatures can be used to facilitate the release of therapeutic agents carried by NPs[8]. Similar to the Photothermal effect, Photothermoacoustic and Photoacoustic effects manifest themselves as the generation of acoustic waves in the NP's surrounding tissue[10] due to the conversion of the absorbed light energy into heat inside a NP. In the Photothermoacoustic effect, the NIR absorption by the NP leads to the temperature increase up to thousands of degrees, the surrounding aqueous medium evaporates forming—in the nanosecond time scale—a gas bubble and leading to an acoustic perturbation and local fluid flow[11,12]. The Photoacoustic effect occurs when the conversion of the light energy into heat inside the NP leads to its deformation, which produces an acoustic wave in the surrounding medium, rather than forms the vapour bubble. The important advantage of this effect for cancer treatment is that in the photoacoustic regime, no heating of the surrounding medium takes place, while the cancer cell damage can be achieved by the pressure pulse generated by the overheated NP. That is search for the appropriate theranostic agent for cancer treatment implies finding NPs that enable photoacoustic regime in the NIR spectral range.

Single-walled carbon nanotubes (SWCNTs) can be such a theranostics agent because their high NIR-absorptive ability[13] enables photothermal therapy[14], which is much more specific and much less aggressive compared to conventional chemo- or radiotherapy. High specificity is, to a large extent, the result of SWCNTs' bioactivity

[1]Center for Physical Sciences and Technology, Sauletekio Ave. 3, 10257 Vilnius, Lithuania. [2]Institute for Nuclear Problems, Belarusian State University, Bobruiskaya 11, 220006 Minsk, Belarus. [3]Belarusian State University, Nezavisimosti Ave. 4, 220030 Minsk, Belarus. [4]Tomsk State University, Lenin Ave. 36, Tomsk, Russia 634050. [5]Institute of Photonics, University of Eastern Finland, Yliopistokatu 7, 80100 Joensuu, Finland. ✉email: lena.golubewa@ftmc.lt

and cellular uptake[15,16], which in turn may make them toxic[17]. The latter—along with the lack of solubility in aqueous media[18] as well as biodistribution and pharmacokinetic issues—significantly suppresses the interest of using SWCNTs in biomedicine. However, recent advances in nanotechnology have enabled the mass production of high-quality single-chirality SWCNTs[19], which can be gently cut[20], purified to the almost invisible degree of metal catalyst contamination[21], and functionalized[22]. This has reopened interest to SWCNTs as cancer theranostics agent[23] because short (100 nm)[24] and properly functionalized[25] CNTs are significantly less toxic than long and bare ones.

The properties of biological materials may be changed considerably by embedding carbon NPs[26]. For example, it has been shown that the addition of 1% of CNTs enhances the thermal conductivity of aqueous suspension[27]. By performing SWCNTs' functionalization or varying the incubation time one may localize SWCNTs either inside the cancer cell[28], on the cancer cell membrane[29], or in the surrounding healthy tissue, for example, when transferring through the blood–brain barrier[28]. SWCNT localization and distribution is a crucial factor determining the efficiency of applied therapies, as different types of the external environment, as well as sizes of agglomerates of dispersed SWCNTs, will influence SWCNT response to NIR irradiation. In the biomedical diagnostics and therapy, either suspension of individual (or bundled) SWCNTs or micron-sized SWCNT agglomerates are used. The latter is also formed as a result of cancer cell endocytosis[4] in vitro, huge SWCNT clusters are formed due to administration of high doses and local accumulation of SWCNTs in mice tissue *in vivo*[30].

The aim of this paper is to optimize the SWCNT-based photonic theranostics recipe of detection and cold photodestruction of cancer cells by:

1. developing theory and performing a numerical simulation of the interaction of the NIR light with the SWCNTs aggregated in living cells or accumulated in the intercellular medium, and revealing the conditions of the cold photodestruction regime;
2. experimental demonstration of the cold photodestruction of the glioma C6 cancer cells that have captured the aggregated SWCNTs inside and comparison with laser treatment of the cells surrounded by individual SWCNTs situated in the extracellular medium.

Results

Theory: interaction of the laser pulses with spherical SWCNT agglomerate embedded into a cancer cell. In the Supplementary Information, we present the theory of the interaction of light with the spatially inhomogeneous (turbid) medium with embedded NPs, which have a sufficiently low (to ignore the collective effects) concentration and physical properties very different from the host medium. The performed numerical simulation for the spherical SWCNT bundles and individual SWCNTs placed in the living tissue allows us to reveal the conditions when the photothermal, photothermoacoustic and photoacoustic effects occur in the tissue embedded with the SWCNTs. Figure 1a,b shows the contour map of the temperature increase and negative pressure that can be achieved at the center of the spherical SWCNT agglomerate having a radius of $R_0 = 1$ μm aggregated inside the glioma cell at the initial temperature of 293 K (20 °C). The results of the numerical simulations are summarized in Fig. 1c, which shows characteristic isobar and isotherms in the laser pulse duration-intensity plane.

The yellow line in Fig. 1c presents an isotherm, which corresponds to the agglomerate heating by $\Delta T = 20$ K, when the agglomerate temperature of $T = 313$ K (40 °C) achieves the functionality threshold[31]. The brown line in Fig. 1c corresponds to the agglomerate heating by $\Delta T = 60$ K, which defines the DNA melting threshold of 353 K (80 °C)[32] that corresponds to the cell death. In the heating range of $20\ \mathrm{K} < \Delta T < 60$ K, the temperature-dependent protein denaturation[33] and inactivation of repair of DNA strand breaks[31] take place that causes disruption of cellular functioning and may lead to the cell death. Since selective anticancer therapy implies avoiding heating of normal tissue, the heating of the agglomerates below $\Delta T = 20$ K is preferable. The dark orange line depicts isobar corresponding to the negative pressure change threshold of 0.7 MPa[34]. Most of biological structures have a sufficiently high resistance to compression and are considerably weaker to tensile stress. If the latter in the negative phase of a pressure wave exceeds the ultimate tensile strength of the medium, there is a high probability of local fragmentation of a cell due to micro-breaks, the formation of microbubbles, and other disturbances in the homogeneity of the structure[35–37]. Acoustic perturbations in the medium can be observed when the pulse duration t_p is shorter than time $t_a \approx 100$ ps of propagation of an acoustic wave through the SWCNT bundle. Photothermal effects prevail at $t_p > t_a$, because of the acoustic perturbation decays during the irradiation time. Thus, for the pulses shorter than 100 ps the dark orange line separates the parameter domain into photoacoustic non-destructive imaging[38], for which nanoparticles are often used as contrast agents[39], and photothermoacoustic regime.

The developed model allows us to distinguish photothermal, photothermoacoustic, and photoacoustic regimes of the interaction of light pulses with SWCNT agglomerates embedded in cytoplasm. This model confirms that the intracellular accumulation of SWCNTs and their agglomeration in micro-sized particles are necessary to implement 'cold' photo-induced cancer cell destruction keeping living bare cells intact.

The performed analysis allows us to visualize the cold photoacoustic destruction area ($\Delta T < 20$ K and $|\Delta P| > 0.7$ MPa), for the SWCNT agglomerates in the living cell. In this area, the irradiation with a laser beam *will not* result in tissue overheating, while the light-induced tensile stress in the SWCNT agglomerate accumulated will destroy the cancer cells. To verify the simulation results we choose for our theranostic experiment laser pulses having an intensity of 2.4×10^6 W/cm^2 and a duration of 10 ps (see the star in Fig. 1c).

Experiment: interaction of picosecond laser pulses with glioma cells. We performed an experimental investigation of the interaction of laser radiation with (1) bare glioma cells (as a control sample); (2) gli-

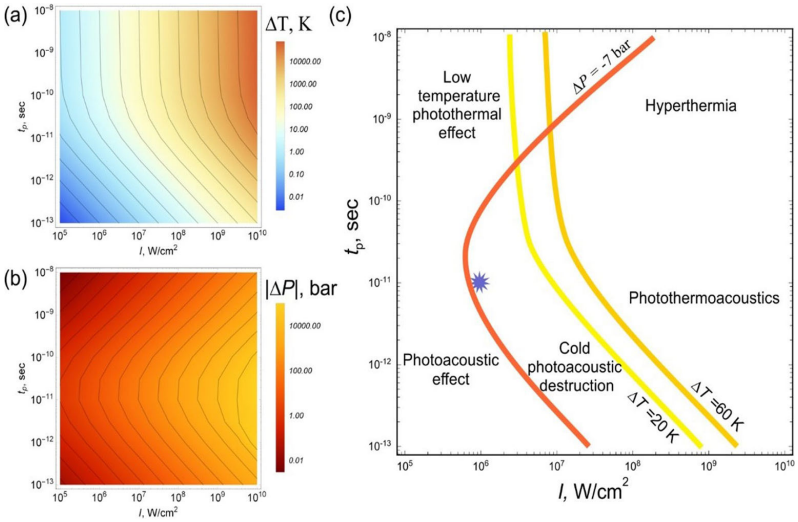

Figure 1. Numerical simulation of the interaction of laser radiation with the SWCNT agglomerate embedded into the living cell. Contour maps of the (**a**) temperature increase and (**b**) negative pressure in the SWCNT agglomerate of $R_0 = 1$ μm (see Supplementary Information for details) aggregated inside the glioma cell on the pulse duration/intensity plane. (**c**) Isotherms at $\Delta T = 20$ K and $\Delta T = 60$ K, respectively, and isobar at $\Delta P = -0.7$ MPa. The star corresponds to the experimental conditions.

oma cells with intracellularly accumulated and aggregated micron-sized SWCNT agglomerates; and (3) glioma cells placed into the extracellular medium with suspended individual SWCNTs.

To visualize both the distribution of the SWCNTs inside the cancer cells and their agglomeration rate we employed G-band (1590 cm^{-1}) and D-band (1330 cm^{-1}) of the SWCNT Raman spectrum. The G-band was used to map the SWCNT distribution in the cytoplasm of the cell. Typical images of cells after their exposure to SWCNTs for 24 h and a typical Raman spectrum of SWCNTs accumulated in the cells are presented in Fig. 2. It was revealed that SWCNTs were accumulated inside rat C6 glioma cells in the form of micron-sized agglomerates, SWCNTs did not enter into the nuclei and remained only in the cytoplasm.

In our experimental conditions, the excitation of the Raman signal with a continuous laser beam at $\lambda_{ex} = 785$ nm did not lead to any observable cell destruction. The laser beam was focused on the largest SWCNT agglomerate inside the cells and the cell was exposed to laser irradiation ($\lambda_{ex} = 785$ nm, 7.2×10^3 W/cm^2, laser spot diameter 2 μm) for 10 min. Re-scan did not show any changes in the state of the cell membrane or the distribution of agglomerates of SWCNTs inside the cell after radiation exposure, as can be seen from Fig. 2a,b. No significant change was observed in the Raman spectra of the SWCNT agglomerate used for irradiation (see Fig. 2e-1(before irradiation) and 2e-2 (after irradiation)). Increasing of the laser intensity up to 2.4×10^6 W/cm^2 and reduction of the scanning step from 2 μm down to 0.5 μm that led to an increase in the scanning time and exposure time of the cell to laser radiation, improved spatial resolution to detect the presence of smaller SWCNT agglomerates (Fig. 2c,d), which were not visualized in the Fig. 2a,b. Nevertheless, a change in the scanning parameters of the sample did not lead to the cell membrane damage and any suppression of its viability.

The same cell was exposed to laser irradiation ($\lambda_{ex} = 785$ nm, 2.4×10^6 W/cm^2, exposure time 30 min, laser spot diameter 2 μm). An increase in intensity and exposure time did not have any effect on cell viability (Fig. 2c,d). Moreover, based on the analysis of the Raman spectrum of CNTs, it could be argued that there was no significant local heating of SWCNTs caused by the conversion of absorbed laser radiation into heat, as there was no increase in the D mode[40] as compared to the spectrum of SWCNTs before irradiation (Fig. 2e 1–4).

Ultra-short laser pulses of high intensity can cause cell damage due to protein coagulation, vaporization, or photoablation[41]. Cells, cultured without SWCNTs, were exposed to picosecond laser irradiation ($\lambda_{ex} = 910.5/1064$ nm). The same laser source was used for simultaneous fast cancer cell visualization by coherent anti-Stokes Raman spectroscopic (CARS) imaging technique (Fig. 3b) performed at 1585 cm^{-1} wavenumber (C = C bending mode in proteins[42]). To exclude the possible harmful influence of picosecond laser pulses having an intensity of 10^6 W/cm^2[43], cell viability was determined before (Fig. 3a) and after (Fig. 3c) the irradiation using fluorescent probe propidium iodide (PI). Exposure of glioma cells to irradiation for approximately 7 min (time for scanning 100 μm × 100 μm area) did not cause any plasma membrane permeabilization, as no PI fluorescence was detected (Fig. 3c).

Using CARS and fluorescent microscopy techniques we demonstrate that glioma cell plasma membrane stays intact and non-permeabilized after being irradiated with 10 ps pulses at $\lambda_{ex} = 910.5/1064$ nm and intensity of

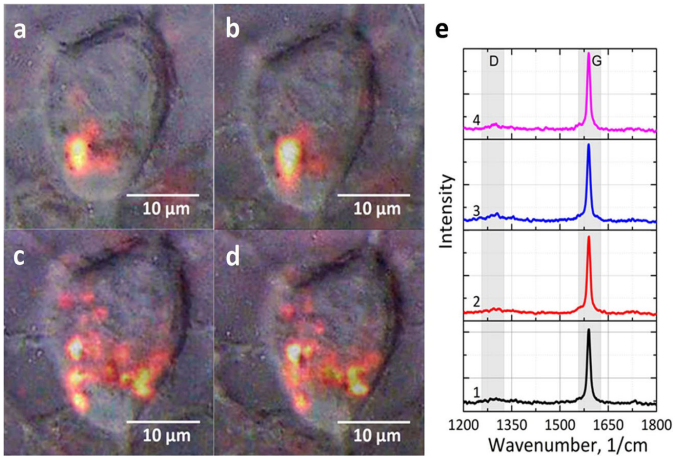

Figure 2. Intracellular accumulation of SWCNTs and structural integrity of C6 glioma cells exposed to continuous laser irradiation with λ_{ex} = 785 nm. (**a**–**d**) images of C6 cells in reflected light superimposed on the map of the Raman G-mode of SWCNTs; (**e**) Raman spectra of SWCNT agglomerates inside the cell. The cell image (**a**) and Raman spectrum (**e-1**) are taken before laser exposure. The cell image (**b**) and Raman spectrum (**e-2**) are taken after irradiation of the cell by a laser beam at the intensity of 7.2×10^3 W/cm^2 for 10 min. The cell images (**c**,**d**) and Raman spectra (**e-3**,**e-4**) correspond to cells before and after laser irradiation for 30 min at the intensity of 2.4×10^6 W/cm^2, respectively.

10^6 W/cm^2. That is, these pulses do not have any destructive effect on the cells and can potentially be used for antitumor therapy and diagnosis.

Glioma cells cultured in the presence of SWCNTs for 24 h effectively accumulated SWCNTs intracellularly, and small SWCNT agglomerates were formed (see micro-Raman spectra in Fig. 2). It was shown, that exposure of cells to SWCNTs for 24 h and their accumulation inside the cell did not influence their viability. No PI fluorescence was detected on the cell membrane surface or somewhere in the external medium and growth surface of a Petri dish in the sample with glioma cells accumulated SWCNTs (Fig. 3d).These data indicate, that all the SWCNTs, detected by Raman microscopy (Fig. 2a–d), were located inside the cell rather than on the membrane[26], and did not adhere to the plastic surface of the Petri dish, which could happen at the cell cultivation stage.

However, the exposition of the cells for 7 min with 10 ps laser pulses at the intensity of 10^6 W/cm^2 and 1 MHz pulse frequency (λ_{ex} = 910.5/1064 nm) led to plasma membrane permeabilization and pore formation, detected simultaneously with irradiation by CARS imaging (Fig. 3e). The CARS signal from cells decreased, but early stages of the violation of the integrity of the cell membrane were visualized. Afterwards, using fluorescent microscopy, violations of the integrity of the cell membrane and its death were demonstrated (Fig. 3f).

To evaluate the importance of the SWCNT intracellular accumulation step, NIR pico-second pulsed light interaction with SWCNTs dispersed in the extracellular medium of cells was investigated. Cells, grown without SWCNTs, but exposed to the medium, containing 5 μg/mL SWCNTs, stayed viable before and after the irradiation with pico-second laser pulses for 7 min because the glioma cell plasma membrane was not permeabilized (Fig. 3g–i).

Therefore our experiment shows that accumulation of SWCNTs inside the cell cytoplasm appeared to be crucial in photo-induced cancer cell destruction by pico-second NIR irradiation. Pulsed irradiation of cells with intracellularly accumulated SWCNTs led to the breaks in cellular membranes and cell death, detected both by CARS and fluorescent microscopy (Fig. 3e–f). Importantly, CARS enables for simultaneous irradiation and real-time visualization of cancer cells.

Simulation of pulsed irradiation interaction with SWCNTs' micron-sized agglomerates and individually dispersed nanotubes fully proved this hypothesis. It was shown that absorption of irradiation by micron-sized agglomerate leads to photoacoustic destruction of glioma cells due to the propagation of the acoustic wave in the NP environment as shown in Fig. S.1b. If the negative pressure (volumetric extension) in the wave exceeds the threshold of $\Delta P_{thresh} \approx$—0.7 MPa, destruction of the medium continuity may occur and lead to the destruction of the membrane integrity of the hosting cell. The developed model shows that laser pulses used in our experiment are capable of achieving the medium continuity destruction threshold. At the same time, local heating in the NP proximity is several degrees (see Supplementary Figure S.1a), which suggests that the photoacoustic mechanism of biostructure damage in this situation should prevail.

The simulation of the interaction of individual SWCNTs with laser pulses also fully supports our experimental results (Fig. 3g–i for experiment and Supplementary Figure S.2 for simulation). The amplitude of the generated

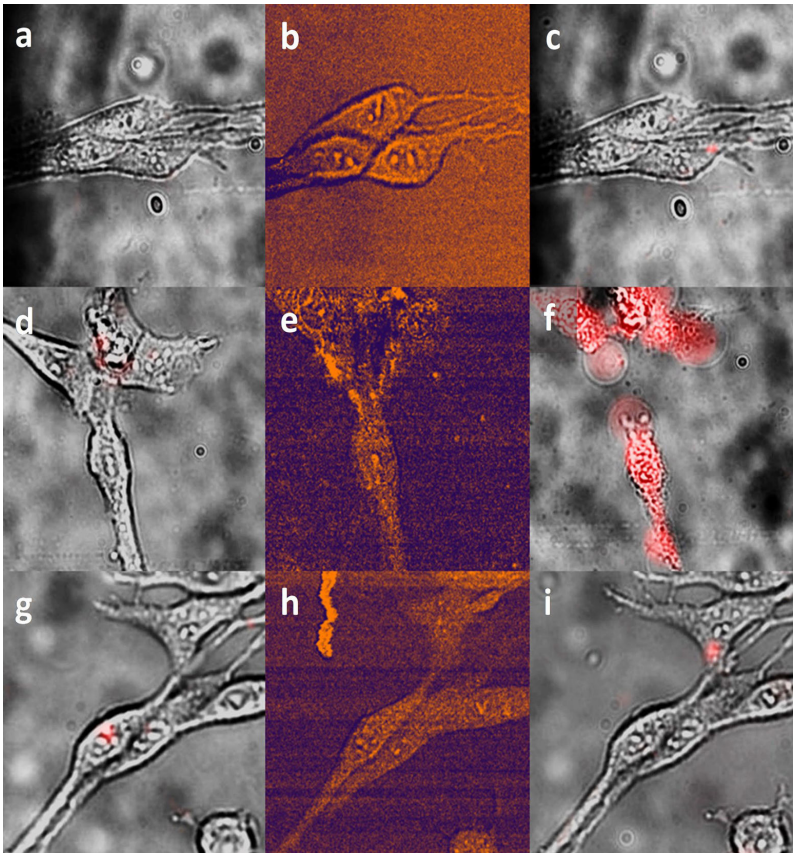

Figure 3. Photo-induced SWCNT-mediated destruction of glioma cells by NIR pico-second pulsed irradiation. (**a**–**c**) Bare C6 glioma cells; (**d**–**f**) C6 glioma cells with accumulated micron-sized SWCNT agglomerates, (**g**–**i**) C6 glioma cells in the presence of the SWCNTs suspension in the extracellular medium. (**a**,**d**,**g**) bright-field images superimposed with PI fluorescence images before irradiation; (**b**,**e**,**h**) CARS images; (**c**,**f**,**i**) bright-field images superimposed with PI fluorescence images after irradiation with 10 ps laser pulses (910.5/1064 nm, 10^6 W/cm^2) for 7 min.

pressure wave is six orders of magnitude lower than that generated in the SWCNT agglomerate. This finding allows us to conclude that in our experimental conditions, the probability of damage to the biostructures due to the generation of acoustic waves by solitary carbon nanotubes is negligible.

Conclusions

We demonstrate that glioma cells are capable of efficient accumulation of SWCNTs to relatively large agglomerates, mainly inside the formed phagolysosomes. These agglomerates enable photo-induced destruction of cancer cells using picosecond laser irradiation. It is worth noting that neither bare cancer cell nor cells with SWCNTs dispersed extracellularly are not damaged under the same irradiation conditions. We also demonstrate that CARS can be effectively used for both visualization of the cancer cell and its photo-induced SWCNT-conditioned destruction, providing strong evidence that this method is a powerful tool for nanotheranostics. The advantage of using stable SWCNT suspensions instead of conventional NPs for photoacoustic therapy is the following: in the case of NPs, not only the cell accumulated NPs will be destroyed, but also normal tissues containing these NPs associated with tumor cells will be damaged. In the case of stable SWCNT suspensions, only cells that have accumulated SWCNTs as agglomerates are destroyed. Individual nanotubes in the extracellular environment are photoacoustically inactive. Therefore, there is no damaging effect on adjacent fluids and tissues.

The performed numerical simulation of the interaction of intense laser pulses with SWCNTs-enriched tissue may be employed to establish a common ground for the comparative study of the scattered literature data, to open a way toward increasing the efficiency of photo-induced CNT-conditioned destruction of tumors, and to reduce the cytotoxic load on the body during anticancer therapy.

Methods

SWCNT-DNA complexes. Single-walled CNTs produced by the HiPCO method (Nanointegris Technology Inc., Batch PO568) in bundles, purified from metal impurities (> 98%) were used throughout all the experiments. SWCNTs diameter varied from 0.8 nm to 1.4 nm (average 1.0 nm). Metallic to semiconducting nanotubes ratio was 1:2. SWCNTs were shortened down to 100–500 nm in length as described in[20] and functionalized by salmon DNA (Sigma-Aldrich, USA). To obtain a DNA solution, 2 mg of the salmon DNA was placed in 6 ml of physiological solution for 2 days at a temperature of 4° C. Then the solution was treated with ultrasonic disperser UZDN-2 T for 30 min at 25% of the maximum power. Then, SWCNT agglomerates were added to 4 ml of the DNA solution and dispersed for 4–6 h at low ultrasonic intensity and room temperature. The resulting suspension was centrifuged for 10 min at 5000 *g*. In this case, SWCNT agglomerates or SWCNTs not coated with a surfactant precipitated. The supernatant was centrifuged again to remove insufficiently dispersed material. The resulting SWCNT-DNA suspension was further used for biological applications. SWCNT-DNA (SWCNTs) concentration was determined via ultraviolet–visible spectroscopy (RV2201 spectrophotometer, ZAO SOLAR, Belarus)[44]. SWCNTs in suspension were stable for up to 4 months. Before each experiment SWCNTs in suspension were additionally centrifuged to remove large agglomerates formed in the suspension.

Cell culture. C6 rat glioma cells (ATCC, CCL-107) were obtained from ATCC, LGC Standards (Ogrodowa 27/29, Kielpin, Poland) and grown in DMEM/F12 (Gibco, USA) medium supplemented with 10% newborn calf serum (Capricorn, Germany) and 80 μg/mL gentamycin sulfate (BelMedPreparaty, Belarus) at 37 °C, 100% humidity, and 5% CO_2. For Raman spectroscopic studies 10^5 cells were seeded per each Petri dish on silicon wafers and grown according to standard protocol. When cells were attached to the silicon surface, SWCNT suspension was added at a final concentration of 5 μg/mL. SWCNT accumulation and distribution inside the cells was investigated after 18–24 h of cells growing in the presence of SWCNTs. For fluorescent microscopy and light exposure studies, cells were seeded at low density (10^4 cells per channel) in 6 channel slide (sticky-Slide VI 0.4, Ibidi, Martinsried, Germany) with a glass coverslip as a substrate. For all experiments we used external Hepes buffer solution of the following composition (in mM): NaCl—126, KCl—3, $MgSO_4$—2, $CaCl_2$—2, Hepes—10, and glucose—6.

Raman spectroscopy of SWCNT distribution inside the cell. For Raman measurements, cells were seeded per each Petri dish on silicon (1 cm × 1 cm) to avoid strong background Raman signal from the glass. After 18 or 24 h incubation with SWCNTs, the cellular monolayer on the slide was washed twice with PBS. Raman spectra of the cell samples were measured using Raman confocal 3D-scanning microscope NanoFinder HighEnd (Lotis TII, Belarus—Tokyo Instruments, Japan) at the excitation wavelength of $\lambda_{ex} = 785$ nm (with a maximum power of about 75 mW). Exposition time was 0.5–2 s, the scanning step was 0.5–2.0 μm. Data are presented using the software packages of OriginPro 8.0 (OriginLab Corp., USA), Microsoft Excel 2007, NanoFinderViewer (Lotis TII, Belarus).

Cells viability determination. To determine cell viability, propidium iodide (PI) as a fluorescent marker of cell membrane permeability was used. PI is a membrane-impermeable weakly fluorescent agent until it binds to DNA or RNA, causing 20–30 increase in fluorescence and 30–40 nm red shift of fluorescence excitation maximum at $\lambda_{ex} = 535$ nm and 15 nm blue shift of fluorescence emission maximum at $\lambda_{em} = 617$ nm[45]. When the cell plasma membrane is not intact and thermally induced pores appear, PI intercalates between the DNA bases inside the cell and strong fluorescence is detected. We used PI at the final concentration of 10^{-6} M in the external buffer solution throughout experiments and replaced PI-containing medium by Hepes buffer without PI washing the cells with continuous fluid flow.

SWCNTs in suspension were added to 2 channels in the 6 channel slide at final concentration 5 μg/mL and cells were cultivated in the presence of these complexes for 24 h before experiments. The other channels contained DMEM/F12 with supplements, used for routine culture procedure.

Cells were irradiated under the microscope using continuous 785 nm laser irradiation of variable light doses on the 3rd day after seeding. For intense pulsed light treatment, a laser diode emitting a series of picosecond pulses was used. Cell samples were divided into three groups: cells without SWCNT-DNA complexes, cells exposed to SWCNT-DNA complexes for 24 h and accumulated SWCNTs inside the cells, and cells grown without SWCNT-DNA complexes, but irradiated in the external medium containing a high dose of SWCNTs (see Fig. 4).

Coherent anti-Stokes Raman spectroscopy (CARS). Home-made CARS system was used. Picosecond 1 MHz laser source (EKSPLA Ltd.) with dual-wavelength was combined with Microscope Olympus IX71 and a piezo scanning system (P-517.3CL, Physik Instrumente GmbH & Co) and utilized for raster-scanning of the sample. The exciting light was focused on the sample with an oil-immersion objective (Olympus, Plan Apochrom., 60X, NA 1.42). For detection of CARS signal the avalanche photodiode (SPCM-AQRH-14, Perkin Elmer), connected to a multifunctional PCI board (7833R, National Instruments) was used. Fundamental wavelength (1064 nm) and tunable-wavelength radiation (700–1000 nm) were used as Stokes and Pump excitation beams, respectively. Scanning of samples was performed at 1585 cm^{-1} wavenumber. For this, the pump beam was tuned to 910.5 nm and the resulting CARS signal within the spectral window from 840 to 782 nm

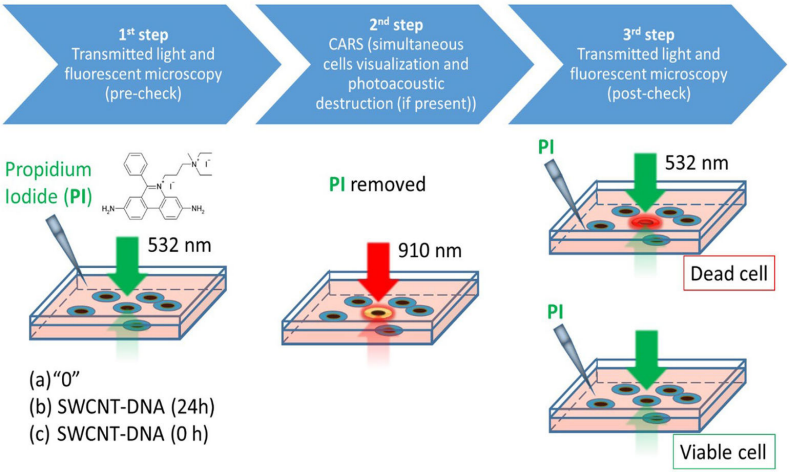

Figure 4. Experimental scheme for determination of glioma cell viability after NIR pulsed irradiation. (**a**) Cells without SWCNTs (control), (**b**) cells accumulated SWCNTs in the cytoplasm as micro-sized agglomerates, (**c**) cells exposed to stable suspension of individual SWCNTs.

was detected. Long-pass (cut-off at 860 nm) and short-pass (cut-off at 780 nm) filters were applied to spectrally separate the CARS signal. Excitation powers of 0.4 mW and 5 mW were employed for Pump and Stokes beams, respectively. Cells visualization was performed using the following set of parameters: laser-pulse duration 10 ps, intensity 10^6 W/cm^2, pulse frequency 1 MHz, scanning step 0.2 μm, acquisition time 1/500 s/pixel. The time for scanning the area of 100 × 100 μm using this set of parameters was 7 min.

Fluorescence microscopy. The fluorescence images were acquired as in[46]. In short, we used a custom-built fluorescence microscope based on a commercial inverted biological Nikon Eclipse Ti-U with a 40 × CFI S Plan Fluor ELWD air objective and operated in the wide-field epi-illumination mode. The 532 nm CW DPSS laser (Crystalaser) was used as the excitation source. The diameter of the excitation spot was about 200 μm. The laser power after the objective was 0.6 mW. The excitation laser was directed into the objective by a 50/50 beam splitter. The resulting fluorescence was filtered off the excitation light with the long-pass filter (HQ545LP, Chroma) and imaged with EMCCD (DU-897E-CS0-UVB, Andor). The detector integration time was 0.1 s and each image was an average of 20 frames.

Received: 8 October 2020; Accepted: 7 December 2020
Published online: 17 December 2020

References

1. Boulnois, J. L. Photophysical processes in recent medical laser developments: a review. *Lasers Med. Sci.* **1**, 47–66 (1986).
2. Hemmer, E., Benayas, A., Légaré, F. & Vetrone, F. Exploiting the biological windows: current perspectives on fluorescent bioprobes emitting above 1000 nm. *Nanoscale Horizons* **1**, 168–184 (2016).
3. Fong, J. F. Y., Yann, H. N. & Sing, M. N. Carbon dots as a new class of light emitters for biomedical diagnostics and therapeutic applications. In *Fullerenes, Graphenes and Nanotubes: A Pharmaceutical Approach* (ed. Grumezescu, A. M.) 227–295 (Elsevier Inc., Amsterdam, 2018).
4. Khosroshahi, M. E. The effect of laser power on photothermoacoustic imaging of blood containing gold nanoparticles and deoxygenation using a frequency-domain phased array probe: an in-vitro assay. *Nanosci. Technol.* **2**, 1–10 (2015).
5. Zhang, Y. *et al.* Noninvasive photoacoustic microscopy of living cells in two and three dimensions through enhancement by a metabolite dye. *Angew. Chemie Int. Ed.* **50**, 7359–7363 (2011).
6. Frangioni, J. V. New technologies for human cancer imaging. *J. Clin. Oncol.* **26**, 4012–4021 (2008).
7. Skripka, A. *et al.* Decoupling theranostics with rare earth doped nanoparticles. *Adv. Funct. Mater.* **29**, 1807105. https://doi.org/10.1002/adfm.201807105 (2019).
8. Chen, Y. W., Su, Y. L., Hu, S. H. & Chen, S. Y. Functionalized graphene nanocomposites for enhancing photothermal therapy in tumor treatment. *Adv. Drug Deliv. Rev.* **105**, 190–204 (2016).
9. Eskiizmir, G., Ermertcan, A. T. & Yapici, K. Nanomaterials: promising structures for the management of oral cancer. In *Nanostructures for Oral Medicine* (eds Andronescu, E. & Grumezescu, A. M.) 511–544 (Elsevier Inc., Amsterdam, 2017).
10. Snook, R. D. & Mitchem, L. Photoacoustic spectroscopy. In *Encyclopedia of Analytical Science* 2nd edn (eds Worsfold, P. *et al.*) 174–180 (Elsevier, Amsterdam, 2005).

11. Holguin, S. Y., Thadhani, N. N. & Prausnitz, M. R. Effect of laser fluence, nanoparticle concentration and total energy input per cell on photoporation of cells. *Nanomed. Nanotechnol. Biol. Med.* **14**, 1667–1677 (2018).
12. Galisteo-González, F., Monasterio, B. G., Gil, D., Valle, M. & Goñi, F. M. Photoacoustic effect applied on model membranes and living cells: direct observation with multiphoton excitation microscopy and long-term viability analysis. *Sci. Rep.* **10**, 1–9 (2020).
13. Wei, X. *et al.* Experimental determination of excitonic band structures of single-walled carbon nanotubes using circular dichroism spectra. *Nat. Commun.* **7**, 1–9 (2016).
14. Liang, C. *et al.* Tumor metastasis inhibition by imaging-guided photothermal therapy with single-walled carbon nanotubes. *Adv. Mater.* **26**, 5646–5652 (2014).
15. Shvedova, A. A. *et al.* Mechanisms of pulmonary toxicity and medical applications of carbon nanotubes: Two faces of Janus?. *Pharmacol. Ther.* **121**, 192–204 (2009).
16. Chelnokova, I. A. *et al.* Effect of single-walled carbon nanotubes on the structural, physical, and mechanical properties of rat glial cell surface. *J. Nanopart. Res.* **22**, 144 (2020).
17. Eatemadi, A. *et al.* Carbon nanotubes: Properties, synthesis, purification, and medical applications. *Nanoscale Res. Lett.* **9**, 1–13 (2014).
18. Wu, H. Q., Wei, X. W., Shao, M. W. & Gu, J. S. Synthesis of zinc oxide nanorods using carbon nanotubes as templates. *J. Cryst. Growth* **265**, 184–189 (2004).
19. Huang, J. Q., Zhang, Q., Zhao, M. Q. & Wei, F. A review of the large-scale production of carbon nanotubes: the practice of nanoscale process engineering. *Chin. Sci. Bull.* **57**, 157–166 (2012).
20. Shuba, M. V. *et al.* Soft cutting of single-wall carbon nanotubes by low temperature ultrasonication in a mixture of sulfuric and nitric acids. *Nanotechnology* **23**, 495714 (2012).
21. Hou, P. X., Liu, C. & Cheng, H. M. Purification of carbon nanotubes. *Carbon N. Y.* **46**, 2003–2025 (2008).
22. Zhou, Y., Fang, Y. & Ramasamy, R. P. Non-covalent functionalization of carbon nanotubes for electrochemical biosensor development. *Sensors* **19**, 392 (2019).
23. Augustine, S. *et al.* Recent advances in carbon based nanosystems for cancer theranostics. *Biomater. Sci.* **5**, 901–952 (2017).
24. Kostarelos, K. The long and short of carbon nanotube toxicity. *Nat. Biotechnol.* **26**, 774–776 (2008).
25. Vardharajula, S. *et al.* Functionalized carbon nanotubes: biomedical applications. *Int. J. Nanomed.* **7**, 5361–5374 (2012).
26. Gong, F. *et al.* Effective thermal transport properties in multiphase biological systems containing carbon nanomaterials. *RSC Adv.* **7**, 13615–13622 (2017).
27. Ding, Y., Alias, H., Wen, D. & Williams, R. A. Heat transfer of aqueous suspensions of carbon nanotubes (CNT nanofluids). *Int. J. Heat Mass Transf.* **49**, 240–250 (2006).
28. Cui, X., Wan, B., Yang, Y., Ren, X. & Guo, L. H. Length effects on the dynamic process of cellular uptake and exocytosis of single-walled carbon nanotubes in murine macrophage cells. *Sci. Rep.* **7**, 1518. https://doi.org/10.1038/s41598-017-01746-9 (2017).
29. Roxbury, D., Jena, P. V., Shamay, Y., Horoszko, C. P. & Heller, D. A. Cell membrane proteins modulate the carbon nanotube optical bandgap via surface charge accumulation. *ACS Nano* **10**, 499–506 (2016).
30. Principi, E. *et al.* Systemic distribution of single-walled carbon nanotubes in a novel model: Alteration of biochemical parameters, metabolic functions, liver accumulation, and inflammation in vivo. *Int. J. Nanomed.* **11**, 4299–4316 (2016).
31. Lepock, J. R. & Borrelli, M. J. How do cells respond to their thermal environment?. *Int. J. Hyperth.* **21**, 681–687 (2005).
32. Marmur, J. & Doty, P. Determination of the base composition of deoxyribonucleic acid from its thermal denaturation temperature. *J. Mol. Biol.* **5**, 109–118 (1962).
33. Schön, A., Clarkson, B. R., Jaime, M. & Freire, E. Temperature stability of proteins: Analysis of irreversible denaturation using isothermal calorimetry. *Proteins Struct. Funct. Bioinf.* **85**, 2009–2016 (2017).
34. Zheltov, G. I., Romanov, O. G. & Bourko, W. D. Physical fundamentals of low-temperature laser ablation of biotissues: quasi-continuous radiation mode. *Dokl. Natl. Acad. Sci. Belarus* **63**, 421–429 (2019).
35. Zheltov, G. I., Lisinetskii, V. A., Grabtchikov, A. S. & Orlovich, V. A. Low-threshold cavitation in water using IR laser pulse trains. *Appl. Opt.* **47**, 3549–3554 (2008).
36. Sánchez, D. *et al.* Noncontact measurement of the local mechanical properties of living cells using pressure applied via a pipette. *Biophys. J.* **95**, 3017–3027 (2008).
37. Wang, M. *et al.* Sonoporation-induced cell membrane permeabilization and cytoskeleton disassembly at varied acoustic and microbubble-cell parameters. *Sci. Rep.* **8**, 1–12 (2018).
38. Strohm, E. M., Moore, M. J. & Kolios, M. C. High resolution ultrasound and photoacoustic imaging of single cells. *Photoacoustics* **4**, 36–42 (2016).
39. Li, W. & Chen, X. Gold nanoparticles for photoacoustic imaging. *Nanomedicine* **10**, 299–320 (2015).
40. Molina-Duarte, J., Espinosa-Vega, L. I., Rodríguez, A. G. & Guirado-López, R. A. Raman spectra of single walled carbon nanotubes at high temperatures: pretreating samples in a nitrogen atmosphere improves their thermal stability in air. *Phys. Chem. Chem. Phys.* **19**, 7215–7227 (2017).
41. Steiner, R. Laser-tissue interactions. In *Laser and IPL Technology in Dermatology and Aesthetic Medicine* (eds Raulin, C. & Karsai, S.) 23–36 (Springer, Berlin, 2011).
42. Prats Mateu, B. *et al.* Label-free live cell imaging by confocal Raman microscopy identifies CHO host and producer cell lines. *Biotechnol. J.* **12**, 1600037 (2017).
43. Schneckenburger, H. *et al.* Light exposure and cell viability in fluorescence microscopy. *J. Microsc.* **245**, 311–318 (2012).
44. Golubewa, E. N., Shuba, M. V., Vasilieu, M. V. & Kulahava, T. A. Application of Raman spectroscopy for analysis of carbon nanotube distribution in living cells. *J. Appl. Spectrosc.* **85**, 1121–1127 (2019).
45. Crowley, L. C. *et al.* Dead cert: measuring cell death. *Cold Spring Harb. Protoc.* **1064–1072**, 2016. https://doi.org/10.1101/pdb.top070318 (2016).
46. Golubewa, L. *et al.* Surface-enhanced Raman spectroscopy of organic molecules and living cells with gold-plated black silicon. *ACS Appl. Mater. Interfaces* **12**, 50971–50984 (2020).

Acknowledgements

This work was financially supported by Horizon 2020 RISE DiSeTCom [Project No 823728], the Research Council of Lithuania Foundation [Joint Project No S-LB-19-4], the Belarusian Republican Foundation for Fundamental Research [Project No F18R-141], the Academy of Finland Flagship Programme, Photonics Research and Innovation (PREIN) [Project No 320166], the Academy of Finland [Project No 298298]. PK is supported by Horizon 2020 IF TURANDOT [Project No 836816]. MS is supported by Tomsk State University Competitiveness Improvement Program. We are thankful for Alesia Paddubskaya (Institute for Nuclear Problems, Belarusian State University, Minsk, Belarus) for fruitful discussions.

Author contributions

L.G., T.K. and P.K. worked out the concept of the research. L.G., R.K., T.K., M.S., D.R. and A.D. conceived and designed the experimental study. Theoretical calculations were performed by I.T. and O.R. M.S. prepared the SWCNT-DNA complexes with the assistance of L.G. L.G. and T.K. designed and performed cell viability assay. D.R. performed the fluorescence measurement. A.D. performed the CARS measurements. L.G. and M.S. performed Raman spectroscopic measurements. The manuscript was written through the contributions of all authors. P.K. and Y.S. provided manuscript review and editing. All authors have approved the final version of the manuscript.

Competing interests

The authors declare no competing interests.

Additional information

Supplementary Information The online version contains supplementary material availlable at https://doi.org/10.1038/s41598-020-79238-6.

Correspondence and requests for materials should be addressed to L.G.

Reprints and permissions information is available at www.nature.com/reprints.

Publisher's note Springer Nature remains neutral with regard to jurisdictional claims in published maps and institutional affiliations.

IOP Publishing Nanotechnology
Nanotechnology 33 (2022) 095101 (15pp) https://doi.org/10.1088/1361-6528/ac3ce4

Visualizing hypochlorous acid production by human neutrophils with fluorescent graphene quantum dots

Lena Golubewa[1,2], Tatsiana Kulahava[2], Aliona Klimovich[3], Danielis Rutkauskas[1], Ieva Matulaitiene[3], Renata Karpicz[1], Nikita Belko[4,5], Dmitri Mogilevtsev[5], Alena Kavalenka[6], Marina Fetisova[7], Petri Karvinen[7], Yuri Svirko[7] and Polina Kuzhir[7]

[1] Department of Molecular Compounds Physics, State Research Institute Center for Physical Sciences and Technology, Vilnius, 10257, Lithuania
[2] Laboratory of Nanoelectromagnetics, Institute for Nuclear Problems of Belarusian State University, Minsk, 220006, Belarus
[3] Department of Organic Chemistry, State Research Institute Center for Physical Sciences and Technology, Vilnius, 10257, Lithuania
[4] Laboratory of Spectroscopy, A. N. Sevchenko Institute of Applied Physical Problems of Belarusian State University, Minsk, 220045, Belarus
[5] Center of Quantum Optics and Quantum Information, B. I. Stepanov Institute of Physics of the National Academy of Sciences of Belarus, Minsk, 220072, Belarus
[6] Department of Biophysics, Physics Faculty, Belarusian State University, Minsk, 220030, Belarus
[7] Institute of Photonics, Department of Physics and Mathematics, University of Eastern Finland, Joensuu, 80101, Finland

E-mail: lena.golubewa@ftmc.lt

Received 18 October 2021, revised 22 November 2021
Accepted for publication 24 November 2021
Published 9 December 2021

Abstract

In living organisms, redox reactions play a crucial role in the progression of disorders accompanied by the overproduction of reactive oxygen and reactive chlorine species, such as hydrogen peroxide and hypochlorous acid, respectively. We demonstrate that green fluorescence graphene quantum dots (GQDs) can be employed for revealing the presence of the hypochlorous acid in aqueous solutions and cellular systems. Hypochlorous acid modifies the oxygen-containing groups of the GQD, predominantly opens epoxide ring C–O–C, forms excessive C=O bonds and damages the carbonic core of GQDs. These changes, which depend on the concentration of the hypochlorous acid and exposure time, manifest themselves in the absorbance and fluorescence spectra of the GQD, and in the fluorescence lifetime. We also show that the GQD fluorescence is not affected by hydrogen peroxide. This finding makes GQDs a promising sensing agent for selective detecting reactive chlorine species produced by neutrophils. Neutrophils actively accumulate GQDs allowing to visualize cells and to examine the redox processes via GQDs fluorescence. At high concentrations GQDs induce neutrophil activation and myeloperoxidase release, leading to the disruption of GQD structure by the produced hypochlorous acid. This makes the GQDs a biodegradable material suitable for various biomedical applications.

Supplementary material for this article is available online

Keywords: graphene quantum dots, neutrophils, myeloperoxidase, hypochlorous acid, sensors

(Some figures may appear in colour only in the online journal)

1. Introduction

Unique electronic and optical properties of graphene quantum dots (GQDs) [1], flakes of multilayer graphene having a lateral size of tens of nanometers, originate from quantum confinement and edge defects [2], although exact mechanisms are not clearly identified [3] and vary significantly depending on the production method [4, 5].

GQDs are chemically inert [6], biocompatible [7], non-cytotoxic or cytogenic [8] and exceptionally reliable for biomedical applications [9]. Passivation of GQDs with oxygen-containing functional groups makes their fluorescence sensitive to redox reactions [10]. These reactions are associated with the overproduction of reactive oxygen (ROS) and chlorine species (RCS) [11, 12] and play a crucial role in the progression of various disorders. GQD fluorescence is also sensitive to the presence of metal ions (e.g. Fe^{3+} [13], Mn^{2+} [14], etc) that exist in active centers [15] of critically essential enzymes. For GQDs produced by the L-glutamic amino acid pyrolysis, peroxidase-like activity was demonstrated [16]. Such a sensitivity of fluorescent GQDs to redox processes in biological systems makes them a promising candidate for the development of low-cost, easily controllable, effective sensing of oxidants. In this regard, establishing the exact mechanisms of the interaction of oxidants with GQDs is an important and urgent problem.

Neutrophils are a significant part of white blood cells involved in the immune response being the first-line defense in the human body. The primary function of neutrophils is the elimination of pathogens and microorganisms as well as damaged cells by phagocytosis and ROS and RCS production [17, 18]. Neutrophils contain azurophilic granules filled with the enzyme myeloperoxidase (MPO) [19]. Phagocytosis is accompanied by the fusion of azurophilic granules with phagocytic vacuole and MPO release toward phagocytosed pathogens [20]. The main product of MPO activation is hypochlorous acid (HClO), which is a strong oxidant and induces the destruction of pathogens inside the phagolysosome [21]. However, when neutrophils cannot engulf the pathogen or necrotic cell, granules can fuse with the plasma membrane and MPO is secreted in the extracellular milieu resulting in the oxidative stress-associated damage of surrounding tissues and inflammatory reaction [22, 23]. Neutrophil-driven inflammation has been considered as a general mechanism underlying many pathological conditions, including atherosclerosis, sepsis, cardiovascular, respiratory, autoimmune and neurodegenerative diseases, and cancer [24, 25]. Therefore, maintaining a balance between the deleterious and beneficial effects of neutrophils is one of the crucial tasks of the inflammation; and effective detection of abnormal neutrophil activation and MPO release allows early-stage diagnosis and thus facilitates treatment and reduces disease complications.

In this paper, we demonstrate that green fluorescent GQDs can be employed as an accurate and specific sensor of oxidant content, predominantly HClO, in both model and cellular systems. Selective modification of GQD structure by hypochlorous acid and GQD inertness towards H_2O_2 is demonstrated by Fourier transform infrared (FTIR) and surface-enhanced Raman spectroscopy (SERS). Measurements of the concentration- and time-dependence of the GQD absorbance, excitation spectra, fluorescence lifetime and spectra allow us to detect hypochlorous acid in a wide range of concentrations (0.01–10.0 mM). Interaction of GQDs with human neutrophils induces their accumulation inside the cells, which is tracked by fluorescence microscopy. Moreover, high concentrations of GQDs are shown to activate neutrophils and MPO release, accompanied by hypochlorous acid production. We confirmed that GQDs are the specific and accurate sensor of RCS in biological systems by visualizing the HClO overproduction via monitoring the fluorescence change.

2. Materials and methods

2.1. Graphene quantum dots (GQDs)

GQDs (green luminescent, water-dispersed, CAS 7440-44-0, Sigma-Aldrich, USA) were used throughout experiments. Due to data provided by supplier topographic height is about 1.0–2.0 nm, diameter is < 5 nm. For living cell studies, GQDs were dissolved in phosphate-buffer saline (PBS), pH = 7.2, at final concentration of 2.5–50.0 μg ml^{-1}. PBS consisted of: 136.9 mM NaCl, 2.7 mM KCl, 2.0 mM $MgSO_4$, 2.0 mM $CaCl_2$, 8.9 mM $Na_2HPO_4 \times 7H_2O$, 1.5 mM KH_2PO_4. Hydrogen peroxide (H_2O_2, Sigma-Aldrich, USA) or sodium salt of hypochlorous acid (NaClO, Sigma-Aldrich, USA) were added to the water suspension of GQDs at a final concentration of 0.01–10.0 mM and kept in the dark for 30 and 90 min.

2.2. Fourier transform infrared spectroscopy

FTIR spectra were recorded using Bruker Alpha II FTIR spectrometer with a Diamond Crystal ATR (Bruker Inc., Germany). Cleaning of the crystal was performed using a Kimwipe with iPrOH and dried before measuring the background spectrum. The spectra were recorded between 4000 and 400 cm^{-1}, $t = 100$ s. 5–10 μl of a sample were placed directly on the diamond crystal plate and the measurement was carried out after the sample was completely dried. The spectrometer was operated with the Opus 7.8 software.

2.3. Raman spectroscopy

Raman spectroscopic studies were performed using Raman spectrometer RamanFlex 400 (PerkinElmer, Inc.) equipped with a CCD camera thermo-electrically cooled to −50 °C. The working power was adjusted to 50 mW, the excitation wavelength was $\lambda_{ex} = 785$ nm, the diameter of the laser spot was ~200 μm, spectra were accumulated 30 times per 10 s to exclude possible irradiation-induced damage of the sample. Spectra were collected from 5 different points and then averaged. Simple background correction was performed. Laser beam was focused inside the cuvette containing GQDs dispersed in water (1 mg ml^{-1}) in case of liquid samples or on the substrate with dried sample.

2.4. Surface-enhanced Raman spectroscopy

SERS measurements were performed using gold-plated black silicon-based SERS-active substrate (bSi/Au) [26] using Raman spectrometer RamanFlex 400 (PerkinElmer, Inc.). 10 μl of GQD water dispersion (1 mg ml^{-1}) or GQD water dispersion treated with 10 mM NaClO or H_2O_2 for 30 min were placed on the bSi/Au and dried in air for 30 min. Measurement parameters were the following: $\lambda_{ex} = 785$ nm, acquisition time 30 cycles per 10 s, laser diode power 50 mW. Partial removal of the surfactant from the GQD-containing bSi/Au substrate was carried out via 5 min treatment of the latter with oxygen plasma. It was problematic to completely remove the surfactant, since a compromise had to be found: prolonged plasma treatment caused strong oxidation of gold and the elimination of the sample from the substrate surface; after insufficient plasma treatment, residual surfactant on GQDs remained.

2.5. UV–vis absorption spectroscopy

Absorbance of GQD water solutions was measured in a 1 cm path length quartz cuvettes using UV–vis spectrophotometer JASCO V-670 (Jasco, USA). To avoid the self-absorption effect, GQD and fluorescein concentrations were held low enough with an absorbance value not exceeding ~0.1.

2.6. Fluorescence spectroscopy

Fluorescence spectra and time-decay measurements were conducted using time-correlated single-photon-counting fluorescence spectrometer F900 (Edinburgh Instruments Ltd, USA). Sample excitation was performed with a picosecond semiconductor pulsed diode laser EPL-470 emitting 72 ps pulses at 470 nm with a repetition rate of 5 MHz (200 ns) (Edinburgh Instruments, Ltd, USA). Measurements were performed in quartz cuvettes of 1 cm at RT. The fluorescence was measured at 90° to the incident excitation beam. The temporal evolution of the fluorescence at $\lambda_{em} = 530$ nm was fitted: using a built-in software (Edinburgh advanced lifetime analysis software) with the following function:

$$Fit = A + B_1 \cdot e^{-t/\tau_1} + B_2 \cdot e^{-t/\tau_2}, \quad (1)$$

where τ_1 and τ_2 are characteristic lifetimes of the fast and slow components of the fluorescence, respectively, $B_{1,2}$ are relevant pre-exponential factors, A describes an additional background intensity. Sample parameters $b_{1,2}$, which are extracted from the two-exponential fitting and are presented in the results and discussion section for data analysis, are relative fluorescence intensities of the ith component, which are defined as:

$$b_{1,2} = \frac{B_{1,2}\tau_{1,2}}{B_1\tau_1 + B_2\tau_2}. \quad (2)$$

Fluorescence excitation spectra were collected using spectral fluorimeter Solar CM2203 (Solar, Belarus). The range of excitation wavelengths was 250–520 nm, fluorescence emission was recorded at $\lambda_{em} = 530$, 550 and 580 nm.

2.7. Calculation of fluorescence quantum yield

The fluorescence quantum yield was calculated using the following equation [27]:

$$\varphi_s = \varphi_f \frac{F_s}{F_f}\frac{A_f}{A_s}, \quad (3)$$

where F is the integrated fluorescence intensity, A is the absorbance at the excitation wavelength of 470 nm, the subscript f stands for a reference compound (fluorescein, Sigma-Aldrich, USA) and s corresponds to the sample. Several measurements of φ_s value were performed for different concentrations and excitation wavelengths and then averaged.

2.8. Neutrophil isolation

Neutrophils were isolated from the whole blood of healthy volunteers (8 persons) invited to donate blood for research in the Republican Scientific Practical Center for Transfusiology and Medical Biotechnology (Minsk, Belarus) after written consent (within the framework of the project No 20210397, Belarusian State Program of Scientific Research 'Convergence-2025'). The heparinized peripheral blood was mixed (1:5) with Dextran 500 (Sigma-Aldrich Chemie GmbH, Germany). In 30 min leucocyte-rich plasma was centrifuged (30 min, 400 g) in a histopak-1077 density gradient according to the standard protocol [28]. Residual erythrocytes were removed using hypotonic lysis during 20 s, after which the osmoticity of the solution was restored by the addition of 0.3 M NaCl solution. Cells were washed with 0.15 M NaCl, and the resulting cell fraction was suspended in RPMI (Sigma, USA) (pH 7.2). 5×10^5 cells ml^{-1} were routinely obtained for further investigations. The content of viable neutrophils in the cell suspension was at least 96%.

2.9. Fluorescence microscopy

Neutrophils for fluorescent microscopy were prepared as follows. Freshly isolated neutrophils were exposed to 50 μg ml^{-1} of GQDs and allowed to adhere to the glass or silicon wafer surface for 30 and 90 min at 37 °C. Adherent cells were washed twice with PBS, fixed with 4% paraformaldehyde (Sigma-Aldrich, USA) for 10 min at room temperature. The fixed cells were washed with PBS and deionized water.

The cytoskeleton of neutrophils was assessed using the CytoPainter Phalloidin-iFluor 532 (Abcam, UK) the MPO distribution in neutrophils was visualized using the MPO-FITC antibodies (Beckman Coulter, France). Adherent cells fixed with 4% paraformaldehyde were treated with 0.2% Triton X-100 for permeabilization. Samples were rewashed with PBS and incubated in the dark with CytoPainter Phalloidin-iFluor 532 at a final concentration of 5 μM or with 20 μl of MPO-FITC antibodies for 30 min at room temperature. The stained cells were washed with PBS and deionized water.

Fluorescence imaging was performed with an inverted Nikon Eclipse Ti-U microscope with 60× NA 1.2 WI Plan Apo VC objective (Nikon) in the wide-field epi-illumination mode. The excitation source was 488 nm CW DPSS laser (Crystalaser). The excitation light was reflected to the

objective by the ZT405/488/532/640rpc-UF2_LaserTIRF dichroic mirror (Chroma) and the resulting fluorescence was filtered off the excitation light with FF01-446/510/581/703 fluorescence filter (Semrock). Fluorescence images were detected with DU-897E-CS0-UVB EMCCD (Andor). Images were additionally magnified 1.5× by the choice of the microscope tube lens so that the corresponding imaged sample area was 91 × 91 μm^2. For each sample, 20 movies of 20 frames each with 0.1 s integration time were acquired. Images for analysis are averages of all frames in a movie.

3. Results and discussion

3.1. GQD characterization via Fourier-transform infrared spectroscopy

In order to characterize the GQDs functional groups, we measured FTIR spectra shown in figure 1. Assignments of functional groups are summarized in table 1. The broad band around 3312 cm^{-1} corresponds to the stretching vibration of the O–H group attached to the GQD edges (see figure 1(b)). The impact of O–H vibrations from water adsorbed on GQDs could not be excluded due to the specificity of measurement procedure. The peaks at 1587 and 1659 cm^{-1} bands correspond to C=C skeletal vibrations, while a broad peak centered at 1016 cm^{-1} corresponds to the merged C–O–C symmetric stretching and C–O–H bending vibrations. 1258 cm^{-1} and 1735 cm^{-1} correspond to the stretching of the C–O and C=O bonds in the carboxylic acid group, respectively, evidencing the presence of the defects in the hexagonal carbon lattice of the graphene sheet [29].

Among FTIR bands that are not relevant to the GQD structure are strong bands at 1357 cm^{-1}, 1456 cm^{-1}, and 2928 cm^{-1}, which correspond to C–H bending and C–H chain stretching vibrations, respectively. These bands may indicate the presence of some surfactant, which could be likely used for GQD functionalization and dispersion [39]. However, C–H stretching may also arise from edge carbon atoms that have not been functionalized by oxygen-containing groups.

3.2. GQD characterization via Raman and surface-enhanced Raman spectroscopy

Typical Raman spectrum of GQD water suspension shown in figure 1(c) (line 1) is featured with characteristic D band (A_{1g} mode) and G band (E_{2g} mode) [40] at 1358 cm^{-1} and 1589 cm^{-1}, respectively. The sensitivity of the Raman spectrometer is insufficient to reveal functional groups attached to the graphene flakes, while D and G peaks are strongly broadened and poorly resolved. The later may indicate the presence of either excessive structural defects, which suppress the performance of the GQDs in the biosensing, or organic molecules associated with the surfactant, which was used to stabilize the suspension.

To reveal the Raman bands corresponding to the functional groups attached to the GQDs or to the surfactant, we employed the SERS techniques by depositing suspension on the black silicon sputtered with gold (bSi/Au) [26]. From the SERS spectrum of the suspension presented in figure 1(c) (line 3) one can see numerous bands indicating the presence of organic molecules in the suspension. Band positions with their assignments in Raman spectra of GQD water solution in SERS spectrum of GQD on bSi/Au are summarized in table 2. The bands in the SERS spectrum of GQDs in the range from 280 to 1050 cm^{-1} are not typical for GQDs but may arise from some surfactant molecules or can be assigned with oxygen-containing groups or hydrocarbon in GQDs (C–O–C bending, CH_2 bending, rocking, and twisting vibrations, C–O and C–C stretching). Bands at 1126 and 1151 cm^{-1} are assigned as the vibration of C–O functional group in GQDs [41]. There is also a strong overlap of D band in GQD spectrum and some other active vibrations in the region around 1358 cm^{-1} for Raman and SERS spectra of GQDs. This overlapping in spectra makes obtaining the extent of sp2/sp3 hybridization of carbon atoms impossible and, thus, analyzes the quality of the GQDs [42].

GQDs on bSi/Au were treated with oxygen plasma for 5 min to remove most of the organic substances (see figure 1(c), spectrum 2, and table 2), but the appearance of the band at 564 cm^{-1} indicates that this procedure caused oxidation of the gold layer on bSi/Au substrate as this band is assigned to AuO. The D band is detected as 1376 cm^{-1} with a wide wing centered at 1280 cm^{-1}. The lower frequency band originates from the edge defects of GQDs [41]. The G band splits into two peaks at 1555 and 1583 cm^{-1} in SERS spectra for both GQDs and GQDs treated with oxygen plasma. This may be a signature of the symmetry breaking due to the adsorption of the GQD to the gold nanostructures providing plasmonic enhancement of the Raman signal [41, 45]. I_D/I_G ratio calculated for plasma-treated GQDs on bSi/Au substrate equals 0.84, which is in good agreement with the data reported in [42].

3.3. GQD UV–vis and fluorescence properties

UV–vis absorption spectra of the GQD water solutions (2.5–50.0 $\mu g\ ml^{-1}$) are presented in figure 2(a). GQDs exhibit absorption peaks at 276, 356, 460 and 488 nm. The absorption peak centered at 276 nm corresponds to the π–π^* transition of sp2 carbon atoms and originates from the quantum confinement effect [29]. An absorption peak at 356 nm is associated with the n–π^* transition and is mainly due to the oxygen functional groups (C=O/COOH) at the GQD edges [29, 43, 46]. Its strong broadening may originate from the functionalization of GQDs with carboxylic groups of surfactant molecules bounded to the GQD edge.

Absorption peaks at 460 and 488 nm are rarely observed in as-prepared GQDs. They may be associated with various surface functional groups, which form surface states having an energy between π and π^* states of C=C. The electron transitions associated with these states may lead to the observed absorption peaks [47] and may originate from C–O group [46]. Alternatively, the peaks at 460 and 488 nm may be a result of the high dimension of conjugation in GQDs [48]. UV–vis

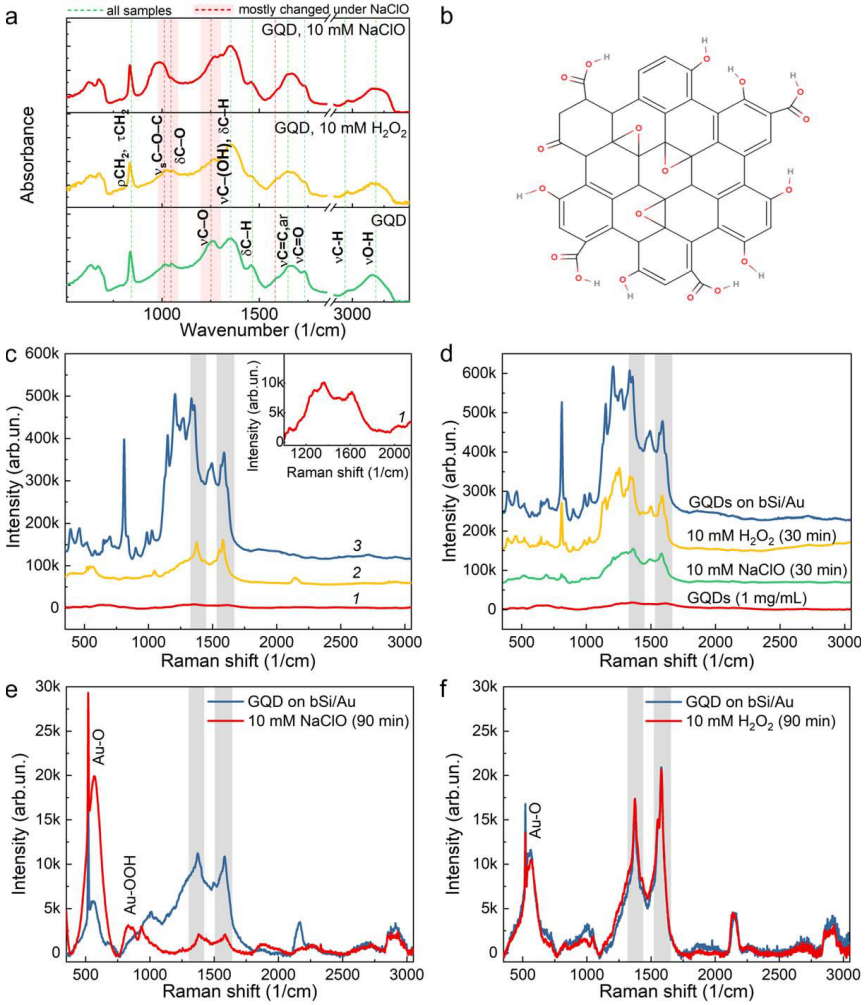

Figure 1. GQD characterization via vibrational spectroscopy: (a) FT-IR spectra of GQDs, GQDs treated with 10 mM of H_2O_2 and NaClO for 30 min; (b) suggested structure of GQD based on FT-IR spectra; (c) Raman spectroscopy and SERS studies of GQDs (1—Raman spectrum of 1 mg ml^{-1} of GQD water suspension, 2—SERS spectrum of GQD treated with oxygen plasma, 3—SERS spectrum of GQDs); (d) Raman spectrum of 1 mg ml^{-1} of GQD water suspension and SERS spectra of GQDs, GQDs treated with 10 mM of H_2O_2 and NaClO for 30 min; (e) SERS spectra of GDQs treated with oxygen plasma in control and after 90 min exposure to 10 mM of NaClO; (f) SERS spectra of GDQs treated with oxygen plasma in control and after 90 min exposure to 10 mM of H_2O_2.

absorbance spectrum also exhibits intense background originating from the scattering on the nanoparticles and decreasing with the wavelength increase. The scattering origin of the background is confirmed by the absence of the background in the corresponding excitation spectra (see figure 2(c)).

Fluorescence spectra of GQDs (2.5–50.0 μg ml^{-1}) at the 470 nm excitation wavelength are presented in figure 2(b). In the whole concentration range, the fluorescence spectrum exhibits a single maximum at $\lambda_{em} = 530$ nm. By using fluorescein as a reference, we estimated the quantum yield (QY) of the 530 nm emission as (17 ± 4) %, $P = 0.95$ (see equation (3) in the materials and methods and supporting information figure S1 available online at stacks.iop.org/NANO/33/095101/mmedia for QY evaluation).

Table 1. Band assignments of FT-IR spectra of GQDs, GQDs treated with 10 mM of H_2O_2 and NaClO for 30 min.

GQD, cm^{-1}	GQD, 10 mM H_2O_2 (30 min), cm^{-1}	GQD, 10 mM NaClO (30 min), cm^{-1}	Assignments
841	841	841	C–O, C–C stretching, CH_2 rocking [30, 31]
1016	1016	983	merged from C–O–C stretching and C–O–H bending [30, 32]
1051	1053		C–O bending [14, 33]
1258	1270	1272	C–O stretching [30]
1357	1353	1353	C–H bending [14, 30, 34]
1456	1454	1456	C–H bending [30, 33]
1587	1587	1591	C=C of GQD [34], aromatic ring stretching [35, 36]
1659	1659	1665	C=O bending vibrations [14, 37], ar. C=C stretching of GQD [14, 33, 38]
1735	1733	1733	C=O [30, 34, 38], [32, 37]
2928	2928	2926	C–H stretch [14, 34, 37, 38]
3312	3368	3368	O–H stretching [37, 38]

Table 2. Band assignments of the Raman spectra of GQD water solution, SERS spectra of GQDs and GQDs treated with oxygen plasma.

GQDs disp., cm^{-1}	GQDs on bSi/Au, cm^{-1}	Plasma-treated GQDs on bSi/Au, cm^{-1}	Assignments
	520	521	Si substrate
		564	AuO (oxidation after plasma cleaning)
	580		Possible surfactant-associated bands (C–O–C bending, CH_2 bending, rocking, and twisting vibrations, C–O and C–C stretching, etc)
	650		
	811		
	839		
	899		
	990		
1055	1028	1049	
	1126		C–O in GQDs [41]
1148	1151		C–O in GQDs [41]
1235	1231		C–O–C from GQDs [43], CH_2 twisting vibration [44]
1280	1273	1280 wide	Edge defects on GQDs [41], COOH or ring type C–OH functional groups [29]
1358	1358	1376	D band (a_{1g}) [40]
	1473	1444 w	C=C vibration, characterizing the passivated functional groups [41], CH_2–CH_2 anti symmetric bending vibration [44]
1496	1494		CH_2–CH_2 symmetric bending vibration [44]
	1564	1555	G band split due to symmetry break [41, 45]
1589	1589	1583	G band (E_{2g} mode) [40]

Excitation spectra measured in the range of 250–520 nm at the emission wavelengths of 530, 550, and 580 nm are presented in figure 2(c). The excitation spectra have three pronounced maxima around 273, 460 and 490 nm, which partially correspond to the absorbance peaks shown in figure 2(a), except band at 360 nm, attributed to n–π^* transition of C=O bond. This indicates that functional groups in GQDs mainly contribute to the fluorescence.

Figure 2(d) shows the fluorescence spectra at excitation wavelengths of 273, 360, 460, 470, and 490 nm, which correspond to peaks in the excitation spectra shown in figure 2(c). One can observe from figure 2(d) that the fluorescence has maximum at 530 nm and its position does not depend on the excitation wavelengths corresponding to the maximum peak positions in the absorbance spectrum. GQD fluorescence may demonstrate both excitation-dependent [46] and excitation-independent behavior [49]. Excitation dependance originates from (i) significant fluctuations of GQD size distribution, (ii) existence of isolated sp2 clusters in the sp3 carbon matrix with various sizes with specific excitation and emission dependent on the sp2 cluster size, or (iii) to a large amount of local atomic defects producing isolated emission centers [50]. Excitation-independent behavior, on the contrary, is explained by the size and surface state uniformity of sp2 clusters in GQDs [51], indicating high uniformity in size, structure and surface passivation with functional groups of

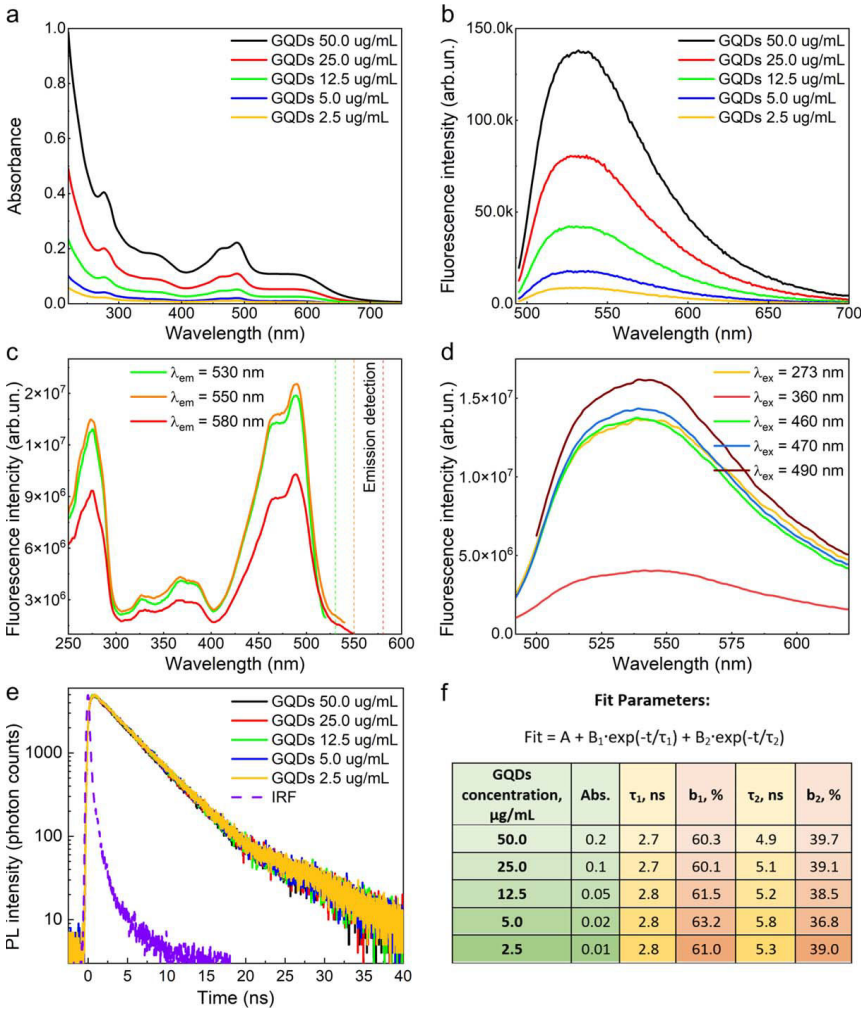

GQDs concentration, μg/mL	Abs.	τ_1, ns	b_1, %	τ_2, ns	b_2, %
50.0	0.2	2.7	60.3	4.9	39.7
25.0	0.1	2.7	60.1	5.1	39.1
12.5	0.05	2.8	61.5	5.2	38.5
5.0	0.02	2.8	63.2	5.8	36.8
2.5	0.01	2.8	61.0	5.3	39.0

Figure 2. Absorbance (a), fluorescence spectra with $\lambda_{ex} = 470$ nm (b), excitation spectra (c), fluorescence spectra at various excitations (d), and fluorescence time decay (e) and lifetime parameters (f) of GQD suspensions with different GQD concentrations.

GQDs in our case. It is worth noting that excitation at 360 nm results in 4-times weaker fluorescence peaks. (Figure 2(d)) demonstrating low radiative relaxation efficiency of the transitions in C=O groups.

The fluorescence decay profiles of GQDs under excitation with the 470 nm laser and calculated lifetimes at different GQD concentrations in water are presented in figures 2(e), (f). One can observe that the fluorescence decay is well approximated by a double exponent with the fast component $\tau_1 = 2.7$ ns and slow component $\tau_2 = 4.9$ ns at relative impacts of 60.3% and 39.7%, respectively. Both components and their impact do not change in the whole range of GQD concentrations.

The obtained values are in good agreement with those published in [52]. We assume that the fast component corresponds to size-independent GQD interband transition [52, 53], while the relaxation mechanism responsible for the slow component of the fluorescence decay is still unclear. It has been demonstrated in [53] that the slow component is size-dependent and is sensitive to edge-state variations. For the GQDs

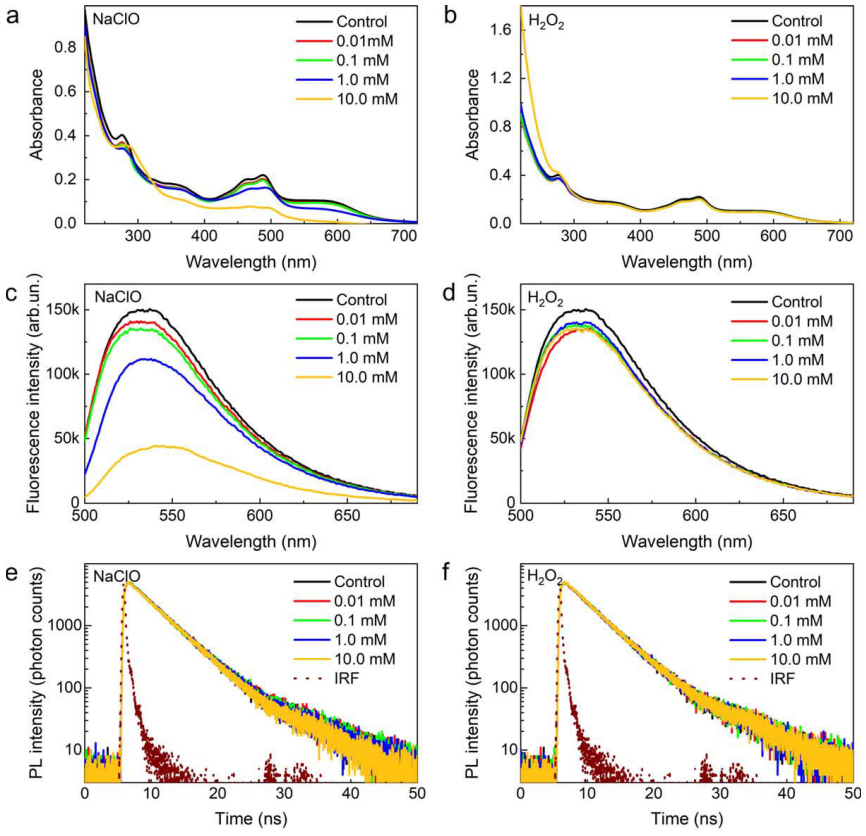

g

NaClO (30 min treatment)

	Control		0.01 mM		0.1 mM		1.0 mM		10.0 mM	
	τ_1	τ_2	τ_1	τ_2	τ_1	τ_2	τ_1	τ_2	τ_1	τ_2
ns	2.7	5.0	2.7	5.0	2.7	5.1	2.4	4.3	1.7	3.8
%	62.3	37.7	61.4	38.6	63.2	36.8	39.5	60.5	17.0	83.0

h

H_2O_2 (30 min treatment)

	Control		0.01 mM		0.1 mM		1.0 mM		10.0 mM	
	τ_1	τ_2	τ_1	τ_2	τ_1	τ_2	τ_1	τ_2	τ_1	τ_2
ns	2.7	5.0	3.7	5.7	3.7	5.9	3.7	6.0	3.7	6.1
%	62.3	37.7	65.8	34.2	72.0	28.0	72.4	27.6	74.5	25.5

Figure 3. Concentration dependence of the modification of spectroscopic properties of GQDs (50 μg ml^{-1} in water): (a) and (b) GQD absorbance spectra, (c) and (d) GQD fluorescence spectra, (e) and (f) GQD fluorescence time decay profiles, (g) and (h) GQD fluorescence lifetime data, under 0.01–10 mM NaClO and H_2O_2 treatment for 30 min, respectively.

modified via esterification, a strong dependence of slow component on the type of ester group is demonstrated [52].

It is worth noting that the shape of the absorption and fluorescence spectra as well as fluorescence lifetime do not depend on the GQD concentrations indicating that there were no agglomerations in the suspension.

3.4. GQD spectroscopic and structural changes under the action of NaClO and H_2O_2

Neutrophil immune response is accompanied by the production of ROS and RCS. Quantitative measurement of their levels in blood or biological fluids (i.e. plasma) as well as in the suspension of isolated neutrophils is of paramount importance. This is because it indicates the redox status of the organism giving an opportunity to reveal a pathological state at the early stages.

To show the potential of using GQDs as a specific sensing system for ROS/RCS, a model experiment was performed by treating GQDs with 10 mM NaClO and 10 mM H_2O_2 for 30 min. The FT-IR structural analysis revealed that after treatment, bands at 1016 and 1051 cm^{-1} disappear, and a new band at 983 cm^{-1} arises (figure 1(a) and table 1) because NaClO modifies oxygen-containing functional

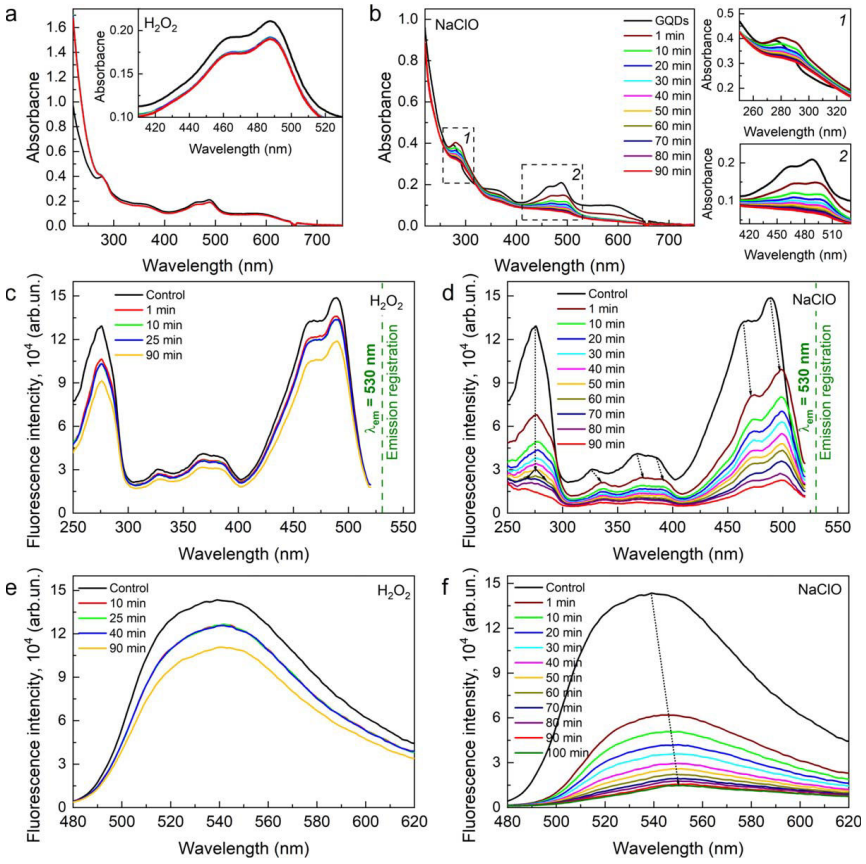

Figure 4. Time-dependent changes of spectroscopic properties of GQDs (50 μg ml^{-1} in water): (a) and (b) GQD absorbance, (c) and (d) GQD excitation spectra, (e) and (f) GQD fluorescence spectra, under 10 mM H_2O_2 and 10 mM NaClO treatment, respectively. Fluorescence measurements were performed using λ_{ex} = 470 nm for excitation.

groups C–O–C, C–O–H and C=O. NaClO also damages the C=C bond resulting in the shift of the relevant band position from 1659 to 1665 cm^{-1}. In contrast to the NaClO, H_2O_2 causes no changes in the GQDs functional groups.

SERS of GQDs treated with 10 mM NaClO and 10 mM H_2O_2 for 30 min also evidences that H_2O_2 does not interact with GQDs in the presence of the surfactant, while NaClO causes significant changes in SERS spectrum (figure 1(d) and table 1). Since the Raman spectra of organic molecules and GQDs are overlapped (see section 3.2), the interpretation of the SERS results is a difficult task. To avoid the surfactant effect, GQDs on bSi/Au substrate were pretreated with oxygen plasma to remove organic molecules and then exposed to NaClO and H_2O_2. NaClO treatment of GQD leads to a drastic decrease of the intensity of the GQDs SERS spectrum and causes Au oxidation as bands corresponding to AuO and Au–OOH appear. H_2O_2 does not affect the GQDs structure (figure 1(f)).

NaClO significantly modifies GQD UV–vis and fluorescence properties in a dose-dependent manner. Treatment of GQD water suspension (50 μg ml^{-1}) with 10 mM NaClO entirely eradicates the absorption peaks associated with the functional groups (maxima at 356, 460 and 488 nm) and significantly reduces the strength and redshifts the peak at the wavelength of 276 nm (figure 3(a)). This is more likely due to carbonic core damage that also seen from FT-IR and SERS spectra. The same concentrations of H_2O_2 induce no changes in GQD UV–vis absorbance spectrum (figure 3(b)). An increase in absorbance in the spectral range of 200–250 nm corresponds to the absorbance of H_2O_2 and is not associated with the GQDs (see supporting information figure S2).

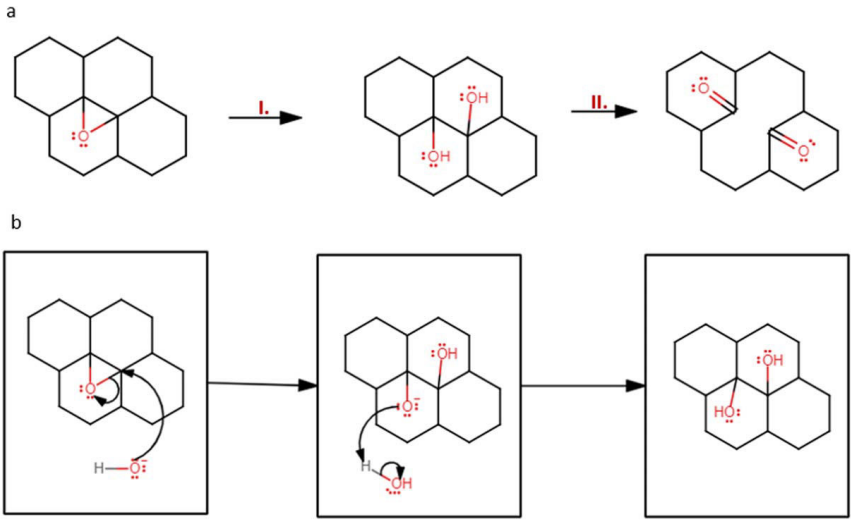

Figure 5. Mechanism of NaClO interaction with epoxide groups in GQDs: (a) two-step scheme of epoxide group modification; (b) epoxide ring opening mechanism.

A significant decrease in absorbance under the NaClO treatment also causes the suppression of the GQDs fluorescence (figure 3(c)) and shifting of the peak position from 530 to 550 nm. As it was expected, over the range of concentrations, H_2O_2 does not affect GQDs fluorescence (figure 3(d)).

Measurements of the fluorescence temporal evolution also reveal changes in the GQDs structure and mechanisms of radiative transition. 0.01–0.1 mM of NaClO induces neither changes in τ_1 and τ_2, nor in their impact. However, the GQD treatment with 10 mM of NaClO leads to the decrease in both τ_1 and τ_2 values from 2.7 and 5.0 ns to 1.7 and 3.8 ns, respectively. This is accompanied by a dose-dependent decrease in the relative impact of the fast component and an increase in the relative impact of the slow component from 62% to 17% and from 38% to 83%, respectively (figure 3(g)). This may be due to the disruption of the carbonic core and modification of C–O–C/C=O/COOH functional groups. Interestingly, H_2O_2 induces the opposite changes in the fluorescence lifetime. Specifically, both τ_1 and τ_2 increase from 2.7 and 5.0 ns in control to 3.7 and 6.1 ns in the 10 mM H_2O_2 sample, respectively. Simultaneously, the relative impact of τ_1 increases from 62% to 74% and that of τ_2 decreases from 38% to 26% in H_2O_2 dose-dependent manner (figure 3(h)).

These changes in absorption and fluorescence properties under NaClO treatment is also time-dependent. During the 90 min treatment of GQDs with 10 mM NaClO, the absorption peaks undergo significant redshift over time and disappear entirely in the end (figure 4(b)). An insignificant decrease in absorption caused by H_2O_2 is observed over the first minutes and does not change for the rest of the measurement (figure 4(a)). This behavior is repeated for the excitation spectra (figures 4(c), (d)). In 90 min the fluorescence intensity of GQDs exposed to 10 mM NaClO drops by more than 14 times compared to GQDs in the control sample (figure 4(f)). At the same time, GQDs fluorescence is insensitive towards H_2O_2 over the same time interval.

Significant redshift in fluorescence spectra under NaClO treatment indicates that the contribution of radiating transitions in C=O bonds increases [43]. This could be associated with the increase of C=O groups and disruption of the carbonic core of GQDs. Together with FTIR and SERS data, indicating the modification of epoxy-groups in GQDs by NaClO, we suppose the following two-step mechanism of GQDs modification (figure 5(a)). In an aqueous solution, NaClO dissociates and hydrolyzes to give hydroxide ions:

$$\mathrm{NaClO} \rightarrow \mathrm{Na^+} + \mathrm{ClO^-},$$

$$\mathrm{ClO^-} + \mathrm{H_2O} \rightleftharpoons \mathrm{HClO} + \mathrm{OH^-}.$$

An epoxide ring is easily opened under basic conditions by the nucleophilic attack of a hydroxide ion on one of the carbons of the epoxide ring, forming two hydroxyl groups at the adjacent carbons. The mechanism of this process is presented in figure 5(b).

In the presence of hypochlorous acid as an oxidizing agent, the hydroxyl groups can be oxidized to carbonyl groups, the bond between the adjacent carbinol carbons being broken (figure 5(a), phase II).

The epoxide ring-opening requires certain conditions: an acidic/basic pH of the medium and the presence of a good nucleophile (a species that has an electron pair and can easily donate, e.g. OH^- formed during the hydrolysis of NaClO). On the contrary, in the presence of hydrogen peroxide, no pH shift from neutral values occurs and H_2O_2 is a poor

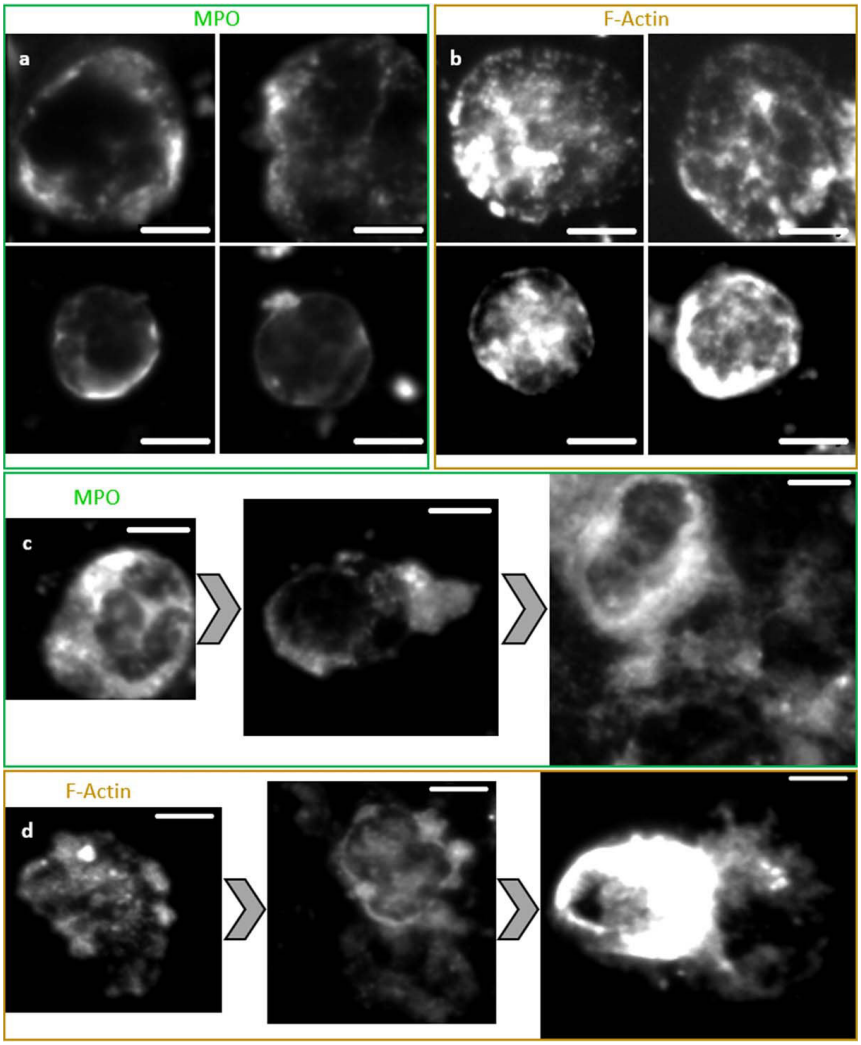

Figure 6. Neutrophil activation process via adhesion over 30 min: (a) MPO distribution in neutrophils without GQDs; (b) F-Actin distribution in neutrophils without GQDs; (c) MPO distribution in neutrophils exposed to 50 μg ml^{-1} of GQDs; (d) F-Actin distribution in neutrophils exposed to 50 μg ml^{-1} of GQDs. MPO antibodies stained with FITC (ex/em: 470 nm/530 nm). F-Actin stained with CytoPainter Phalloidin-iFluor 532 (ex/em: 532 nm/620 nm). Scale bar 15 μm.

nucleophile, so the treatment by a H_2O_2 solution does not affect the structure of GQDs.

Thus, GQDs demonstrate a high potential to be used in an oxidant sensing system with high specificity to the hypochlorous acid that causes structural modification of GQDs. Concentration- and time-dependent changes in UV–vis absorption, fluorescence spectra and lifetime caused by hypochlorous acid make the characterization of oxidation processes in biological systems simple and accurate.

3.5. GQD sensing of human neutrophil activation and hypochlorous acid release

Insensitivity of GQDs to H_2O_2 and high specificity to NaClO allows one to investigate the halogenating activity of MPO in

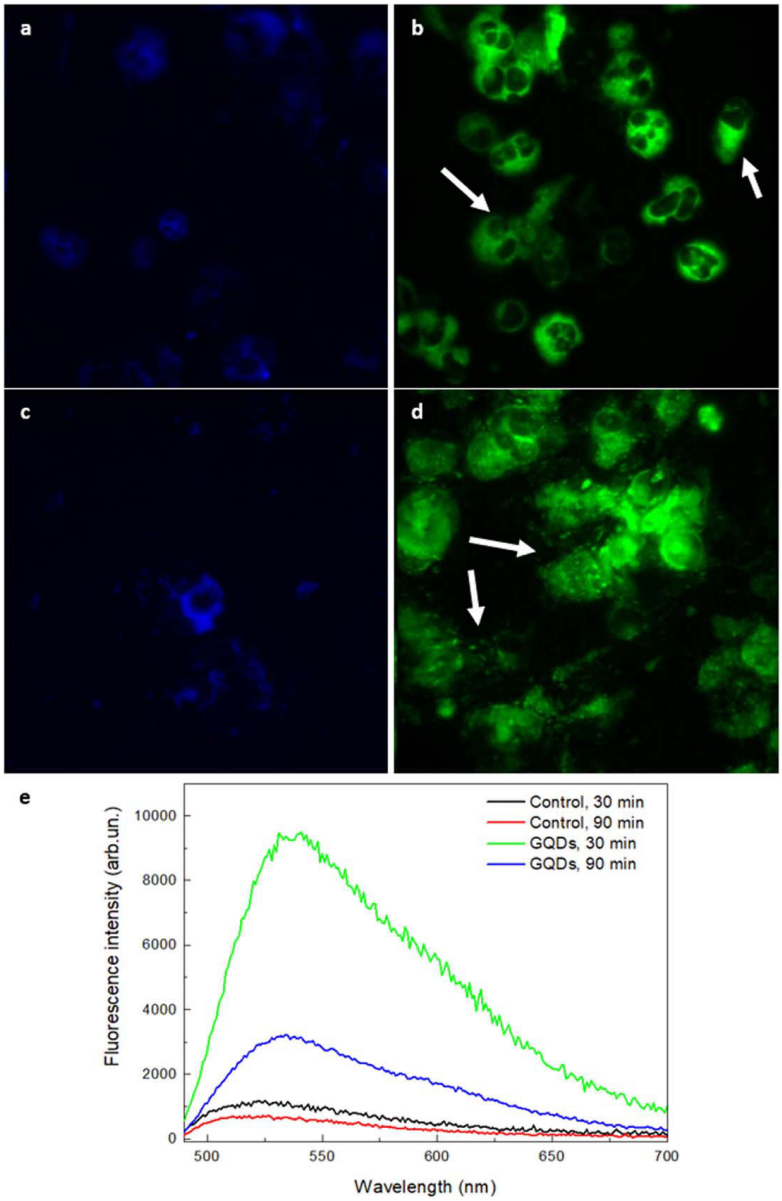

Figure 7. GQD accumulation in neutrophils: (a) neutrophils, 30 min adhesion, autofluorescence (470/530 nm); (b) neutrophils, 30 min adhesion: GQDs (470/530 nm); (c) neutrophils, 90 min adhesion, autofluorescence (470/530 nm); (d) neutrophils, 90 min adhesion, GQDs (470/530 nm); (e) fluorescence spectra of neutrophils in control samples (black and red lines) and pretreated with GQDs (green and blue lines) for 30 and 90 min, respectively. Spectra are averages of spectra from 5 different points in the sample. Excitation was at 470 nm.

neutrophils, as GQDs react only with HClO and do not scavenge H_2O_2, which is the substrate for MPO [54].

In our experiments, neutrophil activation was induced via their adhesion to the Si wafer surface for 30 min [55]. Fluorescence images of MPO distribution and F-actin cytoskeleton are presented in figures 6(a), (b). MPO is localized in the cytoplasm of cells inside the azurophilic granules near the cell membrane [19]. The membrane of neutrophils retains its integrity and no MPO leakage is detected. Neutrophil adhesion induces the condensation of F-actin along the membrane edge as well as around enzyme-containing granules (figure 6(b)). Exposure of adhering neutrophils to GQDs (50 μg ml^{-1}) intensifies the activation process, which is accompanied by the more vigorous spreading of cells on the surface and the appearance of wide lamellipodia. In some cases, the disruption of the membrane integrity and the MPO release to the outer space (figure 6(c)) is accompanied by the F-actin reorganization and the disturbance of the shape-supporting frame in the area proximal to the membrane (figure 6(d)). Interaction of 50 μg ml^{-1} of GQDs with neutrophils during their adhesion induces GQD phagocytosis. Figure 7 depicts the fluorescence of accumulated GQDs in neutrophils after 30 and 90 min of cell exposure to GQDs. As excitation/emission of green fluorescent GQDs is at 488/530 nm, it could overlap with the neutrophil autofluorescence. For this reason, fluorescence images were collected both for neutrophils (figures 7(a), (c)) and neutrophils exposed to GQDs (figures 7(b), (d)). Figures 7(b) and (d) show that GQDs are accumulated in cells and are observed due to their bright fluorescence, significantly exceeding the background autofluorescence. Moreover, data shown in figure 6(b) confirm that 30 min exposure of cells to GQDs leads to the formation of wide lamellipodia by some cells. The integrity of the membrane is disrupted for several neutrophils, and the content of the cell is released to the outer space (figure 7(b), marked with arrows).

More prolonged exposure of cells to GQDs leads to the violation of the cell membrane integrity and the release of the content into the external environment (figure 7(d), marked with arrows). The shape of the distribution of quantum dots on the surface around activated cells defines, that neutrophils are morphologically similar to cells that form neutrophil extracellular traps. Thus, one can suggest that the activation of cells exposed to GQDs occurred via the mechanism of neutrophil extracellular trap formation, which is accompanied by the release of MPO into the extracellular environment [56]. In this case, the activation of MPO should lead to the production of hypochlorous radicals, which should significantly affect the fluorescent characteristics of GQDs. Indeed, the GQDs fluorescence spectra measured from both samples indicate that the activation of MPO and the production of hypochlorous radicals occurred in both cases. The significant redshift of fluorescence maxima of GQD in neutrophils exposed to GQDs for 30 min indicates the damage of the GQD structure by hypochlorous radicals (figure 7(e), green line). More extended interaction of cells with GQDs is reflected in both redshift and a strong fluorescence intensity decrease what could be assigned to the total disruption of GQD structure (figure 7(e), blue line).

4. Conclusions

By using the model and cellular systems (human neutrophils), we demonstrate that GQDs can be used for sensing the hypochlorous acid content. Structural and spectroscopic properties of GQDs are not affected by the H_2O_2 in a wide range of concentrations (0.01–10.0 mM), while hypochlorous acid causes significant structural changes which are reflected in the modification of absorbance, excitation, and fluorescence properties. Moreover, these changes are not associated with the organic surfactant (e.g. PEG), which stabilizes the aqueous GQD suspension. Interaction of GQDs with NaClO (source of OCl^-) leads to the modification of C–O–C/C=O/C–O–H groups, the damage of the carbonic core of GQDs and the formation of excessive C=O groups on the sites of epoxy-groups localization. As a result, absorption (excitation) bands disappear in a time- and dose-dependent manner. Fluorescence spectral peak redshifts. The decrease of the value and relative impact of the fast component of the GQD fluorescence lifetime in the presence of NaClO, is probably associated with the C=C band damage. However, modification of oxygen-containing functional groups induces an increase in both the value and relative impact of the slow component τ_2. All these changes, caused by hypochlorous acid, but not by H_2O_2 are at the core of the investigation of the MPO activation in neutrophils. It is demonstrated that neutrophils accumulate GQDs by the phagocytic pathway. This process is accompanied by neutrophil activation, MPO release and hypochlorous acid production. GQDs allow obtaining data on GQDs distribution in cells and further disruption of cellular membrane integrity by fluorescence microscopy, while GQD fluorescence spectra (intensity and peak position) provide information on the hypochlorous acid production by neutrophils. Moreover, it is demonstrated that neutrophil activation and MPO release causes significant structural damage of GQDs, allowing to assume the initiation of the biodegradation of GQDs by neutrophils.

Summing up, green fluorescent GQDs are a promising material for biomedical sensing applications. They enable selective and accurate sensing of RCS impact in redox processes in biological systems. They are biodegradable and, thus, suitable for various biomedical applications.

Acknowledgments

This work was supported by Horizon 2020 RISE DiSeTCom (Project No 823728), the Belarusian Republican Foundation for Fundamental Research (Project No M20M-075), Belarusian State Program of Scientific Research 'Convergence-2025' (project No 20210397), the Academy of Finland Flagship Programme, Photonics Research and Innovation (PREIN) (Project No 320166), the Academy of Finland (Projects No 298298 and No 334270). We are thankful for

Professor Gediminas Niaura (Center for Physical sciences and Technology, Vilnius, Lithuania) for fruitful discussion on SERS and Raman spectroscopy data, and for Sergey Filippovich and Tsimafei Ramanouski (Chemical Faculty, Belarusian State University, Minsk, Belarus) for assistance in the explanation of the mechanisms of oxidants effects in GQDs.

Data availability statement

The data that support the findings of this study are available upon reasonable request from the authors.

Conflicts of interest

There are no conflicts to declare.

Ethical statement

Healthy volunteers (8 persons) were invited to donate blood for research in the Republican Scientific Practical Center for Transfusiology and Medical Biotechnology (Minsk, Belarus) in accordance with the principles embodied in the Declaration of Helsinki and approved by the Review Board of the National Academy of Sciences of Belarus within the framework of the project No 20210397, Belarusian State Program of Scientific Research 'Convergence-2025'. All participants are aware of intended publication and have given a written consent for it.

ORCID iDs

Lena Golubewa https://orcid.org/0000-0003-2125-6366
Tatsiana Kulahava https://orcid.org/0000-0002-1113-7323
Aliona Klimovich https://orcid.org/0000-0002-4015-3517
Danielis Rutkauskas https://orcid.org/0000-0003-4705-2222
Ieva Matulaitiene https://orcid.org/0000-0001-7664-2331
Renata Karpicz https://orcid.org/0000-0001-5884-4538
Nikita Belko https://orcid.org/0000-0002-9926-3462
Dmitri Mogilevtsev https://orcid.org/0000-0002-9072-7558
Alena Kavalenka https://orcid.org/0000-0001-6813-9154
Marina Fetisova https://orcid.org/0000-0002-7531-3891
Petri Karvinen https://orcid.org/0000-0002-3251-2524
Yuri Svirko https://orcid.org/0000-0002-2927-6233
Polina Kuzhir https://orcid.org/0000-0003-3689-0837

References

[1] Zhang Z, Zhang J, Chen N and Qu L 2012 Graphene quantum dots: an emerging material for energy-related applications and beyond *Energy Environ. Sci.* **5** 8869–90
[2] Zhu S, Song Y, Wang J, Wan H, Zhang Y, Ning Y and Yang B 2017 Photoluminescence mechanism in graphene quantum dots: Quantum confinement effect and surface/edge state *Nano Today* **13** 10–4
[3] Younis M R, He G, Lin J and Huang P 2020 Recent advances on graphene quantum dots for bioimaging applications *Front. Chem.* **8** 424
[4] Fan T, Zeng W, Tang W, Yuan C, Tong S, Cai K, Liu Y, Huang W, Min Y and Epstein A J 2015 Controllable size-selective method to prepare graphene quantum dots from graphene oxide *Nanoscale Res. Lett.* **10** 55
[5] Kang S H, Mhin S, Han H, Kim K M, Jones J L, Ryu J H, Kang J S, Kim S H and Shim K B 2016 Ultrafast method for selective design of graphene quantum dots with highly efficient blue emission *Sci. Rep.* **6** 1–7
[6] Tian P, Tang L, Teng K S and Lau S P 2018 Graphene quantum dots from chemistry to applications *Mater. Today Chem.* **10** 221–58
[7] Tabish T A, Scotton C J, Ferguson D C J, Lin L, Van Der Veen A, Lowry S, Ali M, Jabeen F, Winyard P G and Zhang S 2018 Biocompatibility and toxicity of graphene quantum dots for potential application in photodynamic therapy *Nanomedicine* **13** 1923–37
[8] Yan C, Hu X, Guan P, Hou T, Chen P, Wan D, Zhang X, Wang J and Wang C 2020 Highly biocompatible graphene quantum dots: green synthesis, toxicity comparison and fluorescence imaging *J. Mater. Sci.* **55** 1198–215
[9] Chen F, Gao W, Qiu X, Zhang H, Liu L, Liao P, Fu W and Luo Y 2017 Graphene quantum dots in biomedical applications: recent advances and future challenges *Front. Lab. Med.* **1** 192–9
[10] Barrera J, Ibañez D, Heras A, Ruiz V and Colina A 2017 *In situ* evidence of the redox-state dependence of photoluminescence in graphene quantum dots *J. Phys. Chem. Lett.* **8** 531–7
[11] Ryan B J, Lo Faro M L, Whiteman M and Winyard P G 2016 Reactive oxygen species *Compendium of Inflammatory Diseases* (Basel: Springer) pp 1145–50
[12] Akhigbe R and Ajayi A 2021 The impact of reactive oxygen species in the development of cardiometabolic disorders: a review *Lipids Health Dis.* **20** 1–18
[13] Ju J and Chen W 2014 Synthesis of highly fluorescent nitrogen-doped graphene quantum dots for sensitive, label-free detection of Fe (III) in aqueous media *Biosens. Bioelectron.* **58** 219–25
[14] Lou Y, Ji J, Qin A, Liao L, Li Z, Chen S, Zhang K and Ou J 2020 Cane molasses graphene quantum dots passivated by PEG functionalization for detection of metal ions *ACS Omega* **5** 6763–72
[15] Blanco A and Blanco G 2017 Enzymes *Med. Biochem.* (New York: Academic) pp 153–75
[16] Wu X, Tian F, Wang W, Chen J, Wu M and Zhao J X 2013 Fabrication of highly fluorescent graphene quantum dots using L-glutamic acid for *in vitro*/*in vivo* imaging and sensing *J. Mater. Chem.* C **1** 4676–84
[17] Freeman S A and Grinstein S 2014 Phagocytosis: receptors, signal integration, and the cytoskeleton *Immunol. Rev.* **262** 193–215
[18] Segal A W 2005 How neutrophils kill microbes *Annu. Rev. Immunol.* **23** 197–223
[19] Othman A, Sekheri M and Filep J G 2021 Roles of neutrophil granule proteins in orchestrating inflammation and immunity *FEBS J.* **8** 22
[20] Kiryu C, Makiuchi M, Miyazaki J, Fujinaga T and Kakinuma K 1999 Physiological production of singlet molecular oxygen in the myeloperoxidase-H2O2-chloride system *FEBS Lett.* **443** 154–8
[21] Klebanoff S J 2005 Myeloperoxidase: friend and foe *J. Leukoc. Biol.* **77** 598–625

[22] Arnhold J 2020 The dual role of myeloperoxidase in immune response *Int. J. Mol. Sci.* **21** 1–28
[23] Davies M J and Hawkins C L 2020 The role of myeloperoxidase in biomolecule modification, chronic inflammation, and disease *Antioxidants Redox Signal.* **32** 957–81
[24] Liew P X and Kubes P 2019 The Neutrophil's role during health and disease *Physiol. Rev.* **99** 1223–48
[25] Mollinedo F 2019 Neutrophil degranulation, plasticity, and cancer metastasis *Trends Immunol.* **40** 228–42
[26] Golubewa L *et al* 2020 Surface-enhanced raman spectroscopy of organic molecules and living cells with gold-plated black silicon *ACS Appl. Mater. Interfaces* **12** 50971–84
[27] Zhang X F, Zhang J and Liu L 2014 Fluorescence properties of twenty fluorescein derivatives: lifetime, quantum yield, absorption and emission spectra *J. Fluoresc.* **24** 819–26
[28] Boyum A 1976 Isolation of lymphocytes, granulocytes and macrophages *Scand. J. Immunol.* **5** 9–15
[29] Rajender G and Giri P K 2016 Formation mechanism of graphene quantum dots and their edge state conversion probed by photoluminescence and Raman spectroscopy *J. Mater. Chem.* C **4** 10852–65
[30] Shameli K, Bin Ahmad M, Jazayeri S D, Sedaghat S, Shabanzadeh P, Jahangirian H, Mahdavi M and Abdollahi Y 2012 Synthesis and characterization of polyethylene glycol mediated silver nanoparticles by the green method *Int. J. Mol. Sci.* **13** 6639–50
[31] Vrandečić N S, Erceg M, Jakić M and Klarić I 2010 Kinetic analysis of thermal degradation of poly(ethylene glycol) and poly(ethylene oxide)s of different molecular weight *Thermochim. Acta* **498** 71–80
[32] Philip D 2009 Honey mediated green synthesis of gold nanoparticles *Spectrochim. Acta* A **73** 650–3
[33] Chu X, Wang S and Cao Y 2020 A new fluorescence probe comprising nitrogen-doped graphene quantum dots for the selective and quantitative determination of cerium(iv) *New J. Chem.* **44** 797–806
[34] Raeyani D, Shojaei S, Kandjani S A and Wlodarski W 2016 Synthesizing graphene quantum dots for gas sensing applications *Proc. Eng.* **168** 1312–6
[35] Zhuang J, Li M, Pu Y, Ragauskas A J and Yoo C G 2020 Observation of potential contaminants in processed biomass using fourier transform infrared spectroscopy *Appl. Sci.* **10** 1–13
[36] Bantignies J L, Sauvajol J L, Rahmani A and Flahaut E 2006 Infrared-active phonons in carbon nanotubes *Phys. Rev.* B **74** 195425–6
[37] Iannazzo D *et al* 2019 A smart nanovector for cancer targeted drug delivery based on graphene quantum dots *Nanomaterials* **9** 1–17
[38] Zhang X, Li H, Yi C, Chen G, Li Y, Zhou Y, Chen G, Li Y, He Y and Yu D 2020 Host immune response triggered by graphene quantum-dot-mediated photodynamic therapy for oral squamous cell carcinoma *Int. J. Nanomed.* **15** 9627–38
[39] Liu J *et al* 2020 Surface functionalization with polyethylene glycol and polyethyleneimine improves the performance of graphene-based materials for safe and efficient intracellular delivery by laser-induced photoporation *Int. J. Mol. Sci.* **21** 1540
[40] Justin R *et al* 2016 Photoluminescent and superparamagnetic reduced graphene oxide-iron oxide quantum dots for dual-modality imaging, drug delivery and photothermal therapy *Carbon* **97** 54–70
[41] Wu J, Wang P, Wang F and Fang Y 2018 Investigation of the microstructures of graphene quantum dots (GQDs) by surface-enhanced Raman spectroscopy *Nanomaterials* **8** 864
[42] Chhabra V A, Kaur R, Kumar N, Deep A, Rajesh C and Kim K H 2018 Synthesis and spectroscopic studies of functionalized graphene quantum dots with diverse fluorescence characteristics *RSC Adv.* **8** 11446–53
[43] Das R, Parveen S, Bora A and Giri P K 2020 Origin of high photoluminescence yield and high SERS sensitivity of nitrogen-doped graphene quantum dots *Carbon* **160** 273–86
[44] Yamini D, Devanand Venkatasubbu G, Kumar J and Ramakrishnan V 2014 Raman scattering studies on PEG functionalized hydroxyapatite nanoparticles *Spectrochim. Acta* A **117** 299–303
[45] Matulaitiene I, Barkauskas J, Trusovas R, Račiukaitis G, Mažeikiene R, Eicher-Lorka O and Niaura G 2013 Potential dependence of SERS spectra of reduced graphene oxide adsorbed on self-assembled monolayer at gold electrode *Chem. Phys. Lett.* **590** 141–5
[46] Yogesh G K, Shuaib E P, Kalai Priya A, Rohini P, Anandhan S V, Krishnan U M, Kalyanavalli V, Shukla S and Sastikumar D 2021 Synthesis of water-soluble fluorescent carbon nanoparticles (CNPs) from nanosecond pulsed laser ablation in ethanol *Opt. Laser Technol.* **135** 106717
[47] Li Y, Zhao Y, Cheng H, Hu Y, Shi G, Dai L and Qu L 2012 Nitrogen-doped graphene quantum dots with oxygen-rich functional groups *J. Am. Chem. Soc.* **134** 15–8
[48] Yan X, Cui X, Li B and Li L S 2010 Large, solution-processable graphene quantum dots as light absorbers for photovoltaics *Nano Lett.* **10** 1869–73
[49] Zhang M *et al* 2012 Facile synthesis of water-soluble, highly fluorescent graphene quantum dots as a robust biological label for stem cells *J. Mater. Chem.* **22** 7461–7
[50] Gan Z, Xu H and Hao Y 2016 Mechanism for excitation-dependent photoluminescence from graphene quantum dots and other graphene oxide derivates: Consensus, debates and challenges *Nanoscale* **8** 7794–807
[51] Dong Y, Shao J, Chen C, Li H, Wang R, Chi Y, Lin X and Chen G 2012 Blue luminescent graphene quantum dots and graphene oxide prepared by tuning the carbonization degree of citric acid *Carbon* **50** 4738–43
[52] Tachi S, Morita H, Takahashi M, Okabayashi Y, Hosokai T, Sugai T and Kuwahara S 2019 Quantum yield enhancement in graphene quantum dots via esterification with benzyl alcohol *Sci. Rep.* **9** 1–7
[53] Kim S, Hee Shin D, Oh Kim C, Seok Kang S, Min Kim J, Choi S H, Jin L H, Cho Y H, Won Hwang S and Sone C 2012 Size-dependent radiative decay processes in graphene quantum dots *Appl. Phys. Lett.* **101** 163103
[54] Davies M J 2021 Myeloperoxidase: mechanisms, reactions and inhibition as a therapeutic strategy in inflammatory diseases *Pharmacol. Ther.* **218** 107685
[55] Kuznetsova T, Kulahava T, Zholnerevich I, Amaegberi N, Semenkova G, Shadyro O and Arnhold J 2017 Morphometric characteristics of neutrophils stimulated by adhesion and hypochlorite *Mol. Immunol.* **87** 317–24
[56] Rada B 2019 Neutrophil extracellular traps *Methods Mol. Biol.* **1982** 517–28

NOTES

Vilniaus universiteto leidykla
Saulėtekio al. 9, III rūmai, LT-10222 Vilnius
El. p. info@leidykla.vu.lt, www.leidykla.vu.lt
Tiražas 30 egz.

NUO / SINCE 1579

Fragmentas iš Vilniaus universiteto auklėtinio Alberto Diblinskio (1601–1665) vieno geriausių XVII a. astronomijos veikalų *Centuria astronomica* (Vilnius, 1639), kuriame pateikta astronomijos pasiekimų apžvalga, remiantis stebėjimais teleskopu, atliktais kartu su kitu VU mokslininku, matematiku ir astronomu Osvaldu Krygeriu (apie 1598–1655).

VU biblioteka, BAV 47.10.21

Fragment from *Centuria astronomica* (Vilnius, 1639), one of the most well-known works on astronomy from the 17th c., written by Vilnius University graduate Albertas Diblinskis (1601–1665). It presents an overview of achievements in the field of astronomy, based on observations using a telescope together with another VU scientist, mathematician, and astronomer Osvaldas Krygeris (c. 1598–1655).

VU Library, BAV 47.10.21

bookshop.vu.lt journals.vu.lt

https://doi.org/10.15388/vu.thesis.493